Mechanical phenotyping of cells in microsystems to detect pathologies

Magalie Faivre

To cite this version:

Magalie Faivre. Mechanical phenotyping of cells in microsystems to detect pathologies. Micro and nanotechnologies/Microelectronics. Université Claude Bernard - Lyon 1, 2022. tel-03830595

HAL Id: tel-03830595

https://theses.hal.science/tel-03830595

Submitted on 26 Oct 2022

HABILITATION A DIRIGER LES RECHERCHES

Préparée à
Institut des Nanotechnologies de Lyon, UMR5270

Soutenue publiquement le 15/09/2022, par :

Magalie Faivre

Mechanical phenotyping of cell in microsystems to detect pathologies

Phénotypage mécanique de cellules en microsystème pour la détection de pathologies

Devant le jury composé de :

Philippe Connes Professeur, Université CLaude Bernard, Lyon 1	**Président**
Stéphanie Descroix Directrice de Recherche, CNRS	**Examinatrice**
Yves Fouillet Directeur de Recherche CEA, CEA/Léti	**Rapporteur**
Bruno Lepiouffle Professeur, ENS Cachan	**Rapporteur**
Giovanna Tomaiuolo Professeure Associée, Università degli Studi di Napoli Federico II	**Rapporteure**
Claude Verdier Directeur de Recherche, CNRS	**Examinateur**

Remerciements

Je voudrais remercier tout d'abord l'ensemble des membres du jury : Philippe Connes, Stéphanie Descroix, Yves Fouillet, Bruno Le Pioufle, Giovanna Tomaiuolo et Claude Verdier, d'avoir accepté d'évaluer mon travail et pour les discussions passionnantes durant la soutenance. Un merci tout particulier à Yves, Bruno et Giovanna pour leur regard bienveillant sur le manuscrit et les résultats qui y sont discutés.

Ce manuscrit ne décrit pas les travaux menés durant les 10 dernières années par une seule personne, mais plutôt l'aboutissement d'un ensemble de contributions, obtenues notamment grâce au travail et à l'investissement de tous les gens qui ont interagi avec moi sur ces thématiques. Je veux parler bien évidemment de ceux qui ont été en première ligne : les étudiants que j'ai co-encadrés au fil des années. Il y a les doctorants : Renaud Gelszinnis, Amin Amirouche, Jaime Andrès Martinez SantaMaria, Ali Kheir Aldine and Blandine Allais, que j'ai eu le temps de voir "grandir" et évoluer pour passer du statut d'étudiant à celui de collaborateur. Je voudrais les remercier de leur investissement, moi aussi j'ai beaucoup appris à leur contact. Merci aussi à Josué Esteves pour ces 2 années d'ATER. Merci à tous les stagiaires : Antoine Confavreux, Emilie Testa, Pauline Risson, Laurène, Elisa Cerda, Julien Castellucci, intan putri kusumaningrum, Almudena Humanes Villén, Souhila Sacci, Kirill Akripov, Aela Mauffrey, Amel Bessaa, Lucas Ferry, Ali Kheir Aldine, Enyi Chen, Blandine Simon, Fernando Carlos Hernandez and Adam Habouria.

Avant de remercier mes collègues de l'INL, je voudrais prendre le temps de remercier les différentes directions de l'INL : Guy Hollinger qui m'a si bien accueilli au laboratoire à mon recrutement. Un merci tout particulier à Catherine Bru-Chevallier pour m'avoir soutenue, poussée et avoir cru en moi quand je n'y arrivais pas. Bruno Masenelli pour sa gentillesse et son soutien auxquels j'associe également Ségolène Callard et Jean-Louis Leclerc.
J'en viens donc à mes collègues du groupe LOCI. Merci à Rosaria qui a misé sur moi (j'espère avoir méritée ta confiance). Son amitié, et son soutien indéfectible durant toutes ces années, ont permis de construire la chercheuse que je suis aujourd'hui. Merci à Anne-Laure Deman, Jean-François Chateaux et Marie-Charlotte Audry avec qui j'ai étroitement travaillé. J'ai beaucoup apprécier ce temps partagé à réfléchir, bosser, cuisiner, manger et rigoler. J'espère que ces interactions continueront pendant encore au moins 12 ans. Merci aussi à Pascal Kleimann, Louis Renaud et Yasmina Layouni. Merci aussi à la petite nouvelle Caterina Tomba. Merci pour tes conseils, ta bonne humeur et de m'éviter de manger mes biscuits et autres bonbons toute seule. Merci plus largement à tous les membres de l'équipe DSE, en particulier Yann Chevolot, Claudine Gehin et Emmanuelle Laurenceau. Merci à mes collègues des autres équipes de l'INL : Taha Benyattou, Lotfi Berguiga, Cécile Jamois, Xavier Letartre, grâce à vous j'ai appris tellement sur la photonique et les papillons bleus ;). Laurent Quiquerez, Patrick Pittet merci de votre bonne humeur et de nous démontrer au quotidient que chez LOCI, il n'y a que les meilleurs . . .
Je ne pourrais pas exposer dans ce manuscrit mes thématiques de recherche, sans ceux qui font tourner la salle blanche de l'INL. Jérôme Degouttes, Nicolas Terrier et Patrick Pittet sont au cœur des rouages de cet instrument incroyable qu'est Nanolyon. Ce sont eux qui font qu'aucun problème technique n'est insurmontable et qu'aucune panne n'est irréparable. Je voudrai profiter de l'occasion pour remercier également Jérôme Degouttes pour être mon équipier pour le meilleur et pour l'hygiène et la sécurité depuis 12 ans maintenant. J'ai toujours pu compter sur toi pour m'accompagner, entre autres, à travers les inventaires de la salle de chimie, les formations des nouveaux entrants et la rédaction du DUER. Tu

es le grand maître des plans de prévention.

Merci aussi à mes collaborateurs extérieurs sans qui ce travail interdisciplinaire n'aurait aucun sens. Merci à Charlotte Rivière et Jean-Paul Rieu de l'iLM, Stéphane Picot et Adeline Lavoignat de l'ICBMS, Philippe Connes, Céline Renoux et Elie Nader du LIBM, Hichem Mertani, Jean-Jacques Diaz, Sylvain Lefort et Véronique Maguer-Satta du CRCL et Thomas Grenier de CREATIS.

Enfin, merci à ma famille, ma mère et mon frère pour leur confiance et leurs encouragements, ma soeur Cendrine qui a su me montrer la voie : tu vois la quarantaine et toujours à tout faire comme toi. C'est aussi grâce à eux que j'ai pu tenir la distance. Merci à François qui m'a supporté tout ce temps et qui a su m'apporter tant de choses (si si !!! et même 2 “Thunders”) et à mes filles Emma et Lilou pour leur enthousiasme communicatif. Vous êtes mes expériences les plus réussies.

Contents

List of Figures

List of Tables

Acronyms

AFM	Atomic Force Microscopy
ALAT	ALanine AminoTransferase
AML	Acute Myeloid Leukemia
ANR	Agence National de la Recherche
araC	Cytarabine
ASAT	ASpartate AminoTransferase
ATER	Attaché Temporaire d'Enseignement et de Recherche
BMP	Bone Morphogenetic Protein
BSA	Bovin Serum Albumin
CAT	Collective to Amoeboid Transition
CCD	Charge Coupled Device
CEA	Commissariat à l'Energie Atomique
CLARA	Cancéropôle Lyon Auvergne Rhône-Alpes
CLB	Centre Léon Bérard
CME	Coefficient of Motion Efficiency
CNRS	Centre National de la Recherche Scientifique
CR	Chargée de Recherche
CREATIS	Centre de REcherche en Acquisition et Traitement de l'Image pour la Santé
CRCL	Centre de Rercherche en Cancérologie de Lyon
DEAS	Department of Engineering and Applied Sciences
DI	De-Ionised
DIC	Differential Interference Contrast
DLD	Deterministic Lateral Displacement
DNA	DeoxyriboNucleic Acid
DRRT	Délégation Régionale à la Recherche et à la Technologie
DSE	"Dispositifs pour la Santé et l'Environement"

ECIS	Electric Cell-substrate Impedance Sensing
ECM	ExtraCellular Matrix
EDTA	EthyleneDiamineTetraacetic Acid
EEA	Electronique Electrotechnique et Automatique
EIS	Electrical Impedance Spectroscopy
EMT	Epithelial to Mesenchymal Transition
ESPCI	Ecole Supérieure de Physique et de Chimie Industrielles
FBS	Fetal Bovine Serum
GDR	Groupement de Recherche
gRBC	inflated Red Blood Cell
gRBCs	inflated Red Blood Cells
GUVs	Giant Unilamelar Lipid Vesicles
HDR	Habilitation à Diriger les Recherches
HgbS	Hemoglobin S
HIV	Human Immunodeficiency Virus
hRBC	healthy Red Blood Cell
hRBCs	healthy Red Blood Cells
HS	Hereditary Spherocytosis
ILM	Institut Lumière Matière
i-LUM	“Ingérierie et conversion de LUMière”
INL	Institut des Nanotechnologies de Lyon
i-PDMS	iron-PolyDiMethyl Siloxane
iRBC	malaria infected Red Blood Cell
iRBCs	malaria infected Red Blood Cells
ITO	Indium Tin Oxide
L3	Licence 3
LMI	Laboratoire des Multimatériaux et Interfaces
LOCI	“Lab-On-a-Chip & Instrumentation”
LOC	Lab-On-a-Chip
LPC	LysoPhosphatidylCholine or lysolecithine

M1	Master 1
M2	Master 2
MANOVA	Multivariate ANalysis Of VAriance
MAT	Mesenchymal to Amoeboid Transition
MCF	Maître de ConFérence
MCHC	Mean Corpuscular Hemoglobin Concentration
MEMS	MicroElectroMechanical Systems
NA	Numerical Aperture
OWC	Oscillating Width Channel
OWCLC	Oscillating Width Channel with Longer Constrictions
OWCLE	Oscillating Width Channel with Longer Enlargements
OWCWE	Oscillating Width Channel with Wider Enlargements
OWCWLE	Oscillating Width Channel with Wider and Longer Enlargements
P. falciparum	*Plasmodium falciparum*
PAA	PolyAcrylAmide
PBS	Phosphate-Buffered Saline
PCL	Poly CaproLactone
PDMS	PolyDiMethyl Siloxane
PEO	PolyEthylene Oxide
PFF	Pinched Flow Fractionation
PhC	Photonic Crital
PhCs	Photonic Critals
PhD	Doctorate of Philosophy
PhDs	Doctors of Philosophy
PMMA	PolyMethyl MethAcrylate
POC	Point-Of-Care
PolyNIPAM	Poly-N-isopropylacrilamide
PS	Penicillin-Streptomycin
RBC	Red Blood Cell
RBCs	Red Blood Cells
ring-iRBCs	malaria infected Red Blood Cells with a ring stage parasite
RPMI	Roswell Park Memorial Institute medium
rRBC	rigidified Red Blood Cell

rRBCs	rigidified Red Blood Cells
RT-DC	Real Time Deformability Cytometry
SCA	Sickle Cell Anemia
SEM	Scanning Electron Microscopy
T-rRBC	Thermally Rigidified Red Blood Cell
T-rRBCs	Thermally Rigidified Red Blood Cells
UCBL	Université Claude Bernard Lyon 1
UJF	Université Joseph Fourier Grenoble 1
ULC	Unique Long Constriction
WBCs	White Blood Cells
YAP	Yes associated protein

Glossary

Symbols

3T3

3T3 is a fibroblast cell line that was isolated from a mouse embryo. 4, 57

H

HepG2

HepG2 is a cell line exhibiting epithelial-like morphology that was isolated from a hepatocellular carcinoma of a 15-year-old, White, male youth with liver cancer. 49

HL-60

HL-60 cells are promyeoloblasts isolated from the peripheral blood by leukopheresis from a 36-year-old, Caucasian female with acute promyelocytic leukemia. HL-60 cells predominantly show neutrophilic promyelocytic morphology. 5, 42, 43, 58, 88, 134

M

MCF-10A

MCF-10A is an epithelial cell line that was isolated from the mammary gland of a White, 36-year-old female with fibrocystic breasts. They ar used as heathy models of cancerous cells. 49, 56

MCF-7

MCF7 are epithelial cells isolated from the breast tissue of a 69-year-old, White, female patient with metastatic adenocarcinoma. MCF-7 present epithelial characteristics, low motility and high cohesiveness, used as cancerous models of breast cancer cells. 3, 4, 41, 42, 45, 49, 51, 56

MDA-MB-231

MDA-MB-231 are epithelial cells isolated from the breast tissue of a 51-year-old, White, female adenocarcionma patient. MDA-MB-231 cells are motile, highly invasive and poorly cohesive cells, used as metastatic models of breast cancer cells. 3, 4, 41, 42, 44–46, 48–53

ML2-R

ML2-R is a sub-population of ML2-S resistant to chemotherapy. They are obtained by maintaining the ML2-S under 1 µM of araC during the culture. 8, 10, 11, 84, 86–88, 133, 134

ML2-S

ML2-S or ML2 cells have been established from the peripheral blood of a 26-year-old man with acute myeloid leukemia (AML M4) at diagnosis of AML (following T-non-Hodgkin lymphoma and T-ALL). 7, 8, 10, 11, 84–88, 133–135

modMCF-7

modMCF-7 are chemically modified MCF-7 cells, generated by treating MCF-7 cells with 100 nM 12-O-tetradecanoylphorbol-13-acetate for 18 h. modMCF-7 cells show a dramatic increase (18-fold) in their invasiveness and their metastatic potential [134]. 56

P

Panc-1

Panc-1 is a cell line exhibiting epithelial morphology that was isolated from the pancreatic duct of a 56-year-old, White, male with epithelioid carcinoma. 42

T

THP-1

THP-1 is a monocyte isolated from peripheral blood from an acute monocytic leukemia patient. It is used as a model for White Blood Cells. 5, 59, 130

W

Walker 256 carcinosarcoma cells

Walker 256 carcinosarcoma is a rat tumor cell line. 43

CurriculumVitae

Magalie Faivre
32 bis rue Eugène Pons
69004 LYON
born 21/08/1980, Echirolles (38)
2 children born in 2016 and 2019

Chargée de Recherche at INL UMR 5270
http://inl.cnrs.fr
magalie.faivre@univ-lyon1.fr
+33 (0)4 72 43 16 43

Microfluidics and microsystems for biotechnologies

Education

- **PhD in Biophysics** Université Joseph Fourier Grenoble 1 (UJF), 2006, under the supervison of Dr. Annie Viallat (Laboratoire de Spectrométrie Physique, Grenoble), Pr. Howard A. Stone (Department of Engineering and Applied Sciences (DEAS), Harvard University, Cambridge USA) and Dr. Brigitte Pépin-Donat (CEA, Grenoble).
- **Master Chimie Physique Moléculaire et Structurale** (UJF), 2003.
- **Maîtrise de Sciences Physiques** (UJF), 2002.

Professional experience

- **Development of microfluidic diagnostic tools based on the exploitation of cells mechanical properties.**
  Centre National de la Recherche Scientifique (CNRS)/Institut des Nanotechnologies de Lyon (INL) UMR5270, Lyon : Chargée de Recherche CNRS, since January 2011.
  Development and characterization of fluidic microsystems allowing the detection of a pathology based on a modification of mechanical properties of the cells involved.

- **Encapsulation of a nano-emulsion and *in vivo* released by ultrasounds application.**
  Ecole Supérieure de Physique et de Chimie Industrielles (ESPCI) Paris-Tech/Laboratoire Microfluidique, MEMs et Nanostructures, Paris : Post-doctoral position, 2009-2010.
  Preparation and characterization of a double emulsion of the type water/oil/nano-emulsion of water and study of the release by vaporisation of the oil phase under the action of ultrasounds.

- **Development of a microsystem performing biomedical analyses on a drop of capillary blood.**
  Commissariat à l'Energie Atomique (CEA) Minatec/LETI/Département des Technologies pour la Biologie et la Santé, Grenoble : Post-doctoral position, 2007-2009.
  Development and adaptation of biological protocols in microsystems (confidential industrial project).

- **Drop, vesicles and Red Blood Cells : deformability and behavior under flow.**
  Laboratoire de Spectrométrie Physique, Grenoble et Harvard University/DEAS, Cambridge, USA : PhD, 2004-2006.
  Preparation and characterization of objects (vesicles and drops) with tunable mechanical

properties and study of blood cells mechanical properties through the development of microfluidic tools.

- **Experimental studies of red blood cells and multiphase flows in microfluidic devices.**
  Harvard University / DEAS, Cambridge, USA : Internship (9 months), 2004.
  Production of emulsions (bi or tri-phasic) in microsystem and studies of mechanical properties of blood cells under flow in confined geometry.

- **Dynamic of isolated red blood cells under flow.**
  Laboratoire de Spectométrie Physique, Grenoble : Undership (6 months), 2003.
  Study of the behavior of Red Blood Cells under shear near a wall.

Scientific supervision

▷ **1 Attaché Temporaire d'Enseignement et de Recherche (ATER)**

- 2014 – 2016 **J. Esteves**, *Development of a microfluidic switch able to separate cells upon their mechanical signature*, (founding UCBL 2014 – 2015 and founding INSA 2015 – 2016).

▷ **5 Doctors of Philosophy (PhDs)**

- 2012 – 2015 **R. Gelszinnis** 33% Co-supervision with Anne-Laure Deman (33%) and Rosaria Ferrigno (34%), *Approches microfluidiques pour la séparation de cellules parasitées*, (defended on the 02/07/2015).
- 2014 – 2017 **A. Amirouche** 50% Co-supervision with Rosaria Ferrigno (50%), *Integration of functions dedicated to the mechanical solicitation and characterization of biological cells in microfluidic devices*, (defended on the 25/11/2017).
- 2015 – 2019 **J.A. Martinez SantaMaria** 10% Co-supervision with Eric McAdams (40%) and Rosaria Ferrigno (50%), *Interdigitated Indium Tin Oxide (ITO) sensor for Electric Cell-substrate Impedance Sensing (ECIS) monitoring of breast cancer cells*, (defended on the 05/02/2019).
- 2019 – ... **A. Kheir AlDine** 45% Co-supervision with Taha Benyattou (45%) and Rosaria Ferrigno (10%), *Microsystème optofluidique pour la mesure de propriétés mécaniques de cellules uniques*, (defense scheduled in 2022).
- 2020 – ... **B. Allais** 45% Co-supervision with Marie-Charlotte Audry (45%) and Anne-Laure Deman (10%), *Etude de la déformabilité de cellules par Microscopie à Force Atomique et écoulement en constrictions microfluidiques*, (defense scheduled in 2023).

▷ **18 interns**

- 2011 (6 months) **Antoine Confavreux**, Master 2 (M2), *Migration dirigée de cellules cancéreuses dans un gradient microfluidique : Application au tri cellulaire*.
- 2012 (2 months) **Emilie Testa**, Master 1 (M1), *Approches microfluidiques pour la séparation de cellules parasitées*.
- 2014 (6 months) **Pauline Risson**, M2, *Caractérisation de la stabilité d'un gradient microfluidique appliquée à la chimiotaxie de cellules cancéreuses*.
- 2015 (2 months) **Laurène Dupont**, M1, *Study of the migratory behavior of cancer cells on*

micro-structured tracks.

- 2015 (2 months) **Elisa Cerda**, M1, *Development and characterization of a microfluidic model network of the cerebral microvasculature*.
- 2015 (6 months) **Julien Castelluci**, M2, *Etude de la migration de cellules cancéreuses sur des substrats microstructurés en 3D*.
- 2016 (2 months) **Intan Putri Kusumaningrum Hansen**, M1, *Effect of the geometry a microchannel with oscillating width on the flow of Red Blood Cells*.
- 2016 (2 months) **Almudena Humanes**, M1, *Développement d'un microsystème polymère pour reproduire la méthode de transmigration de cellules métastatiques avec microfluidiques*.
- 2016 (6 months) **Souhila Saci**, M2, *Optimisation d'un système microfluidique pour l'étude de la transmigration à l'échelle des cellules individuelles sous confinement et d'un système de confinement à l'échelle cellulaire*.
- 2017 (2 months) **Kirill Arkhipov**, M1, *Cancer Cell Migratory Response to Nano-structured Substrates*.
- 2018 (3 months) **Aela Mauffrey**, Stage d'Application ECL, *Fabrication of microsystems to study cell transmigration*.
- 2018 (2 months) **Amel Bessaa**, M1, *Impact of surface-area-to-volume ratio, internal viscosity and membrane viscoelasticity on red blood cell deformability*.
- 2018 (2 months) **Lucas Ferry**, Licence 3 (L3), *Influence de la topographie du substrat pour le criblage de substances chimiothérapeutiques*.
- 2019 (6 months) **Ali Kheir AlDine**, M2, *Microsystème optofluidique pour la mesure de propriétés Mécaniques de Cellules uniques*.
- 2020 (6 months) **Enyi Chen**, M2, *Développement d'un traitement d'images embarqué pour la détection de cellules pathologiques par cytométrie de déformabilité*.
- 2020 (6 months) **Blandine Simon**, M2, *Déformabilité des Globules Rouges par Microscopie à Force Atomique et réseaux de constrictions microfluidiques*.
- 2021 (2 months) **Fernando Carlos**, M1, *Evaluation of inter-patients variability in measurement by mechanical cytometry*.
- 2022 (2 months) **Adam Habouria**, M1, *Detection of pathological Red Blood Cells by mechanical cytometry*.

Grants

The projects noted "(PI)" or "(P)" correspond to projects in which I was Principal Investigator or Partner, respectively.

- **P** (2011-2012) Labex Imust, *Impedance-based microfluidic devices for drug screening in cancer (MICASCREEN).* In collaboration with LPMCN and CRCL (PI: LPMCN, J.P. Rieu).
- **P** (2011-2014) ANR BLANC INTERNATIONAL, *Developing new microfluidic chambers for cancer cell screening (ONCO-SCREEN).* In collaboration with INL, CRCL, IBN (Singapour), (PI: INL, R. Ferrigno).
- **P** (2012-2013) CNRS PEPS *Creation of 3D in-vivo tumor like environment for drug screening (SOFT-CAN)*. In collaboration with ILM and CRCL (PI: ILM, C. Rivière).
- **PI** (2014-2015) CNRS PEPS, *Study of the interaction between parasited Red Blood Cells*

and the wall of blood vessels in neuro-malaria (NEURO-PALU). In collaboration with ICBMS and HCL (PI: INL, M. Faivre).

- **P** (2015-2016) ONCOSTARTER (CLARA), *In vivo-like Microfluidic Platform for Analysis of Cancer cell Transmigration (IMPACT)*. In collaboration with ILM and CRCL (PI: CRCL, J.J. Diaz).
- **PI** (2018 – 2019) CNRS PEPS, *Physical Approaches for Parasite Infected Cell Analysis (PAPrICA)*. In collaboration with ICBMS and HCL (PI: INL, M. Faivre).
- **P** (2022 – 2026) ANR PRC, *Optical nanotweezer for single CELL stuDies: from mANipulation to mechaniCal propErties (CellDance)*. In collaboration with ICBMS and LIPhy (PI: INL, T. Benyattou).
- **P** (2022 – 2026) PACK AMBITION RECHERCHE, *Systèmes microfluidiques pour l'étude biophysique et le tri de spores de champignon (*Botrytis cinerea*) phytopathogène (BOTRYPATH)*. In collaboration with MAP and CONIPHY (PI: INL, J.F. Chateaux).

Animation of the scientific community

- Co-organization of the 1st Workshop "Cancer Cell on Chip" in Lyon, June 2012 ($\sim$ 100 attendants).
- INL workshop for "la fête de la Science" in 2015, 2016, 2017 and 2018.
- Co-organization of the 2nd Workshop "Cancer Cell on Chip" in Lyon, April 2019 ($\sim$ 100 attendants).

Expertise

- Expertises for grants:
  - Cancéropole PACA grant, for the call "Emergence" (2018).
  - Tec21: Engineering solutions for the 21st century's increasingly complex challenges (2018 and 2022).
- 2 expertises "Crédit Impôt Recherche" for Délégation Régionale à la Recherche et à la Technologie (DRRT) of Préfecture du Languedoc-Roussillon (2015).
- Jury member for Doctorate of Philosophy (PhD) price of Val de Marne (2013).
- Member of PhD jury:
  - Mélanie Robert on the 03/12/2021 (LIBM, Lyon): invited member.
  - Pierre Taraconat on the 17/01/2020 (IMAG, Montpellier): jury member.
  - Céline Renoux on the 13/12/2018 (LIBM, Lyon): invited member.
  - Hadrien Lamotte on the 11/12/2017 (CEA/Léti, Grenoble): jury member.
  - Antoine Confavreux on the 13/10/2014 (LPMCN, Lyon): invited member.
- Expertises for peer-reviewed international journals:
  - Biomedical Microdevices (2),
  - Microfluidics and Nanofluidics (2).
- Jury member of selection committee for Maître de ConFérence (MCF) recruitment:
  - Poste MCF 28, Université Jean Monnet (2015),
  - Poste MCF 63, Ecole Centrale de Lyon (2021).

Administrative and collective activities

- "Agent de prévention" on the Université Claude Bernard Lyon 1 (UCBL) bulding of INL since 2012.

- “Sauveteur Secouriste du Travail” since 2018.
- Implementation of an experimental space for the manipulation of biological agents (Biosafety Level 1) and nanoparticles in the Nanolyon technological plateform, budget ∼ 40k€ (2012).
- Conception of a laboratory (Biosafety Level 2) as part of the new building INL/CPE.
- Member of INL Laboratory Council since 2021.
- Member of the scientific and strategic committee of the technological plateform NanoLyon since 2021.
- Member of the steering committee of the Groupement de Recherche (GDR) “Micro et Nanofluidique” since 2021.
- Teaching:
  - TP clean room for 5^{th} year Polytech Lyon (2014 and 2015).
  - Tutoriales for Electronique Electrotechnique et Automatique (EEA) Doctoral School (2104 and 2015).
  - Tutoring in Physics and Chemistry, DEUG SVST, 2001 – 2002, Univeristé Joseph Fourier, Grenoble.

Distinction

- 2011 Sylvia Sorkin Greenfield Award for the best scientific paper in **Medical Physics**.

Publications and communications

Total of 21 publications, 1 book chapter, 5 Patents, 1221 collected citations, h-factor = 13 (Scopus). The publications corresponding to my PhD are labeled “T” (for thesis) and the publications associated with some advising are labeled “E”, the name of the advised students are underlined.

▷ Papers in peer-reviewed international journals (P)

[P01]**T** T. Ward, **M. Faivre**, M. Abkarian and H.A. Stone, *“Microfluidic flow focusing: Drop size and scaling in pressure versus flow-rate driven fluid pumping”*, **Electrophoresis**, 26(19):3716-3724, (2005), `https://doi.org/10.1002/elps.200500173`.

[P02]**T** **M. Faivre**, C. Campillo, B. Pepin-Donat and A. Viallat, *“Reversible giant vesicles filled with Poly(N-isopropylacrylamide) sols or gels”*, **Progr. Colloid. Polym. Sci.**, 133:41-44, (2006), `https://doi.org/10.1007/3-540-32702-9_7`.

[P03]**T** M. Abkarian, **M. Faivre** and H.A. Stone, *“High-speed microfluidic differential manometer for cellular-scale hydrodynamics”*, **Proc. Natl. Acad. Sci. USA**, 103(3):538-542, (2006), `https://doi.org/10.1073/pnas.0507171102`.

[P04]**T** **M. Faivre**, M. Abkarian, K. Bickraj and H.A. Stone, *“Geometrical focusing of cells in a microfluidic device: A route to separate blood plasma”*, **Biorheology**, 43(2):147-159, (2006).

[P05]**T** M. Abkarian, **M. Faivre** and A. Viallat, *“Swinging of red blood cells under shear flow”*, **Phys. Rev. Lett.**, 98(18):188302, (2007), `https://doi.org/10.1103/PhysRevLett.98.188302`.

[P06]**T** M. Abkarian, **M. Faivre**, R. Horton, K. Smistrup, C.A. Best-Popescu and H. A. Stone, *“Cellular-scale hydrodynamics”*, **Biomed. Mater.**, 3(3):034011, (2008), `https://doi.org/10.1088/1748-6041/3/3/034011`.

[P07]**T** T. Ward, **M. Faivre**, H.A. Stone, *"Drop production and tip-streaming phenomenon on microfluidic flow focusing device via interfacial saponification chemical reaction"*, **Langmuir**, 26(12):9233-9239, (2010), https://doi.org/10.1021/la100029q.

[P08] O. Couture, **M. Faivre**, N. Pannacci, A. Babataheri, V. Servois, P. Tabeling and M. Tanter, *"Ultrasound internal tattooing"*, **Med. Phys.**, 38(2):1116-1123, (2011), https://doi.org/10.1118/1.3548068.

[P09] **M. Faivre**, P. Peltié, A. Planat-Chrétien, M.L. Cosnier, M. Cubizolles, C. Nogier, C. Négrier and P. Pouteau, *"Coagulation dynamics of a blood sample by multiple scattering analysis"*, **J.** Biomed. Opt., 16(5):057001, (2011), https://doi.org/10.1117/1.3573813.

[P10]**T** F. Quemeneur, C. Quillet, **M. Faivre**, A. Viallat and B. Pépin-Donat, *"Gel phase vesicles buckle into specific shapes"*, **Phys. Rev. Lett.**, 108(10):108303, (2012), https://doi.org/10.1103/PhysRevLett.108.108303.

[P11]**E** **M. Faivre**, R. Gelszinnis, J. Degouttes, N. Terrier, C. Rivière, R. Ferrigno and A.L. Deman, *"Magnetophoretic manipulation in microsystem using i-PDMS microstructures"*, **Biomicrofluidics**, 8(5):054103 (2014), https://doi.org/10.1063/1.4894497.

[P12] J. Marchalot, J.F. Chateaux, **M. Faivre**, H. Mertani, R. Ferrigno and A.L. Deman, *"Dielectrophoretic capture of low abundance cell population using thick electrodes"*, **Biomicrofluidics** 9:054104 (2015), https://doi.org/10.1063/1.4928703.

[P13] D. Le Roy, D. Dhungana, L. Ourry, **M. Faivre**, R. Ferrigno, A. Tamion, V. Dupuis, V. Salles and A.L. Deman, *"Anisotropic ferromagnetic polymer: a first step for their implementation in microfluidic systems"*, **AIP Advances**, 6(5):056604, (2016), https://doi.org/10.1063/1.4943927.

[P14]**E** C. Renoux, **M. Faivre**, A. Bessaa, L. Da Costa, P. Joly, A. Gauthier and P. Connes, *"Impact of surface-area-to-volume ratio, internal viscosity and membrane viscoelasticity on red blood cell deformability measured in isotonic condition"*, **Scientific Reports**, 9:6771, (2019), https://doi.org/10.1038/s41598-019-43200-y.

[P15]**E** A. Amirouche, J. Esteves, A. Lavoignat, S. Picot, R. Ferrigno and **M. Faivre**, *"Dual shape recovery of Red Blood Cells flowing out of a microfluidic constriction"*, **Biomicrofluidics**, 14(2), 024116 (2020), https://doi.org/10.1063/5.0005198.

[P16]**E** **M. Faivre**, C. Renoux, A. Bessaa, L. Da Costa, P. Joly, A. Gauthier and P. Connes, *"Mechanical signature of Red Blood Cells flowing out of a microfluidic constriction is impacted by membrane elasticity, cell surface-to-volume ratio and diseases"*, **Frontiers in Physiology**, 11:576 (2020), https://doi.org/10.3389/fphys.2020.00576.

▷ Book chapters

[B01] G. Villanueva, A. De Pastina and **M. Faivre**, (2019), Engineering of micro/nano bio systems: fundamental and applications, Book chapter 4: *Mechanics for fluids and biology*, ISBN:978-981-13-6549-2.

▷ Peer-reviewed international conference proceedings (Pr)

[Pr01] E. Sollier, M. Cubizolles, **M. Faivre**, Y. Fouillet, J.L. Achard, *"A passive microfluidic device for plasma extraction from whole human blood"*, **IEEE Eng. Med. Biol. Soc.**, 7030-7033, (2009), https://doi.org/10.1109/IEMBS.2009.5333314.

[Pr02]**E** R. Gelszinnis, **M. Faivre**, J. Degouttes, N. Terrier, R. Ferrigno and A.L. Deman, *"Magnetophoretic manipulation in microsystem using i-PDMS microstructures"*, **Proceedings of the 17th International Conference on Miniaturized Systems for Chemistry and Life Sciences**, µTAS 2013 - 27-31 October 2013 - Freiburg, Germany, (2013).

[Pr03]**E** J. Marchalot, R. Gelszinnis, A.L. Deman, **M. Faivre**, J.F. Chateaux, C. Rivière, H. Mertani and R. Ferrigno, *"Manipulation of rare cells in microfluidic device using magnetophoresis and dielectrophoresis based on composite-PDMS"*, **Proceedings of the 4th European Conference on Microfluidics**, Microfluidics 2014 - Limerick, December 10-12, 2014, (2014).

[Pr04]**E** A. Amirouche, J. Esteves, R. Ferrigno and **M. Faivre**, *"The role of the energy dissipation in the high speed mechanical relaxation of the Red Blood Cells"*, **Proceedings of the 20th International Conference on Miniaturized Systems for Chemistry and Life Sciences**, µTAS 2016 - 09-13 October 2016 - Dublin, Ireland, (2016).

[Pr05]**E** J.A. Martinez Santa Maria, A. Montalibet, E. McAdams, **M. Faivre** and R. Ferrigno, *"Effect of electrode material on the sensitivity of interdigitated electrodes used for Electrical Cell-Substrate Impedance Sensing technology"*, **IEEE Eng. Med. Biol. Soc.**, (2017), `https://doi.org/10.1109/EMBC.2017.8036948`.

[Pr06]**E** A. Amirouche, **M. Faivre**, J.F. Chateaux and R. Ferrigno, *"Determination of Red Blood Cell fatigue using electrodeformation"*, **IEEE Eng. Med. Biol. Soc.**, (2017), `https://doi.org/10.1109/EMBC.2017.8037632`.

▷ Patents (Pat)

[Pat01]**T** H.A. Stone, M. Abkarian, **M. Faivre** and K. Smistrup, *"Pressure determination in microfluidic systems"*, WO2007014336A1 (2007).

[Pat02] M.L. Cosnier, P. Caillat, M. Cubizolles, **M. Faivre**, P. Peltié, C. Peponnet, P. Pouteau, C. Vauchier and L. Talini, *"Appareil et dispositif consommable pour effectuer des analyses sanguines"*, WO2010128221A1 (2010).

[Pat03] **M. Faivre**, P. Caillat, M. Cubizolles, C. Peponnet and C. Vauchier, *"Method and apparatus for counting thrombocytes"*, US8699777B2 (2010).

[Pat04] P. Pouteau, **M. Faivre**, P. Peltié, C.A. Planat, *"Method and a device for characterizing the coagulation or sedimentation dynamics of a fluid such as blood or blood plasma"*, US9494604B2 (2010).

[Pat05] M. Cubizolles, M.L. Cosnier, M. Faivre and P. Pouteau, *"Method for assaying plasma enzymes in whole blood"*, US20110104712A1 (2011).

▷ Communications orales (C)

[C01]**T** **M. Faivre**, T. Ward, M. Abkarian and H.A. Stone, *"Production of surfactant at the interface of a flowing drop: Interfacial kinetics in a microfluidic device"*, **American Physical Society Meeting "Division of fluid mechanics"**, Seattle, USA, (November 2004).

[C02]**T** **M. Faivre**, K. Bikraj, M. Abkarian and H.A. Stone,*"Geometrical focusing of cells in a microfluidic device"*, **American Institute of Chemistry and Engineering Annual Meeting**, Cincinnati, USA, (November 2005).

[C03]**T** **M. Faivre**, M. Abkarian, K. Smistrup and H.A. Stone, *"High-speed microfluidic differential manometer: for cellular-scale hydrodynamics"*, **American Physical Society Meeting "Division of fluid mechanics"**, Chicago, USA, (October 2005).

[C04]**E** **M. Faivre** (Invited speaker), C. Rivière, A. Confavreux, A.L. Deman, M. Brun, J.F. Chateaux, J.P. Rieu and R. Ferrigno, *"Migration of cancerous cells in microfluidic devices"*, **EMSG Symposium**, Ardgour, Scotland, (September 2011).

[C05] A. Confavreux, P. Rupprecht, L. Golé, C. Vézy, **M. Faivre**, H. Mertani, C. Rivière, R. Ferrigno and J.P. Rieu, *"A tapered channel microfluidic device for comprehensive cell adhesion of breast cancer cell lines"*, **Workshop "Cancer Cell on Chip"**, Lyon, France (June 2012).

[C06] J. Marchalot, J.F. Chateaux, **M. Faivre**, A. Confavreux, C. Rivière, J.P. Rieu, H. Mertani, A.L. Deman and R. Ferrigno, *"Cell Lysis and sample treatment in a microfluidic environment"*, **Cancer cell on chip workshop**, Lyon, France, (June 2012).

[C07]**E** A. Confavreux, **M. Faivre**, H. Mertani, R. Ferrigno, C. Rivière, and J.P. Rieu, *"A tapered channel microfluidic device to analyse cancer cells adhesion properties"*, **GDR Micro-Nano-Systèmes – Micro- Nano-Fluidique**, Bordeaux, France, (Juillet 2012).

[C08]**E** J. Marchalot, R. Gelszinnis, A.L. Deman, J.F. Chateaux, **M. Faivre** and R. Ferrigno, *"Approaches based on composite PDMS for implementation of actives functions in Lab-on-a-chip"*, **GDR Micro- Nano-Systèmes – Micro- Nano-Fluidique**, Bordeaux, France, (Jully 2012).

[C09] A. Confavreux, **M. Faivre**, H. Mertani, C. Rivière, R. Ferrigno and J.P. Rieu, *"Microfluidic tools for the analysis of the interplay between cancer cells detachment and migration"*, **GDR Micro- Nano-Systèmes – Micro- Nano-Fluidique**, Bordeau, France, (Jully 2012).

[C10] A. Confavreux, **M. Faivre**, H. Mertani, C. Rivière, R. Ferrigno and J.P. Rieu, *"Microfluidic tools for the analysis of the interplay between cancer cells detachment and migration"*, **DeGennes Days & PhysCell**, Hyères, France, (September 2012).

[C11] **M. Faivre** (Invited Speaker), *"Transmigration of cancer cells: From deformation to migration in microsystems"*, **Microfabrication for cell biology Club**, Paris, France, (May 2013).

[C12]**E** R. Gelszinnis, **M. Faivre**, J. Degouttes, N. Terrier, R. Ferrigno and A.L. Deman, *"Magnetophoretic manipulation in microsystem using i-PDMS microstructures"*, **µTAS**, Freiburg, Germany, (October 2013).

[C13] A. Confavreux, **M. Faivre**, C. Rivière, H. Delanoë-Ayari, H. Mertani, R. Ferrigno and J.P. Rieu, *"Interplay between cell-substrate adhesion, random migration & chemotactic motility for highly invasive cancer cell lines"*, **CellMech**, Obergurgl, Astria, (October 2013).

[C14] A. Confavreux, **M. Faivre**, C. Rivière, H. Delanoë-Ayari, H. Mertani, R. Ferrigno and J.P. Rieu, *"Interplay between cell-substrate adhesion, random migration & chemotactic motility for highly invasive cancer cell lines"*, **Nanobiotech**, Montreux, Suitzerland, (November 2013).

[C15] A. Confavreux, **M. Faivre**, H. Mertani, C. Rivière, R. Ferrigno and J.P. Rieu, *" Interplay between cell-substrate adhesion and random and chemotactic mobility for highly invasive cancer cell lines"*, **GDR CellTiss**, Lyon, France, (November 2013).

[C16]**E** **M. Faivre**, J. Marchalot, R. Gelszinnis, A.L. Deman, J.F. Chateaux, C. Rivière, H. Mertani and R. Ferrigno, *"Manipulation of rare cells in microfluidic devices using magnetophoresis and dielectrophoresis based on composite-PDMS"*, **Microflu**, Limerick, Irland, (December 2014).

[C17]**E** A. Amirouche, J. Esteves, R. Ferrigno and **M. Faivre**, *"Deformability as a new physical biomarker"*, **Namis international Autumn school**, Montréal, Canada, (Jully 2015).

[C18]**E** A. Amirouche, J. Esteves, R. Ferrigno and **M. Faivre** (Invited speaker), *"Cinétique, déformation et relaxation mécanique de globules rouges sous écoulement confiné : Quel est le rôle de la dissipation ?"*, **Journée thématique INSIS**, Paris, France, (Jully 2015).

[C19] **M. Faivre** (Invited speaker), *"Dynamical behavior of cancer cells migrating on nano- and micro-patterned substrates"*, **Physics of Cancer**, Leipzig, Germany, (September 2015).

[C20]**E** J.F. Chateaux, J. Castelluci, C. Rivière, H. Mertani and **M. Faivre**, *"Dynamical behavior of cancer cells migrating on nano- and micro-patterned substrates"*, **Mechanobio-Lyon: Mechanobiology and physics of life in Lyon**, Lyon, France, (January 2016).

[C21]**E** A. Amirouche, J. Esteves, R. Ferrigno and **M. Faivre**, *"Mechanical relaxation of Red Blood Cells under confined flow: the role of dissipation"*, **Mechanobio-Lyon: Mechanobiology and physics of life in Lyon**, Lyon, France, (January 2016).

[C22]**E** J.A. Martinez SantaMaria, E. McAdams, B. Massot and **M. Faivre** and R. Ferrigno, *"Characterization of interdigitated electrodes for ECIS assays"*, **Namis international Autumn school**, Tokyo, Japan, (September 2016).

[C23]**E** A. Amirouche, J. Esteves R. Ferrigno and **M. Faivre**, *"Analysis of Red Blood Cells relaxation time flowing out of microfluidic constrictions reveals the impact of buffer viscosity and flow speed"*, **µTAS**, Dublin, Irland, (October 2016).

[C24]**E** J.A. Martinez SantaMaria, A. Montalibet, E. McAdams, **M. Faivre** and R. Ferrigno, *"Influence du matériau d'électrode sur la sensibilité de la mesure de bioimpédance ECIS"*, **Forum Impédance**, Paris, France, (December 2016).

[C25]**E** A. Amirouche, R. Ferrigno, J.F. Chateaux and **M. Faivre**, *"Microsystèmes fluidiques biomimétiques pour la santé"*, **Journée de la Faculté des Sciences et Technologies de l'UCBL**, Lyon, France, (June 2017).

[C26]**E** J.A. Martinez SantaMaria, A. Montalibet, E. McAdams, **M. Faivre** and R. Ferrigno, *"Effect of electrode material on the sensitivity of interdigitated electrodes used for Electrical Cell-Substrate Impedance Sensing technology"*, **EMBC**, Jeju Island, North Korea, (Jully 2017).

[C27]**E** A. Amirouche, **M. Faivre**, J.F. Chateaux and R. Ferrigno, *"Determination of Red Blood Cell fatigue using electrodeformation"*, **EMBC**, Jeju Island, South Korea, (Jully 2017).

[C28]**E** A. Amirouche, R. Ferrigno and **M. Faivre**, *"Impact of channel geometry on the discrimination of mechanically impaired Red Blood Cells in passive microfluidics"*, **EuroSensors**, Paris, France (October 2017).

[C29]**E** J.A. Martinez SantaMaria, A. Montalibet, E. McAdams, **M. Faivre** and R. Ferrigno, *"Comparison of ITO and IrOx-modified ITO interdigitated electrodes for electrical cell substrate Impedance sensing (ECIS) applications"*, **EuroSensors**, Paris, France (October 2017).

[C30]**E** A. Amirouche, J. Esteves, R. Ferrigno and **M. Faivre**, *"Flow of healthy and thermally rigidified erythrocytes in a microfluidic rheometer"*, **Blood Flow**, Paris, France, (October 2017).

[C31]**E** A. Amirouche, J. Estéves, R. Ferrigno and **M. Faivre** (Invited speaker), *"Microfluidic characterization of mechanical phenotype to discriminate pathological Red Blood Cells"*, **Workshop Lab-On-a-Chip**, Besançon, France, (May 2018).

[C32]**E** C. Renoux, **M. Faivre**, A. Bessaa, P. Joly and P. Connes, *"Dual mechanical characterization of Red Blood Cells: Role of surface area, internal viscosity and membrane rigidity"*, **Joint Meeting of The European Society for Clinical Hemorheology and Microcirculation, The International Society of Clinical Hemorheology and The International Society of Biorheology**, Cracow, Poland, (Jully 2018).

[C33] **M. Faivre**, G. Coupier and E. Franceschini *“Propriétés mécaniques des globules rouges pour des solutions suspendantes isodenses”*, **Journées annuelles du GDR Mecabio**, Marseille, France, (December 2019).

[C34]**E** B. Allais, M.C. Audry-Deschamps, C. Boisson, C. Renoux, P. Connes and **M. Faivre**, *“Microfluidic Deformability Cytometer applied to Sickle Cell Disease analysis”*, **Journées annuelles du GDR Mecabio**, On-line, France, (January 2021).

[C35] **M. Faivre** (Invited speaker), *“Microfluidic Deformability Cytometer or When the sensor is the channel itself. . . ”*, **IEEE Sensors French Chapter Seminar**, On-line, France, (March 2021).

[C36] **M. Faivre** (Invited speaker), *“Cytomètre de défomabilité microfluidique pour la détection de pathologies sanguines”*, **Journée scientifique du Labex PRIMES**, On-line, France, (January 2021).

Former research contributions

I did my PhD (2004-2006) between two labs, (i) the “Stone group” at the DEAS from Harvard University (Boston, USA) and (ii) the Laboratoire de Spectrométrie Physique from UJF (Grenoble), under the supervision of Howard A. Stone (Harvard Professor), Brigitte Pépin-Donat (Senior Researcher CNRS) and Annie Viallat (Senior Researcher CNRS). I was studying the influence of RBCs deformability on their behavior under flow. Indeed in order to understand the rheological aspects of blood in the microcirculation, it is important to understand the physical principles which govern the motion of Red Blood Cells (RBCs) at the single cell scale. However, the interplay between stress undergone by the cells and the response of the deformable objects are very complex. For example, the flow exerts an hydrodynamic stress on the RBCs which, in return disturb the flow by adapting their shape to the external stress. Therefore during my PhD, we have investigated the influence of their different mechanical components on the response of RBCs flowing in confined or semi-confined environments. The study of the dynamics of blood cells in the micro-circulation was made possible thanks to the development of microfluidic tools mimicking physiological and pathological situations.

A first part of this work was dedicated to the flow of isolated RBCs in semi-confined geometries. The two types of behaviors, experienced by RBCs under flow near a wall, are now well documented in the literature: the uniform solid-like rotation and the “tank-treading” motion, where the cell maintains a constant orientation with its membrane rotating around the internal fluid. Near the transition between both movements, we have highlighted a new regime superimposed with the “tank-treading” motion, characterized by the oscillation of the cell’s orientation around a mean value. These oscillations, typical in elastic objects, are interpreted as a signature of the RBCs mechanical properties. To explain these results, we proposed a simple model based on a fluid ellipsoid taking into account its membrane elasticity and a shape memory [115]. The comparison between our experimental observations and our model allowed to extract an estimate of the RBCs membrane shear modulus (0.8 – 4.4 Pa) in good agreements with measurements reported in literature.

We have also looked at the behavior of RBCs flowing in highly confined geometries. We have particularly developed a geometry allowing the simultaneous measurement of (i) the increase in pressure drop associated with the flow a single RBC in a close-fitting channel, and (ii) the dynamic deformation of this cell [66]. Our study demonstrated that the amplitude of the pressure drop associated with the flow of a RBC in a microfluidic channel, varies linearly with its volume and its deformability [114, 116] This device allowed the measure of the pressure associated with the lysis (rupture of the cellular membrane) of a RBC flowing in the channel. The obtained value ($\sim$ 0.4 Psi) is of the same order of magnitude than measurements performed by micropipette aspiration.

After investigating the behavior of isolated RBCs, we looked closer at the dynamic response of more concentrated suspensions. One of the most famous hemodynamical phenomenon is the Fåhraeus effect which refers to the diminution of the cell concentration in capillaries smaller than the reservoirs they are connected to. This diminution can be explained by the apparition of a cell-free layer near the walls. We have demonstrated that a rapid variation of the channel section, coupled with the deformability of the cells, increases artificially the cell-free layer near the walls downstream [120]. These results are interpreted in terms of a drift force undergone by the RBCs in the region of higher shear, *i.e.* the constriction. We have taken advantage of this principle to perform plasma extraction from a whole blood sample. By adapting the geometry in an appropriate way, the cells can be focused in such a way that plasma can be extracted near the walls. An enrichment of the cells of 24% was estimated in the center of the channel, which correspond to an extraction of 24% of the plasma.

In parallel of the investigation of actual human RBCs deformability, we have developed and characterized bio-mimetic objects with complex and tunable mechanical properties. For instance, we developed responsive Giant Unilamelar Lipid Vesicles (GUVs) using two different strategies: either by modifying their internal media or by changing their membrane properties. First, we have prepared GUVs enclosing a Poly-N-isopropylacrilamide (PolyNIPAM) gel. Such gel presents a phase transition when external conditions - such as temperature, solvent composition or osmotic pressure - are modified: the gel swells and shrinks in a reversible way [P02]. We also used lipids presenting a sol/gel transition upon the temperature. Such transition has been shown to change the organisation of the lipid bylayer which modifies the visco-elastic properties of the membrane [51].

Then I did a Postdoc at Laboratoire des Composants Intégrés pour le Vivant (CEA Minatec/LETI/Département des Technologies pour la Biologie et la Santé, Grenoble) from 2007 to 2009. My research activities were focused on whole blood as a biological fluid, in the prospect of developing Lab-On-a-Chip (LOC) to perform blood analyses. The project consisted in the integration of 3 different blood tests on the same chip: (i) the count of platelets, (ii) the measurement of coagulation time and (iii) the dosing of 2 leaver-related proteins ASpartate AminoTransferase (ASAT) and ALanine AminoTransferase (ALAT). This work has led to the filling of 4 patent applications [138, 121, 158, 118] and the publication of one article [122].

I did a second Postdoc at Laboratoire Microfluidique, MEMS et Nanostructures (ESPCI, Paris) from 2009 to 2010. I have worked at the encapsulation of a nano-emulsion containing some contrast agent. The preparation of a double-emulsion of the type water/oil/nano-emulsion of a water-soluble contrast agent, was performed using flow focusing microfluidic chips. The stability of the double-emulsion and the control released of the contrast agent *via* the application of ultrasounds was characterized [150]. Indeed, under the action of ultrasounds, the oil phase can be vaporized, thus leading to the release of the inner water phase. Finally, we have demonstrated the possibility to released locally the contrast agent and to “tatoo” tissue. The suspension of double-emulsion was injected in the micro-circulation of a chicken embryo and the molecule of interest was released *in situ* using a conventional ultrasound scanner. These ultrasound-inducible multiple emulsions could be used to deliver large amounts of contrast agents, chemotherapy, and genetic materials *in vivo*.

Finally, I was recruited at the Institut des Nanotechnologies de Lyon (INL, UMR5270) as a junior researcher (Chargée de Recherche (CR)) in January 2011. I joined the “Microfluidique & Microsystèmes” team, which was renamed the “Lab-On-a-Chip & Instrumentation” (LOCI) team in 2017, and became part of the “Dispositifs pour la Santé et l’Environement” (DSE) team in 2020. The DSE team focuses on the design and the fabrication of microsystems integrating sensors for healthcare and environmental monitoring. These devices are dedicated to the collection of chemical, biochemical or physical data in order to perform analyses at molecular, cellular, tissue or physiological levels. More precisely, the objective of the LOCI group is to develop LOC for life sciences and environment, with a strong instrumental component whether in their fabrication or in their implementation. In this Habilitation à Diriger les Recherches (HDR) manuscript, I will focus on the work performed for the past 10 years or so at INL.

Chapter 1

Introduction

Cells mechanical behavior is inextricably related to their intra-cellular composition and architecture, particularly the cytoskeleton. The cytoskeleton is a complex 3D network of biopolymers (actin microfilaments, intermediate filaments and microtubules) which primarily defines cell shape and mechanical response to physical stresses and plays a central role in mechanotransduction, mitosis and migration [20]. Actin microfilaments are linear polymers that prevent overall cell deformation in response to external stimuli and can polymerize into helicoidal filaments and depolimerize within minutes to facilitate cell motion. Intermediate filaments form an intracellular intricated network connecting the nucleus to the plasma membrane and other organelles. They provide cell structural integrity and resist tension at strain levels where actin networks do not retain their structural integrity [187]. Microtubules consist in tubulin polymers that contribute to the transport of intra-cellular components within the cell and resist compression. Both the composition and the organization of these combined elements participate to the cell mechanical phenotype [20]. The interaction of a cell with its environment can also dramatically influence its mechanical properties. Indeed when spread on a surface, adherent cells exhibit a different cytoskeleton conformation than when in suspension, leading to differences in mechanical response to solicitations [192].

In the case of adherent cells, the polymerization / depolymerization of cytoskeleton components in response to both intracellular and extracellular stimuli may significantly alter the global cell mechanical signature. This is especially noticeable during biological processes such as cell division, or cell-cell contacts where extensive cytoskeletal remodeling occurs. The cell membrane also contributes to the cell mechanical properties due to its connections to the cytoskeleton. It passes strains and stresses on the intracellular tensile and compressive components. For small deformations, membrane viscoelasticity can contribute to overall cell mechanical behavior.
It is especially relevant when cells are in suspension, which is the case in flow-based approaches, where viscoelastic characteristics of the membrane plays a role in the cell distribution within the channel [190]. The presence of the nucleus and other organelles can contribute locally to the mechanical properties of the cell according to their physical size. High-resolution mechanical mapping of flattened cells using AFM presents different rigidity, depending if the measurement has been performed over the nucleus or over cytoplasmic and cytoskeletal areas [49].

The RBC membrane possesses a unique structure responsible of their remarkable mechanical properties (deformability, elasticity, shear resistance, etc...) allowing them to go through the small capillaries of the microcirculation. RBCs have an elastic 2D mesh-like spectrin cytoskeleton anchored to the internal side of a lipid bilayer [147]. The membrane of the erythrocyte encloses a cytoplasm made of hemoglobin - allowing the transportation of oxygen through the organism - which viscosity at 25℃ is 10 mPa.s. Together with the cytoplasmic fluid and the absence of nucleus and other organelles, the membrane controls the overall deformability of the cell. Under normal conditions, the membrane deforms at constant area and exhibits both elastic and viscous behaviors. The extension of the membrane is governed by the lipid bilayer, which tends to resist area expansion. The shear resistance of the membrane is directly linked to the density of spectrin and thus, to the cytoskeleton [173].

One of the primary applications of the mechanical phenotyping is the identification of pathological cells. Indeed various pathologies and modifications of cell states are reported to influence cell mechanical properties. For example, variation of RBCs deformability is associated with malaria [61], white blood cells deformability varies in sepsis [129] and acute respiratory distress syndrome [203], increase deformability of metastatic cancer cells [188] have been observed, finally drop of stiffness during stem cell differentiation [172] have been highlighted. A better understanding of cell deformability and its interactions with physical environment may imply enormous developments in disease diagnostics, therapeutics and drug screening assays.

For more than 10 years now, my research interests focus on the development of microfluidic diagnostic tools or functions based on the modification of cellular mechanical properties. These multidisciplinary approaches meet the ever-growing need of novel biophysical techniques to perform diagnosis.

Both in emerging and in developed countries, the achievement of an early and precise diagnosis has been identified as an important societal and economic challenge. Indeed, it allows a rapid initiation of the appropriate therapy, minimize the propagation of infections which decreases the associate coasts and limit the development of resistance to therapeutic molecules. A very promising approach is the development of microfluidic diagnostic tools which provide numerous advantages over conventional macroscale methods in terms of sample volume, low cost and integration in a complete chain of analysis in LOC devices. LOC devices allow a miniaturization, an automation, a portability and a rapidity of execution ; as many qualities which are required by the specifications of the so called Point-Of-Care (POC) diagnosis. As far as the analysis of cells populations is concern, the use of LOC provides many advantages over traditional approaches: (i) the dimension of microfluidic channels (10-100 µm) are of the same order of magnitude than cell size, (ii) the possibility to parallelize the analysis on a same chip, (iii) the simple integration of several classical analytical functions (mixing, sorting, lysis, pre-concentration. . .) on a chip, (iv) the possibility to reproduce biomimetic micro-environments, closer to *in vivo* conditions than the classical well plate and finally (v) the possibility to visualize and quantify the behavior of cells in real time.

Up until now, many devices for the diagnostic or the therapeutic follow-up of some diseases (cancer, malaria, Human Immunodeficiency Virus (HIV), heart diseases. . .), are based on the detection and the quantification of biomarkers (antibodies, antigens, DeoxyriboNucleic Acid (DNA) sequence) by molecular analyses. Even though those conventional and long-established methods are robust, they have drawbacks related to the use of reagents (shelf life, storage constraints, cost. . .) which can be an issue, especially for an off-site use in POC devices. The emergence of non-conventional detection allowing to address these challenges are therefore needed.

In this context, my research focuses on the development of microfluidic functions enabling the manipulation, concentration, detection or sorting of cell populations by exploiting their physical properties and more specifically their deformability in order to diagnose or to monitor the patient's medical condition. The originality of my approach lies in the development of innovative geometries allowing to exalt the alteration of mechanical properties of the cells of interest.

The work carried out since I arrived at INL has been structured around the development of microfluidic tools dedicated to 2 different cell types:

- Cells in adhesion on a substrate (cancer cells for example), which migrate willingly. I have addressed for the first time these aspects during the development of a sorting function based on the specific chemotactic response of cancerous and metastatic cells in microsystems (Agence National de la Recherche (ANR) project ONCOSCREEN, 2011 – 2014). This project - which will not be detailed in this manuscript - was the occasion for me to develop new skills and to interact with new collaborators which leads to the emergence of innovative approaches combining mechanical and migratory properties of cancer cells.
- Circulating cells (like RBCs for instance) which are passively carried out by the flow. This point

was studied through the development of LOC dedicated to the detection and the therapeutic follow up of malaria and the link between resistance to chemotherapy and mechanical response of acute myeloid leukemia cells.

Therefore, my HDR manuscript will be divided into 2 distinct main parts:

The Chapter 2 will be devoted to the exploitation of cellular motility - which is closely interconnected with deformability - to either identify or to sort cancer cells upon their metastatic characteristics, playing with the topography of the substrate. I will introduce the first results obtained on the migration of 2 breast cancer cell lines with various aggressiveness, under confinement. Then, I will present the study of the migration of the same 2 breast cancer cells on substrates implementing nano-patterning. These 2 approaches have been developed thanks to the involvement of many L3, M1 and M2 interns, therefore it is less achieved than the thematic on RBCs, which benefited from PhD students. I was also involved in the PhD steering committee of Jaime Andrès Martinez SantaMaria, who developed an electrical impedance system with interdigitated electrodes of ITO for screening applications of anticancer drugs [86]. ITO has the advantage of being transparent, hence allowing quantitative impedance measurements of breast cancer cells, that could be coupled to optical measurements in a microfluidic environment. I made the choice not to discuss this work in the present manuscript because my input has been limited with respect to the biological part (studies on the division up to confluence and effect of chemotherapeutic drugs on the cancer cell lines).

In the Chapter 3, I will report and discuss the results obtained on the development of different microsystem functions exploiting the alteration of the physical properties of circulating cells in relation with their physio-pathological state. In a first part, I will present the work realized during the PhD of Amin Amirouche, the M1 internship of Amel Bessaa and the M2 internship of Blandine Simon, on the flow of RBCs in the microfluidic deformability cytometer. Some of this work was also addressed during Josué Esteves ATER. In a second part, I will present a characterization of the pressure drop geometry and its optimization for the detection of impaired RBCs upon their volume and/or their mechanical properties. Most of the numerical optimization on RBCs was performed during the ATER of Josué Esteves. We will also use this approach to perform the mechanical characterization of nucleated cancer cells. Finally, in the third part, I will report the proof of concept of an innovative function based on nano-optical tweezers to mechanically characterize RBCs. This study has been performed by Ali Kheir Aldine during both his M2 internship and his PhD co-advised by Taha Benyattou from the “Ingérierie et conversion de LUMière” (i-LUM) team at INL.
Please note that the microfluidic function allowing the sorting of circulating cells according to their magnetic properties [123, 168, 77], developed by Renaud Gelszinnis during his PhD is presented in Appendix A.

Finally the Chapter 4 will present some conclusions about the research conducted so far and some reflections on the questions that I would like to address in the next 5 years.

Le comportement mécanique des cellules est inextricablement lié à leur composition et à leur architecture intracellulaire, en particulier à leur cytosquelette. Le cytosquelette est un réseau 3D complexe de biopolymères (microfilaments d’actine, filaments intermédiaires et microtubules) qui définit principalement la forme de la cellule et sa réponse mécanique aux contraintes physiques. Il joue un rôle central dans la mécanotransduction, la mitose et la migration.[20]. Les microfilaments d’actine sont des polymères linéaires qui empêchent la déformation globale de la cellule en réponse à des stimuli externes. Ils peuvent se polymériser en filaments hélicoïdaux et se dépolymériser en quelques minutes pour faciliter le mouvement de la cellule. Les filaments intermédiaires forment un réseau intracellulaire intricationnel reliant le noyau à la membrane plasmique et aux autres organelles. Ils assurent l'intégrité structurelle de la cellule et résistent à des niveaux de tension où les réseaux d'actine ne conservent pas leur intégrité structurelle [187]. Les microtubules sont constitués de polymères de tubuline qui contribuent au transport des composants intracellulaires à l'intérieur de la cellule et résistent à la compression. Tant la composition que l'organisation de ces éléments combinés participent au phénotype mécanique de la cellule [20]. L'interaction d'une cellule avec son environnement peut également influencer considérablement ses propriétés mécaniques. En effet, lorsqu'elles sont étalées sur une surface, les cellules adhérentes présentent une conformation du cytosquelette différente de celle qu'elles ont lorsqu'elles sont en suspension, ce qui entraîne des différences dans la réponse mécanique aux sollicitations [192].

Dans le cas des cellules adhérentes, la polymérisation / dépolymérisation des composants du cytosquelette en réponse à des stimuli intracellulaires et extracellulaires peut modifier de manière significative la signature mécanique globale de la cellule. Ceci est particulièrement visible lors de processus biologiques tels que la division cellulaire ou les contacts cellule-cellule, où un remodelage important du cytosquelette se produit. La membrane cellulaire contribue également aux propriétés mécaniques de la cellule en raison de ses connexions avec le cytosquelette. Elle transmet les déformations et les contraintes sur les composants intracellulaires en traction et en compression.

Pour de petites déformations, la viscoélasticité de la membrane peut contribuer au comportement mécanique global de la cellule. Elle est particulièrement pertinente lorsque les cellules sont en suspension, ce qui est le cas dans les approches basées sur l'écoulement, où les caractéristiques viscoélastiques de la membrane jouent un rôle dans la distribution des cellules dans le canal [190]. La présence du noyau et d'autres organelles peut contribuer localement aux propriétés mécaniques de la cellule en fonction de leur taille physique. La cartographie mécanique à haute résolution par AFM, de cellules aplaties présente une rigidité différente, selon que la mesure a été effectuée sur le noyau ou sur les zones cytoplasmiques et cytosquelettiques [49].

La membrane des globules rouges possède une structure unique responsable de leurs remarquables propriétés mécaniques (déformabilité, élasticité, résistance au cisaillement, etc...) leur permettant de traverser les petits capillaires de la microcirculation. Les globules rouges possèdent un cytosquelette élastique en spectrine à mailles 2D ancré sur la face interne d'une bicouche lipidique. La membrane de l'érythrocyte renferme un cytoplasme composé d'hémoglobine - permettant le transport de l'oxygène dans l'organisme - dont la viscosité à 25°C est de 10 mPa.s. Avec le liquide cytoplasmique et l'absence de noyau et d'autres organelles, la membrane contrôle la déformabilité globale de la cellule. Dans des conditions normales, la membrane se déforme à surface constante et présente des comportements à la fois élastiques et visqueux. L'extension de la membrane est régie par la bicouche lipidique, qui a tendance à résister à l'expansion de la surface. La résistance au cisaillement de la membrane est directement liée à la densité de spectrine, et donc au cytosquelette [173].

L'une des principales applications du phénotypage mécanique est l'identification des cellules pathologiques. En effet, diverses pathologies et modifications des états cellulaires sont rapportées comme pouvant influencer les propriétés mécaniques des cellules. Par exemple, une variation de déformabilité des globules rouges est associée au paludisme [61], la déformabilité des globules blancs varie dans la sepstisémie [129] et le syndrome de détresse respiratoire aiguë [203], une augmentation de la déformabilité des cellules cancéreuses métastatiques [188] a été observée, enfin une baisse de la rigidité au cours de la différenciation des cellules souches [172] a été mise en évidence. Une meilleure compréhension de la déformabilité des cellules et de ses interactions avec l'environnement physique pourrait entraîner d'énormes développements dans le diagnostic des maladies, le suivi thérapeutique et le criblage de médicaments.

Depuis plus de 10 ans, mes intérêts de recherche portent sur le développement d'outils de diagnostic ou de fonctions microfluidiques, basés sur la modification des propriétés mécaniques des cellules. Ces approches multidisciplinaires répondent au besoin toujours croissant de nouvelles techniques biophysiques pour réaliser des diagnostics.

Dans les pays émergents comme dans les pays développés, l'obtention d'un diagnostic précoce et précis a été identifiée comme un enjeu sociétal et économique important. En effet, il permet d'initier rapidement le traitement approprié, de minimiser la propagation des infections - ce qui diminue les coûts associés - et de limiter le développement de la résistance aux molécules thérapeutiques. Une approche très prometteuse est le développement d'outils de diagnostic microfluidiques qui offrent de nombreux avantages par rapport aux méthodes conventionnelles à grande échelle en termes de volume d'échantillon, de faible coût et d'intégration dans une chaîne complète d'analyse dans des dispositifs laboratoires- sur-puce (ou Lab-On-a-Chip, LOC). Les dispositifs LOC permettent une miniaturisation, une automatisation, une portabilité et une rapidité d'exécution ; autant de qualités qui sont requises par les spécifications du diagnostic au chevet du patient. En ce qui concerne l'analyse des populations de cellules, l'utilisation de LOCs offre de nombreux avantages par rapport aux approches traditionnelles : (i) l'adéquation entre les dimensions des canaux microfluidiques et la taille des cellules, (ii) la possibilité de paralléliser l'analyse sur une même puce, (iii) l'intégration simple de plusieurs fonctions analytiques classiques (mélange, tri, lyse, pré-concentration), (iv) la possibilité de reproduire des micro-environnements biomimétiques, plus proches des conditions *in vivo* que la plaque à puits classique et enfin (v) la possibilité de visualiser et de quantifier le comportement des cellules en temps réel.

Jusqu'à présent, de nombreux dispositifs pour le diagnostic ou le suivi thérapeutique de certaines maladies (cancer, malaria, VIH, maladies cardiaques), sont basés sur la détection et la quantification de biomarqueurs (anticorps, antigènes, séquence d'ADN) par des analyses moléculaires. Bien que ces méthodes conventionnelles et établies de longue date soient robustes, elles présentent des inconvénients liés à l'utilisation de réactifs (durée de conservation, contraintes de stockage, coût) qui peuvent poser problème, notamment pour une utilisation hors site, dite au chevet du patient. L'émergence de méthodes de détection non conventionnelles permettant de relever ces défis est donc nécessaire.

Dans ce contexte, mes recherches portent sur le développement de fonctions microfluidiques permettant de manipuler, concentrer, détecter ou trier des populations cellulaires en exploitant leurs propriétés physiques et plus particulièrement leur déformabilité afin de diagnostiquer ou de suivre l'état de santé du patient. L'originalité de mon approche réside dans le développement de géométries innovantes permettant d'exalter l'altération des propriétés mécaniques des cellules d'intérêt.

Le travail effectué depuis mon arrivée à l'INL s'est structuré autour du développement d'outils microfluidiques dédiés à 2 types cellulaires différents :

- Les cellules adhérantes, qui migrent sur un substrat (cellules cancéreuses par exemple). J'ai abordé pour la première fois ces aspects lors du développement d'une fonction de tri basée sur la réponse chimiotactique spécifique des cellules cancéreuses et métastatiques dans des microsystèmes (projet ANR ONCOSCREEN, 2011 – 2014). Ce projet - qui ne sera pas détaillé dans ce manuscrit - a été l'occasion pour moi de développer de nouvelles compétences et d'interagir avec de nouveaux collaborateurs ce qui conduit à l'émergence d'approches innovantes combinant les propriétés mécaniques et migratoires des cellules cancéreuses.
- Les cellules circulantes (comme les cellules sanguine par exemple) qui sont entraînées passivement par le flux. Ce point a été étudié à travers le développement de LOCs dédiés à la détection et au suivi thérapeutique du paludisme et à l'étude du lien entre la résistance à la chimiothérapie et la réponse mécanique des cellules de leucémie myéloïde aiguë.

Par conséquent, mon manuscrit d'HDR sera divisé en 2 parties distinctes :

Le chapitre 2 sera consacré à l'exploitation de la motilité cellulaire - qui est étroitement liée à la déformabilité - pour identifier ou trier les cellules cancéreuses en fonction de leurs caractéristiques métastatiques, en jouant sur la topographie du substrat. J'introduirai les premiers résultats obtenus sur la migration, sous confinement, de 2 lignées cellulaires du cancer du sein de différente agressivité. Ensuite, je présenterai l'étude de la migration de ces 2 mêmes lignées cellulaires sur des substrats mettant en øeuvre des nanostructures.

Ces 2 approches ont été développées grâce à l'implication de nombreux stagiaires de L3, de M1 et de M2, elles sont donc moins abouties que la thématique sur les globules rouges, qui a bénéficiée d'étudiants en thèse. J'ai également participé au comité d'encadrement de thèse de Jaime Andrès

Martinez SantaMaria, qui a développé un système d'impédance électrique avec des électrodes interdigitées d'ITO pour des applications de criblage de médicaments anticancéreux [86]. L'ITO présente l'avantage d'être transparent, permettant ainsi des mesures quantitatives d'impédance sur des cellules cancéreuses, qui pourraient être couplées à des mesures optiques dans un environnement microfluidique. J'ai choisi de ne pas discuter de ce travail dans le présent manuscrit car ma contribution a été limitée à la partie biologique (études sur la division jusqu'à confluence et effet des médicaments chimiothérapeutiques sur les lignées de cellules cancéreuses).

Dans le chapitre 3, je rapporterai et discuterai les résultats obtenus sur le développement de différentes fonctions de microsystèmes exploitant l'altération des propriétés physiques des cellules circulantes en relation avec leur état physio-pathologique. Dans une première partie, je présenterai les travaux réalisés pendant la thèse d'Amin Amirouche, le stage M1 d'Amel Bessaa et le stage M2 de Blandine Simon, sur le flux de globules rouges dans un cytomètre microfluidique de déformabilité. Certains de ces travaux ont également été abordés lors de l'ATER de Josué Esteves. Dans une seconde partie, je présenterai une caractérisation de la géométrie de la chute de pression et son optimisation pour la détection des globules rouges de volume et/ou de propriétés mécaniques altérés. La plupart des optimisations de la géométrie du dispositif pour les globules rouges ont été réalisées par des méthodes numériques pendant l'ATER de Josué Esteves. Nous utiliserons également cette approche pour réaliser la caractérisation mécanique de cellules cancéreuses nucléées. Enfin, dans la troisième partie, je rapporterai la preuve de concept d'une fonction innovante basée sur des nano-pinces optiques pour caractériser mécaniquement les globules rouges. Cette étude a été réalisée par Ali Kheir Aldine au cours de son stage de M2 et de sa thèse co-encadrés par Taha Benyattou de l'équipe i-LUM de l'INL.
A noter que la fonction microfluidique permettant le tri des cellules circulantes en fonction de leurs propriétés magnétiques [123, 168, 77], développée par Renaud Gelszinnis au cours de sa thèse est présentée en Annexe A.

Enfin, le chapitre 4 présentera une conclusion globale sur les recherches menées jusqu'à présent et quelques réflexions sur les questions que j'aimerais aborder dans les 5 prochaines années.

Chapter 2

Microsystems for adherent cells

2.1 Context

There are an estimated two million deaths per year in most developed countries due to the various types of cancer, putting a major burden on their healthcare systems. Cancer research, whether it concerns diagnosis or the development of new therapies remains a crucial challenge for society. Significant improvements in surgery, radiotherapy, chemotherapy and patient care are responsible for increased survival rates of patients with breast cancer. However, cancer is still a lethal disease mainly due to the metastatic spreading of tumor cells that accompanies oncogenic progression [37]. Metastasis is a complex process [35] characterized by (i) local infiltration of tumor cells into the adjacent tissue, (ii) endothelial transmigration of cancer cells into blood vessels (also referred to as intravasation), (iii) transport in the circulatory system, (iv) transmigration outside the vasculature (extravasation) and (v) subsequent colonization and proliferation in remote organs (Figure 2.1).

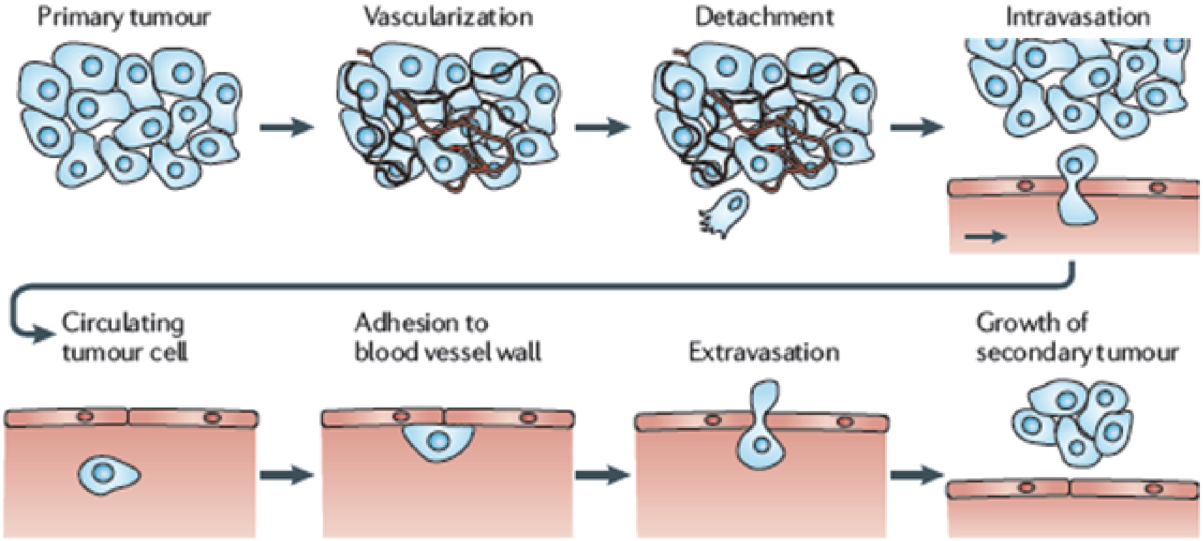

Figure 2.1: Schematic representation of the metastatic process. Cells detach from the vascularized primary tumor, penetrate the surrounding tissue, enter nearby blood vessels (intravasation) and circulate in the vascular system. Some of them eventually adhere to blood vessel walls and are able to extravasate and migrate into the local tissue, where they can form a secondary tumor. From [35].

The molecular and mechanical rearrangements associated with the acquisition of the invasive phenotype are not fully understood and clearly represent a major challenge for the development of new cancer clinical strategies based on personalized diagnosis, prognosis and drug screening. During cancer cells progression to metastasis, tumor cells show important changes in their morphology, migratory properties

and their secretory activity (see Figure 2.2). Cells from a primary tumor can disseminate collectively as protruding sheets and strands with epithelial phenotype. At some point, they can then shift towards an individual mode of migration, a process known as the EMT during which cells lose their cadherin-dependent cell to cell adherents junctions, flatten and elongate, enabling them to migrate within the architecturally complex 3D ECM [91].
Cancer cells break out from their constrained environment following intense proteolytic activity and undergo additional morphological changes required to penetrate into blood and lymph vessels before metastatic spreading. These additional cytoskeleton rearrangements are supported by the lowering of cellular integrins, responsible for cell attachment to the ECM. It is visually characterized by a switch from fibroblast-like morphology to a spherical amoeboid type. It is also concomitant to the apparition of an amoeboid-type of movement and hence was termed the MAT [96]. Spherical cells are able to move very rapidly using non-integrin receptors and by applying low traction forces on the contact surface. They also display increased capacity of dissemination through connective tissue and a higher rate of transfer between organs and blood.

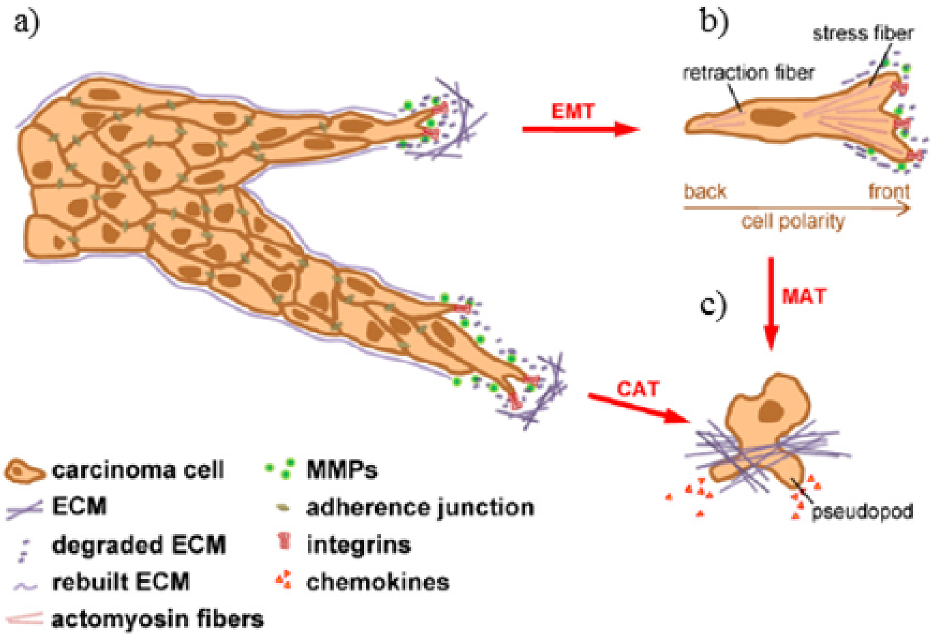

Figure 2.2: a) In collective invading cell sheets, the tumor cell at the invasive front promote focal adhesions and ECM rearrangement while following cells maintain their adherence, tight and gap junction. b) A single cancer cell can detach from the epithelial cluster by undergoing an EMT through rearrangement of the cytoskeleton. This mesenchymal-like cell is able to move freely by forming focal adhesions and rearranging the ECM. c) The fastest way of cell invasion is the amoeboid cell movement, which leads to a total loss of cell polarity. This characteristic can be acquired in two ways: either by CAT or the MAT. From [205].

Cell motility is an active process dependent on cytoskeletal dynamics and cellular deformability. The nucleus rigidity and the overall deformability of the cells are two major characteristics that influence their migratory behavior in very various situations such as physical confinement. For example, intravasation and extravasation requires cells to deform in order to pass through the narrow interstitial space in the endothelium. Therefore, there is a strong interplay between the cell mechanical and migratory properties. Since metastatic cells acquire strong abilities to invade and migrate, their mechanical phenotype could be an important indicator of the cancer aggressiveness, *i.e.* its capacity to develop metastasis.

At the present day, diagnosis of cancer is mainly based on clinical and anatomopathological data regarding tumor size, the presence of invaded lymph nodes, the detection of metastases using high-resolution imaging technologies for macro-metastases and detection of circulating tumor cells in blood samples

for micro-metastases [36, 10]. But, even though metastasis is recognized as the main cause of cancer death, no marker or test exist yet that could be used in clinical setting to predict the recurrence of cancer. At the present day, there is no marker or clinical test that can predict in a reliable way the recurrence of metastatic cancers. Recently, high throughput analysis *i.e.* transcriptomics have been developed in order to improve diagnosis accuracy [169], but one major drawback of all these methods is that they either rely on chemically fixed samples or molecular extracts obtained from a heterogeneous cell population.
A very substantial progress in cancer diagnosis and prognosis would be to use biophysical characteristics of patient's cancer cells including their index of motility, invasiveness and deformability, as more relevant indications of their intrinsic capabilities in terms of metastatic spreading and drug-response. If coupled to clinical analysis, these information will help in decision-taking concerning the choice of treatment and the probability of tumor resurgence. Clearly, this would require large amount of biopsy material if tested using conventional *in vitro* techniques, especially if taking into account the importance of the anatomopathological examination of the full biopsy for the clinician. Fortunately, the emergence of nanotechnologies has now made it possible to envision the development of micro devices that would closely mimic *in-vivo* environment and process very small amounts of biological material. Moreover, thanks to the miniaturization of the system, it would not only provide relevant indicators of the metastatic potential of the tumors, but also allow the study of their response to various chemotherapeutic drugs to go towards personalized medicine.

2.1.1 *In vitro* cell migration assays

As discussed previously, during the metastatic process, cells encounter ECM environments of varying stiffness, degree of confinement, etc... Cell migration in tissues depends on a balance between propulsive forces produced by the cell and physical cues such as stiffness and pore size of the ECM. In order to decipher the basic principles underlying single cell migration, an approach consisting in proposing simple elementary constrains is proposed. Those simple elements can then be combined together in order to take into account the complexity of the different cellular microenvironments found *in vivo*. In this context, and thanks to the possibilities offered by microfabrication techniques, various cell migration assays have been developed [88] as illustrated in Figure 2.3.

Among the different techniques reported in literature, we can cite the confinement assays between flat substrates and the migration assays inside straight microchannels or 3D collagen matrices. The major difference is the degree of confinement, which is greater inside microchannels and 3D matrices where cells are confined on 2 axes versus 1 for the flat substrates configuration. PDMS microchannels are usually preferred to 3D collagen matrices to perform migration assays under confinement because hydrogels can lack precise control of the pore size and due to the difficulty to image and accurately track cells in 3D hydrogels over time. The introduction of geometric constrictions in the microchannels permits to probe the deformability of the cells organelles - mainly the nucleus - which often constitutes a limiting factor for cells migrating through dense matrices. Migration assays under confinement can also be implemented using thin printed lines of adhesive molecules on a 2D substrate. Indeed, migration of thin line has been shown to promote migration mode similar to that observed in 3D environments [13, 15]. Topographical effect on cell migration - also known as contact guidance - can be studied using nano-grooves. Indeed at the close vicinity of the tumor, the rearrangement of the ECM structure causes collagen fibers to be radially aligned hence promoting the invasion of cancer cells into the stroma [137, 164]. Transmigration assays consist in the study of the migration of cells through the endothelium. It has been classically studied using multi-compartments plastic dish where endothelial monolayers are cultured on top of membranes in which flow can be applied.

2.2 Dynamical behavior of cancer cells migrating under confinement

As stated earlier, the ability of the cells to deform is a major characteristic that rule migration behavior, along with their adhesiveness to the substrate.

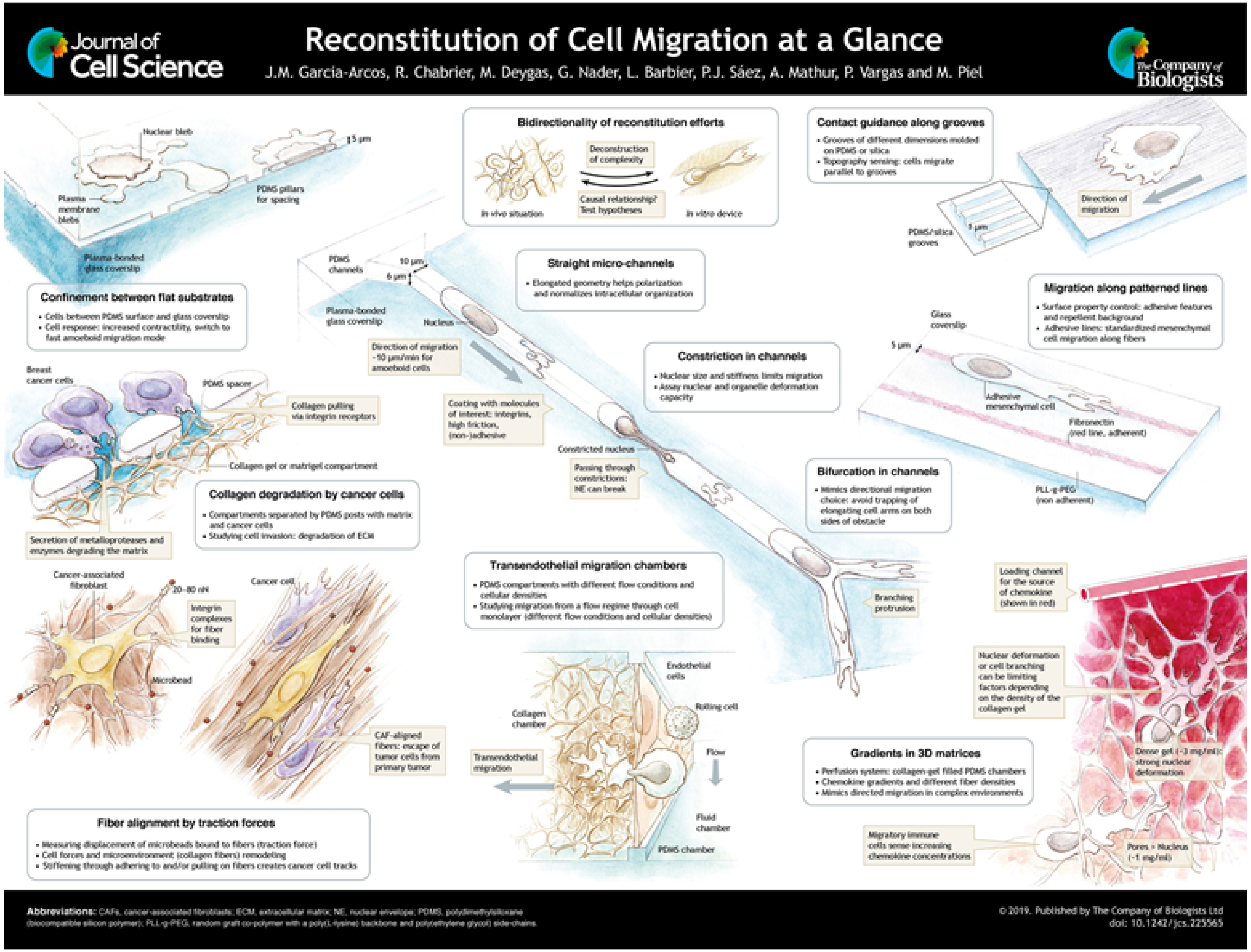

Reconstitution of Cell Migration at a Glance

J.M. Garcia-Arcos, R. Chabrier, M. Deygas, G. Nader, L. Barbier, P.J. Sáez, A. Mathur, P. Vargas and M. Piel

Bidirectionality of reconstitution efforts

Contact guidance along grooves

- Grooves of different dimensions molded on PDMS or silica
- Topography sensing: cells migrate parallel to grooves

Confinement between flat substrates

- Cells between PDMS surface and glass coverslip
- Cell response: increased contractility, switch to fast amoeboid migration mode

Straight micro-channels

- Elongated geometry helps polarization and normalizes intracellular organization

Migration along patterned lines

- Surface property control: adhesive features and repellent background
- Adhesive lines: standardized mesenchymal cell migration along fibers

Constriction in channels

- Nuclear size and stiffness limits migration
- Assay nuclear and organelle deformation capacity

Collagen degradation by cancer cells

- Compartments separated by PDMS posts with matrix and cancer cells
- Studying cell invasion: degradation of ECM

Bifurcation in channels

- Mimics directional migration choice: avoid trapping of elongating cell arms on both sides of obstacle

Transendothelial migration chambers

- PDMS compartments with different flow conditions and cellular densities
- Studying migration from a flow regime through cell monolayer (different flow conditions and cellular densities)

Gradients in 3D matrices

- Perfusion system: collagen-gel filled PDMS chambers
- Chemokine gradients and different fiber densities
- Mimics directed migration in complex environments

Fiber alignment by traction forces

- Measuring displacement of microbeads bound to fibers (traction force)
- Cell forces and microenvironment (collagen fibers) remodeling
- Stiffening through adhering to and/or pulling on fibers creates cancer cell tracks

Abbreviations: CAFs, cancer-associated fibroblasts; ECM, extracellular matrix; NE, nuclear envelope; PDMS, polydimethylsiloxane (biocompatible silicon polymer); PLL-g-PEG, random graft co-polymer with a poly(L-lysine) backbone and poly(ethylene glycol) side-chains

© 2019. Published by The Company of Biologists Ltd
doi: 10.1242/jcs.225565

Figure 2.3: Among the *in vitro* cell migration assays available in the literature, some technique probe the behavior of cells under confinement between two flat substrates, through straight or constricted channels, along patterned lines or through 3D matrices. From [88].

Thus, mechanical and migratory properties are closely interconnected. Here, we propose to elucidate the cellular mechanisms underlying one critical step in tumor progression: the endothelial transmigration, which is still mechanically poorly understood. Moreover, Shen et al. have recently reported that confined-migrated cells present a significantly higher survival rates than 2D cultured cells when expose to a variety of chemotherapeutic drugs or radiative treatments [166]. Their data suggest that confined-migrated cancer cells acquire a resistance, which is partially attributed to an increase ability to efflux drugs. Therefore proposing the kind of microfluidic platform that we aim to develop would allow performing drug screening assays on cells under confined migration. This could thus provide breakthrough in the development of new anticancer treatments, specifically targeting metastatic therapy resistant cancer cells.

2.2.1 State of the art of migration assays under confinement

The gold standard of transmigration assays is the transwell migration assay (or Boyden chamber assay) [179] where cells are seeded in the upper compartment and allowed to migrate through a porous membrane, with an accurately defined pore size, into the lower compartment in which medium containing an attractant - chemo-attractant or high concentration of serum - is present (see Figure 2.4a). The number of cells which have migrated through the membrane is then counted. However, the main disadvantage of this technique is that it is an endpoint assay, *i.e.* one cannot observe the cells during the passage. Therefore, thanks to recent advances in microfluidic technologies, new methods have been developed to allow live imaging during the passage of cells through small pores. As already mentioned, confinement assays can be implemented in different ways: cells can be squeezed between 2 flat substrates, migrating inside microchannels or through 3D collagen matrices. Here, only the assays performed within microchannels will be addressed.

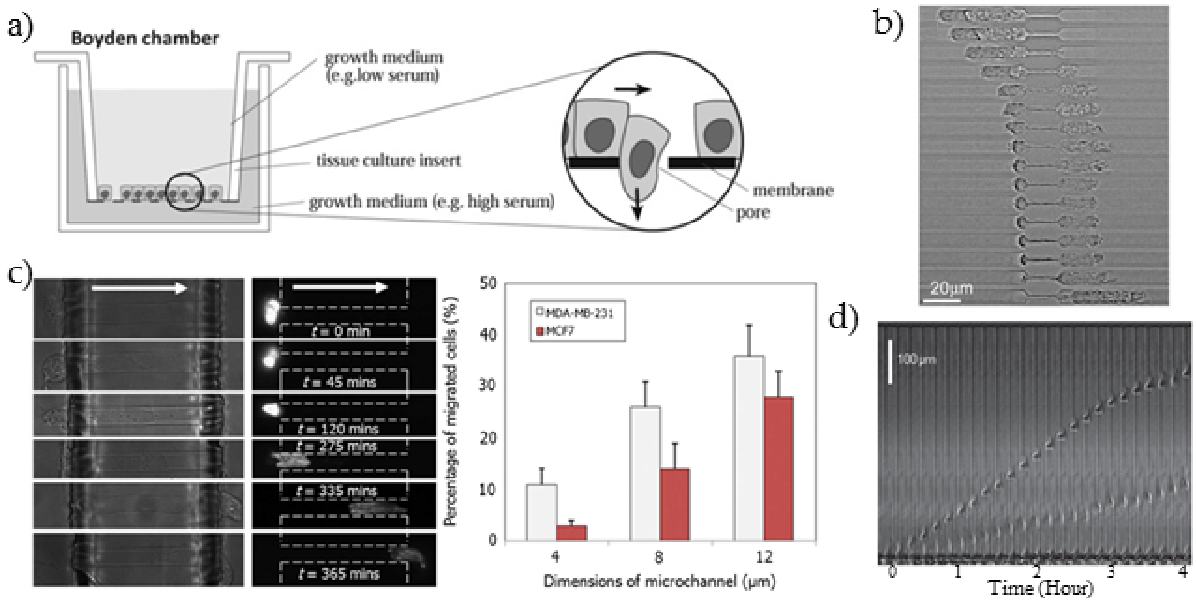

Figure 2.4: a) Schematic illustration of the Boyden chamber setup. Cells are free to migrate from the upper chamber to the lower one in which medium containing a chemo-attractant is present, through a porous membrane. From [146]. b) Sequential frames over 4 hours illustrating the displacement of one cell presenting amoeboid characteristics and another one with mesenchymal morphology, inside the same channel. From [32]. c) DIC and fluorescent images showing migration of MDA-MB-231 cells through an 8 µm wide microchannel, allowing the visualization of the elongation and de-condensation of the stained nucleus in the microchannel. d) Transmigration profiles of MDA-MB-231 and MCF-7 cells in different widths of the microchannels. From [213].

PDMS microfluidic systems implementing geometric restrictions have been developed to mimic the physical constraints, which are inherent in 3D environments found within the extracellular matrix or the endothelial barrier. Several publications report the study of cancer cells migration in such environment [99, 27, 32, 213, 48]. They report that, even in absence of chemotaxis, when MDA-MB-231 cells are mechanically constrained inside channels (typically 3 to 20 µm wide and 3 to 10 µm high), their motility was continuous and persistent in one direction for several hours unlike the classical motility on flat surfaces, when motile and stationary phases alternate frequently [32]. The study of single cells migration allowed identifying the phenotypes associated with the different observed behaviors: amoeboid morphology is associated with fast confinement-promoted migration whereas the slower classical motility on flat surfaces is attributed to mesenchymal one [48] (see Figure 2.4b).
Fu et al. have been studying the migration of MDA-MB-231 and MCF-7 breast cancer cells in PDMS microgaps of widths ranging from 4 to 12 µm [213] in presence of a chemoattractant gradient. They highlight that the deformation of the nucleus is the rate-limiting step during the transmigration process as illustrated on Figure 2.4c. They also report the transmigration profiles of MDA-MB-231 andMCF-7 for different microchannel widths as illustrated in Figure 2.4d. They provide evidence that MDA-MB-231 tend to travel more through the micro-gaps than MCF-7, hence demonstrating that motility under confinement is a marker of the cell invasion [213]. Cancer cells tend to become more motile as they progress through metastasis and that such changes are associated with decreased stiffness [218].

Despite these pioneering studies, the mechanical and biological mechanism of cell motility in confinement is still unclear. Integrin-independent migration have been observed in reconstituted 3D gels for white blood cells such as leukocytes [198], lymphoctytes [156], and dentritic cells [156], as well as for invasive cancer cells that underwent the MAT [96]. Similar behavior has been reported in reconstituted confined environment, *i.e.* microchannels, for dendritic cells [57], and invasive cancer cells such as breast cell lines MDA-MB-231, as described above [48] or pancreatic cancer cells Panc-1 [27]. In both cases (reconstituted 3D gels or PDMS confined environment), the integrin-independent motility is associated with a lack of defined focal adhesion structure [48, 194]. The enhanced motility in that type of 3D environment is not well described by the classical picture of cell motion that characterize mesenchymal cells migrating on 2D susbtrates - series of actin polymerization to extend protrusions and formation of new adhesion sites at the leading edge, myosin-II contraction to move the cell body forward and de-adhesion at the trailing edge - and is close to the amoeboid-type of locomotion (rounded cell morphology with membrane blebs) [197]. Even cells that express very low level of adhesion to the substrate are showing increase motility under confined environment.

Several physical mechanisms have been proposed to explain how cells can transfer force to the substrate during migration in absence or with low focal adhesions [46, 26].
For example, the “chimneying” mechanism reefers to the ability of a cell to laterally push on surrounding substrates, allowing for protrusion expansion at the front of the cell, and high cortical contractility at the rear [175]. This mechanism, illustrated in Figure 2.5a, is named after a climbing technique based on pushing off opposing rocks [95]. Such mechanism is consistent with a recent observation of HL-60 cells migrating in confined microchannels. Indeed Wilson et al. reported that the cells display two distinct actin networks at the leading edge: a network polymerizing against the membrane at the cell front and a network polymerizing perpendicularly to the channel walls [95]. This second network could be responsible for exerting pressure on the surrounding walls and thus contribute to the chimneying process of the cell. A model by Lim et al. predicted that increasing confinement boosts intracellular pressure, causing the formation of larger blebs at the leading edge of the cell, which would result in higher cell speed [54]. In the case of excessive confinement, intracellular pressure build up so much that blebs spontaneous form at the rear of the cell, removing cell polarity and thus stalling migration. An experimental paper by Yip et al. quantified normal stresses generated by HL-60, displaying amoeboid-like behavior while confined between 2 PAA substrates, on the walls to be of the order of 200-400 Pa [16]. In adhesive migration cells typically exert stresses on the substrat in the hundreds of Pa, with peaks in the kPa range on strong focal adhesion [145, 139]. They report that cell velocity are maximum for intermediate confinement, and that too high confinement impede migration, which is consistent with Lim’s model [54].

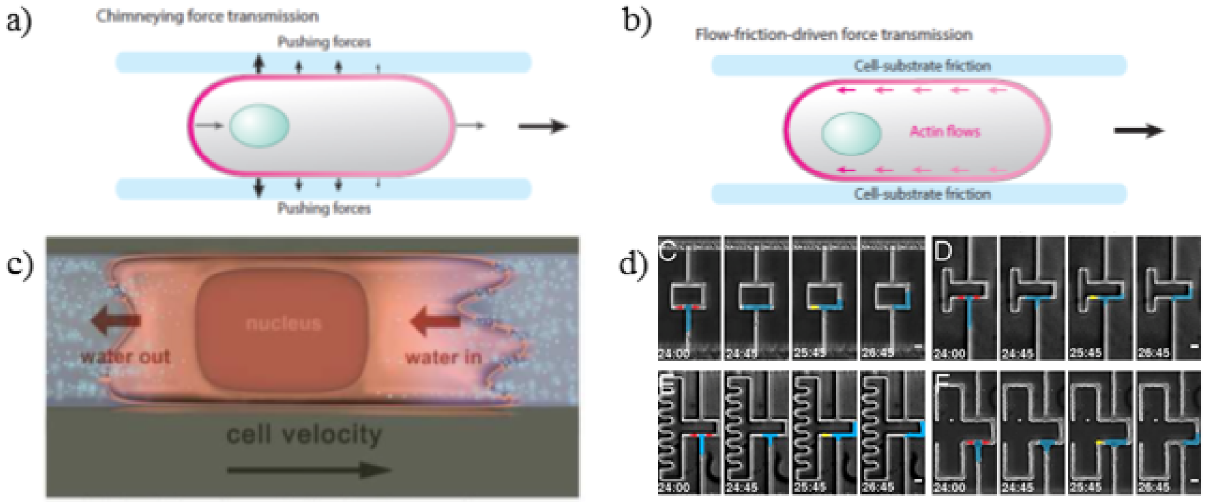

Figure 2.5: Examples of physical mechanisms for the generation and transmission of forces during integrin-independent migration. a) Chimneying mechanism, b) Flow-friction-driven mechanism. Adapted from [46]. c) Water permeation through the cell membrane. From [106]. d) Illustration of the asymetric hydrolic pressure gradients. Time lapse images of cell migrating in channels with different hydrodynamic resistance ratios of 4×(C), 8×(D), 32×(E), and dead end (F). Cells are false-colored in blue for visibility, red and yellow arrows indicate the cell entering the bifurcation and the retracting the non-persistent leading edge respectively. From [67].

Another proposed mechanism is the flow-friction-driven force transmission (see Figure 2.5b). It is based on nonspecific friction between the cell and the substrate to transmit intracellular forces generated by flows of the actomyosin cortex within the cell [176, 202]. An experimental study from Bergert et al., investigating the mechanics of nonadhesive Walker 256 carcinosarcoma cells migrating in microchannels, reported that the shape and cortex dynamics were consistent with friction-based mechanism [117]. Direct fiction measurements coupled to the quantification of actomyosin flows revealed that the force exerted by the cells onto the substrate were much lower than for adhesive cells ($\leq$ 1 Pa).
Water permeation through the cell membrane (also referred to as the Osmotic Engine Model) has been reported as a possible mechanism for cell migration in confinement [106]. The mechanism describes confined cell migration depending on osmotic and hydrostatic pressure differences across the cell membrane at both the cell leading and trailing edges as illustrated in Figure 2.5c. For instance, the experimental application of a hypotonic or a hypertonic shock, at the cell leading or trailing edge respectively has been demonstrated to allow overcoming the chemotaxis effect and causing the cell migration towards the higher osmolarity region. They measure a highly polarized distribution of ion pumps and aquaporins along the longitudinal surface of cells with an intense signal at the cell leading edge has been observed [105].
Asymetric hydrolic pressure gradients has also be proposed as explaination to cell migration under confinement [67]. Confined HL-60 cells migrating in microchannels with bifurcations are able to identify and chose a path of lower hydraulic resistance even in presence of chemotaxis. The decision-making dynamics are a 2 steps process: (i) generation of two asymmetric leading edges and (ii) retraction of the shortest leading edge as illustrated in Figure 2.5d with various hydrodynamic resistance ratios. In the first step, as the leading edges extend, they experience an external load, namely the column of fluid ahead of them, and thus sense the hydraulic pressures in each branches.

More experimental data are clearly needed to decipher and fully understand the origin of force generation in each type of confined situation; in particular in the case where the rigidity of the walls on which the cells are moving is comparable to the one of epithelial cells ($\sim$ 3-4 kPa) or collagen matrices ($\sim$ 100 Pa).

Most *in vitro* cell migration assays in microchannels use microfabricated PDMS microsystems. Recently, other elastomers and hydrogels including collagen, agarose gels, PAA or PolyMethyl MethAcrylate (PMMA) have been used to take into account the stiffness of the substrates. The number of publications dealing with the combined effect of confinement and microchannel stiffness on cell motility, remains very low. Pathak et al. were among the first to investigate the interplay between pore-size and rigidity of microchannels in the regulation of glioma tumor cell migration [11]. Their results presented in Figure 2.6 reveals a biphasic dependency of the cell migration velovity regarding the substrate stiffness. In narrow PAA channels, cells exploit traction forces which are not supported by soft substrates (0.4 kPa) - leading to low migration speed - whereas stiff matrices ($\geq$ 10 kPa) support such high traction forces that focal adhesions are too stabilized that they impede migration. The limitation associated with substrate stiffness can be overcame by increasing further the confinement, which then imposes the traction forces to align with the channel. Therefore it exists an intermediate ECM stiffness, where cells present higher polarization, corresponding to optimum migration velocity.

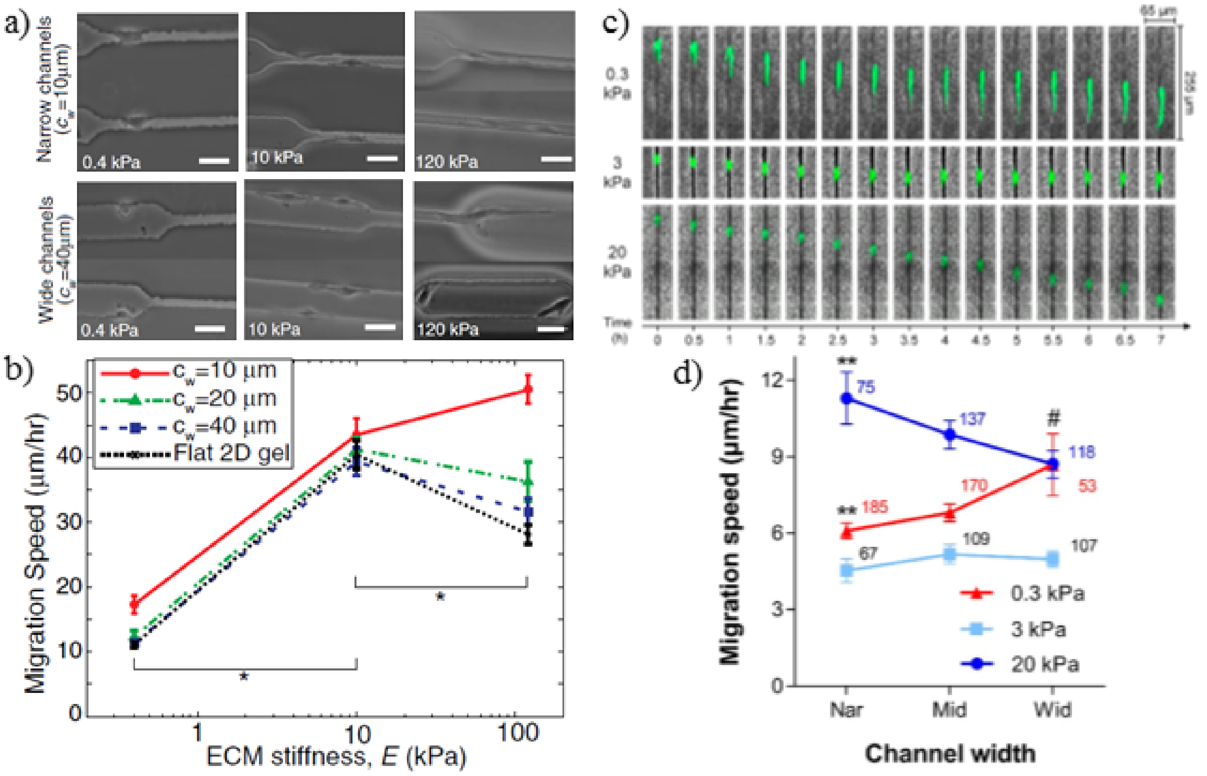

Figure 2.6: a) Phase contrast images of cells migrating inside PAA channels of varying stiffness and width. b) Migration speed versus ECM stiffness for different channel widths, noted C_w and flat 2D gels. From [11]. c) Typical images of MDA-MB-231 cells migrating in 8 µm wide hydrogel microchannels of different stiffness and d) cell migration speeds versus the channel width (Nar, Mid,and Wid correspond to channel width ranges of 3.5-5, 8, and 10-14 µm respectively). From [131].

Recently, Wang et al. reported that the channel stiffness significantly influenced the regulation of channel width on MDA-MB-231 migration speed [131]. As reported previously they confirmed that migration speed increases with confinement in stiff microchannels (20 kPa). However, their results highlight that in soft microchannels (0.3 kPa), the migration speed increases with channel width, which contradicts the findings by Pathak et al. These discrepancies are explained in terms of nuclear drag forces that increases with confinement when microchannel width becomes comparable or smaller than the nuclear size [131], which was not the case in Pathak et al. This nuclear drag is consistent with previous work on the interruption of the migration of tumor cells and neutrophils migrating through pores that are less than 10% of the cross-section of their nucleus [97]. Wang et al. also reported that confinement associated with channel stiffness induced the MAT of cancer cells. Indeed, their findings support the assumption that in stiff collagen microchannels, cells tend to migrate with amoeboid mode, when they tend to experience mesenchymal mode in soft microchannel. These different results point out the need for a better understanding of the dynamic cell behavior in confined and soft environment.

In this context, our approach is to develop microfluidic tools allowing the characterization or the exploitation of specific intrinsic migratory behavior of cancerous and metastatic cells in biomimetic environments. The IMPACT project aims at developing a new LOC exploiting cancerous cells functional properties. It consists in developing a microfluidic platform implementing soft pores as a model system to study the migration of metastatic cells trough the endothelial lining of blood vessels. The selected models to perform the proof of concept of this study are breast cancer cell lines : (i) a metastatic cell line, MDA-MB-231, which are motile mesenchymal cells, highly invasive and poorly cohesive, and (ii) a cancerous but non metastatic cell line, MCF-7, which presents epithelial characteristics, less motility and high cohesiveness.

2.2.2 Migratory behavior of breast cancer cells between pillars

As highlighted in Figure 2.1, when entering (intravasation) and exiting (extravasation) the vascular vessels, cancer cells need to transmigrate across the endothelial layer of the vessel walls [41, 174] which stiffness and geometric confinement creates serious challenges to the cancer cells, requiring them to sustain drastic deformations [14, 155]. As illustrated in the previous state of the art, cell transmigration has been studied in presence or in absence of chemo-attractant molecules, under confinement which size has been selected in order to significantly deform the cells. However, we can question the relevance of such geometries as the length of the geometric restrictions considered ($\sim$100 µm) is very far from the typical thickness of the endothelial barrier ($\sim$20 µm).

The microfluidic platform that we developed, uses networks of 20 µm in diameter pillars, as illustrated by the SEM image of a micro-structured PDMS substrate (Figure 2.7a). Such geometry defines “shorter” pores, which aspect ratio is more relevant regarding the *in vivo* conditions. The dynamic response of cells is observed using phase contrast video-microscopy coupled with an environmental chamber allowing the observation of cells, in physiologic conditions (temperature, hygrometry ans CO_2 environment) *in situ* in our microsystems for several days. The migratory behavior of MDA-MB-231 within pillar networks was studied as the spacing between the pillars is reduced, while keeping the post diameter equal to 20 µm. A mixture of collagen type IV (20 µg/mL) and 0.02% Bovin Serum Albumin (BSA) in PBS, at 298.8/1.2 v/v is used to favor cell adhesion on the PDMS substrate as previously developed [7]. Typical migratory responses of the metastatic cells are presented in Figure 2.7b.

Readouts such as the mean cell speed and the CME are measured in order to quantify the dynamical response of the cells. Figure 2.7c reports the mean speed at which cells migrate on the micro-patterned substrate regarding the spacing between the pillars. The graph shows no particular variation of cell velocity when cells migrate through pillar networks or 2D substrates. Moreover, cells present similar migration speed when confinement is increased in the range 25 to 10 µm; which is surprising as higher migration speeds are usually associated with higher confinement as reported in literature [11, 213]. This difference could be explained by the fact that our setup lack vertical confinement. Indeed, in the previous studies, cells are touching 4 walls, when in our experiments, cells are touching the ground substrate and the neighboring pillars but not the top cover, the height of the platform being 30 µm.
We also looked at the persistence of migration undergone by the cells through the estimation of the CME, defined as the ratio between the cell net displacement and the total length of the path traveled. Indeed, as illustrated by the sketch in Figure 2.7d, if the cell has a random walk, then the length of its traveled path will be much larger than the associated net displacement, leading to a CME close to 0. In contrast, if a cell maintain its polarity, the length of the traveled path will be comparable to the net displacement, leading to a CME tending towards 1. The Figure 2.7d represents the evolution of the CME when the geometric confinement of cells is modified. We remind the reader that we are working

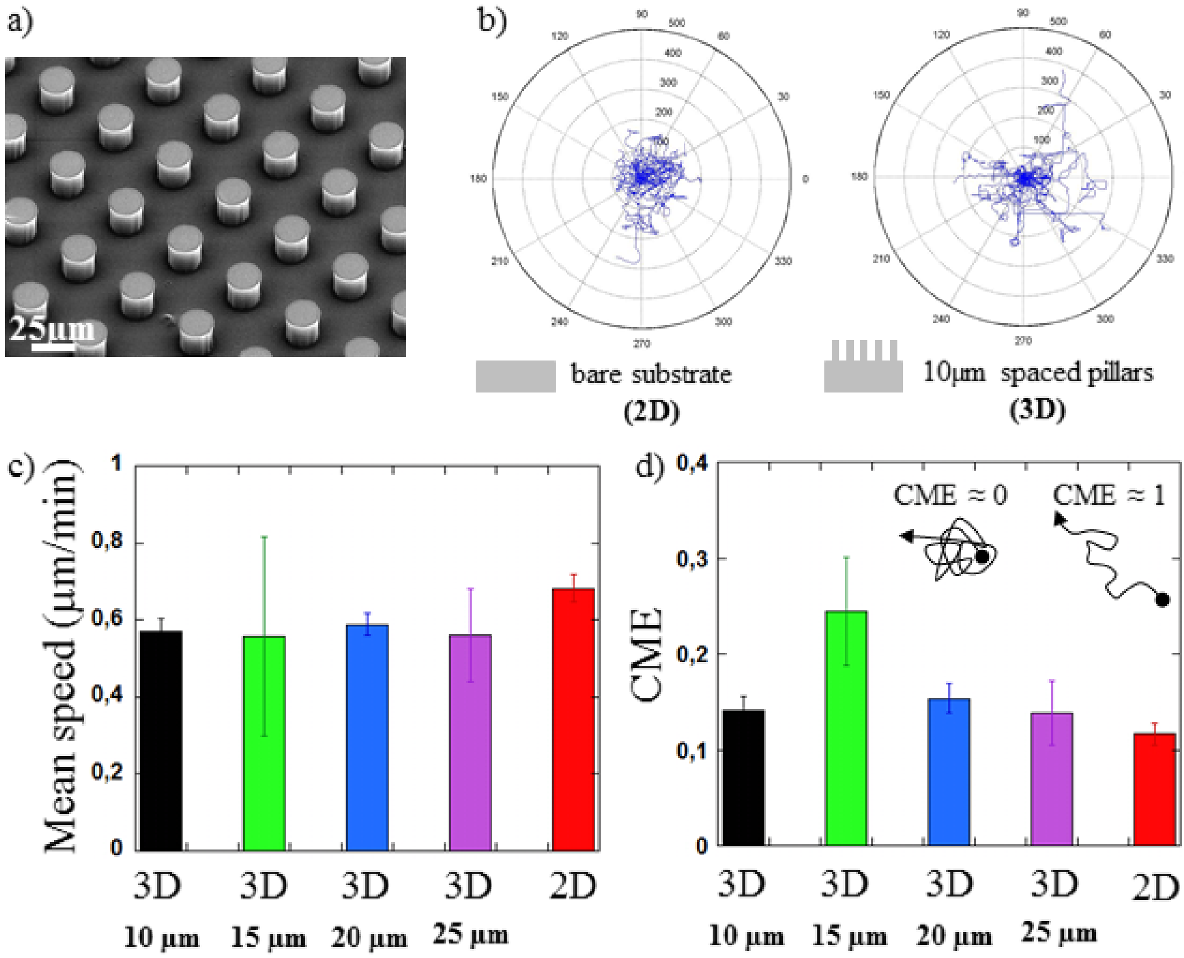

Figure 2.7: a) SEM observation of a typical micro-structured substrate in PDMS used to study the transmigration. The diameter of the pillars and their height are fixed at 20 µm and the distance to the closest neighbors is 20 µm. b) Normalized trajectories of metastatic breast cancer cells MDA-MB-231 migrating on (left) a bare substrate (noted 2D) and (right) through a 10 µm spaced pillar network (noted 3D). Evolution of c) the mean cell speed and d) the CME as a function of the type of substrate. The error bars represent the standard error calculated over more than 100 cells per conditions.

in absence of chemotactic gradient. CME rises from roughly 0.1 for cells on a bare 2D substrate, up to 0.25 through a network of 15 µm spaced pillars, indicating that cells seem to migrate in a more directed way when confinement is increased. We attribute such rise to a guidance effect due to the pillars, 15 µm being just below the typical size of MDA-MB-231. A recent study, about the behavior of mesenchymal stem cells in a micropillar confinement assay, reported that for high confinement (corresponding to 5 µm spaced micropillars), cell trajectories were more persistent than for larger spacing [142]. However, CME decreases back to $\sim$ 0.15 for higher confinement.

More experiments are needed in order to understand this biphasic variation of the cell persistence regarding the pore size, with an optimum condition around 15 µm, especially since it is not accompanied by a similar behavior regarding the migration speed, as expected.

We were also interested in investigating the effect of the pore deformability, in order to meet the *in vivo* environment. Indeed during transmigration, metastatic cancer cells deform to reach the blood circulation, applying a force on the endothelial cells which in return also deform. To take that into account, we propose to develop hydrogel-based microsystems with Young modulus of the same order of magnitude than that of endothelial cells ($\sim$ 4 kPa [52]). Most of the previous studies reported in literature use PDMS, which is the most common polymer material to prepare microsystems in laboratories. Yet, PDMS Young modulus is far more important (∼ 2 MPa [30]). To the best of our knowledge, very few publications [11, 84] reports the use hydrogels to study the migratory behavior of cancer cells, and those research implement rather long microchannels. We are currently trying to prepare microsystems implementing pillar networks using either PAA or collagen. One particular advantage of PAA is the possibility to vary the respective quantities of polymer and curing agent, in order to tune the rigidity of the hydrogel within a biomimetic range 1-5 kPa. In the contrary varying collagen stiffness, through tuning collagen concentration, would at the same time lead to varying adhesion ligand density which plays a major role in the migration process. Preliminary results has been obtained, as presented in Figure 2.8. Finally, PAA microsystems have been realized in collaboration with Institut Lumière Matière (ILM) (see Figure 3.4b) and we hope to be able to perform the first transmigration assays soon.

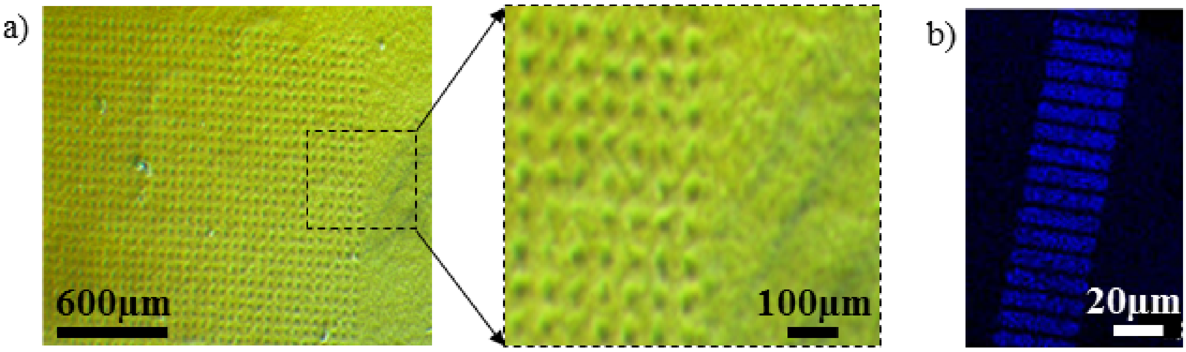

Figure 2.8: Preliminary results obtained on the fabrication of hydrogel based micro-patterned substrates. a) Bright field images of pillar Network molded in Collagen type I and b) fluorescent image of a PAA microsystem implementing 30 µm long and 5 µm large channels. The presence of fluorescent nanoparticles dispersed within the hydrogel allows the visualization of the channel walls.

This thematic has been conducted, in collaboration with ILM and Centre de Rercherche en Cancérologie de Lyon (CRCL), through several internships: Julien Castelluci (M2), Almudena Humanes (M1), Souhila Saci (M2), Aela Mauffrey (M1) and Lucas Ferry (L3). This was made possible in particular thanks to the funding of a ONCOSTARTER project (∼ 40 k€ over 1 year for 3 teams) by Cancéropôle Lyon Auvergne Rhône-Alpes (CLARA). The preliminary results obtained on this subject have allowed to submit 5 funding applications (ANR blanc, Plan Cancer, Pack Ambition Recherche) between 2015 and 2017. Unfortunately, none of them was selected. However these results allowed to strengthen existing collaborations and to initiate new ones.

2.3 Dynamical behavior of cancer cells migrating on nano-patterned substrates

When cancer cells spread away from the primary tumor, they tend to follow the trajectories of lymphatic or blood vessels, nerves, collagen fibers, white matter tracts, or other heterogeneous structures in tissues [32]. *In vivo* cells constantly pull, align and rearrange the ECM, generating features with specific topography at various scales down to tens of nm [71, 39]. It has been shown that the structure of the ECM surrounding the tumors guides the migration of invading cells [164]. Local modifications of the stroma structure at the vicinity of the tumor induces collagen fibers to rearrange into radially aligned configurations, hence promoting the escape of cancer cells from the tumor [137, 164]. Moreover, the presence of aligned nanofiber trails oriented radially from the tumor has shown clinical correlation to increased metastases and poor patient prognosis [144]. Therefore, the study of the impact of substrate topography on cell migration - also referred to as contact mediated guidance or contact guidance phenomenon - is highly relevant especially in the context of cancer.

Therefore, in this context, I have initiated another project at INL, in collaboration with Jean-François Chateaux, aiming at studying the migration of cancer and metastatic cells on nano-structured substrates. One original aspect of this project is the method used to produce nano-patterned PDMS substrates. Several substrate-related parameters were investigated such as pattern size and polarity.

2.3.1 State of the art of migration on nano-patterned substrates

Migrations assays on nano-patterned substrates use microfabricated ridges-grooves or posts-pits [28, 79]. Producing such substrates with well defined topographical features can be achieved by various techniques, including nanoimprint lithography [211], capillary force lithography [107], ultraviolet assisted lithography [191], embossing, photolithography, and micromachining [17]. Recently, Puliafito et al. reported a novel technique able to plastically deform micropatterned polymeric substrates using light, thus allowing to study the effect of tunable nanotopography on cell behavior [12]. Cell migration onto substrates implementing random or aligned fibers have also been studied [162, 104, 143]. For instance, the alignment of cells, of many different origins, parallel to these grooved substrates have been reported in literature [39, 76, 47, 19, 38, 43, 189]. We illustrate it here, in Figure 2.9a which represents MDA-MB-231 cells cultured on substrates implementing fibers.

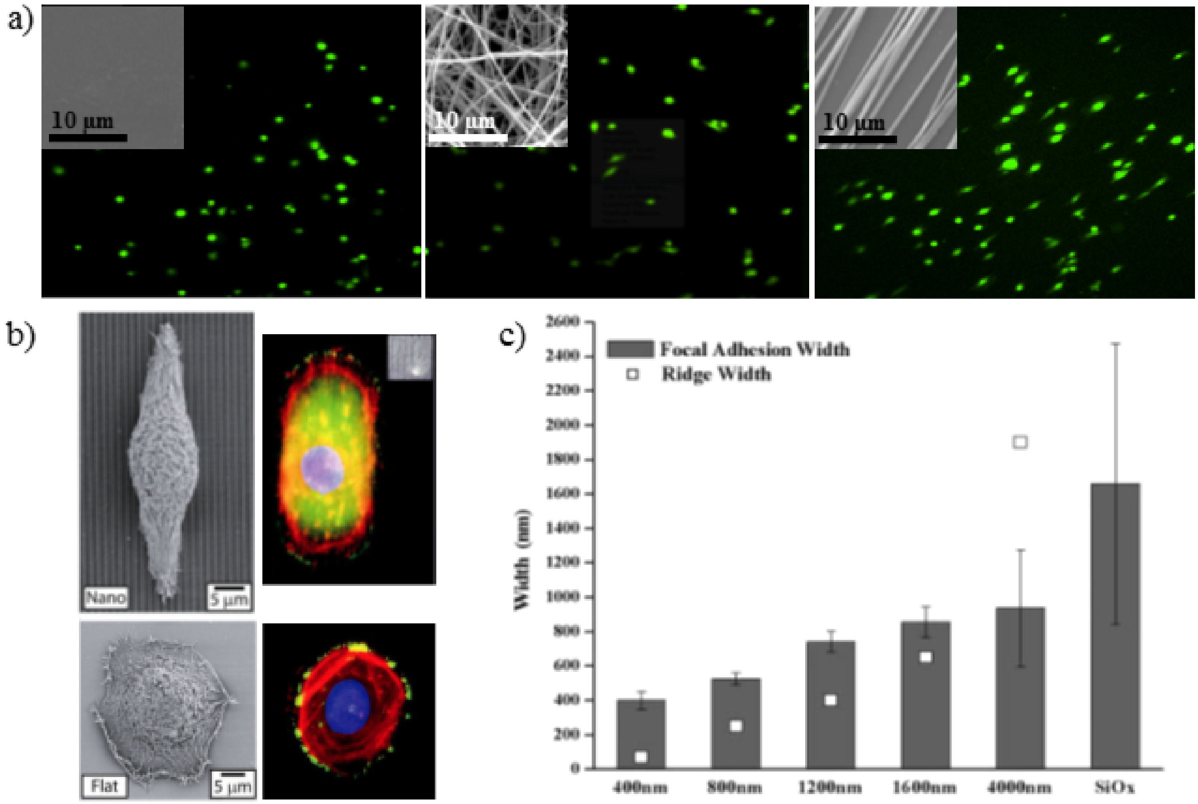

Figure 2.9: a) Confocal microscopic images displaying MDA-MB-231 cell morphology according to the topography of the substrate; topography is illustrated in the insets: (left) flat tissue culture polystyrene, (center) random and (right) aligned electrospun PCL nanofibers. Adapted from [143]. b) SEM and epifluorescent images of human corneal epithelial cells cultured on (top) a substrate with 600 nm deep grooves and 70 nm wide ridges on a 400 nm pitch, and (bottom) smooth substrate. Cells are stained for actin (red), vinculin (green) and the nucleus (blue). c) Average focal adhesion widths versus the pitch size, for cells cultured on smooth or patterned substrates; the corresponding ridge width is indicated (open squares). Adapted from [15].

We can distinguish that on aligned mat, they tend to elongate along the fibers direction unlike those cultured on both randomly organized fibers or flat surfaces. Teixeira et al. also highlighted the difference in shape and structural organization of human corneal epithelial cells in presence (top) or in absence (bottom) of aligned grooves on the substrate [15]. They have not only found that focal adhesions and stress fibers tend to align along the topographic features, but also that the size of the focal adhesions was dictated by the width of the ridges on the underlying substrates as illustrated in Figure 2.9b and c.

There is also increasing evidence that micro- and nano-topographies influence cell migration [98, 18, 83, 29]. Several theories have been proposed to explain the phenomenon of contact guidance such as : (i) intrinsic protein patterning promoted by discontinuities in features, (ii) asymmetric focal adhesion distribution formation due to the presence of features or (iii) preferential actin polymerization inducing the formation of filopodia parallel to the features [28]. The adhesion and migration of HepG2 cells on microtextured poly(glycolic-*co*-lactic)acid copolymer substrates - implementing 3 µm micropores - were found to be enhanced, with a diffusion coefficient twice as large than that on flat surfaces [29]. A study performed on T lymphocytes and T lymphoma cells migrating on substrate with or without 10 µm wide grooves revealed that surface topography can influence the migratory response of the two cell types in different ways [18]. Lymphocyte cells were found to migrate faster than lymphoma ones and to be more diffusive on flat substrates, whereas on grooved substrates, although both cell speeds were comparable, lymphocyte cells became more persistent and the lymphoma cells more diffusive.

Nelson et al. have reported the specific behavior of healthy mammary epithelial cells (MCF-10A) and breast cancer cell lines (MDA-MB-231 and MCF-7) migrating on 800 nm aligned PCL electrospun fibers compared to 700 nm random ones [143]. Aligned PCL nanofibers induced more efficient migration - traduced by higher net displacements and higher total traveled distances - for all cell lines compared to randomly-oriented nanofibers, even in absence of chemotactic gradient. Such results resemble the migratory behavior of MDA-MB-231 cells seeded in 3D collagen matrices with random or aligned collagen fibers [104]. However, unlike in 3D collagen matrices, cells migrating on aligned electrospun fibers presented a substantial increase in migration velocity for all cell lines [143]. Yao's group reported that nanofibers alignment, not only increases vimentin expression [216], but also orchestrates cytoskeletal reorganization and promotes the speed and persistence of migration of cancer cells [73]. Diehl et al. reported that human corneal epithelial cells tend to migrated along features direction on pitches ranging from 400 to 4000 nm, whith a maximum migratory velocity reached for 1600 nm pitches, where cells are the most elongated [98]. Nanogrooves smaller than the critical size of 75 nm wide and 33 nm deep have been reported to fail to induce alignment of rat osteoblastic cells [43]. A study performed on Human corneal epithelial cells suggested that groove depth plays a major role in the capacity of cells to sense nanofeatures such as ridges [15]. While nanoridges promote bidirectional guidance to both benign and metastatic breast cancer cells, asymmetric sawtooth-like structures unidirectionally bias the movement of breast cancer cells [180]. This bias in cell migration was measured in the same direction as, and is thought to arise from, asymmetries in the direction of actin polymerization. Topographic gradients represent another way to guide cell migration unidirectionally [39, 79, 80]; a phenomenon refereed to as topotaxis, which will not be discussed here.

2.3.2 Preparation of nano-patterned PDMS substrates

As presented in the previous section, several papers have reported the study of cells dynamics while migrating on nanopatterned substrates. In 2012, when we started this project, most of the studies used substrates implementing nanofeatures obtained from lithography techniques. Few of them were already using fibers deposited in a random or organized way in order to evaluate the effect of substrate nanotopography on the migration of cells. We decided to use an original method (at least it was then) to prepare nano-structured PDMS substrates using soft-lithography to replicate electrospun nanofibers. PEO polymer fibers of controlled diameter ($\sim$ few hundreds of nm) were produced by electrospinning as reported elsewhere [163]. The electrospinning setup used in this study has been developed by Jean-François Chateaux (INL) and is illustrated in Figure 2.10a. Briefly, 2 g of PEO were dissolved in water to obtain a homogeneous solution. 1 mL of the solution was loaded into a glass syringe with a 24G-gauge stainless steel needle. The nanofibers were produced using a computer controlled pressure system in the range 0.1-1 Bar to feed the fibers, a collection distance of $\sim$30 cm and an applied voltage in the range 9-20 kV. It allows the deposition of both randomly distributes and aligned fibers as presented in Figure 2.10b. The size of the nanofibers can be tuned by adjusting (i) the needle gauge, (ii) the electric field applied and (iii) the polymer concentration (which impacts the solution viscosity).

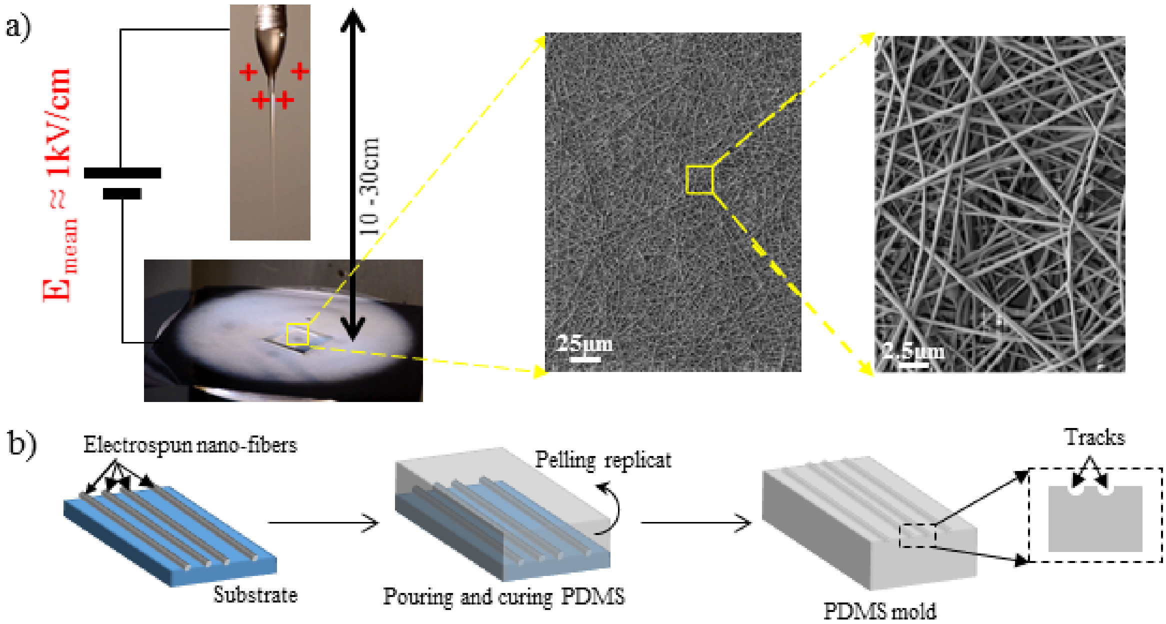

Figure 2.10: a) Schematics illustrating the electrospinning method. b) SEM images of some of the aligned electrospun PEO fibers.

At each conditions, several identical sets of fibers were produced: one set was used to determine the mean size of the fibers thanks to SEM imaging, the other ones were used to prepare the nanostructured substrates, according to the procedure briefly presented in Figure 2.10c. After silanization of the electrospun fibers, the mats were molded with PDMS at room temperature for 1 week in order to avoid fiber degradation due to temperature during the curing process at 70°C. PDMS substrates were then immersed in water in order to dissolve any traces of polymer that may have remained attached to the substrate. The substrates present grooves (corresponding to the fiber prints) with width ranging from 170 to 360 nm over several mm long. A mixture of collagen (20 µg/mL) and 0.02% BSA in PBS at a ratio 298.8/1.2 v/v is used to favor cell adhesion onto the PDMS substrates, as previously reported [7]. Substrates are placed at the bottom of a petri dish and covered with cell culture media. Breast cancer cells are let to adhere all night onto the substrate in the incubator before it is placed in an environmental chamber under microscopic observation.

2.3.3 Migratory behavior of breast cancer cells on 360 nm wide tracks

The behavior of cells migrating on various substrates are recorded for several days (1 picture every 5 minutes) and analyzed. Cell trajectories are extracted using image J ® software and represented with the same initial position. The first obvious effect of the presence of large nano-structuration of the substrate is the alignment of most of the cells along the grooves as presented on the SEM pictures in Figure 2.11a. On the contrary, when cells are placed over a flat PDMS substrate - without topography - cells adhered randomly, without following any particular direction. Figure 2.11b represents the normalized trajectories of MDA-MB-231 cells on both bare and 360 nm aligned grooved substrates respectively. Cells migrating on bare substrates follow an isotropic random walk, as the trajectories do not show any preferred direction. On the contrary, cells migrating on substrates implementing 360 nm wide tracks, present an oriented migration along the same direction as the grooves, hence suggesting that the presence of nano-patterns influences the direction of cell displacement.

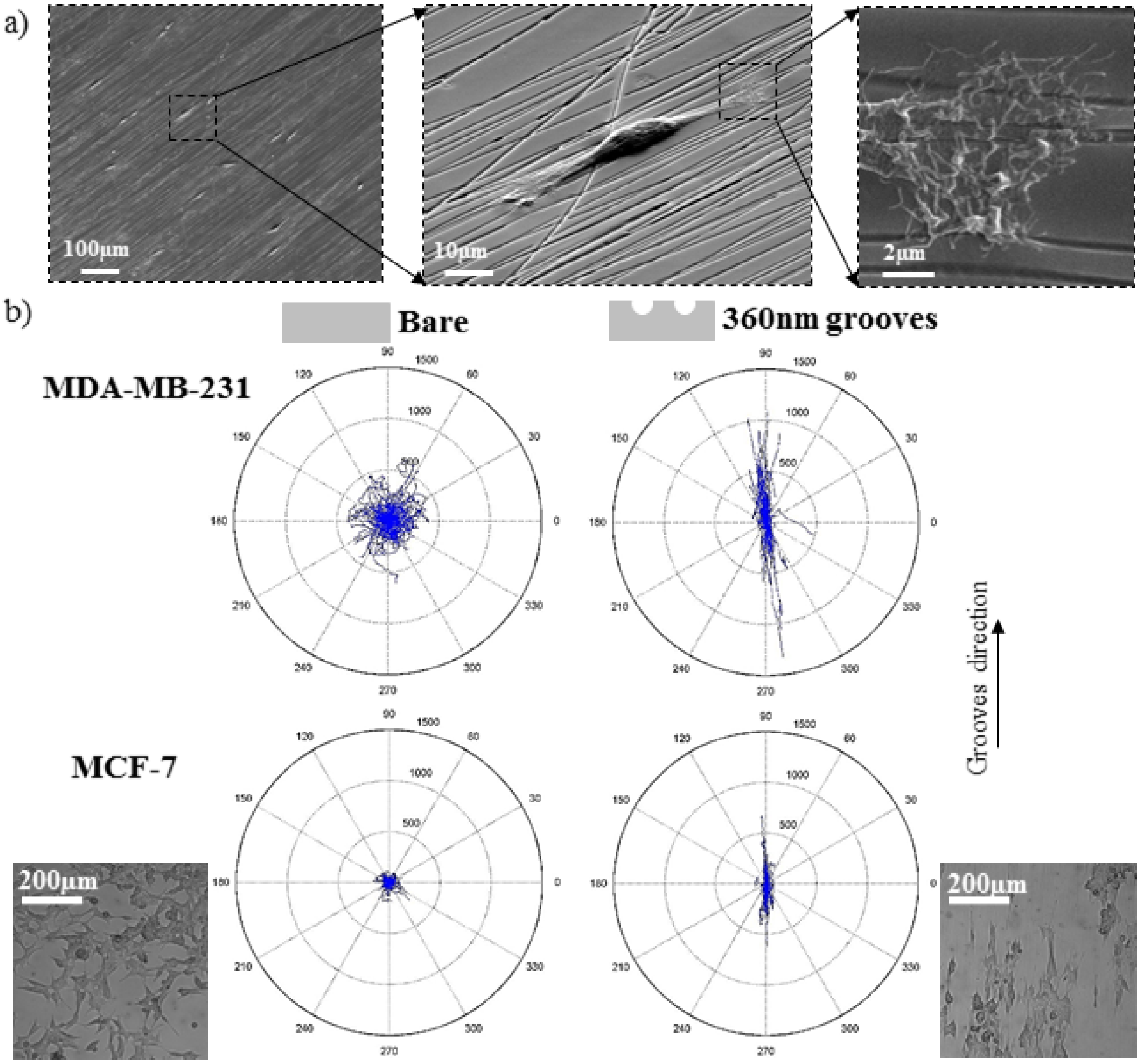

Figure 2.11: a) SEM pictures of MDA-MB-231 cells adhered on a substrate implementing 360 nm grooves. Normalized trajectories of MDA-MB-231 and MCF-7 migrating on (left) bare substrates and (right) substrates implementing 360 nm vertical grooves. The trajectories of several hundreds of cells are represented for each conditions. The two pictures are video-microscopic images of MCF-7 cultured on a bare substrate and a PDMS surface implementing 360 nm wide grooves.

A similar behavior has been observed with non-metastatic breast cancer cell line MCF-7: on bare substrates isolated cells present a random migration, whereas they experience oriented migration on 360 nm tracks. The trajectories of MCF-7 are aligned with the grooves direction, *i.e.* vertically. However, the native difference in motility between the two cell lines are maintained. Indeed, MCF-7 being epithelial cells, they are highly cohesive, as illustrated on the two pictures in Figure 2.11b and thus present low motility. This explains why trajectories of MDA-MB-231, which exhibit mesenchymal individual migration, are longer than that of MCF-7 for the same migration time. Those results are in good agreement with those reported in literature since then.

2.3.4 Effect of tracks size

We have repeated this experiment while varying the mean track widths, through the variation of the mean electrospun fibers diameter. The normalized trajectories of MDA-MB-231 migrating on substrates implementing grooves of different width are presented in Figure 2.12a. Surprisingly, cells migrating on PDMS substrates implementing grooves which width is equal or below 270 nm, move randomly, in a similar way to bare substrates. These results suggest that it exists a threshold groove size beneath which cells migration is no longer influenced by the nano-patterns on the substrate. Such threshold values have been previously reported for rat osteoblastic cells migrating on nanogrooves smaller than 75 nm in width and 33 nm in depth [43], hence suggesting that the threshold value is cell line dependent. However to the best of our knowledge, it is the first time that this size effect is observed for MDA-MB-231, as almost none of the publications on the subject deal with topographic features below 500 nm.

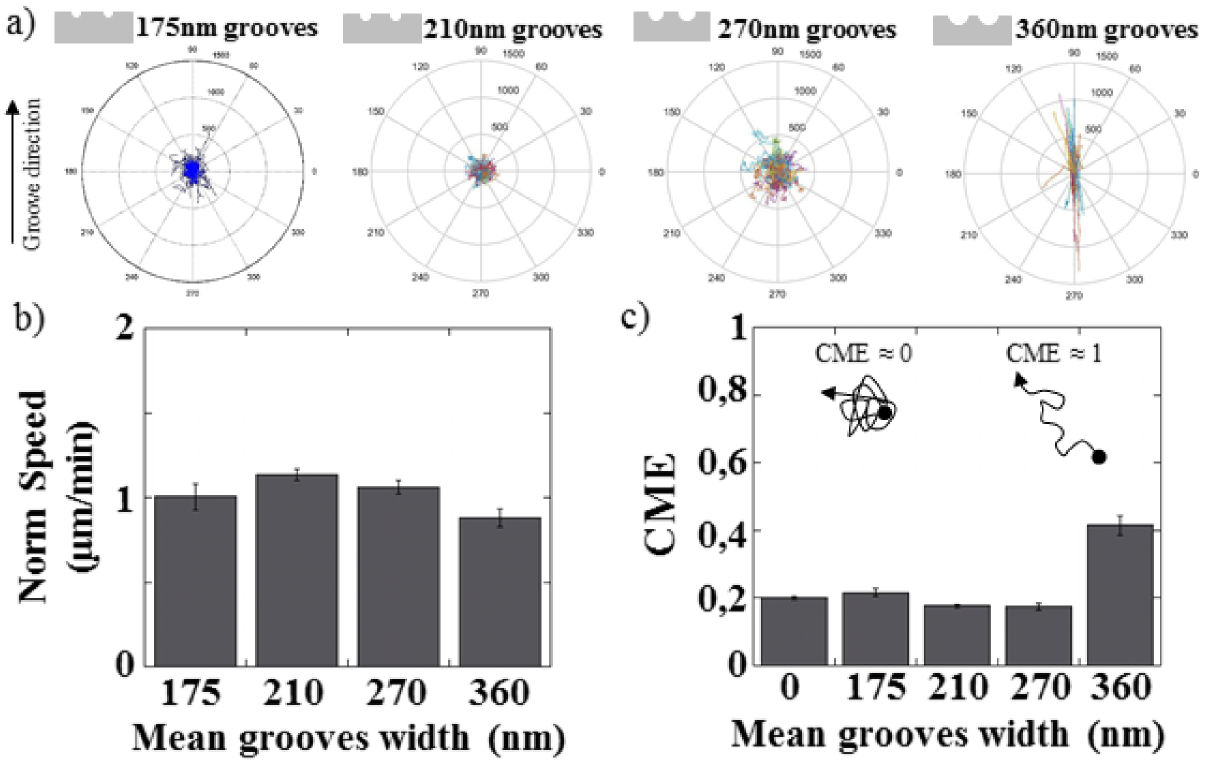

Figure 2.12: a) Normalized trajectories of MDA-MB-231 migrating on substrates implementing various sizes of grooves. The trajectories of several hundreds of cells are represented for each conditions. b) Mean normalized speed of cells - *i.e.* mean speed of cells migrating on a nano-structured substrate, normalized by the mean speed of cells migrating on a bare substrate - according to the grooves dimensions. c) Mean CME of cells migrating on different substrates. The error bars represent standard error.

The mean velocity of cells migrating on the nano-patterned PDMS substrates were recorded and normalized by the mean velocity of cells migrating on bare substrates simultaneously. The results are presented in Figure 2.12b. The presence of nanostructuration on the substrates does not influence significantly the mean velocity at which cells migrate on it. Although a substantial increase in velocity was observed on MDA-MB-231 migrating on 800 nm aligned electrospun PCL fibers compared to the flat reference [143], we want to stress that the present nanofeatures were substantially smaller (from 175 to 360 nm). Another difference between the two studies lies in the surface chemistry, which as been identified to play a crucial role in the cellular migration. Indeed, PCL fibers were deposited onto tissue culture treated polystyrene and directly used as substrates, on the contrary our PDMS nanotracks were treated with a mixture of type 4 collagen and BSA to promote cell adhesion to the substrate.
The type of migration have been quantified and compared between the different substrates, through the

calculation of the CME (see Figure 2.12c). As a reminder the CME traduces the efficiency of displacement of an object by comparing the distance between its initial and final positions to the total length traveled by the object to reach the final position. As expected, the random migratory behavior of cells on nano-patterns smaller than the threshold value, is associated with low CME values, CME ~ 0.2. On the contrary, the migration of MDA-MB-231 on nano-patterns larger than the threshold value, is associated with a large increase of the CME. Thus this traduces the increase of the efficiency of migration of the cells that do not migrate randomly anymore but follow a preferred direction corresponding to the groove direction. However, it can be noticed that the CME value (here 0.4) remains quite low compared to 1, which can be explained by the fact that the cells are following the groove orientation however they do not maintain the direction of migration during a long period of time. Instead, they tend to go back and forth on the grooves, hence oscillating in direction. In order to induce unidirectional migration, on might consider coupling patterned substrate with chemotaxis [143], or use gradient of topographic features [39] or asymmetric nanopatterns [180].

2.4 Conclusion

We have been presenting our study on the migration of metastatic breast cancer cells through a series of PDMS posts which spacing has been decreased ranging from 25 and 10 µm. Preliminary results suggest the existence of a critical size of pillar spacing, for which random cell migration is abandoned in favor of directed migration. The development in collaboration with ILM of hydrogel-based microsystems, allows to study the impact of the substrate deformability on this critical value.

We have also presented the first results on the migration of the same cell line on nano-patterned substrates. We reported that above a certain critical fiber diameter, the cells presented a directed migration, rather than the random walk they were experiencing at lower diameters. It would be interesting to evaluate if the critical diameter is cell line depend, because it could then be exploited to spatially isolate cells from a mixture.

Although they were less developed than the approaches for circulating cells discussed later, these studies have the merit of proposing approaches that were quite innovative at the time they were initiated. Indeed, at the time, whether it is the development of hydrogel-based microsystems for the study of cancer cell transmigration, or the development of substrates reproducing certain topographical features of the ECM, very few publications proposed similar work. Unfortunately, the state of the art having progressed much faster than our research, the results presented here - mainly obtained by M1 interns advised between 2012 and 2017, due to a lack of financial and human resources - have already been reported in the literature.
These results have been presented at an invited oral communication at “Physics of Cancer” in September 2015, at a regionnal workshop “Mecanobio-Lyon” in January 2016 and at the “Faculté des Sciences et Technologies de l’Université Lyon 1” day in June 2017.

Chapter 3

Microsystems for circulating cells

3.1 Context and state of the art of circulating cell mechanical phenotyping [113]

A wide variety of experimental biophysical assays have been used to probe deformability of living cells. Basically, the mechanical phenotyping techniques can be classified into three categories:

- the "collectives" techniques which deliver an averaged measurement on a large cells population,
- the "single cell" techniques allowing mechanical characterization on individual cells,
- the microfluidic techniques which aims at performing single cells analysis over a large population to reach high throughput.

3.1.1 "Collective" techniques

"Collective" techniques, such as viscosimetry [109], rheometry [65] and ektacytometry [148], are performed on diluted or whole blood samples, hence ensuring the analysis of the sample in few minutes. However, these techniques, delivering an averaged measurement on the totality of the RBCs population, are not able to detect the variation of deformability of few cells within a sample. Thus, they are not suitable for the diagnostic or the therapeutic follow-up of diseases affecting limited number of cells, such as malaria where the proportion of mechanically affected RBCs in a sample may be as low as 0.002% [195]. However, one may note that ektacytometry is currently present and used routinely in the hospital to monitor and study diseases such as SCA or HS, where a large proportion if not all of the cells from the samples are impacted by the mechanical changes.

3.1.2 "Single cell" techniques

In parallel, single cell analysis methods have been developed. For example AFM and other indentation techniques allow monitoring the cell deformation in response to a force applied through physical compression or indentation of a probe and can be used to extract cell elastic and viscoelastic properties. In micropipette aspiration, either a portion or a whole cell is aspired into the opening of a micropipette while monitoring the extension of the membrane, leading to the evaluation of the viscoelastic properties locally or at the whole-cell level, respectively. Unlike AFM and micropipette aspiration, optical tweezers are attractive mechanical assays because they do not necessarily require mechanical contact with the target cells. Optical tweezers uses a highly focused laser beam to create a 3D light gradient exerting a force on the cell, relying on the dielectric contrast with the surrounding media. Although these conventional techniques are well-established, they require sophisticated equipment and skilled personal and most importantly they are extremely low throughput (of the order of several tens of cells per day typically), which makes it unadapted to diagnostics and biomedical applications, where millions of cells per tens of minutes need to be processed.

3.1.3 Microfluidic techniques

Due to a match between cellular length scales and typical sizes accessible by microfabrication methods, microfluidic technologies propose attractive engineered micro-environments for the study of cellular mechanics compatible with high throughput. The different approaches can be classified into two distinct categories. In a first category refereed to as active microfluidics, the mechanical solicitation relies on the application of an external force that can be optical, electrical, magnetic, acoustic. . . In the contrary, the passive microfluidics category deals with techniques where only the hydrodynamics, and thus the channel geometry responsible for the flow generated, is responsible for the mechanical deformations undergone by the sample. Regarding the state of the art of cell mechanical phenotyping, few approaches presented in the literature are active (optical and electrical based solicitation), however most of them are passive techniques.

We first describe the active microfluidic techniques to mechanically characterize cells. For example, a microfluidic version of the optical tweezers has been developed by Guck et al. [75]. It consists in a two-beam laser trap optimized to serially deform isolated cells flowing through a microfluidic channel. The system is sufficiently sensitive to detect changes between non-malignant (MCF-10A), cancerous (MCF-7) and even metastatic (ModMCF-7) human breast epithelial cells [75], or measure the elasticity of iRBCs [89] with a throughput of 1 cell/min. One drawback of this technique however, is the exposure of cells to the laser beam during stretching.

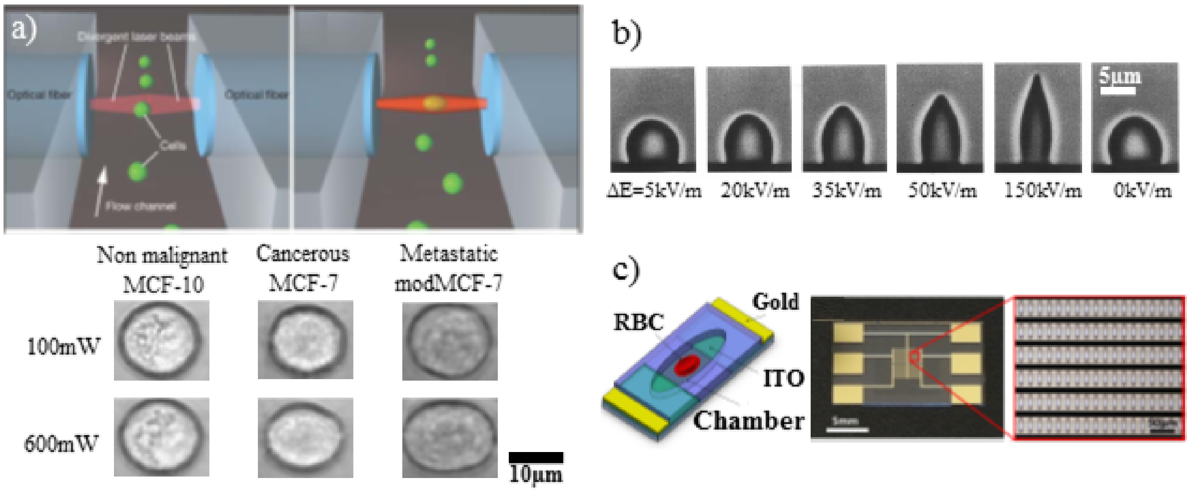

Figure 3.1: a) Principle of the optical stretcher developed by Guck et al. Flowing cells get stretched when intercepting the laser beam. Correlation between elongation and metastatic characteristic of breast cell lines has been observed. (Reproduced from [75], copyright (2005) by the Biophysical society, with permission from Elsevier). b) Electro-deformation of a RBC; cell elongation increases with the applied electric field (reproduced from [63], with permission from Elsevier). c) Schematic view and actual pictures of the single-cell microchamber array chip allowing mechanical characterization with improved throughput (Reproduced from [69] with the permission of AIP Publishing).

Transient deformation of cells in a high-frequency electric field is exploited in electro-deformation assay [63]. Using analytical models or numerical simulations, quantitative measurements of hRBC shear modulus μ = 6.1× 10^{-6} N/m and membrane viscosity η_m = 3.4× 10^{-7} N.s/m are obtained and present a good agreement with the micropipette results of Evans et al. [42]. One drawback of electro-deformation is the necessity to suspend the cells in a buffer of low conductivity, which add sample preparation steps prior to analysis and lead to rapid aging of the cells [63].

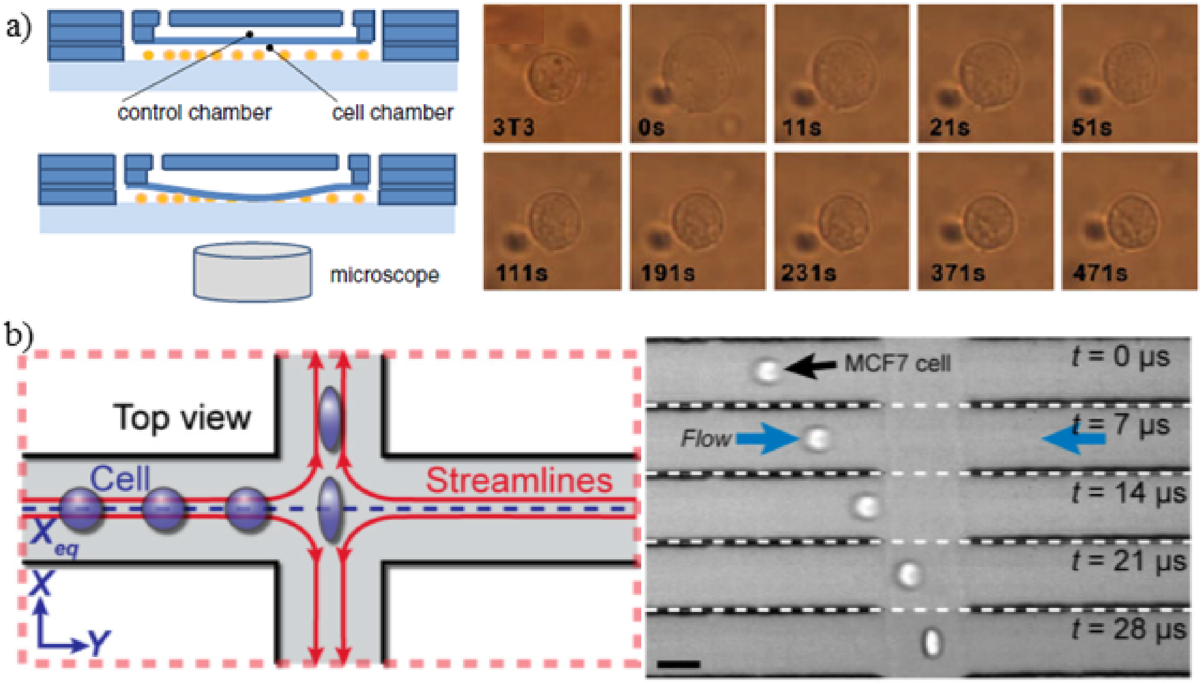

Figure 3.2: a) Schematic of the principle of compression experiments. Sequence of relaxation of a 3T3 cell after compression is stopped (Reproduced from [56], copyright The authors (2010), with permission of Springer). b) Schematic view and sequence of deformation of a focused cell being stretched when entering the extensional flow region (Reproduced with permission from [40]).

The discrimination of two different cell types (neutrophiles and fibroblasts) known to have different cytoskeletal structures has been reported using microfluidic compression experiments [56]. The method relies on the observation of the deformation resultant of the cell compression by an actuated flexible membrane. The relaxation time — $i.e.$ the characteristic time necessary for the cells to recover their equilibrium shape as compression is stopped — is used to discriminate two cell lines. Compression experiments with MicroElectroMechanical Systems (MEMS), to probe living cells stiffness, have also been reported in the literature [125, 21]. They usually rely on the controlled displacement of a moving actuator compressing the cell against a fixed part.

Perhaps the simplest method and the most present in literature to measure cellular mechanical properties while achieving high-throughput, is by monitoring cell deformations as they flow through microfluidic channels. Cellular deformability can be challenged either by the walls of the device or by the associated hydrodynamic stress without any contact, thus limiting the impact of cell membrane adhesion with channel boundaries. In the following, we chose to present the previous results obtain with passive microfluidics according to the channel geometry complexity rather than according to the cell types, as most of these approach can be applied to any cell types.
RBCs are highly deformable and their deformability can therefore be challenged using hydrodynamic stress generated by microfluidic channels wider than the typical size of the cell. For example, Lee et al. [193] reported the monitoring of RBC deformation in a hyperbolic converging microchannel. They showed that the extensional flow is more efficient to induce cell deformation than a shear flow, as RBCs presented deformation index of 0.51 and 0.29 at 3 Pa respectively. Such approach was used to detect the decrease in deformability of RBCs following heat treatment. Gosset et al. [40] proposed an automated microfluidic tool using inertial focusing to uniformly deliver cells to a stretching extensional flow where cells are deformed at high strain rates. They characterized the deformability of populations of leukocytes and malignant cells in pleural fluid samples. They predicted disease state in patients with

cancer and immune activation with a sensitivity of 91% and a specificity of 86% at high throughput (2000 cells/s).

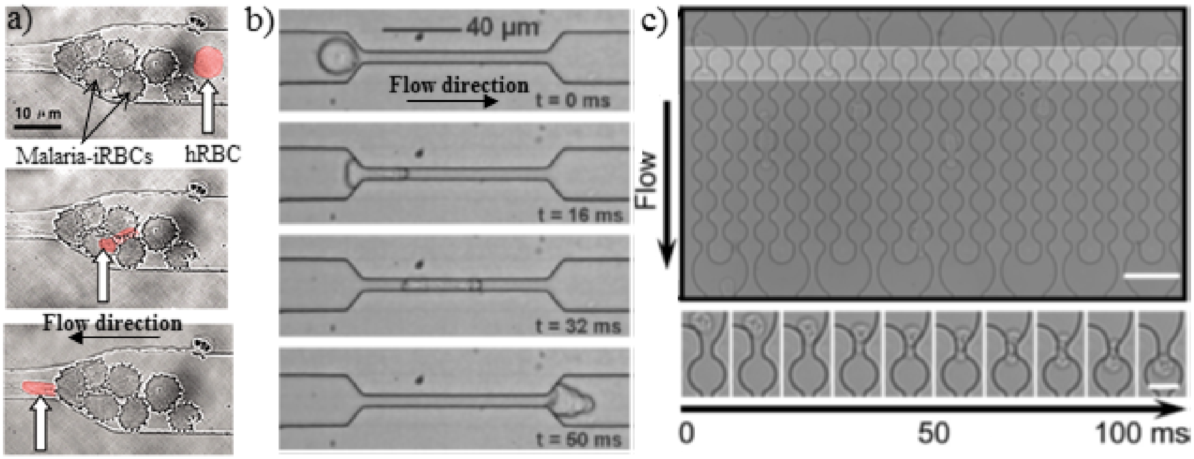

Figure 3.3: a) Video-microscopic images showing iRBCs being stuck at the entry of a geometric narrowing, whereas a healthy cell (in red) managed to deform past the blocage (Reproduced with permission from [90], copyright (2003) National Academy of Sciences, U.S.A.). b) Sequence of deformation of a human pancreatic tumor cell flowing through a constriction (Reproduced from [187], copyright (2007) with permission of Elsevier). c) Image of the multi-constriction array, which consist in 16 channels each implementing a series of 5 constrictions. Sequence of deformation of a single HL-60 cell during flow through a 5 µm constriction; transit time of 80 ms is measured (Reproduced from [100] with permission of the Royal Society of Chemistry).

Constriction channels with dimensions smaller than the typical size of a single cell provide a simple and powerful tool to probe cell deformability. Several types of geometric restrictions have been reported in literature to quantify cell mechanical phenotype, using however the same type of readout (transit time, deformation index and relaxation time). For example Selby et al. [90] reported the use of a well-defined geometrical constriction ranging from 8 to 2 µm in width and controlled pressure gradients in order to discriminate hRBCs and iRBCs. They report that as parasites develop within the host cell, the increase of RBCs rigidity prevent their passage through smaller constrictions. The distinction between non-malignant and cancerous cells flowing in similar geometries was demonstrated using entry time [68, 219] — defined as the time necessary for the cell to deform and enter completely into the microchannel — and deformation index measurements [219].

Flow of cells in 16 parallel channels implementing multiple constrictions has also been reported [100]. The study revealed that transit time scales indeed with cell size and that simultaneous transit events occurring across neighboring constrictions can influence transit time [100]. A comparable geometry was used to quantify the effect of taxol — an anti-cancer drug — on the transit time of tumor cells [128] through the serial constrictions. The results show that when traveling through the first constriction, cells treated with taxol undergo longer transit times than untreated cells, however for subsequent transits the difference was smaller between the two groups [128]. Herricks et al. [196] reported that ring-iRBCs get blocked upstream whereas hRBCs reached positions further downstream in converging channels.

The dynamic behavior of RBCs flowing through arrays of 15 µm pillars, either slowly through 5-2 µm wide gaps or rapidly along 10 µm wide channels has been studied [81]. They observed that mechanically impaired RBCs — either due to heat treatment or issued from iRBCs or from patients with HS — tend to accumulate in narrow slits more frequently than normal hRBCs, hence demonstrating their increased rigidity. Similarily, Bow et al. [62] have monitored dynamic mechanical responses of 10^3–10^4 individual RBCs using converging or diverging obstacles. They have experimentally demonstrated that differences in RBC deformability, highlighted by differences in transit velocity, are enhanced in geome-

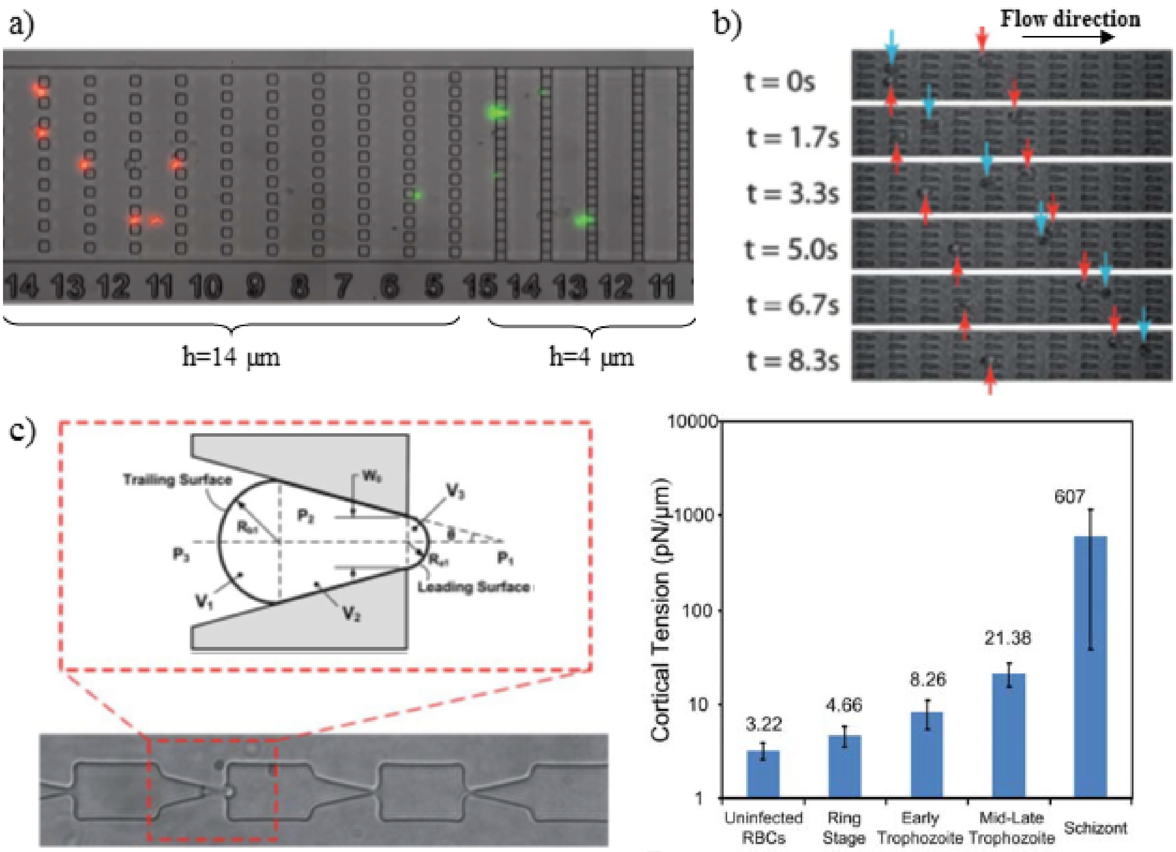

Figure 3.4: a) Illustration of the deformability-based separation. Stiff THP-1 cells (treated by glutaraldehyde) labelled in red are trapped in larger pores than compliant THP-1 cells (treated by Latrunculin-A) labelled in green (Reproduced from [160] with permission of the Royal Society of Chemistry). b) Time-lapse images of ring-iRBCs (red arrows) and hRBCs (blue arrows) flowing in the device; the hRBC travels faster than the iRBC (Reproduced from [62] with permission of the Royal Society of Chemistry). c) Microfluidic adaptation of the micropipette aspiration technique. RBCs are deformed when passing the funnel constriction and the associated geometric model. Measured cortical tension of hRBCs and iRBCs in various stages of infection (reproduced from [165] with permission of the Royal Society of Chemistry).

tries with sharper corners, for a given pressure difference. The influence of an anti-malaria drug (Artesunate) on the dynamic deformability of ring-infected iRBCs was also evaluated [182]. After Artesunate treatment, they observed a 50% decrease in the transit velocity of iRBCs whereas only 10% in speed reduction is observed for hRBCs. A limitation to constriction channels however is the influence of size and adhesiveness on cells behavior, which makes it difficult to emphasize the role of deformability alone. Indeed, recent studies trying to take the cell size into account have been reported in the literature [1]. They showed that cell size significantly influences travel times and that for a given volume, stiffer cells have longer transit times than compliant ones. However, efforts still need to be made to characterize adhesion and/or friction between channel walls and cell membrane, for example by varying the walls coating. Nyberg et al. [100] have reported variability in transit time measurements as the PDMS device ages after plasma treatment; they attribute such discrepancies to modifications in channel surface properties. Another drawback of this approach is the need to adapt precisely the size of the constriction to dimensions of cells of interest to avoid clogging or deform significantly the cells.

Guo et al. [165] proposed an adaptation of the conventional micropipette aspiration technique into microfluidic format. The geometry of the microfluidic micropipette aspiration device implements multiple funnel-shaped constrictions with openings ranging from 5 down to 1 µm. As a cell is flowing in the device, it gets trapped at the nozzle of a funnel, the pressure difference is manually increased until the RBC is allowed to squeeze past the restriction. The threshold pressure is used to determine the intrinsic stiffness of each cell. Using the same mathematical model as in conventional pipette aspiration technique, $i.e.$ considering the RBC as a liquid-drop with constant volume, they managed to extract the cell cortical tension. iRBCs by early (ring) through late (schizont) developmental stages of the parasite were shown to be 1.5 to 200-fold stiffer than uninfected cells as already reported in the literature [23]. However, the rectangular cross-section of the geometry can rise concerns about the validity of applying conventional micropipette models to retrieve cellular mechanical properties.

3.1.4 Balance sheet

Although they present many advantages such as possible automation, absence of labeling and compatibility with high throughput, each microfluidic mechanical characterization technique has some drawbacks. In optical stretching, cells are exposed to the power of the laser which may damage them and electro-deformation requires a change in suspending media; such low conductivity buffer may accelerate aging of the cells. Multi-steps soft lithography processes are needed to implement the flexible membrane in compression experiments. A disadvantage of constriction channels is the persistent possibility of device clogging. Indeed, as the section of the constriction is smaller than the typical size of the cells, one need to adapt carefully the width of the constriction. A group proposed recently an improvement with the development of a constriction channel with tunable section [208, 217]. One of the walls of the constriction was replaced by a thin membrane, which deflection is controlled *via* external pressure. In case of channel obstruction by larger particles or cellular aggregates, the increase of the applied pressure causes the augmentation of the constriction cross-section through deflection of the membrane, thus removing the obstruction.

Up to recently, the various techniques presented above presented the same limitation in terms of throughput because of the use of high-speed video-microscopy for monitoring cellular mechanical responses such as the deformation index. Indeed, even when using automated post-processing routines, the huge amount of image data to analyze imposes computational power and remains time consuming. In replacement of high-speed camera, electrical impedance measurements has been reported in the literature to detect RBCs [72] and cancer cells [1] deformation in constriction channels, with a throughput of 100 cells/s. In 2015, Jochen Guck's group has proposed an automated Real Time Deformability Cytometry (RT-DC) able to perform continuous cell mechanical characterization of large populations (above 100 000 cells) with throughput greater than 100 cells/s [151, 132]. Their system consists in the real-time measurement of the deformation associated with the passage of cells into a constriction channel. They report that RT-DC is sensitive to cytoskeletal alterations and can distinguish cell-cycle phases, track stem cell differentiation into distinct lineages and identify cell populations in whole blood by their mechanical fingerprints. More recently, Deng and Chung [212] proposed a similar device allowing nearly real-time analysis of transient deformation of cells hitting a wall at a T-junction. Their automated process allows the mechanical characterization of cells at a throughput of 2000 cells/s.

Finally, the last challenge that still need to be addressed is the translation of raw parameters such as entry time or deformation index into cellular intrinsic mechanical characteristics such as Young's modulus or cortical tension. Indeed, intrinsic deformability parameters are independent of the setup (viscosity, flow speed, etc…) and allow the comparison of data obtained with various techniques and by various research groups. Therefore there is a strong need for theoretical framework and mechanical modeling of the cellular response in order to extract intrinsic mechanical properties.

Deformability can therefore bring information on the physiopathological state of cells, but it can also be exploited in order to concentrate, trap, manipulate and sort cells as discussed in the following section. The particular behavior of a cell can thus become a signature of its specific deformability. For an extensive review of all the techniques developed to separate cells upon their deformability, readers can look at [113].

In the following sections, we proposed 2 approaches based on the flow of cells in capillary smaller than the typical size of the cells of interest. First, we will present results obtained on RBCs, obtained mainly during the PhD of Amin Amirouche, as well as the internships of Amel Bessaa (M1 student) and Blandine Simon (M2 student). The results presented in 3.2 could provide a solution for the therapeutic follow-up of malaria. Then we will report the mechanical characterization of RBCs - for which Josue Esteves made some numerical simulations on this project during his 2 years of ATER - and nucleated circulating cells using the pressure drop measurements. Finally, we will discuss the development of nano-optical tweezers to mechanically characterize RBCs, performed during the PhD of Ali Kheir Aldine co-advised with Taha Benyattou and in collaboration with Lotfi Berguiga and Cécile Jamois (INL, i-LUM team).

3.2 RBCs in microfluidic deformability cytometry [3, 124, 2]

In the present section, we propose to evaluate a specific geometry to perform mechanical phenotyping of RBCs. We first introduce the design of the microfluidic geometry and discuss its advantages. Then, we experimentally investigate thoroughly the dynamics of hRBCs flowing through the microsystem. We document how the experimental parameters (buffer viscosity, channel width, flow speed, etc...) may influence this dynamics. Finally, we demonstrate the ability of the geometry to allow discrimination of healthy and mechanically impaired RBCs, on artificially rigidified and pathological cells.

3.2.1 The oscillating width channel

The geometry - referred to as the OWC - consisted in a microchannel implementing a series of 5 µm wide constriction associated with a 25 µm wide enlargement as illustrated Figure 3.5. Each restriction and widening has a length of $L_e = L_n$ = 10 µm. This width oscillation is repeated over a total length of 290 µm. Through the study, the main width of the channel inlet/outlet, W_o, has been varied (W_o = 15, 25 and 50 µm) while keeping a fixed height of 5 µm. The geometry has been selected in order to strongly deform the cells ; indeed when flowing through the constrictions, RBCs tend to get elongated along the flow direction and to get stretched perpendicular to the flow direction when they flow through the enlargements. Due to the repetition of the width oscillation, the cells are sequentially elongated and stretched, hence ensuring a periodic solicitation of the cells. The frequency of solicitation can be easily tuned by adjusting the velocity of the pressure driven-flow.

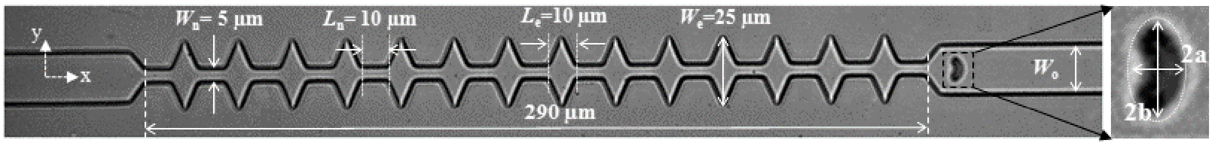

Figure 3.5: Microscopic image of the OWC microsystem. The channel is composed of 15 oscillations of width. The different dimensions of the geometry are reported on the picture ; W_o has been varied between 15 and 50 µm. The insert shows the close-up of a RBC where the two axes along and normal to the flow direction, respectively $2a$ and $2b$ are illustrated.

Another advantage of the OWC geometry is the centering effect. This effect is crucial for the study of cell dynamics at the exit of the last restriction, as it requires a symmetrical shape recovery process, as well as equivalent stress conditions between cells. Indeed, cells may enter the geometry at positions that cannot be controlled. When using a channel implementing a single 10 µm long and 5 µm wide constriction, cells entering at an random position y_i tend to follow the same streamline, resulting in cells exiting at various positions $y_f = y_i$ (data not shown here). It is very complicated to compare the behavior of cells which do not witness the same speed, and therefore which do not experience the same stress.

On the contrary in the OWC geometry, cells tend to exit the last narrowing at the same y_f, associated with the half of W_o (y = 0 was arbitrarily chosen to be the center line of the channel), whatever its position when entering the microchannel y_i. We can explained this phenomena by a lift force that pushes the deformable objects away from the walls; here the constriction is so narrow, $i.e.$ the walls are so close to each other, that the RBCs end up centered. This lift force occurs mainly within the constrictions where the shear stress is maximum, which is coherent to results obtained in similar geometries where enlargements are both wider and longer (OWCWLE see Appendix B).

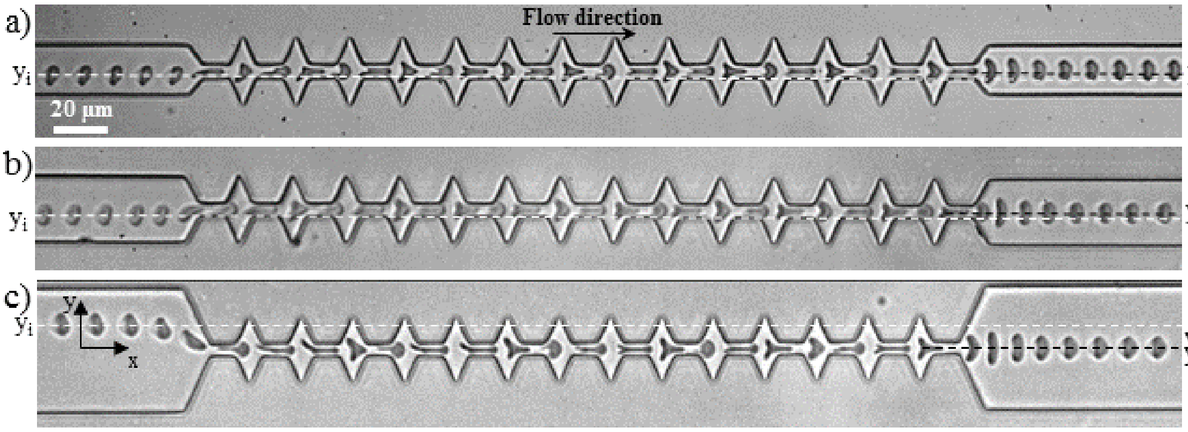

Figure 3.6: Time lapse microscopic images of RBCs flowing through the OWC geometry for : (a) W_o = 15 µm (η_{out} = 31.5 mPa.s and V_{cell} = 1820 µm.s^{-1}), (b) W_o = 25 µm (η_{out} = 31.5 mPa.s and V_{cell} = 2194 µm.s^{-1}) and (c) W_o = 50 µm (η_{out} = 31.5 mPa.s and V_{cell} = 1979 µm.s^{-1}). The dashed lines highlight the shift between the initial position y_i and the final position y_f.

Figure 3.6 presents 3 examples (one for each value of W_o tested) of cells entering the channel close to a wall and being centered after undergoing the series of deformation in the oscillating part of the device ; hence insuring that all the cells are exposed to the same stress and thus an easier interpretation of the data. We also note that the drift ($|y_i - y_f|$) is more pronounced for wider channels (typically 50 µm). We quantified the centering effect in a 50 µm wide channel, by evaluating the shift undergone by the cells $|y_i - y_f|$ versus $|y_i|$, for various outer viscosities ηout and several cell speeds V_{Cell}. The results presented in Figure 3.7 illustrates that even for cells entering the channel in highly off-centered positions (corresponding to large $|y_i|$), they tend to exit the channel centered (y_f = 0), which is traduced by $|y_i - y_f|$ tending towards $|y_i|$, *i.e.* the slope of the linear regression tending towards one. The centering effect does not seem to be affected by the cell velocity, V_{Cell} but rather by the external viscosity η_{out}; a higher drift is associated to a higher η_{out} for the same entry position $|y_i|$.
We have verified that the repetition of the restriction did not impact the behavior of RBCs exiting the geometry. Indeed, it has been reported in literature [92, 215, 136, 184] that the application of a stress too high or for a too long period of time can induce a mechanical fatigue of the cells. For example, Simmonds et al. report that RBCs present impaired deformability when exposed to physiological levels of shear stress [136] (above 40 Pa) for 1 to 64 s. Other studies report that cyclic mechanical solicitations of RBCs lead to significantly greater loss of membrane deformability, compared to continuous deformation under the same maximum load and duration [184]. Therefore, the recovery time of hRBCs were measured and compared after a single 10 µm long geometric restriction and at the exit of the 15 repetitions of the restriction. This study has been conducted in channels with a main width of 15 µm as illustrated in the inset of Figure 3.8a which presents the recovery curves of two hRBCs flowing in both geometries. In order to facilitate the comparison and the interpretation of the data. The time has been arbitrarily set to be the exit of the last constriction. We can see that the two recovery curves superimpose perfectly hence highlighting that there is no influence of the number of restrictions on the behavior of healthy RBCs exiting a 5 µm wide and 10 µm long constriction, *i.e.* D_{out} and τ_r. We also measured the shape recovery time of healthy RBCs in both geometries for different cell speeds. Figure 3.8b reports the inverse of recovery time, 1/τ_r as a function of the cell speed. Cell speed - which is measured in the 15 µm wide section of the channel, far away after the exit of the restriction - is varied through the

applied pressure at the entry of the microfluidic chip. Due to a difference in hydrodynamic resistance of both geometries, the same applied pressure results in different cell velocities. We showed that $1/\tau_r$ varies linearly with the cell speed. We verified that cells flowing in both geometries respond the same way as all the data collapse on the same linear regression, underlying that at a given cell speed, healthy cells present the same recovery time. Therefore we can conclude from those results that no irreversible deformations in the RBC membrane, nor mechanical fatigue could be detected in our approach.

3.2.2 Stretching versus unfolding

Video-microscopic recordings allow the visualization of the cells deformation as they flow inside the microfluidic device (Figure 3.9). The cell entering the geometry presents a parachute-like shape, typical of RBC confined flow. As it approaches the first constriction, the cell gets compressed which is traduced by its elongation in the flow direction. Then it undergoes a stretching along the y-axis when entering the widening, but before reaching its maximum deformation, the cell is already compressed by the next constriction, leading to a triangular shape. This cycle of compression-elongation is repeated due to the series of width oscillation.

Finally, as it exits the last narrowing, the cell relaxes to its parachute-like shape in two possible ways, depending on the experimental conditions:

- At high speed and high viscosity of the carrier fluid, the first relaxation mode - **the stretching behavior** - is characterized by a sudden increase of the axis of the cell (normal to the flow direction ($2b$) as it exits the last constriction, before returning back slowly to a steady shape as illustrated in the schematic and the time lapse (Figure 3.9a).
- At lower speed and lower viscosity, the cell undergoes the same compression-elongation cycles and behaves qualitatively similarly, even if the resulting deformation is less important than in the previous mode (Figure 3.9b). However at the exit, the cell which is compressed due to the last narrowing, recovering directly its parachute-like shape, without being stretched in the y-direction. This mode is referred to as **the unfolding behavior**.

Post processing of the recorded movies permitted the extraction of the cell dimensions in each image. *Via* the adjustment of the cellular contour with an ellipse, both axis $2a$ and $2b$, the dimensions of the ellipse along and perpendicular to the flow direction respectively, can be extracted. The actual deformation of the RBCs flowing in our geometry can be quantified using the deformation index $D = \frac{(2a-2b)}{(2a+2b)}$.

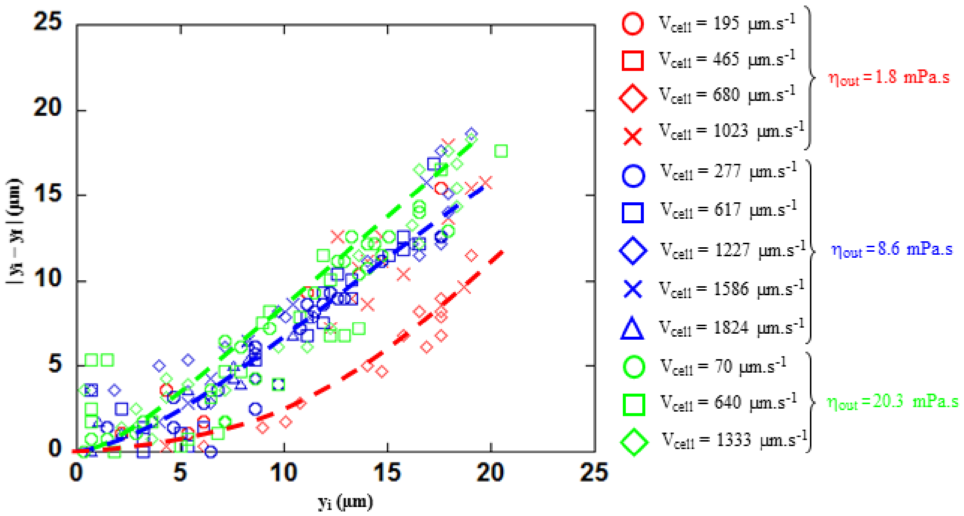

Figure 3.7: Quantification of the drift $|y_i - y_f|$, versus the cells initial position $|y_i|$ for various η_{out} and V_{cell}, in a microchannel where W_o = 50 µm. The dashed lines are guides for the eyes.

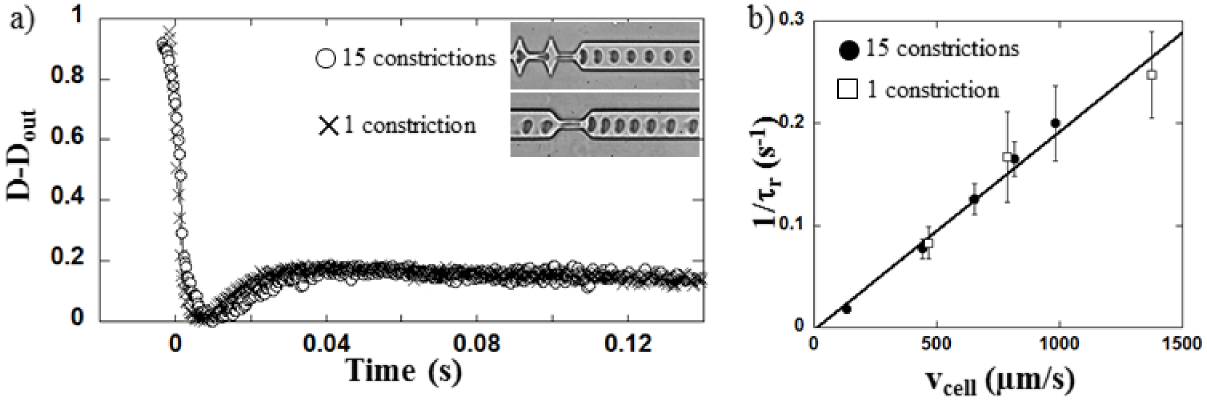

Figure 3.8: a) Deformation index D versus time for two hRBCs flowing in a 15 µm wide channel implementing either a single 10 µm long and 5 µm wide constriction or 15 repetitions of a 10 µm long constriction of same width. The origin of the time has been arbitrarily set to be the exit of the last constriction. V_{cell} = 500 µm/s and η_{out} = 31.5 mPa.s. The deformation index has been normalized by the extension at the exit such as both cells present the same D_{out}. b) Evolution of $1/\tau_r$ versus cell velocity at the exit for both geometries for η_{out} = 31.5 mPa.s.

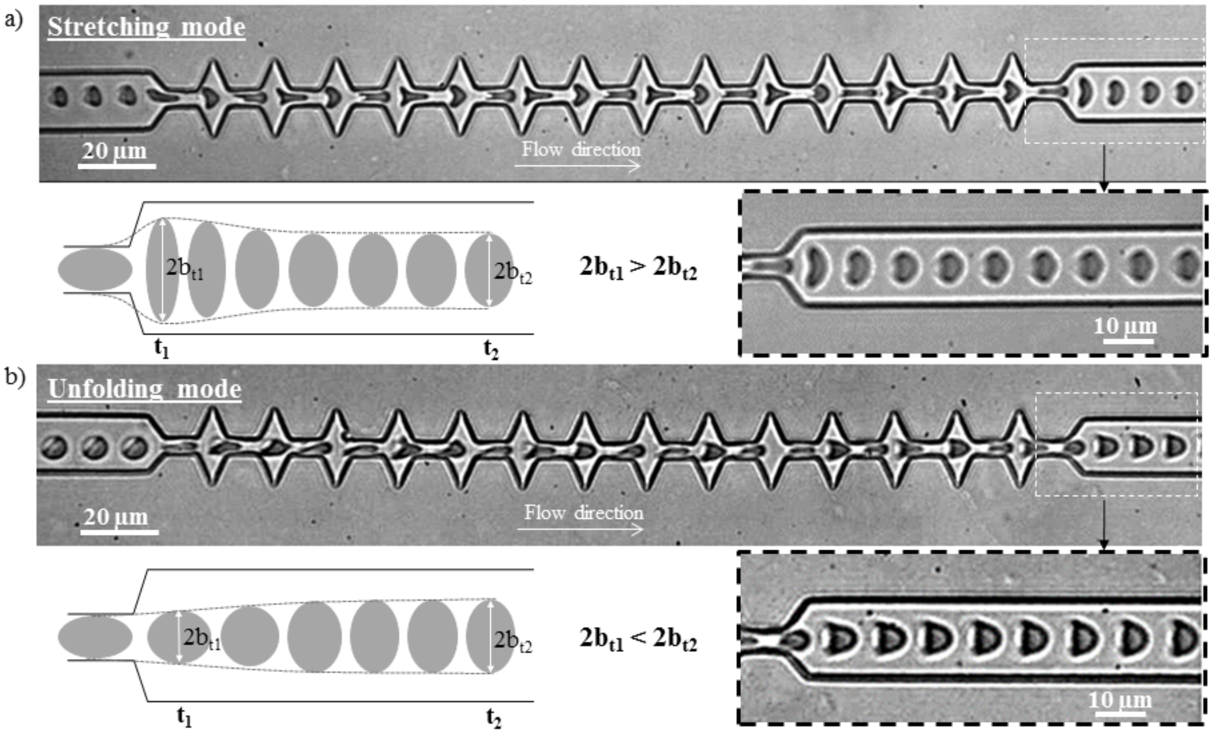

Figure 3.9: Sequence of deformation of 2 hRBCs under flow a) at high (η_{out} = 31.5 mPa.s and $V_{cell} = 533$ µm.s^{-1}) and b) at low speed and external viscosity (η_{out} = 1.3 mPa.s and $V_{cell} = 483$ µm.s^{-1}). Along the geometry, both cells get compressed and elongated perpendicular to the flow direction when entering each narrowing and widening respectively. As they exit in the stretching mode, the cell is stretched by the extensional flow before relaxing to the parachute-like shape, unlike in the unfolding mode where the cell relaxes directly from the compression without being stretched. The schematics show a representation of the typical deformation in the two behaviors at two different times t_1 and t_2

As an example, the variation of D associated with the sequences of deformation presented previously are reported Figure 3.10. As the RBCs maintains their parachute-like shape, in the 15 µm wide zone of the channel, the corresponding deformation index is relatively constant and nearly close to zero, hence traducing a projected area roughly circular. The following oscillations in D traduce the deformation undergone by the RBCs in response to the variation of channel width. Indeed, D increases to positive values ($2a > 2b$) due to the cell compression by the constriction (see upper snapshot) leading to its elongation in the flow direction. In the contrary, when entering an enlargement, it tends to be stretched in the y-direction (see lower snapshot) corresponding to a decrease in D which can reach negative values ($2a < 2b$) depending on the experimental conditions.

In the stretching behavior (Figure 3.10a), after reaching a maximum value at x = 285 µm (corresponding to the cell compression inside the last narrowing), the sudden drop of D traduces the large cell stretching due to its flow out of the last narrowing. Finally, after reaching a minimum at a position x $\sim$ 295 µm (corresponding to the maximum stretching once out of the last constriction), D returns to its initial value and reaches a plateau ; this corresponds to the cell shape recovery. In the case of the unfolding behavior presented in Figure 3.10b, D reaches a maximum at x = 285 µm, however, it decreases directly according to an exponential decay to reach the plateau corresponding to the equilibrium shape.

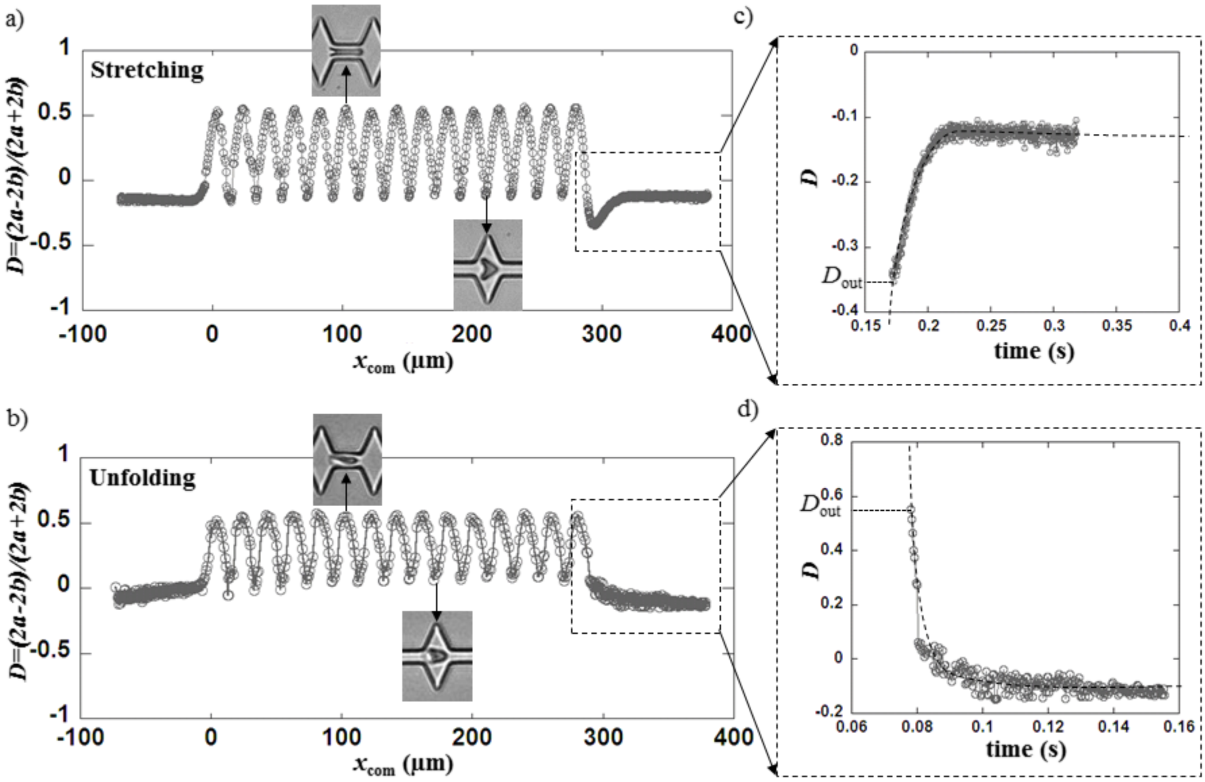

Figure 3.10: Variation of the deformation index $D = \frac{(2a-2b)}{(2a+2b)}$ versus the position of the cell's center of mass for a) the stretching and b) the unfolding behaviors. The origin of the graphs has been arbitrarily chosen to be the entry of the first narrowing. c) and d) Representation of D versus time of the two previous curves. Only the time window corresponding to the shape recovery is reported. The exit of the last narrowing has been arbitrarily chosen to be t = 0. The dashed lines are exponential fits allowing the determination of the recovery time τ_r.

In order to extract the shape recovery time τ_r, the variation of D between the maximum deformation at the exit, noted D_{out}, and the equilibrium shape corresponding to the plateau value is represented as a function of time (see close-up Figure 3.10). The experimental data are fitted using an exponential growth or decay depending on the relaxation mode, stretching or unfolding respectively, thus giving recovery time τ_r values.

3.2.3 Shape recovery time

We have investigated the influence of the hydrodynamic experimental conditions on the shape recovery of healthy RBCs, by varying both the buffer viscosity and flow speed. The results are presented as a recovery diagram (Figure 3.11), where the recovery mode is plotted as a function of η_{out} and V_{cell}. Because we did not have direct access to the flow velocity, we chose to use the cell speed after exiting the last constriction instead. For $V_{cell} \geq$ 400 µm.s^{-1}, the transition between the two recovery modes is mainly dictated by η_{out} : stretching was observed for $\eta_{out} \geq$ 5 mPa.s, whereas unfolding was obtained for $\eta_{out} \leq$ 2 mPa.s. In the frontier zone (highlighted by the dashed line), we noticed experimentally a mixed behavior, where a portion of the RBC population experienced stretching, while the other one experienced unfolding. The percentage of the stretching behavior increased with the cell velocity, hence highlighting that the transition depends also on V_{cell}. At lower cell speed, $V_{cell} \leq$ 350 µm.s^{-1}, the transition between the two relaxation modes depended strongly on both V_{cell} and η_{out}.

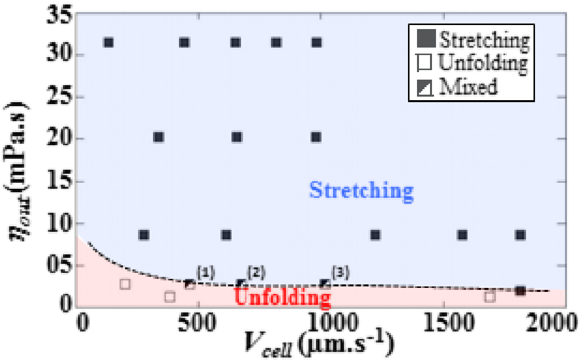

Figure 3.11: Experimental shape recovery diagram representing unfolding (open squares) or stretching (solid squares) behaviors according to the cell velocity V_{cell} and the viscosity of the surrounding medium η_{out}. The mixed behavior refers to a mode where a portion of the RBCs experiences unfolding whereas the rest of the population undergoes stretching. The percentages of stretching were (1) 27%, (2) 50% and (3) 55% respectively. The dashed line is a guide for the eyes representing the transition between the two modes.

By increasing the viscosity and velocity of the carrier fluid, we tuned the viscous hydrodynamic stress probed by RBCs, which leads to a transition in shape recovery behavior. Indeed the diagram reveals that at low viscous stress, the cell resists the deformation and recovers a steady shape according to the unfolding mode. Whereas, when the viscous stress is sufficiently high, the RBC gets stretched at the exit and experiences stretching. Therefore the Capillary number ($Ca = \frac{St.2b}{\mu}$, where St is the hydrodynamic stress, $2b$ the typical size of the cell and μ its shear modulus), ratio of the fluid viscous forces to the RBC elastic properties, can be used to describe the shape recovery of RBCs. In parallel, the viscous stress St undergone by RBCs at the exit of our geometry was estimated using the equation 3.1. In a diverging channel, St can be expressed [60] as:

$$St \sim 3\eta_{out} \left[|\partial(u,x)| + |\partial(v,y)| \right] \tag{3.1}$$

In order to estimate St probed by the cells at the exit, we used Comsol Multiphysics® to perform 3D numerical simulations of buffer solutions, at various viscosities, flowing in the geometry in absence of any object (see Figure 3.12). We calculated the local stress St, according to equation 3.1, for various conditions of η_{out} and V_{Fluid}, V_{Fluid} corresponding to the maximum velocity of the parabolic profile at the exit of the last constriction. In a first approximation, we considered the velocity gradients at the exit of the oscillating width channel in absence of cells. As expected, Figure 3.13 illustrates that St increases linearly with V_{Fluid} and varies also with η_{out}. We report on the graph, the domains where each of the recovery modes is observed experimentally, assuming in a first approximation that $V_{Fluid} \sim V_{cell}$. From

Figure 3.13, we could estimate a range of local stress, St_{thresh}, corresponding to the frontier between the two modes.

For hydrodynamic stresses larger than St_{thresh}, RBCs are deformed and underwent a stretching behavior, whereas for lower stresses, they experienced unfolding. For η_{out} = 2.8 mPa.s and V_{Fluid} ranging from 460 to 1018 µm.s^{-1}, the zone of the relaxation diagram where the mixed behavior was observed, we estimated St_{thresh} to be between 0.6 and 1.4 Pa. Using this threshold stress and reading the graph in Figure 3.13, we can estimate that unfolding behavior would be observed for V_{cell} below 140 µm.s^{-1} and 25 µm.s^{-1}, for η_{out} = 8.6 mPa.s and 31.5 mPa.s, respectively. This was consistent with our experimental observations for these two viscosity values. Indeed, minimum velocities that we could reach experimentally were V_{cell} = 277 µm.s^{-1} for η_{out} = 8.6 mPas.s and V_{cell} = 133 µm.s^{-1} for η_{out} = 31.5 mPa.s, values above the extrapolated frontier values found previously. Therefore, we only observed stretching for these buffer viscosities.

RBC elastic shear modulus has been previously reported in literature to be μ = 2.5–9 µN.m^{-1} [44, 181], allowing the calculation of the Capillary number to be of the order of $Ca \sim 1$, thus confirming that the shear modulus drives the transition between the 2 recovery behaviors of RBCs. It would be interesting to try to determine if the study of RBC shape recovery at the exit of a microfluidic constriction could be a novel way to evaluate RBC elastic shear modulus. Although experiments performed with mechanically altered RBCs are required in order to demonstrate it. Stiffer RBCs would have to be flown at several speed in our geometry, while being suspended in buffers with various viscosities in order to determine the associated threshold stress St_{thresh}. But more importantly a quantitative measurement of the Young modulus of the impaired RBCs would be necessary to validate our hypothesis.

We quantified the deformation of RBCs according to the experimental conditions, $i.e.$ at various η_{out}, V_{cell} and for three different main channel widths (W_o = 15, 25 and 50 µm, all the other parameters - dimensions and number of constrictions - being maintained constant). RBCs deformation at the exit D_{out} and the associated recovery time τ_r were measured. In the case of cells returning to a steady

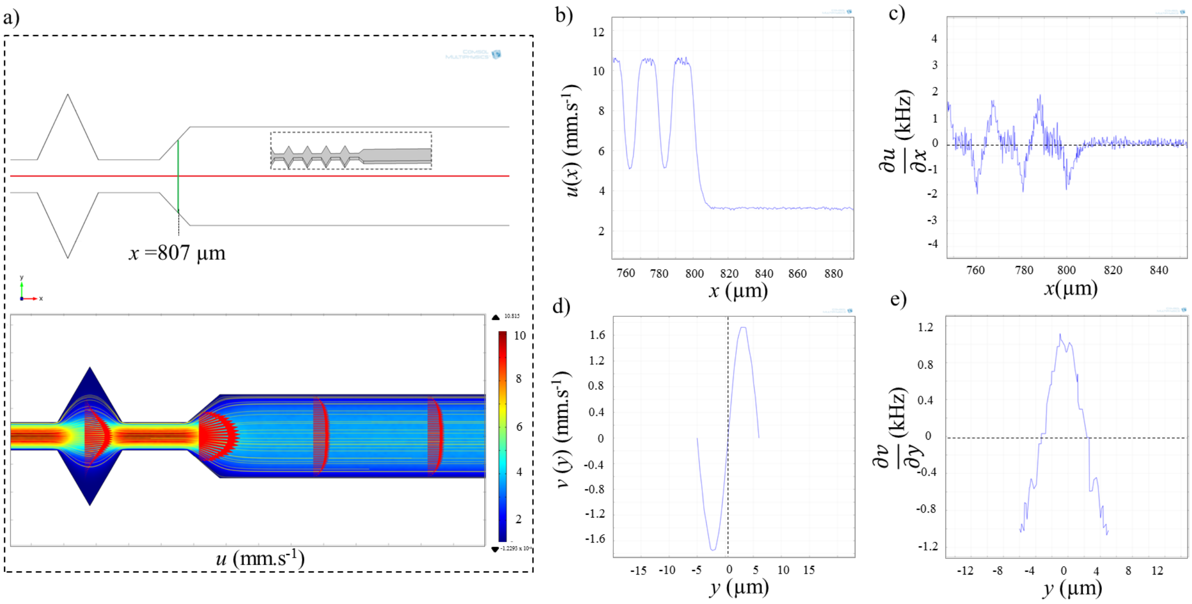

Figure 3.12: Representation of the estimated applied stress St at the exit of the last geometrical constriction versus the flow velocity V_{Fluid} at this location and the external medium viscosity η_{out} showing the two behaviors regions (unfolding/stretching) as well as the threshold stress St_{thresh}. The inset shows a close-up on the origin of the plot. Gray zone represents the transition zone. Numerical simulations were performed using W_o = 15 µm.

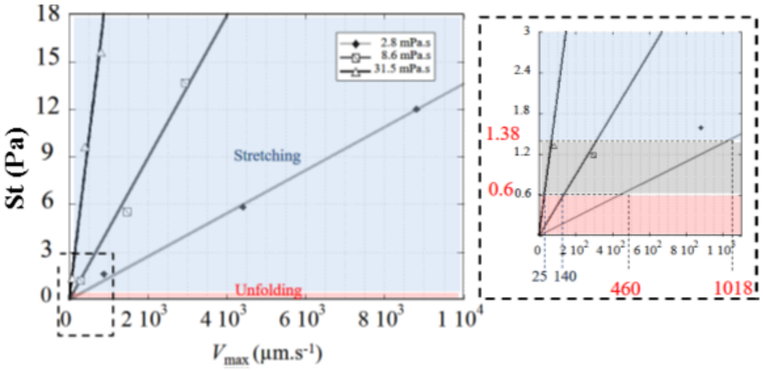

Figure 3.13: Representation of the estimated applied stress St at the exit of the last geometrical constriction versus the flow velocity V_{Fluid} at this location and the external medium viscosity η_{out} showing the two behaviors regions (unfolding/stretching) as well as the threshold stress St_{thresh}. The inset shows a close-up on the origin of the plot. Gray zone represents the transition zone. Numerical simulations were performed using W_o = 15 µm.

shape according to the unfolding mode (Figure 3.14a), the maximum deformation D_{out} experienced by cells flowing through the last geometric constriction, is independent of both parameters V_{cell} and W_o. Indeed, in the unfolding behavior, D_{out} corresponds to the cell compression in the last narrowing which remains constant through the whole study, and therefore only depends on the constriction dimensions. Figure 3.14b presents the evolution of $1/\tau_r$ as a function of V_{cell}, η_{out} being fixed at 1.3 mPa.s, for two values of W_o. The results show that $1/\tau_r$ is increasing linearly - thus τ_r is decreasing - when V_{cell} increases. Such behavior has already been reported by Prado et al. [58] for the relaxation time measured as the time necessary for RBC, initially at rest in a capillary, to adopt a steady shape when the flow is suddenly started. We can also mention that data issued from different W_o aligned on the same linear regression (Figure 3.14b), hence demonstrating that the recovery time in the unfolding mode was not impacted by the width of the channel, but is rather governed by the cell mechanical properties.

In the case of the stretching mode, the maximum deformation at the exit D_{out} is not influenced by the cell speed V_{cell} in the tested range (data not shown). We explain this result by the fact that although the applied stress is increased with the flow speed, RBCs transit through the high stress region more rapidly when V_{cell} increases. Consequently, the increase of St is counterbalanced by the short time RBCs spent in this region. The Figure 3.14c presents the effect of W_o on D_{out}. For each external viscosity and W_o, the data from different cell speed conditions were pooled. The graph reveals that, for a fixed external viscosity (η_{out} = 31.5 mPa.s), cells are more stretched at the exit of a 50 µm wide channel than when W_o = 25 or 15 µm. This behavior is attributed here to the fact that as St is higher than St_{thresh}, RBCs will deform according to the applied stress which is larger in a 50 µm than in a 15 µm wide channel. Regarding the recovery time, we retrieved in the stretching behavior, the linear relationship between 1/τ_r and V_{cell} (Figure 3.14d). The graph also reveals that for a given cell velocity, 1/τ_r increases - $i.e.$ τ_r decreases - when W_o is decreased, which is consistent with the fact that cells take longer time to recover from a more deformed state. Moreover, by plotting 1/τ_r versus V_{cell}/W_o, we can collapse all the data on a single line as illustrated by the inset in Figure 3.14d. This indicates that, in the stretching mode, the recovery time is directly imposed by the flow. Previous studies in the literature have observed the decrease of RBC recovery time upon the increase of cell velocity and explained it through energy dissipation [152].

We report the effect of η_{out} on RBCs elongation and shape recovery at the exit. Figure 3.15a reveals that D_{out} increased as η_{out} is raised, which is consistent with the increase of the hydrodynamic stress. One would expect to observe a longer recovery time at higher external viscosity, as more elongated cells take longer time to recover a steady shape. However, Figure 3.15b points out that $1/\tau_r$ increases, and therefore τ_r decreases, with the viscosity of the suspending medium. We explain this behavior in terms of a coupling between the cell and the external medium which may impact energy dissipation. Such dependency upon η_{out} was previously observed while measuring relaxation time using the startup flow

Unfloding behavior:

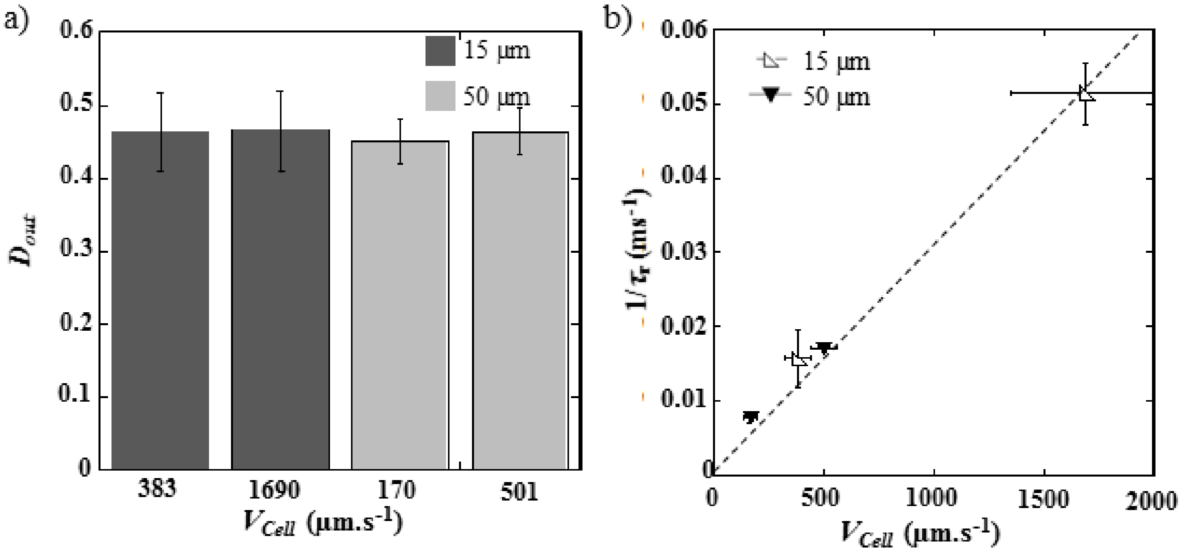

Stretching behavior:

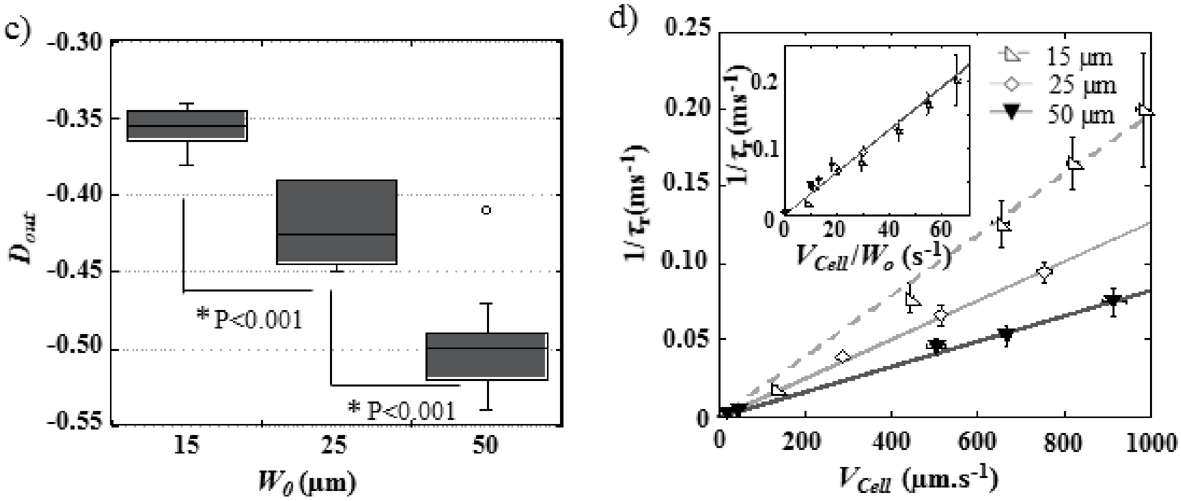

Figure 3.14: Evolution of a) the cell deformation D_{out} at the exit of the last constriction and b) 1/τ_r with the cell speed V_{cell}, for healthy RBCs experiencing the unfolding behavior in channels of different main widths W_o. The external viscosity η_{out} was set at 1.3 mPa.s. c) Evolution of D_{out} versus the main channel width W_o, for the stretching behavior (η_{out} = 31.5 mPa.s). d) 1/τ_r as a function of V_{cell}, for healthy RBCs undergoing stretching at the exit of channels with different widths W_o (η_{out} = 31.5 mPa.s). For both recovery modes, each point represents a statistic of at least 20 RBCs. P represents the P-value of the t-test.

of RBCs [58] and ecktacytometry [152]. Although such techniques report the measurement of relaxation time, *i.e.* time necessary for the cells to relax to their equilibrium stress-free shape, we retrieved here the same features on the study of the time necessary to recover a steady shape while still under flow. We may notice that our measurements of τ_r in unfolding mode are starting around 129 ms, typically for η_{out} = 1.3 mPa.s and V_{cell} = 170 µm.s^{-1}, which is in good agreement with relaxation time values previously reported in literature ($\tau \sim$ 100-300 ms [44, 181]) and with the calculation made by Hochmuth [177] using the Kelvin-Voigt model. But they can also reach values as low as 4 ms, in stretching mode for η_{out} = 20.3 mPa.s and V_{cell} = 1500 µm.s^{-1}. These results illustrate that, during the flow of RBCs out of

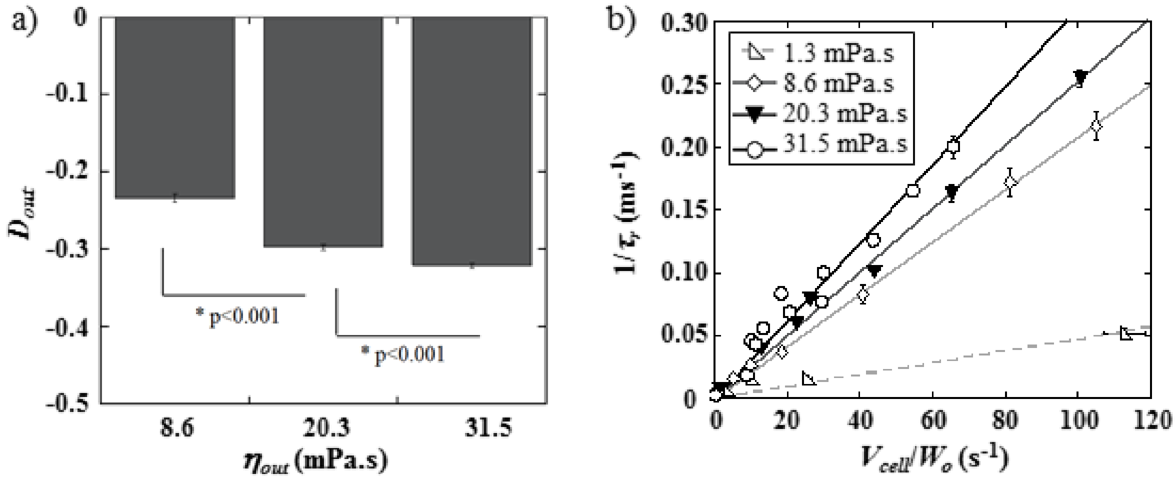

Figure 3.15: a) Evolution of D_{out} versus the external medium viscosity, η_{out}, for W_o = 15 µm. The data have been obtained by pooling the various V_{cell} conditions for each η_{out} in the stretching mode. b) 1/τ_r as a function of V_{cell}/W_o, for various conditions of η_{out}. Each point represents a statistic of at least 20 RBCs. P represents the P-value of the t-test.

a constriction, τ_r varies with the flow conditions ($i.e.$ η_{out} and V_{cell}/W_o). However, it can be assimilated to the cell intrinsic relaxation time dependent on the membrane mechanical properties only at very low flow speed and buffer viscosity.

We then decided to investigate if the study of the recovery process of RBCs exiting our microfluidic geometry could be used to probe their deformability. This could bring new insights into the detection of pathologies impacting RBCs deformability. In a first time, artificially rigidified RBCs were used to evaluate the relevance of our approach to detect any alteration in the cell mechanics.

3.2.4 Shape recovery time of artificially rigidified RBCs

Although τ_r has been found to be impacted by the experimental hydrodynamic conditions, we have evaluated if it could be used to discriminate artificially rigidified RBCs from healthy ones, at fixed geometry (W_o) and hydrodynamic conditions (η_{out} and V_{cell}). RBCs deformability was altered using two chemical treatments, known to affect RBCs membrane surface area [148, 141] and membrane deformability [148, 141, 201], LPC (from egg yolk with Mw = 505 g/mol) and diamide, respectively.

LPC was incubated with washed RBC, for 5 min at room temperature, at final concentrations ranging from 0 to 1.0 µmol/mL of cells, according to the protocol reported by Clark et al. [141]. After treatment, RBCs were suspended in a buffer which viscosity was set to 31 mPa.s before been injected in the microsystem (W_o = 50 µm) at a pressure of 200 mbar, in order to observe the stretching behavior.
LPC treated RBCs behaved qualitatively similarly to healthy RBCs as illustrated in Figure 3.16a and b. They got compressed and stretched according to the width of the channel, and got elongated by the extensional flow at the exit before recovering a stationary shape. However, a reduction of the amount of deformation experienced by the cells can be visually detected on the picture while undergoing the same amount of stress.
These observations are confirmed by the measurements of the amplitude of deformation, ΔD versus LPC concentration upon treatments (Figure 3.16c). LPC treatment at a concentration up to 0.5 µM had no significant impact on the amplitude of deformation of RBCs compared to hRBCs. However, treatment with higher concentrations led to a significant reduction of the amplitude of deformation ΔD (Figure 3.16c). Figures 3.16d and 3.16e show the evolution of the elongation at the exit, D_{out}, and the recovery time, τ_r, respectively. The stretching at the exit, D_{out}, and the recovery time, τ_r were gradually decreased upon increasing LPC concentration; hence showing that RBCs deformability drops gradually

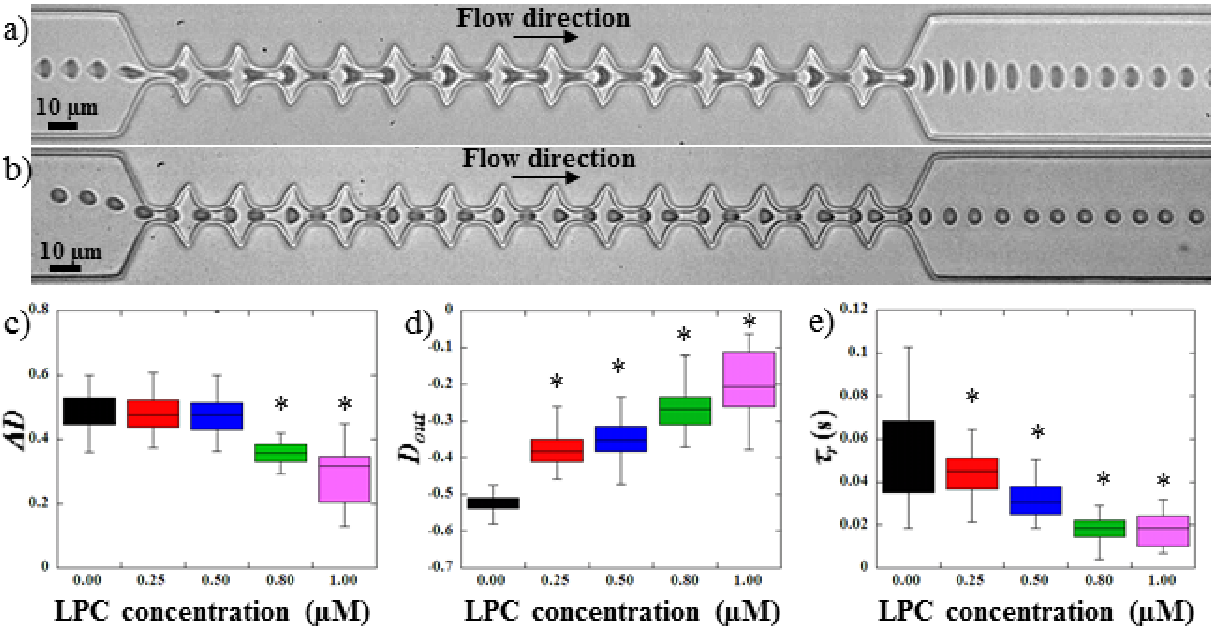

Figure 3.16: Sequence of deformation of a) a hRBC and b) a 1 µM LPC treated RBC flowing in the geometry. Evolution of c) the amplitude of deformation ΔD, d) the stretching at the exit D_{out} and e) the recovery time τ_r, versus LPC concentration. * Different from control sample (0 µM), $p < 0.05$.

with the concentration of LPC.

As previously described [70, 201] washed RBCs were also incubated with diamide at final concentrations ranging from 0 to 1.0 mM for 1H00 at 37℃. Previous works used diamide to rigidify the RBCs membrane [148, 141, 201], it has been reported to increase shear modulus caused by the cross-linking between spectrins [148]. Figure 3.17 illustrates the effect of diamide treatment with concentrations ranging from 0.1 to 1.0 mM. Figure 3.17a presents the typical sequence of deformation of a diamide treated RBC at 1mM. As for LPC treatments, RBCs deformability was clearly reduced when the cell was incubated with diamide, although the qualitative behavior of the cells was similar to that of healthy RBCs. Diamide treated cells showed a slight, yet statistically significant, drop in the amplitude of deformation ΔD, as illustrated in Figure 3.17b. Nevertheless, upon incubation with diamide, elongation at the exit D_{out}, of treated RBCs was reduced (Figure 3.17c), although the measurements were not able to make a distinction between the different diamide concentrations. Diamide treatment also impacted the recovery time τ_r of RBCs as highlighted by the decrease from 0.048 s for healthy RBCs to roughly 0.013 s for diamide treated cells (Figure 3.17d).

From the results presented above, it seems that ΔD is not sensitive enough to clearly detect modifications of the cells mechanical properties. This may be explained by the fact that this parameter is highly impacted by the various off-centered initial positions of the cells when entering the zone of interest. However, the measurements of the maximum elongation at the exit D_{out} and the RBCs recovery time τ_r can be used to discriminate healthy from chemically treated RBCs. But whether these readouts can differentiate between the different chemical concentrations is unclear. In the case of a visco-elastic object such as a RBC, the relaxation time, and therefore the recovery time, is linked to the deformed state. Indeed, τ_r decreases as D_{out} decreases, $i.e.$ it takes less time to recover from a less elongated shape. Figure 3.18 represents 1/τ_r versus D_{out}, for the different concentrations of diamide and LPC as well as the healthy samples. It can be clearly observed on the figure that, while healthy RBCs mechanical signature is limited to low 1/τ_r ($<$ 50 s^{-1}) values and strong elongation (D_{out} $<$ -0.5), chemically rigidified RBCs present lower elongation at the exit associated with shorter recovery time. This representation allows to discriminate easily the chemically rigidified RBCs from the healthy ones (blue zone). Moreover, it

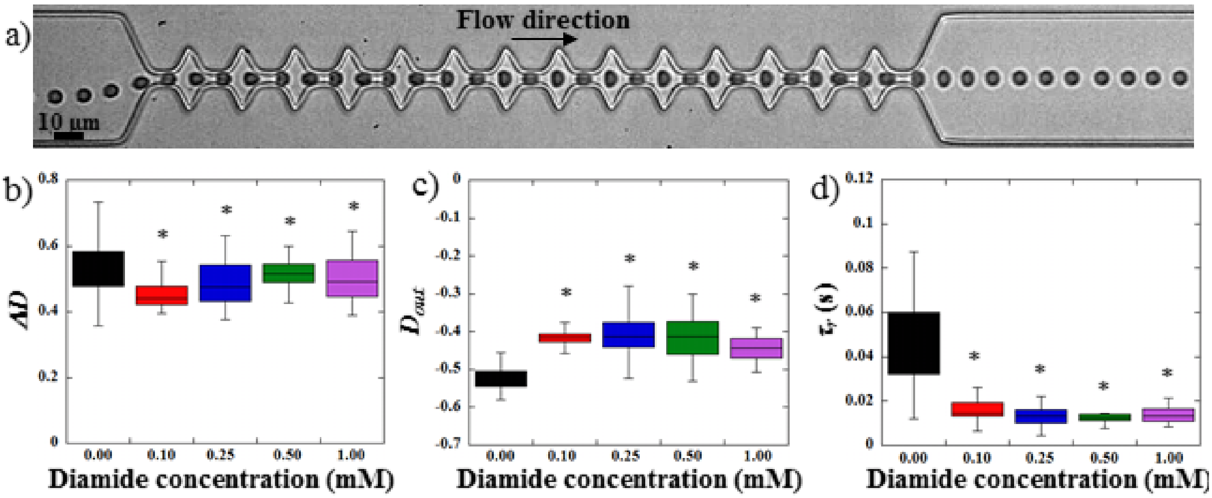

Figure 3.17: a) Sequence of deformation of a 1 mM diamide treated RBC flowing in the geometry. Evolution of b) the amplitude of deformation δD, c) the stretching at the exit D_{out} and d) τ_r, the recovery time versus diamide concentration. *Different from control sample (0 mM), p $<$ 0.05.

is possible to differentiate the two treatments as all the data points associated with LPC treated cells are located in a region of the graph (yellow zone) while diamide treated RBCs are located in another region (pink zone). Although both treatments lead to an increase in the overall cell rigidity, which is traduced by a lower D_{out} and a shorter τ_r, we can distinguish the effect of increased membrane stiffness from the effect of excess surface area.

The results obtained with chemically treated cells highlight that our microsystem is not only able to quantify the RBCs ability to deform, but also to provide a direct signature of the composition and architecture of their membrane. Hence demonstrating that the recovery time traduces the cell intrinsic mechanical properties, if cells undergo the same hydrodynamic stress, $i.e.$ they are submitted to the same external viscosity and flown at the same speed, in the same geometry. We suspect that our microfluidic approach could be useful to differentiate and diagnose different kind of RBC disorders according to the origin of

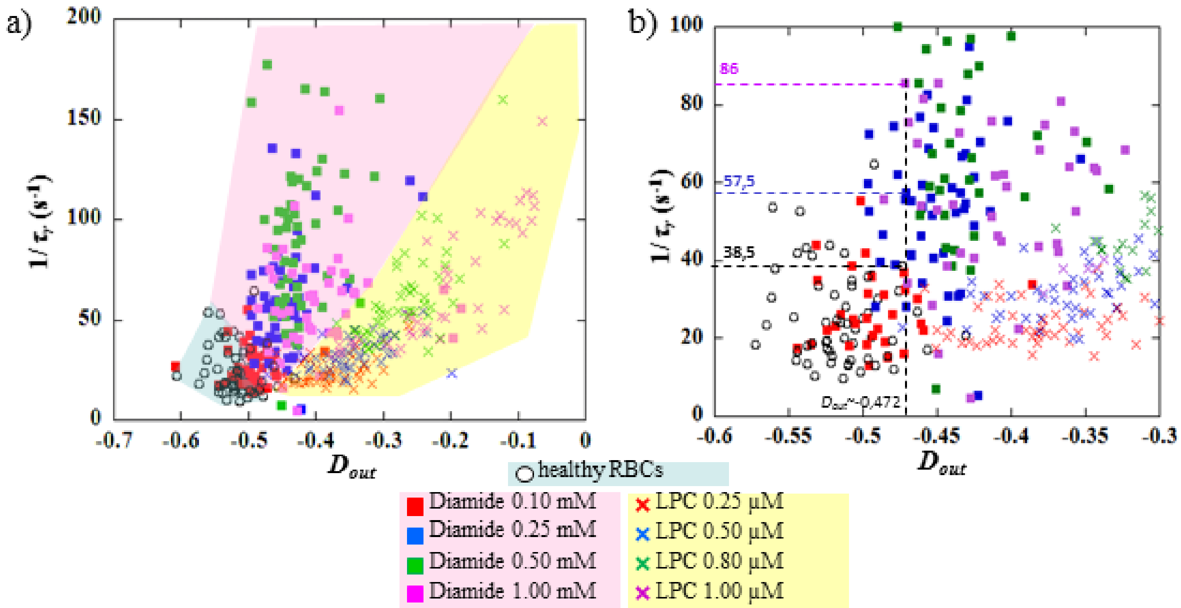

Figure 3.18: Evolution of 1/τ_r versus D_{out} for healthy, Diamide and LPC treated RBCs.

the affection (RBC membrane disorders, changes in surface-to-volume ratio, etc. . .).

3.2.5 Shape recovery time of pathological RBCs

In order to evaluate the potential of our microsystem to detect pathological cells, we have performed preliminary experiments on patients with HS and SCA. Blood samples from 3 healthy individuals, 3 patients with HS and 2 SCA patients were collected in EthyleneDiamineTetraacetic Acid (EDTA) tubes. The protocol was approved by the “Hospices Civils de Lyon – CPP Est” Ethics Committee (L14-127).
HS is a genetic disorder which is known to alter RBC mechanics [108]. The morphologic signature of HS is the presence of microspherocytes (smaller spherical RBCs), which is caused by loss of RBC membrane surface area, leading to an abnormal osmotic fragility. SCA RBCs are characterized by an abnormal intracellular polymerization of hemoglobin molecules resulting, through a cascade of events, in decreased deformability and increased adhesion [214]. *Plasmodium falciparum* iRBCs were also studied and compared to hRBCs.
iRBCs suspensions were obtained by culture of *Plasmodium falciparum* parasites. Parasitemia was improved by gradient centrifugation technique [183] in order to reach values of the order of 80%. *Plasmodium falciparum* (causing malaria) infected RBCs are known to experience a drastic diminution of their deformability due to the presence of the parasite in the host cells. Moreover, the presence of proteins secreted by the parasite within the membrane, modifies its mechanical response.

Figure 3.19 reports the measurements of $1/\tau_r$ as a function of D_{out} for 3 HS patients, 2 SCA patients and an enriched suspension of *Plasmodium falciparum* iRBCs compared to healthy donors. As illustrated on the Figure 3.19a, RBCs from HS patients showed an increase of $1/\tau_r$ compared to hRBCs, while RBCs from SCA patients had both a decrease in D_{out} and a slight increase in $1/\tau_r$ (Figure 3.19b). The Figure 3.19c highlights the strong decrease in recovery time between *Plasmodium falciparum* iRBCs and healthy ones; indeed, iRBCs recover a stationary shape roughly twice as fast as healthy cells. This difference can be explained by the measurement of D_{out} which reveals that iRBCs elongate roughly 1.6 times less that hRBCs. These findings underline that it takes less time for iRBCs to recover from a less elongated state. Such increase in $1/\tau_r$ is expected because these 3 diseases are known to increase cell stiffness [108, 173, 149, 50, 59, 62]. Although one would have expected that samples from HS patients response similarly to LPC treated cells - both being associated with a loss of membrane surface area - other modifications of HS RBCs may explain the difference of microfluidic signatures between both samples. For instance, HS blood also contains dense RBCs (usually more than 4% of RBCs with Mean Corpuscular Hemoglobin Concentration (MCHC) $>$ 41 g/dL) which may impact the behavior of the cells under confinement [108, 148]. A MANOVA analysis showed that the distribution of RBCs according to D_{out} and $1/\tau_r$ was significantly different between HS, SCA, iRBCs and control individuals ($p < 0.05$).

It can be seen on the Figure 3.19 that the inter-cells variability within a sample was higher in malaria infected suspension than in the two other pathologies. This discrepancy could be attributed to the highly heterogeneous composition of the suspension. Indeed, the sample is composed of both hRBCs and iRBCs; the iRBCs being themselves infected by parasites at different developmental stages, leading to different mechanical signatures [165, 23]. To a lower extent variability within a SCA sample can be observed, which could be explained by the presence of more or less dense cells in SCA This would suggest the possibility to retrieve information about the composition of the different sub-populations of the sample with our approach.

Although only few patients were tested, our preliminary results seem to highlight that our microfluidic device could be sensitive enough to make a distinction between healthy and pathological RBCs. Nevertheless, HS patients included in this study were issued from the same family, $i.e.$ presenting the same genetic molecular modifications, and it remains unknown whether our system is able to discriminate RBCs from HS patients with different molecular modifications (ankyrin, α-spectrin, β-spectrin . . .). However, in this particular HS family, with the same RBC membrane molecular defect, we retrieved consistently, in the 3 affected relatives, the same microfluidic signature.

Heterogeneity of pathological RBCs

In SCA, due to mutation in the beta globin gene, a pathological hemoglobin protein, called hemoglobin S, is synthetized. With less oxygen, the abnormal hemoglobin S can cause rigid, non-liquid protein strands to form within the RBCs. These rigid strands can change the morphology of the cell, causing the sickled RBCs that gives the disease its name. Each SCA blood samples can therefore be characterized by an Hemoglobin S (HgbS) level traducing the degree of the disorder. We try to look into more details at the response of SCA RBCs flowing in our geometry in order to evaluate if our approach could be sensitive enough to detect different HgbS level.

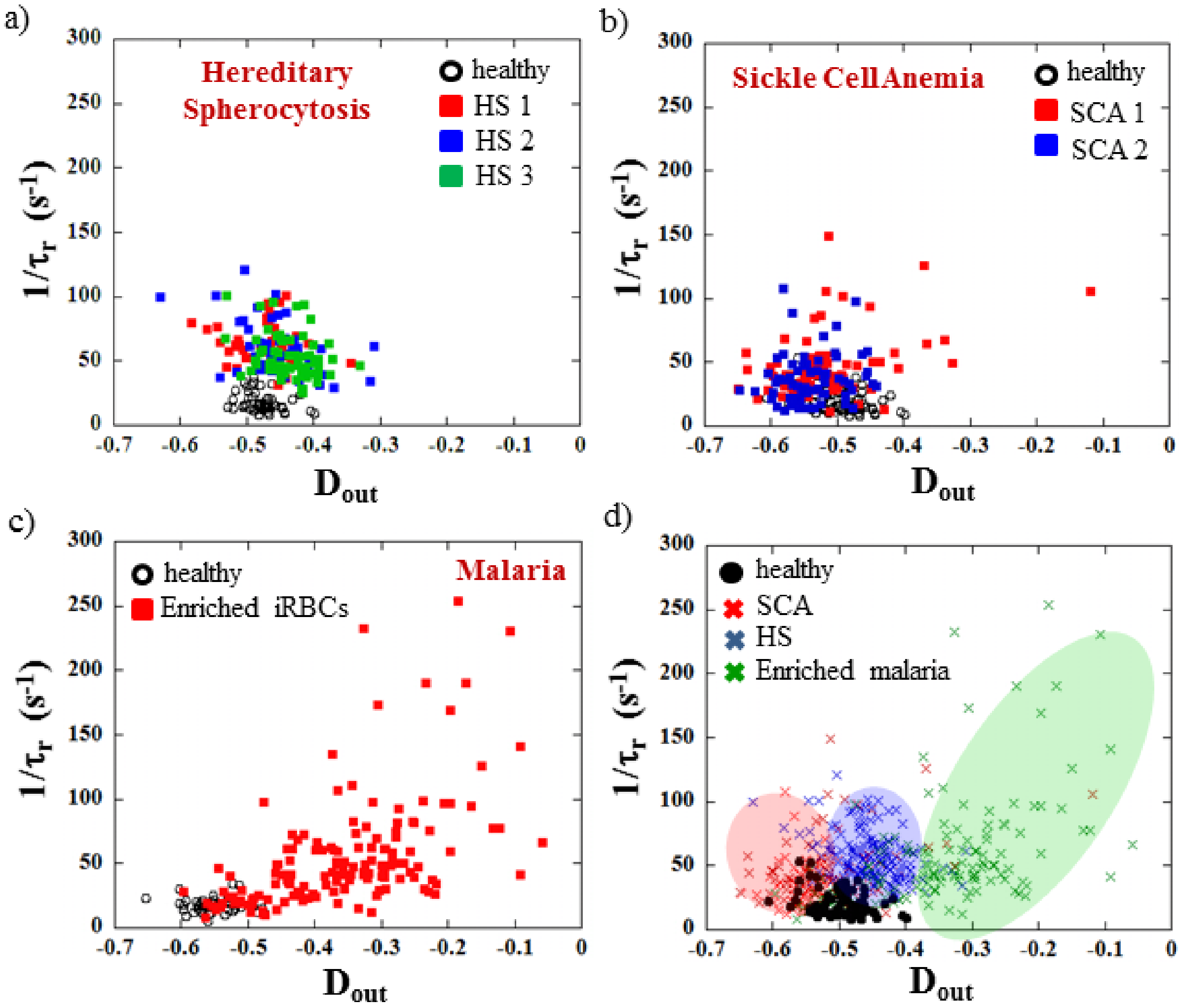

Figure 3.19: D_{out} versus $1/\tau_r$ for a) hRBCs (solid black circles) and 3 HS patients, b) hRBCs (solid black circles) and 2 SCA patients and c) hRBCs and enriched *Plasmodium falciparum* iRBCs. A MANOVA statistical analysis revealed that the RBCs distribution was significantly different between the four groups ($p < 0.05$ between HS and healthy RBC, $p < 0.05$ between SCA and healthy RBCs, $p < 0.05$ between iRBCs and healthy RBCs, $p < 0.05$ between HS and SCA, $p < 0.05$ between HS and iRBCs and $p < 0.05$ between iRBCs and SCA). d) The 4 types of samples (with all the patients pooled) gathered on the same graph. Ellipses are guide for the eyes.

3.2.6 Conclusion

We have presented a study on the behavior of hRBCs flowing passively in a microfluidic channel with oscillating width. We first documented the existence of two shape recovery modes for the RBCs to return to its equilibrium shape at the exit of the last constriction. Moreover, at the frontier between the 2 modes, we have correlated the local hydrodynamic stress experienced by RBCs to their elastic shear modulus. An estimation of μ in a range of [4.2-9.66] µN.m^{-1} was made which is in good agreement with values from literature [44, 181]. Finally, we investigated the dependency of D_{out} and τ_r upon the experimental conditions such as the cell velocity V_{cell}, the main channel width W_o, as well as the external medium viscosity η_{out}. Indeed, we reported that D_{out} increased with the external viscosity η_{out} and the channel width W_o, whereas the shape recovery time τ_r strongly dropped according to V_{cell}/W_o and η_{out} as already published [152, 58].

Differences between healthy and chemically treated cells were highlighted by the measurement of both the extension at the exit, D_{out}, and the shape recovery time τ_r. Although the measures were not able to distinguish between the different chemical concentrations, the representation of 1/τ_r versus D_{out} reveals that our approach is able to discriminate the effect of membrane surface area from membrane elasticity. Therefore our approach seems able to provide a direct signature of RBCs membrane composition and architecture.
Our preliminary results highlight that the mechanical responses of healthy and pathological RBCs are not only different but also suggest that the discrimination between the three disorders may be possible, although more experiments using actual blood samples from patients with malaria and HS samples from various RBC disorders are needed. To our knowledge, this is the first attempt to evaluate the specificity of a passive microfluidic approach to perform diagnosis based on the alteration of RBC deformability. The single cell approach, while analyzing a statistically relevant population, could also provide complementary information (quantification of the heterogeneity of the cell population) that might be of great importance for the diagnosis and prognosis.

3.2.7 Future developments

A first attempt to automatize the discrimination has been realized at the end of Amin Amirouche's PhD. Indeed, to facilitate the detection automation, we favored an approach based on the cell residence time in the oscillating width section of the channel. Indeed, the passage of cells at specific location, $i.e.$ at the entry and at the exit of the zone of interest can be easily detected using photodiodes or electrodes. We have evaluated if the residence time - if fact the cell speed - within the oscillating zone of the channel was sensitive enough to traduce a modification of cell mechanical properties. The results presented in Appendix B are interesting but the exploitation of D_{out} and 1/τ_r seems much more promising.

Therefore, a collaboration with Thomas Grenier from Centre de REcherche en Acquisition et Traitement de l'Image pour la Santé (CREATIS) has been initiated. The aim of this collaboration is twofold: (i) to optimize and automatized the image analysis in order to increase the throughput and reach values compatible with diagnostic applications, and (ii) to use machine learning to help deciphering the physiological state of blood samples.

3.3 Optimization and exploitation of the pressure drop measurement

The flow of RBCs in close-fitting channel can also provide information on the cellular mechanical phenotype, using other readouts. For example the way a cell, flowing in a channel which dimensions are smaller than the cell size, "blocks" the flow of liquid may traduce its ability to deform. The principle of this method, referred to as the pressure drop measurement, is reminded in the first section. Following developments of the pressure drop measurement are then presented.

3.3.1 Principle of the pressure drop measurement

During my PhD, we proposed a high-speed microfluidic approach to measure the dynamical pressure-drop variations associated with the flow of individual cells in confined geometries [114, 116]. The principle is briefly reminded here. The chip is composed of two identical channels illustrated in Figure 3.20a; a test channel and a reference one. The cells suspension is injected in the upper channel whereas a solution of contrast agent is injected in the lower one. The two channels merge on the right side of the chip and the distribution of the two fluids (co-flow virtual interface) is visualized thanks to the contrast agent. In absence of cells flowing in the upper channel, the virtual interface is centered, hence traducing the equilibrium between the pressures in the two channels.

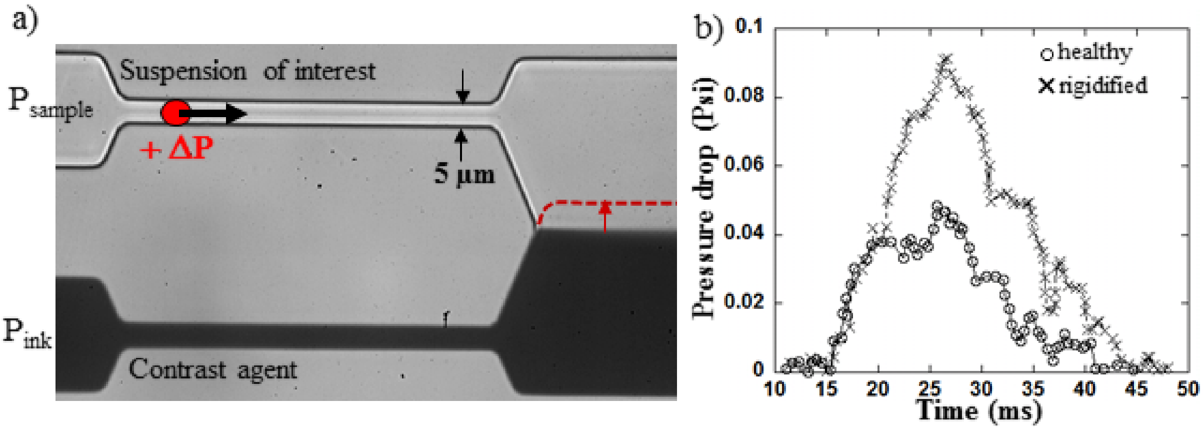

Figure 3.20: a) The specific geometry of the device allows the measurement of the pressure drop ΔP (presented in absolute value) induced by the flow of a close-fitting cell in the upper channel, visualized by the deflation of the interface (here illustrated in red). b) Measured pressure drop versus time for a hRBC and a rRBC after 0.001% glutaraldehyde treatment. Adapted from [119].

When a deformable cell enters the upper channel, an additional hydrodynamic resistance is added to the channel resistance, leading to changes in the local pressure profile, thus inducing a displacement of the virtual interface. Thanks to an appropriate calibration, the deflation of the interface can be converted into a pressure drop measurement. The authors have shown that the amplitude of pressure drop depends on both the volume and the deformability of the cells under study. Indeed, pressure-drop measurements are able to discriminate White Blood Cells (WBCs) and RBCs, as well as healthy and chemically rRBCs [114]. Khan et al. [219] applied this approach to the mechanical characterization of healthy and cancerous brain cells. The two cell lines were differentiated using entry time and to a little extend pressure drops, rather than on speeds and elongations. They observed that brain tumor cells have a longer entry time, thus suggesting that the well-spread idea that cancer cells are more deformable than benign cells may not apply to brain cancer cells [219].

3.3.2 Influence of the microsystem geometry on its sensitivity

A first attempt of optimization has been performed on the pressure drop geometry during the ATER of Josue Esteves. 2D numerical simulations, performed with Comsol Multiphysics®, have allowed to highlight the importance of the geometry on the sensitivity of the system, *i.e.* its ability to induce a large deflation of the interface for a given increment of pressure ΔP. The geometry of the pressure drop device has been modified in order to make them symmetrical for simplicity of analysis and ease of utilization. Indeed, they are now constituted of two inlet (on the left) and two outlet channels (on the right) merging in a central cavity of length L and width w, as illustrated in Figure 3.21a.

As explained previously, the pressure drop measurement requires a calibration curve to convert the displacement of the virtual interface. To do so, the pressures of both inlet P_{sample} and P_{ink} are set identical

in order to get an interface centered in the central cavity, as illustrated in Figure 3.21a-left. During my PhD, it was shown that the value of P_{sample} impacted α, as larger α were associated with lower P_{sample} [119]. Here P_{sample} is chosen to be equal to P_{ink} and set at 5 Psi. Then P_{sample} is gradually modified (Figure 3.21a-right) and the associated displacement of the virtual interface is measured. A typical calibration curve is presented in Figure 3.21b, where the data is fitted with a linear regression, which slope α is extracted. The slope of the calibration curves for different geometries are compared in order to clarify the effect of the different parameters on the sensitivity of the measurement. The parameters of the central cavity investigated are the length of the central cavity, L, its width w and its aperture angle θ ; this parameters are defined on the Figure 3.21a.
The results of the study are illustrated on Figure 3.21c. For a given width w, $|\alpha|$ tends to increase when L is decreased. and tends to rise at fixed cavity length, when the width is increased. The graph also reveals that, when the cavity length L is fixed at 100 µm and w is increased, $|\alpha|$ slightly rises, which traduces an improvement of the sensitivity. Therefore, it seems that, for a given pressure drop ΔP, the displacement of the interface is maximum when L is small and w is large, $i.e.$ the central cavity is short and wide.

The effect of the aperture angle θ was also investigated. Numerical simulations for various L and w conditions were performed for θ ranging from 60° to 160°. The results are presented in Figure 3.22 in terms of the variation of $|\alpha|$ versus the aspect ratio of the central cavity. We can first see that the results confirm that the sensitivity is larger when the aspect ratio of the central cavity is small, with L the smallest possible. Then, we can note that $|\alpha|$ is enhanced when θ is increased, for fixed dimensions of the central cavity. For example, in a geometry where L = 20 µm and L/w = 0.5, $|\alpha|$ rises from 2.11 for θ = 60° to 6.53, when θ = 160° as reported in the zooms of Figure 3.22. These results tend to suggest

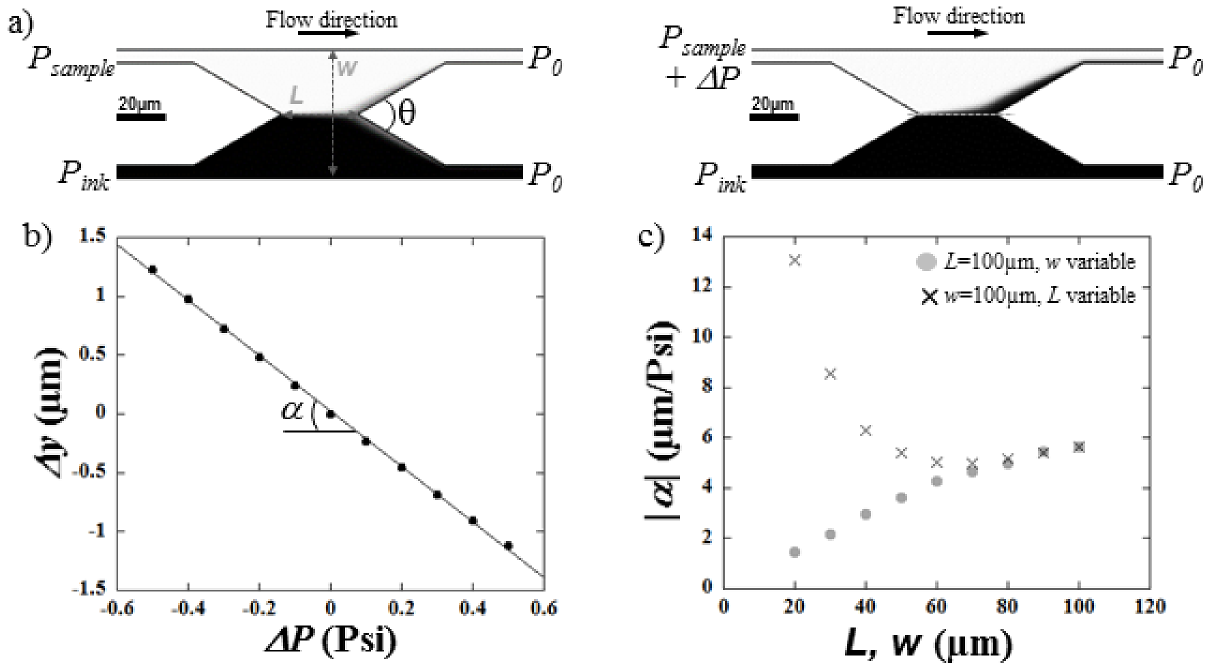

Figure 3.21: a) Images of a pressure drop geometry generated by numerical simulations; the geometric parameters of the central cavity L, w and θ are defined. On the left, the inlet pressures are identical and set to be 5 Psi, leading to an interface centered, Whereas on the right P_{sample} has been decreased of 0.5 Psi, leading to a displacement of the virtual interface. b) A typical calibration curve obtained by numerical simulations for θ = 60°, L = 30 µm and w = 50 µm. The slope α of the linear regression traduces the sensitivity of the system. c) Evolution of the sensitivity parameter $|\alpha|$ for different geometries. One of the dimensions of the central cavity was fixed at 100 µm while the other one has been varied from 20 to 100 µm, for θ = 60°.

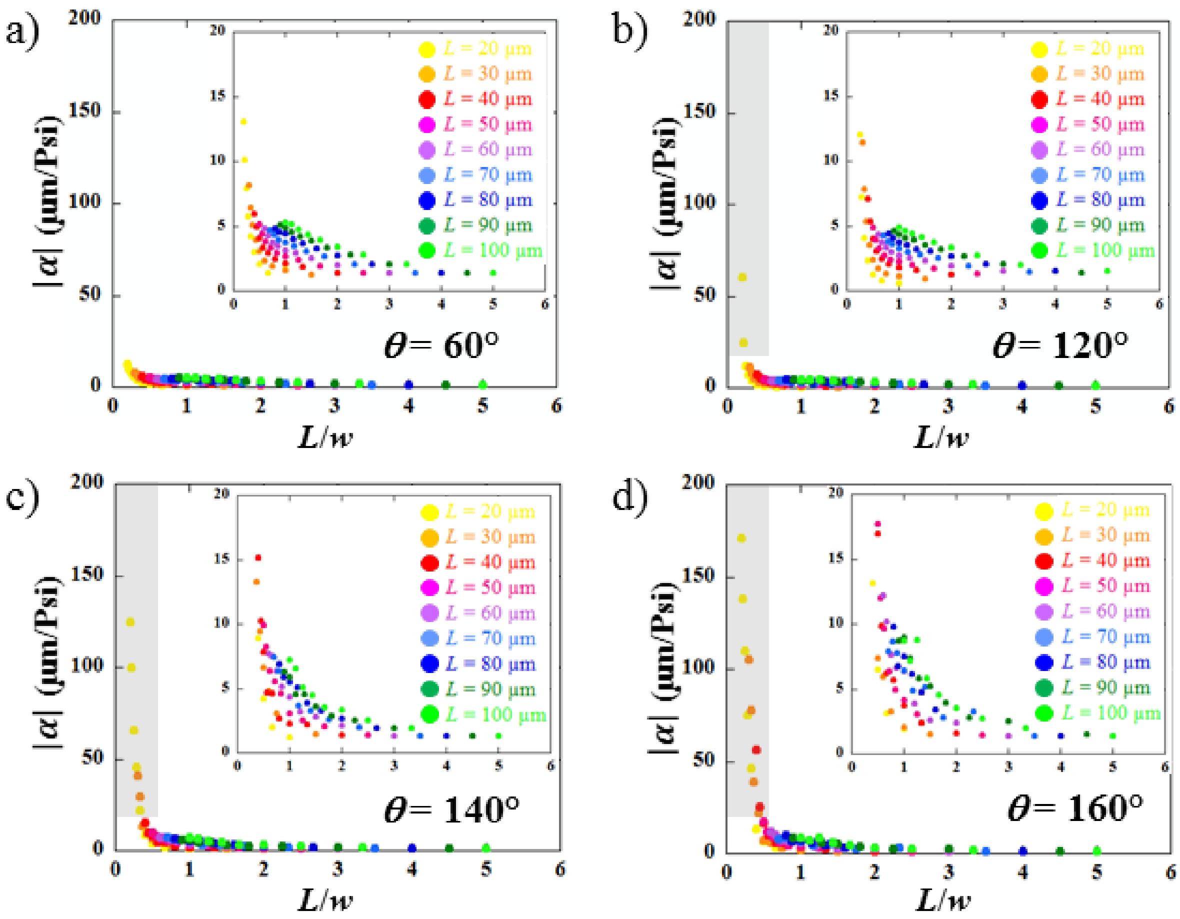

Figure 3.22: Evolution of the sensitivity $|\alpha|$ versus the aspect ratio of the central cavity L/w for various cavity lengths L and different aperture angles a) θ = 60°, b) θ = 120°, c) θ = 140° and d) θ = 160°.

that the larger the aperture angle - corresponding to “flatter” central cavity - the higher is the sensitivity. However, when the aperture angle is increased above 60°, some $|\alpha|$ values are misleading ; these values are highlighted by a gray rectangle. Indeed, for certain aspect ratios, the calibration curves start to appear non-linear as presented in Figure 3.23. When the calibration curve is no more linear, then the sensitivity $|\alpha|$ is extracted from the data by fitting with a linear regression the data points between -0.1 and 0.1 Psi. Nevertheless, the extracted sensitivity is only valid for low ΔP and is not necessarily valid for any object under consideration. For example, for θ = 140°, L = 20 µm and w = 80 µm, the sensitivity $|\alpha|$ is estimated to be 65.8 µm/Psi. This suggests that for a given ΔP of -0.4 Psi, the displacement of the virtual interface would be of the order of 26 µm. However, because of the non-linearity of the calibration in this range of ΔP, the value of the interface shift is closer to 11.5 µm.

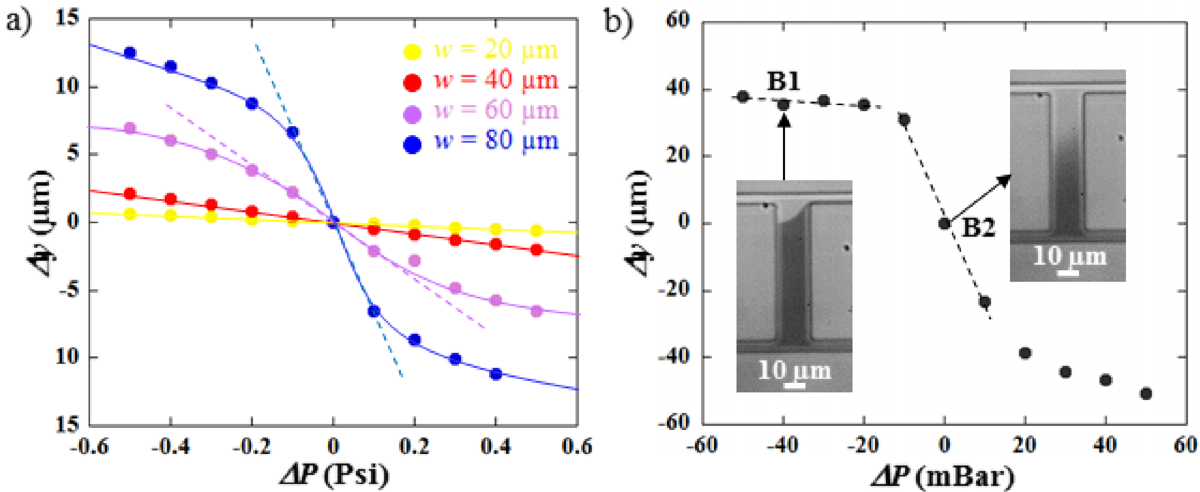

Figure 3.23: a) Calibration curves for different geometries for θ = 140°, L = 20 µm, obtained from numerical simulations. Solid lines represent a guide for the eyes, whereas dashed lines illustrate the linear regressions used to extract α reported in Figure 3.22. b) Experimental calibration curve for a microsystem with θ = 180°, L = 20 µm, w = 100 µm and h = 5 µm. The inlet pressure of the lower channel is fixed at P_{ink} = 165 mBar and the pressure applied at the entry of the upper channel P_{sample} is varied. The pictures of the device, B1 and B2, illustrate the position of the virtual interface corresponding to the upper pressure 160 mBar and 200 mBar, respectively.

There is another argument to prevent the use of a central cavity with a flat side (typically θ = 180°). In fact, depending on the flow velocity, if the flat cavity’s aspect ratio is too low, diffusion of the contrast agent is observed - particularly at the equilibrium between the two pressures (picture corresponding to B2 in Figure 3.23b) - hence making difficult the detection of the virtual interface. This diffusion phenomena is attributed to the apparition of recirculations interfering with the main flow. Nevertheless, a way to overcome such inconvenient, is to perform the measurement using inlet pressures that do not reflect the equilibrium between the two entry channels, as for example (picture corresponding to B1 in Figure 3.23b). However, the corresponding slope α is lower around the position corresponding to B1 than that of B2.

For the next sections regarding RBCs, we will implement a design with the central cavity having the following dimensions : L = 100 µm, w = 5 µm, h = 5 µm and θ = 170°. The inlet pressure of the sample to be characterized is fixed at P_{Sample} = 100 mbar. To avoid the re-circulations and the diffusion phenomena, the pressure of the contrast agent is set such as the virtual interface is shifted towards the upper channel, similarly to B1 from Figure 3.23b. The calibration curve is measured around this new “starting position”.

3.3.3 Effect of the cell confinement on the pressure drop measurement

In this section, we have investigated how the confinement of the cells affected the corresponding pressure drop measurement. To do so, we have varied the width of the constrictions, noted W_c while maintaining the length of the constriction at 100 µm. The flow of hRBCs through the device is recorded and analyzed. The typical deformation curve associated with the displacement of the cell in the geometry is illustrated in Figure 3.24.

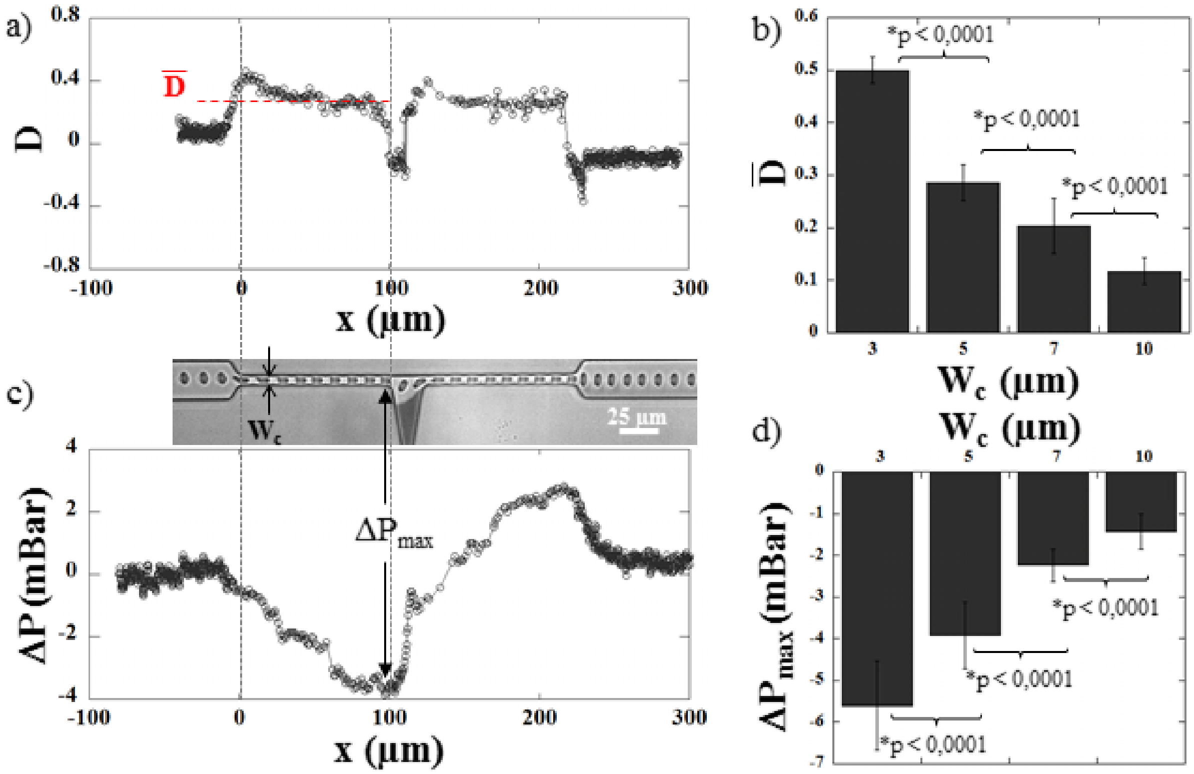

Figure 3.24: a) Deformation curve associated with the flow of a hRBC in the device with a 5 µm. The entry of the constriction has arbitrarily been chosen as the origin of the cell displacement. The plateau value corresponding to the stationary shape, $\bar{D}$, adopted by the cell inside the constriction is defined by the dashed red line. b) Evolution of the stationary shape $\bar{D}$, as a function of W_c, the width of the constriction. Error bars represent standard deviation calculated from 20 cells. p represents the p-value of the t-test. c) The evolution of the excess pressure drop corresponding to a) is also presented. P_{sample} has been fixed at 300 mBar and P_{ink} is chosen such as the virtual interface is shifted upwards. The maximum pressure drop, noted ΔP_{max}, is defined as the minimum of the curve. d) Evolution of ΔP_{max} versus W_c. Error bars represent standard deviation calculated from 20 cells. p represents the p-value of the t-test.

We first looked at the behavior of hRBCs flowing in the optimized geometry, while the width of the constriction, W_c was varied from 3 to 10 µm. P_{sample}, the pressure applied at the entry of the sample channel was fixed at 300 mBar and P_{ink} was chosen such as the virtual interface is shifted upwards as illustrated on the sequence of deformation Figure 3.24a. The deformation curve (upper graph) traduces the typical behavior of a hRBC flowing through the device. The cell enters the geometry undergoing a parachute-like shape typical from confined flow. Then as it approaches from the entry of the constriction, it gets stretched and deformed along the flow direction. This is traduced by an increase of D around x = 0, before it reaches a plateau value corresponding to a stationary shape $\bar{D}$, highlighted by the red dashed line. When the cell exits the constriction, D drops before increasing again as it enters the second branch of the device. The two branches being exactly symmetrical, the same deformation of the cell can be observed in the second constriction. Finally, the cell gets slightly stretched at the exit of the second constriction, which is traduced by a sharp drop of D, before recovering a stationary shape corresponding to the final plateau (Figure 3.24a). In the rest of this study, we will consider that only the behavior of the cells in the first branch of the device - $i.e.$ everything that is on the left of the central cavity - is of interest. We have investigated the effect of the confinement on the stationary shape, $\bar{D}$, adopted by the cells within the constriction. The results are presented in Figure 3.24b. As expected, the graph reveals that cells are more deformed in the direction of the flow, when flowing in narrower constrictions ; hence traducing of the higher confinement.

Because of the presence of the cell, the pressure profile in the device is modified and the virtual interface is moving in the central cavity. This displacement of the virtual interface is converted into a change in pressure thanks to the calibration. The excess of pressure drop corresponding to the Figure 3.24a is presented in Figure 3.24c. The excess of pressure drop is normalized to be zero as the cell enters the device. Then as the cells approaches and enters the narrowing, ΔP is decreasing. The maximum value ΔP_{max}, which corresponds to the minimum of the curve, is reached around x = 97 µm and worth -3.88 mBar. The position of this minimum can be explained by the fact that inside the constriction, both the front and the back of the cell experience the same speed which is traduced by a stationary shape. When approaching the exit of the constriction, the front of the RBC slows down due to the increase of the section of the geometry, while the front - which is further from the exit - is maintaining its velocity. Consequently, the cells tend to get compressed, which corresponds to the maximum confinement and thus to the maximum of excess pressure drop. Shortly after reaching this minimum, the curve rises strongly, hence traducing the exit of the cell from the constriction. Then as the cell is flowing in the central cavity, its proximity to the virtual interface makes it useless to look any further at the measurement.

One aspect which is surprising, is the absence of a plateau value in the ΔP graph. Indeed, the shape of the cells within the constriction tend to stabilize - which is traduced by the establishment of the plateau $\bar{D}$. One would expect that the excess of pressure drop associated would also stabilize. However at this magnification, no plateau can be observed, whatever the width of the constriction W_c. The mean of the ΔP_{max} calculated over the different cells of the sample, is presented as a function of the channel width W_c in Figure 3.24d. We have found that the pressure drop, associated with the flow of hRBCs, is increasing with confinement. This was expected as the pressure drop traduces directly how the cell is blocking the constriction, hence modifying the flow in the device. One may notice that, changing the width of the constriction, while maintaining P_{sample} fixed at 300 mBar, would also modify the flow speed inside the geometry, in addition to the confinement. However, it has been verified on a much wider range, that flow speed did not influence drastically the value of the pressure drop associated with hRBCs flowing in a given constriction (data not shown here).

Another aspect that was investigated is the influence of the inlet pressure P_{sample} on the pressure drop measurement. Previous studies demonstrated that the sensitivity of the pressure drop was increased when P_{sample} was low, *i.e.* that for a given pressure drop value, the corresponding displacement of the virtual interface was greater [114]. However, the influence of the inlet pressure on the actual value of the pressure drop associated with the flow of a given object in a fixed geometry was only looked in on a small range of pressure. Therefore, we measured the pressure drop associated with the flow of hRBCs in the previous geometry with W_c = 5 µm on a much larger range for P_{sample}. Figure 3.25 presents the results.

As reported in the Figure 3.25a, P_{sample} does not seems to impact the pressure drop value up to 300 mBar but at higher pressure - typically 400 mBar - a strong increase in ΔP_{max} has been recorded, which was unexpected. According to Figure 3.24, larger ΔP is associated with higher confinement, which is itself related to higher deformation state, as cells of given volume has to deform more to fit in a narrower channel. At higher pressure, the cells may undergo larger deformations in the constricted channel due to higher hydrodynamic stress. However in this particular case, the higher deformation state would implicate that the cell is “blocking” less the channel than with lower pressure, as the deformation state is greater for the same W_c. This would be inconsistent with the increase of pressure drop observed. Moreover, the stationary state of deformation of the cell within the constriction - presented in Figure 3.25b - do not show any differences that might explain the sharp increase in ΔP_{max} measured. For now, we

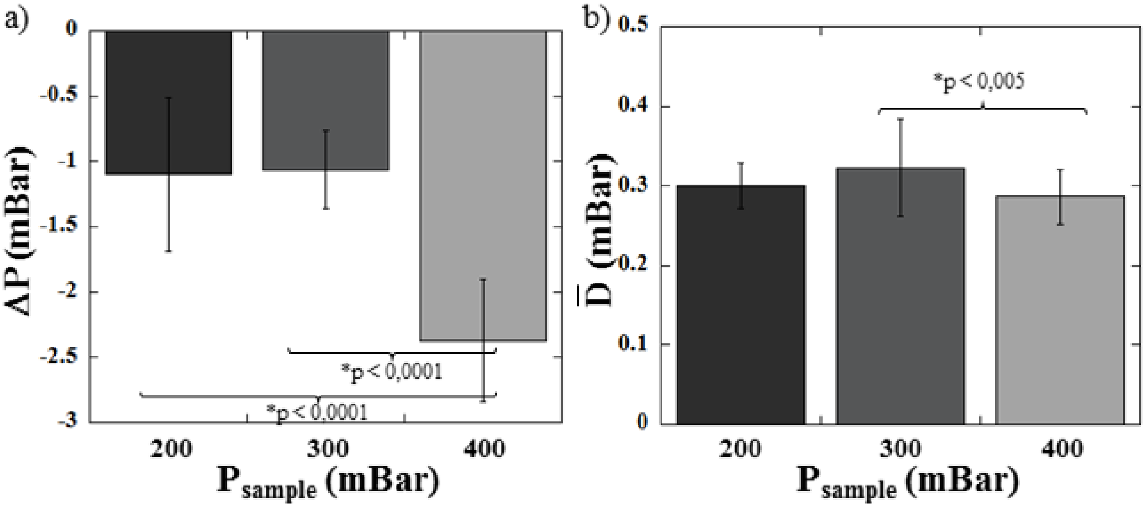

Figure 3.25: a) ΔP_{max} associated with the flow a hRBC in a 5 µm wide constriction for different P_{sample}. b) Associated steady state deformation $\bar{D}$ undergone by the cells. Error bars represent standard deviation calculated from 20 cells. p represents the p-value of the t-test.

haven't found any explanation to this surprising result.

3.3.4 Application to the discrimination of impaired RBCs

In order to demonstrate that the pressure drop measurement can be used to discriminate healthy from impaired RBCs, two types of altered RBCs samples were investigated in the geometry presented previously and compared to hRBCs : (i) gRBCs and (ii) diamide rRBCs.

First the volume of RBCs was varied and its influence on the measurement of the excess pressure drop was investigated. For the study, gRBCs are obtained by suspending hRBCs in an hypotonic buffer, typically Phosphate-Buffered Saline (PBS) at 200 mOsmol. The viscosity of the hypotonic buffer was increased to 31.5 mPas.s by addition of Dextran polymer (Mw = 2× 10^6 g.mol^{-1}) at a concentration of 9% w/w, in order to maintain the same conditions than for hRBCs. In order to equilibrate the osmotic pressure on both side of the membrane, water will enter the cell, thus inflating it. The main difference between hRBCs and gRBCs is their volume, which has been reported to be equal to 94 fL and 116 fL respectively, while maintaining a surface area of 135 µm^2 [45]. The typical behavior of inflated RBCs is qualitatively similar to that of healthy ones as illustrated on the sequence of deformation in Figure 3.26a. The maximum excess pressure drop of inflated and hRBCs is represented in Figure 3.26b upon W_c. For W_c = 10 µm, we have not found any statistical difference between the pressure drop measurement of both samples. In such a wide constriction, none of the RBCs really "block" the channel, thus leading to a very low associated pressure drop. We report that, for $W_c \leq$ 7 µm, gRBCs are associated with statistically higher excess of pressure drop than hRBCs. One may notice that the values of ΔP_{max} associated with gRBCs flowing in a 3 µm wide constriction, are highly dispersed. This illustrates that the pressure drop measurement can be quite sensitive, as it is direct quantification of the way the object obstructs the constriction. We attribute such variability to small variations of volume inside the gRBCs population that induce to important changes in "blockage" hence leading to very different pressure drop values.

The rRBCs were obtained upon diamide treatment. As previously described [70, 201], washed hRBCs were incubated with diamide at a final concentration of 1.0 mmol/L for 1H00 at 37℃. Cells were then suspended in the same viscous buffer as previously (*i.e.* dextran 9% w/w in PBS) and injected in the device at P_{sample} = 300 mBar. The typical behavior of diamide rRBCs is qualitatively similar to that of healthy ones as presented on the sequence of deformation in Figure 3.26c. The maximum excess

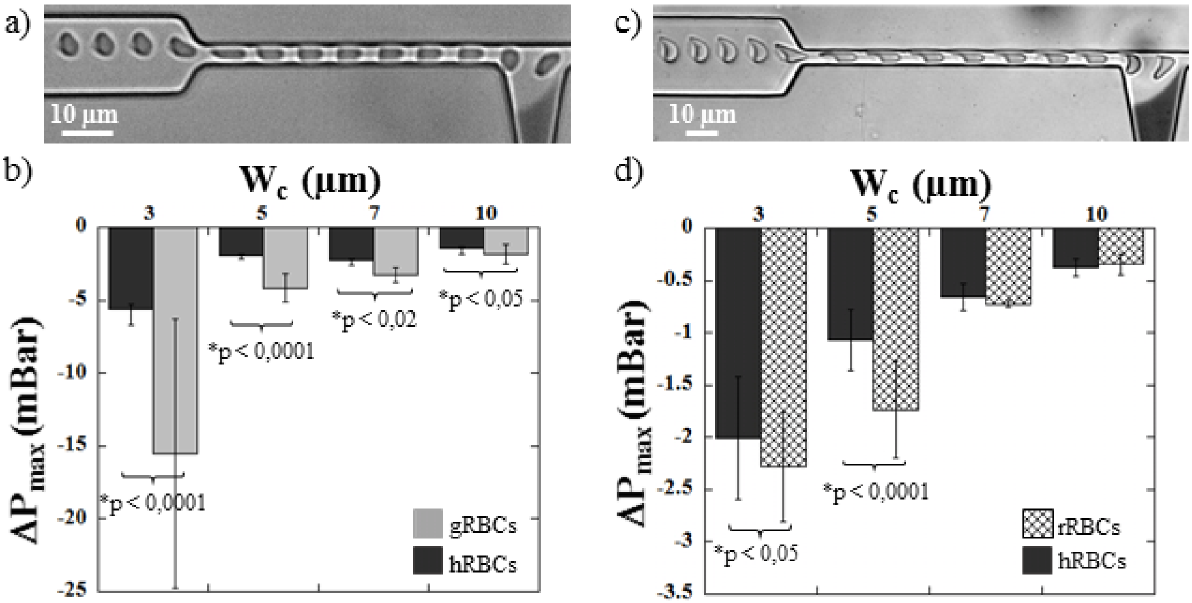

Figure 3.26: a) Sequence of deformation of a gRBC in the pressure drop device, with W_c = 5 µm. b) Maximum excess pressure drop ΔP_{max} for both hRBCs and gRBCs, versus W_c. Error bars represent standard deviation calculated from 20 cells. p represents the p-value of the t-test. c) Sequence of deformation of a diamide rRBC, for W_c = 5 µm. d) Evolution of ΔP_{max} versus W_c, for hRBCs and rRBCs. Error bars represent standard deviation calculated from 100 cells. p represents the p-value of the t-test.

pressure drop of rRBCs is measured and compared to that of hRBCs (Figure 3.26d) according to W_c. We retrieve the same behavior as for gRBCs; ΔP_{max} is increasing with confinement, *i.e.* decreasing W_c. For W_c above 5 µm, no statistical difference between the pressure drop measurement of hRBCs and rRBCs has been measured. Whereas, when cell confinement is sufficiently high, rRBCs are associated with statistically higher excess of pressure drop than hRBCs. Finally, the difference in ΔP_{max} values associated with hRBCs, measured in this experiment and in the one with gRBCs, is attributed to the natural variability in RBC properties form one blood donor to another. For example, the mean excess pressure drop associated with hRBCs flowing in a 5 µm wide restriction is measured to be $\sim$ -1.9 mBar from Figure 3.26b and $\sim$ -1.1 mBar from Figure 3.26d. As demonstrated earlier, the volume has a strong impact of the pressure drop measurement. Therefore, smaller hRBCs may be associated with lower ΔP_{max}.

We have demonstrated here that cell volume and rigidity has an influence on the pressure drop measurement. Indeed, rigidified and inflated RBCs have been found to increase the value of the pressure drop, as they block the constriction in a more efficient way than hRBCs. These results are in good agreement with previous studies [114, 119].
We have seen from 3.26b, that the mean ΔP_{max} associated with hRBCs and gRBCs have been measured to be very different. We can even see from 3.27, that the ΔP_{max} associated with gRBCs is always superior to that induced by hRBCs, hence traducing their difference of volume. For instance for W_c = h = 5 µm, we have measured that ΔP_{max}(hRBCs) = -1.89 ± 0.27 mBar and ΔP_{max}(gRBCs) = -4.15 ± 0.94 mBar. Figure 3.27 presents the intrinsic variability of ΔP_{max} for each population. We can define a critical excess pressure drop ΔP_c = -2.6 mBar, allowing to discriminate both populations as illustrated by the dashed line in Figure 3.27. Above ΔP_c, all the data arise from gRBCs, whereas below this value, all the data points are associated with gRBCs. One could imagine, that by monitoring continuously the pressure drop signal associated with a diluted suspension of RBCs, it would be possible to identify and even count the different sub-populations composing the mixture: signals below and above ΔP_c being associated with each cell types.

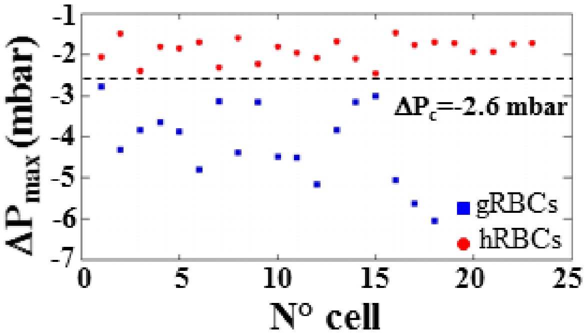

Figure 3.27: The variability of ΔP_{max} for each sample permits to define a critical value ΔP_c allowing to discriminate hRBCs from gRBCs.

One may wonder if this technique is suitable for cells with a more complex architecture than RBCs, such as nucleated cells.

3.3.5 Mechanical characterization of nucleated circulating cells

The presence of a nucleus in the cells might conceal the effect of their mechanical signature. To assess if the pressure drop measurement is adapted to the mechanical characterization of nucleated cells, we propose to investigate the mechanical signatures of two AML cell lines. AML are heterogeneous pathologies affecting children and adults. Despite the recent progress in therapies, they are essentially based on cycles of intensive chemotherapy and most of AML patients are not cured with a survival rate of roughly 20% at 5 years. Recent analysis at CRCL and Centre Léon Bérard (CLB) have highlight an increase in mechano-sensitives pathways (Bone Morphogenetic Protein (BMP) and Yes associated protein (YAP)) in commercial AML resistant cell lines as well as in samples from AML patients in relapse [185]. Interestingly, those properties are also found prevalent in cell lines resistant to chemotherapy compared to sensitive ones, which is associated with an increase in cellular adhesion on various substrates. We propose to investigate if the modulation of mechano-sensitive pathways and adhesion mechanism is associated with a raise of the intrinsic cell stiffness in resistant AML cell lines. Therefore, we could determine if their mechanical properties can help predict the response of cells to treatment.

In this context, we propose to experimentally evaluate the mechanical signature of 2 AML cell lines: ML2-S and ML2-R, respectively sensitive and resistant to Cytarabine (araC) - a chemotherapy indicated in the treatment of hematological cancers, in particular acute leukemias - using pressure drop measurements. Because suspended nucleated cells have a much higher reduced volume than RBCs ($\sim$ 1 against 0.69, respectively) and a lower deformability, the blockage of the flow induced by the presence of the particle inside the narrowing is larger for AML than for erythrocytes. Therefore, in the present study, a non-optimized pressure drop geometry was used (see Figure 3.28).
It corresponds to two identical 100 µm wide micro-channels implementing a narrowing, which width W_c has been varied in the range 7 - 13 µm, whereas the height of the device was fixed at 17 µm. On the right on the chip, the two channels merge into a 400 µm wide chamber. Such dimensions for the exit chamber have been selected in order to induce symmetric extension and shape recovery at the exit of the constriction. Indeed, in the original geometry, the exit chamber was not symmetrical above and below the constriction. Therefore, the cells tended to sustain asymmetric stretching and undergo asymmetric shape recovery [114].

The cells were collected and diluted to the appropriate concentration - typically 10^6 cells/mL - before being transferred in a culture medium (Roswell Park Memorial Institute medium (RPMI) + 1% Penicillin-Streptomycin (PS) + 10% Fetal Bovine Serum (FBS)) containing 9% dextran w/w to reach a viscosity of 30.5 mPa.s at room temperature. A mixture of PBS + 9% dextran w/w containing some ink was

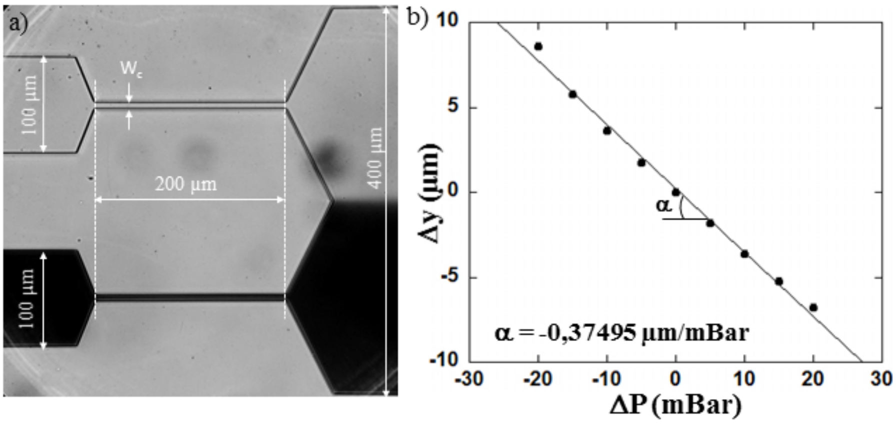

Figure 3.28: a) Picture of the geometry used to characterize the AML cells. The suspending fluid has a viscosity of 30.5 mPa.s. b) An example of calibration curve obtained.

injected in the lower channel to visualize the virtual interface. For each experiment, a calibration curve was obtained in order to determine the sensitivity of the channel. A typical calibration curve is reported in Figure 3.28b. The experiments involving constrictions with W_c = 7 and 10 µm were repeated 6 times and duplicates have been performed for W_c = 13 µm.

From the video-microscopic recordings, we extracted the deformation index associated with the passage of the cells in the constriction, as well as the pressure drop measured in the system. The typical behavior of AML cells flowing in the device is presented in Figure 3.29.

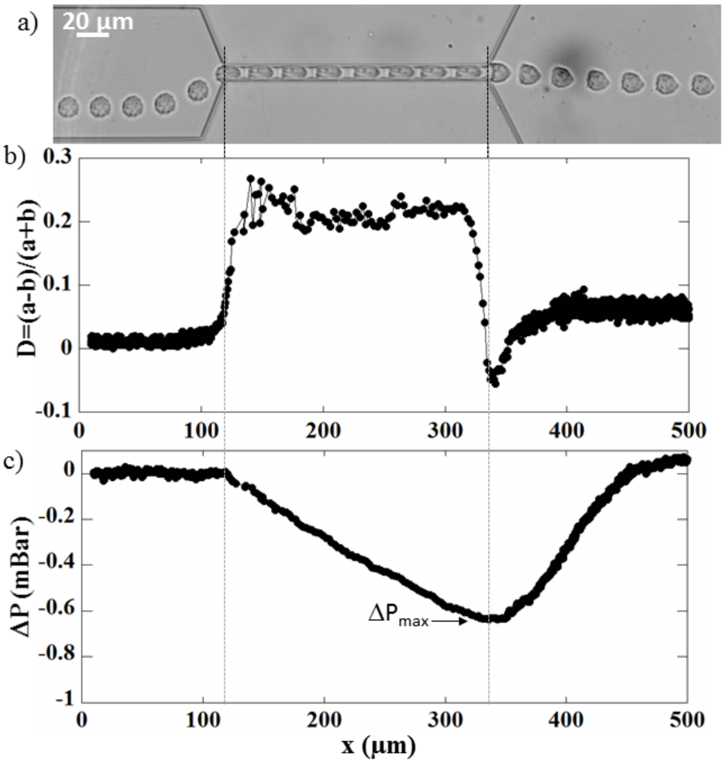

Figure 3.29: a) Sequence of deformation of a ML2-S flowing in the device. Evolution of b) the associated deformation index D and c) the associated pressure drop, versus the position of the cell's center of mass in the device.

On the sequence of deformation (Fig. 3.29a), we can see that the cell appeared round at the entry and squeeze into the constriction. Inside the narrowing, the cell assumed a bullet-like shape, *i.e.* flat at the back and profiled at the front. At the exit of the constriction, the cell got slightly stretched perpendicular to the flow direction. We can also see on the sequence of deformation that, as the cell gets stretched, the back curvature is becoming concave, before recovering its stationary shape. This mechanical response is traduced by the evolution of the deformation index, which is qualitatively quite similar to that of RBCs as reported in Figure 3.24a. Finally as for RBCs, the maximum of the pressure drop, noted ΔP_{max}, occurred when the cells exits the constriction.

Unlike RBCs, eucaryotic cells present a polydispersity in size which depends on their stage in the division process. For example, cells which are just about to undergo division tend to be larger than daughter cells. Therefore, in order to evaluate their volume which will impact the pressure drop measurement, as discussed previously in the case of gRBCs, we have estimated the cells size. The radius a_0 was calculated from the projected surface area of each cell while flowing in the 100 µm wide channel as illustrated in the inset in Figure 3.30a. ML2-S cells radius have been measured between 4 and 10 µm. For $a_0 < 8\mu$m, the estimation is considered valid because the cells diameter remains inferior to the channel height (h = 17 µm); the cells experience thus spherical shapes. For $a_0 \geq 8\mu$m, the cell diameter becomes comparable to the channel height, which can lead to cells undergoing "pancake-like" shapes and thus an over-estimation of a_0.

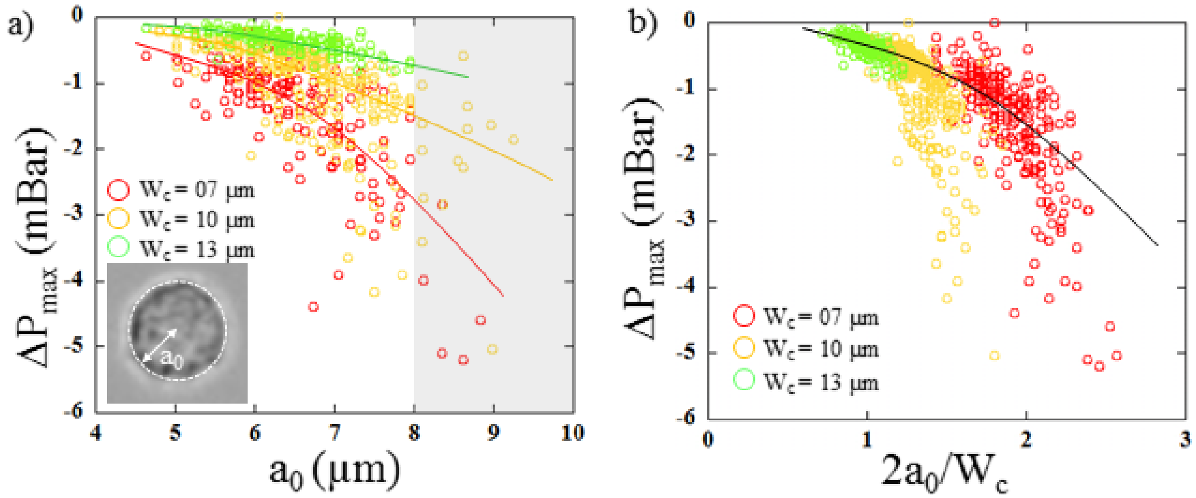

Figure 3.30: ΔP_{max} associated with the flow of ML2-S in constriction with different width W_c according to a) the cells initial radius a_0 and b) the ratio of the cell diameter to the the constriction width $2a_0/W_c$. Lines are just guides for the eyes. The gray zone corresponds to possibly over-estimated a_0 values.

Figure 3.30a presents the ΔP_{max} values associated with ML2-S cells according to their typical size a_0. The zone of the graph corresponding to possibly over-estimated a_0 has been highlighted in gray. As expected, excess pressure drop increases with cell radius and therefore with cell volume, although it does not seem to be a linear relationship. Moreover, for a given size, as the cell blocks more efficiently the flow in the constriction, *i.e.* as W_c decreases, the excess pressure drop value increases. In order to compare ML2-S with different volumes flowing in constrictions with different widths, we also reported the evolution of ΔP_{max} versus $2a_0/W_c$ in Figure 3.30b. The aspect ratio between the cells size and the constriction, noted $2a_0/W_c$, traduces the way cells are going to obstruct the flow. The data issued from the different experiments tend to follow the same trend, hence demonstrating that cells with different sizes flowing in different constrictions present the same ΔP_{max} if they modify the flow in a similar way.

As reported previously, the pressure drop measurement is sensitive to both cell volume and deformability. Therefore, in order to be able to discriminate any difference in deformability, we need to compare the maximum pressure drop of both cell lines for a given size. Thus, Figure 3.31a-c present a comparison of the $\overline{\Delta P_{max}}$ associated with the flow of ML2-S (plain) and ML2-R (hatched), in the different constrictions, calculated according to the cell radius a_0. We first retrieved the main results from Figure 3.30a: for a

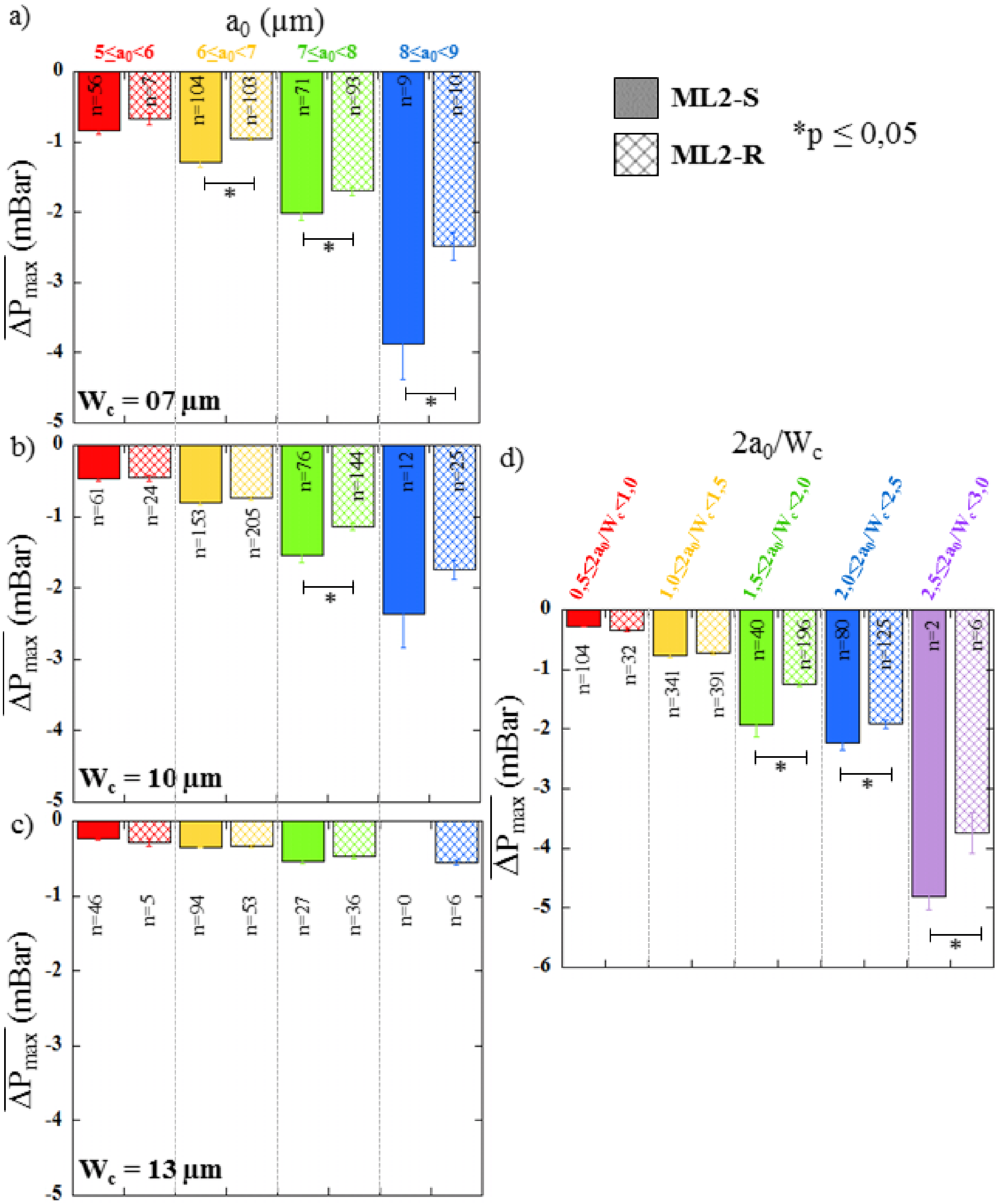

Figure 3.31: Comparison of the mean maximum pressure drop $\overline{\Delta P_{max}}$ associated with the flow of ML2-S (plain) and ML2-R (hatched) in a) 7 µm, b) 10 µm and c) 13 µm wide constrictions, according to the cell radius a_0. d) $\overline{\Delta P_{max}}$ of ML2-S (plain) and ML2-R (hatched) versus $2a_0/W_c$. The error bars represent the standard error. n represents the number of cells investigated in the corresponding category. The comparison between the $\overline{\Delta P_{max}}$ of ML2-S and ML2-R, resulting from a t-test with p-values $p^* < 0.05$ are indicated on the graph.

given size range, the $\overline{\Delta P_{max}}$ of cells flowing in constrictions with decreasing width, rises. We can also see on the graphs that, whatever the cells radius, ML2-S are associated with lower values of $\overline{\Delta P_{max}}$ compared to ML2-R and that for all the values of W_c investigated. For example, ML2-S with a radius between 7 and 8 µm are associated with $\overline{\Delta P_{max}}$ = -2.02 -1.55 and -0.54 mBar whereas ML2-R are associated with $\overline{\Delta P_{max}}$ = -1.70, -1.14 and -0.48 mBar, for W_c = 7, 10 and 13 µm respectively. This suggests that ML2-S are more rigid than their counterparts. The difference between the 2 populations is larger as W_c is decreased. It is also more statistically relevant for larger cells, which is coherent with the fact that larger cells will block in a more efficient way the geometric constriction. One may notice that a larger population has been observed for 6 $\leq a_0 <$ 8 because the size distribution of ML2-S cells is centered around 7 µm.
Since we have previously established that ΔP_{max} is related to $2a_0/W_c$, we have also reported our results in terms of occupation rate of the constriction by the cells in Figure 3.31d. 5 different ranges of occupation rate have been defined ranging from 0.5 to 3. Once again ML2-S show lower values of $\overline{\Delta P_{max}}$ than the chemotherapeutic resistant cell line. For the higher occupation rates, the difference between the 2 AML cell lines is larger despite the fact that very few cells corresponding to 2.5 $\leq 2a_0/W_c <$ 3 has been recorded.

In order to confirm those results, the Young modulus of ML2-S and ML2-R have also been evaluated by AFM (see Appendix C). Figure 3.32a presents 3 typical curves obtained respectively on a Petri dish, on a ML2-S and a ML2-R cells. The Petri dish is used as a reference because considered rigid in the range of forces applied with the cantilever. Figure 3.32b reports the distributions of Young Modulus obtained from the analysis of 29 ML2-S and 38 ML2-R. Details on the AFM measurements on AML cell lines can be found in Appendix C. ML2-R are almost twice more deformable than ML2-S, as the mode of the distribution of the resistant strain is estimated to be $\sim$ 45 Pa, by opposition with the sensitive one which mode is estimated to be 70-80 Pa as detailed in Appendix C. Such Young modulus are of the same order of magnitude than that of HL-60 - which are model AML cells - reported in literature ($<$ 100 Pa [209] and 200 – 1400 Pa [135]).

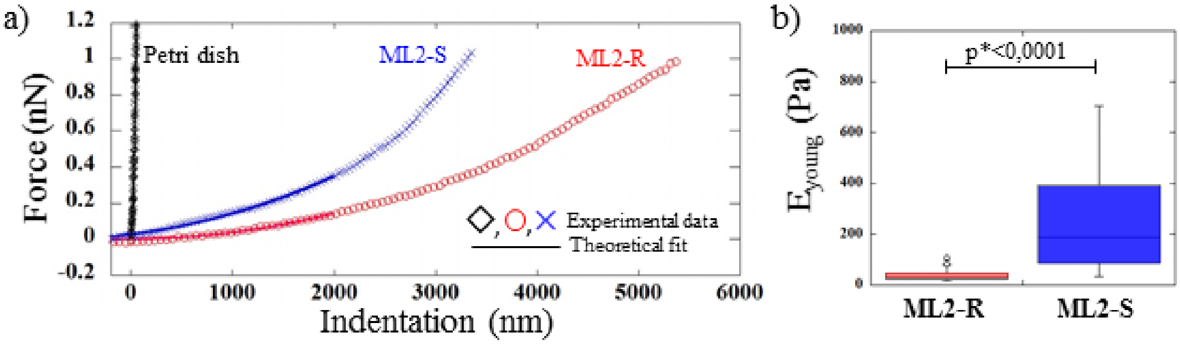

Figure 3.32: a) Typical AFM curves (dashed lines) performed on a reference surface such as a Petri dish (black diamonds), a ML2-S cell (blue crosses) and a ML2-R cell (red circles) and corresponding fits (solid lines) performed on the first 2 µm of indentation. b) Distribution of corresponding Young modulus obtained for the 2 cell lines. Experiments were performed on 29 ML2-S and 38 ML2-R.

Those conclusions are also in good agreement with the mechanical characterization performed with the microfluidic technique. One can also notice that the variability among the ML2-S is much more important than for the ML2-R, although we cannot explain it for now. As illustrated on the histogram of Figure C.1b from Appendix C, the distribution of Young's modulus of ML2-S appears to be a right skewed distribution. The fact that the strain resistant to chemotherapy is more deformable than the sensitive one, might be coherent with the fact that aggressiveness - *i.e.* resistance to therapeutic drugs - is usually associated with high malignancy and metastatic characteristic. Yet, it is now well documented that metastatic cells are usually more deformable than cancerous ones.

3.3.6 Conclusion and future developments

In this section, we have demonstrated that the pressure drop technique is suitable for discriminating RBCs upon difference in deformability but also in volume. This aspect is very interesting for RBCs in particular as the cells present a very narrow size distribution within a sample. Therefore, this approach could be used to detect pathologies such as HS, as it impacts strongly the RBCs volume. We plan on performing such demonstration soon.

Finally, we have demonstrated that the pressure drop measurement was also suited for nucleated cells. The ability of the pressure drop measurement to discriminated, via a difference in mechanical signature, between resistant and sensitive to chemotherapy AML cell lines, might bring new insight for the physicians and oncologists. Indeed, mechanical signature of AML cells could help predict their response to chemotherapy. In order to demonstrate this hypothesis, we would like to confirm our preliminary data and to test primary cells. Thanks to our collaborators from CRCL and CLB, we have access $\sim$50 samples, either from blood or bone marrow samples, taken at the time of diagnosis from AML patients. Because those patients have been treated and followed at the CLB, we have access to their response to treatment and possibly to new samples in the event of a relapse.

3.4 Nano-optical tweezers to assess the mechanical signature of RBCs

As presented in Section 3.1.4, the main limitation of the microfluidic techniques relies on the amount of data to post-process due to the use of high-speed video-microscopy for the monitoring of cellular mechanical. In this section, we propose to introduce the development of a novel approach to characterize mechanically soft objects based on the use of photonic cristals. This study has been initiated in collaboration with Taha Benyattou (INL) and arises from the combination of photonic concepts developed by the i-LUM team and biomechanical concepts mastered by the DSE team. This work was performed mainly during Ali Kheir Aldine M2 internship and PhD (co-advised with Taha Benyattou). The associated ANR project CELLDANCE started in January 2022. We will present some background in photonics, state of the art of conventional and evanescent field based optical tweezers for life sciences applications, before introducing our approach.

3.4.1 Principles of optical trapping

Classical optical tweezers, which were first proposed by Askin in the 70's [4], relied on the use of a tightly focused laser beam, down to the diffraction limit, using a high numerical aperture objective lens [31, 93]. An object located at the vicinity of the focus point undergoes two optical forces: the scattering force and the gradient force. The scattering force or radiation pressure, noted $\overrightarrow{F_{scat}}$ in Figure 3.33a, is oriented along the direction of propagation of the laser. It originates from the transfer of a quantity of motion from the photons to the object they interact with. In order to be significantly affected, the object must have a size of the same order of magnitude than the wave length of the photon.

By opposition, the gradient force, noted $\overrightarrow{F_{grad}}$ on Figure 3.33a is oriented normally to the direction of propagation of the laser beam. This force comes from the gradient of the electromagnetic field intensity. It tends to attract and trap at the center of the focused beam - where the intensity is maximum - objects having a refractive index higher than that of the surrounding buffer. The gradient force will be the leading force involved in the optical trapping. The total optical force magnitude therefore depends on the profile of the trap and the electric polarizability of the object, which is related to its dimensions and the permittivity contrast between the particle and the buffer.

Thanks to the generation of optical forces in the range of pN, implemented at a very precise location, optical tweezers had been largely used to 3D manipulate particles in the nano- micrometer range as illustrated in the next Section 3.4.2. However, some limitations may hinder their use regarding the manipulation of bio-molecules due to spot size limitation and sensitivity towards high power. As stated

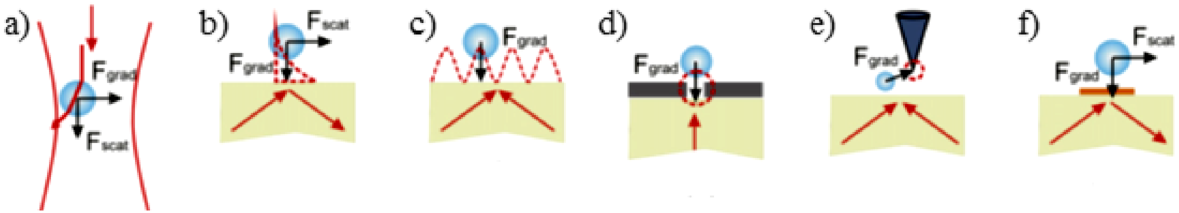

Figure 3.33: a) Schematic of a classic optical trap in an aqueous medium. A particle entering the light beam, will stay trapped in the beam waist because of the radiation pressure force. b-g) Schematics of the different trapping configurations using evanescent field : b) total reflection, c) reflection of 2 waves creating interference fringes, d) plasmonic structures, e) metallic tip and f) surface plasmons at metal/dielectric interface. From [130].

earlier, the size of the laser spot is limited by diffraction, which therefore reduce the associated amplitude of the total optical force. One strategy to increase the gradient force is to increase the light intensity. However, Ashkin et al. [6] have demonstrated that 109 nm polystyrene particles have lasted 25 s before being destroyed, while 85 nm latex beads deteriorated so rapidly that it was impossible to perform any measurements. Another strategy is to exploit nano-photonics, which exploit the evanescent field generated by nanostructures to confine the light at a much smaller scale than the diffraction limit. Indeed the transverse confinement of surface fields allows trapping particles close to the surface. In the simplest configuration where a plane wave is totally reflected at the interface of the material, the particle is attracted towards the surface by the gradient force and guided along the in-plane k-vector by the scattering force as illustrated in Figure 3.33b [126].

Other configurations overcoming the use of high numerical aperture objectives have been proposed in literature. Large periodic arrays of evanescent traps formed by two interfering counter-propagating evanescent waves were reported [206, 207] (see Figure 3.33c). Light confinement at the output of a sub-wavelength aperture in a metallic layer [94, 112] or at the extremity of a metallic tip [111, 154] have been reported to amplify the evanescent field. The two approaches are illustrated in Figures 3.33d and e respectively. Surface plasmons supported at metal/dielectric interfaces have been reported in literature to optically manipulate objects [130] (see Figure 3.33f). Three types of approaches takes advantages of evanescent waves in order to trap particles in near field : (i) wave guides, (ii) plamonic nanostructures and (iii) Photonic Critals (PhCs).

Materials with photonic band gaps are artificial structures presenting a periodic modulation of the dielectric constant in one or several directions [186]. Another way is to create a cavity in the photonic cristal by drilling holes in a substrate that is transparent regarding the wavelength of radiation that the bandgap is designed to block. In our approach, we will focus on the use of PhCs allowing the confinement of the evanescent optical field in a small, controlled volume defined by the cavity dimensions, hence increasing the associated gradient force. Although very few applications of PhCs in the life science area have been reported in literature, they have demonstrated its benefits including the ability to trap biological materials without damaging it.

Implementations of conventional optical tweezers applied to the mechanical characterization of RBCs are presented in the following section. Examples of PhCs applications for life sciences domains are also reported.

3.4.2 State-of-the-art of optical tweezers for bio applications

Conventional optical tweezers have been largely used to manipulate atoms, molecules and biological particles (bacteria, viruses and cells) [130, 5]. This approach have also been used to assess the elastic properties of a single strand of DNA by pulling on the molecule through the micro-spheres attached at each end [53]. The optical forces have also been used to probe the mechanical properties of biological cells; especially RBCs. For example, by stretching RBCs *via* the trapping 2 micro-particles diametrically attached to their membrane [181] as illustrated by Figure 3.34a.

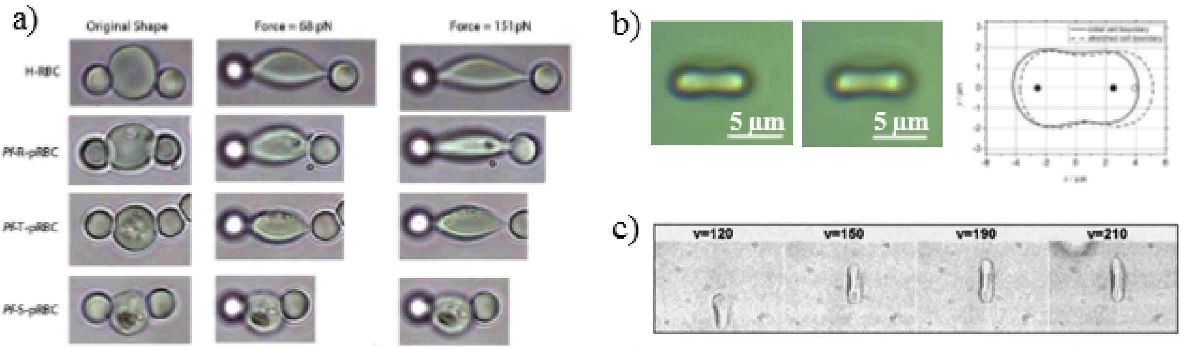

Figure 3.34: a) Optical images of hRBCs (noted H-RBC on the figure) and *P. falciparum* iRBCs, at different stage of parasite maturation, (noted *Pf*-R-RBC, *Pf*-T-RBC and *Pf*-S-RBC for ring, trophozoite and schizonte iRBCs respectively), submitted to different constant forces using a dual beam optical tweezers to pull on particles diametrically attached to the cells surface. Adapted from [188]. b) Another embodiment without the use of micro-beads to probe the RBC mechanical properties. Side view of a RBC, (left) at rest and (middle) under stretching. (right) Representation of the RBC contour corresponding to the 2 precedent states. The black dots indicate the laser spots before stretching, while the white dots indicate the right laser spot position at the time of the maximum deformation. Adapted from [167]. c) Illustration of the deformation of a RBC dragged *via* an optical tweezer, at a velocity ranging from 150 to 210 µm/s in the buffer. From [178].

The opposite motion of the two micro-beads leads to the cell deformation. By knowing the applied constraint and by measuring the mechanical response of the cell, the shear modulus μ can be deduced from the following Equation [181]:

$$D = D_0 - \frac{F}{2\pi\mu} \tag{3.2}$$

where, D and D_0 are respectively the diameter variation and the original diameter in the direction perpendicular to the applied force F. The same type of experiment can be performed without the use of micro-particles attached to the membrane, but by using the a dual beam optical trap to directly deform the cells, as reported in literature [200, 167]. More recently, a microfluidic version of the optical tweezers have been reported by Guck et al. with a throughput of 1 cell/min, as already discussed in the Section 3.1 and illustrated in Figure 3.1.

Other types of mechanical characterization involving optical tweezers have been reported in literature. For example, Saraogi et al. have reported Changes in the spectrum of the Brownian fluctuations of single trapped hRBCs and malaria iRBCs [161]. Huruta et al. have exploited the deformation of trapped cells dragged at a constant velocity within a liquid (typically plasma), using an optical tweezer [178]. The measurement of the cell length as a function of its velocity can be used to extract the shear modulus μ from the Equation 3.3.

$$L = L_0 + (\frac{\eta L_0^2}{\mu Z_{eq}})V \tag{3.3}$$

where L_0 is the length of the cell at rest, η is the fluid viscosity and $Z_{eq} = \frac{Z_1 Z_2}{Z_1+Z_2}$, with Z_1 and Z_2, the distance of the cell to the lower and upper wall of the microfluidic chamber, respectively.

Regarding the use of PhCs for bio-applications, the first proof of concept of the trapping of bacteria using PhCs has been reported in literature in 2013 [204]. Later, another research team have successfully combined measurements on brownian motion and transmission to differentiate the Gram-type of bacteria trapped on a PhC cavity [171]. Donato et al. [25] have proposed an electro-photonic approach to analyze and monitor the response of individual bacteria to antibiotics. Trapped bacteria are exposed to antibiotics and the corresponding changes in the optical properties and motility of the bacteria are monitored through changes of resonance wavelength and transmission intensity in the PhC cavity. Kang et al. [157] have demonstrated the real time trapping and detection of the association of the influenza virus to the corresponding antibodies immobilized at the surface of a PhC. To the best of our knowledge, there are no study reporting the exploitation of PhCs trapping of cells to probe their deformability.

In the following section, we will detail the PhC configuration used during our study and the first results obtained so far.

3.4.3 Optical nanotweezers approach to probe single cell deformability

We have already discussed how a PhC cavity can be used to efficiently 3D trap a particle thanks to the gradient forces. Moreover, information about the object can be extracted from the reflectivity spectrum of the cavity. In particular, by measuring the reflectivity as a function of the wavelength of radiation, the resonance of the cavity, *i.e.* the wavelength for which the reflectivity drops, can be measured. The resonance depends essentially on the refractive index of the environment at the vicinity of the PhC surface. In the case of a particle present onto the cavity, this overall refractive index can be of course influenced by the refractive index of the object, but also by the effective surface of interaction between the object and the optical field generated by the cavity. The effective surface of interaction between the object and the evanescent field varies with both the size of the object and its position relative to the cavity.

In this project, the originality of our approach relies on the use the PhC to both apply optical forces to deform single cells and tracking the subsequent deformation using the resonance. Figure 3.35 presents a schematic representation of our method's principle. A photonic resonance is excited from free space by a laser source to generate an intense photonic mode at the surface of the device. The mode is extended over an area larger than the size of the particle. Such mode induces optical forces that will attract the cell towards the surface of the PhC cavity. For a soft particle, the optical forces are expected to be strong enough to deform it, leading to an increase of the effective surface of interaction. This deformation will induce a red-shift of the spectral position of the optical resonance. This spectral shift can therefore be related to the ability of the cell to deform and allow us to assess its mechanical properties.

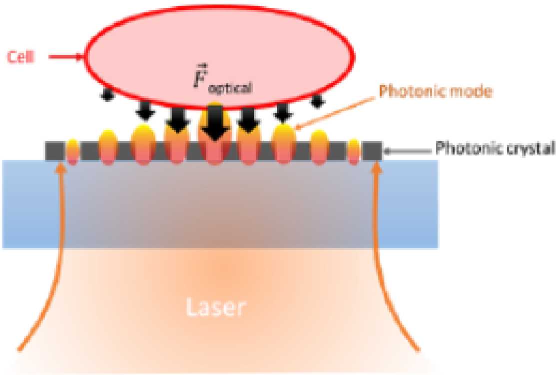

Figure 3.35: A photonic resonance is excited from free space by a laser source to generate an intense photonic mode. The optical forces generated will induce the deformation of a soft cell. The flattening of the cell onto the surface will be associated with a red-shift of the PhC resonance.

In order to perform the first proof of concept, we first decided to de-correlate the generation of optical forces to induce the cell deformation, and the reading of this deformation using the resonance. Therefore as described in the next section, two different laser sources will be implemented in the setup : the first one to trap and deform the cell, while the second one will be used to read the effect of the change in shape on the resonance.

3.4.4 Description of the PhC cavity and the experimental setup

In our study, we have used a 2D square mesh PhC, with a double period, which dimensions and picture are reported in Figures 3.36a) and b). The size of the cavity has been chosen to be 5 µm × 5 µm. The fabrication process won't been discussed here as it has been previously reported [110]. The PhC substrates were kept immersed in De-Ionised (DI) water since fabrication and in between experiment. The PhC cavities have been characterized prior to use and quality factors Q as high as 11000 were measured. High Q values are associated with good coupling of the excitation source with the resonance of the cavity, which will induce a larger shift of the resonance for a given event.

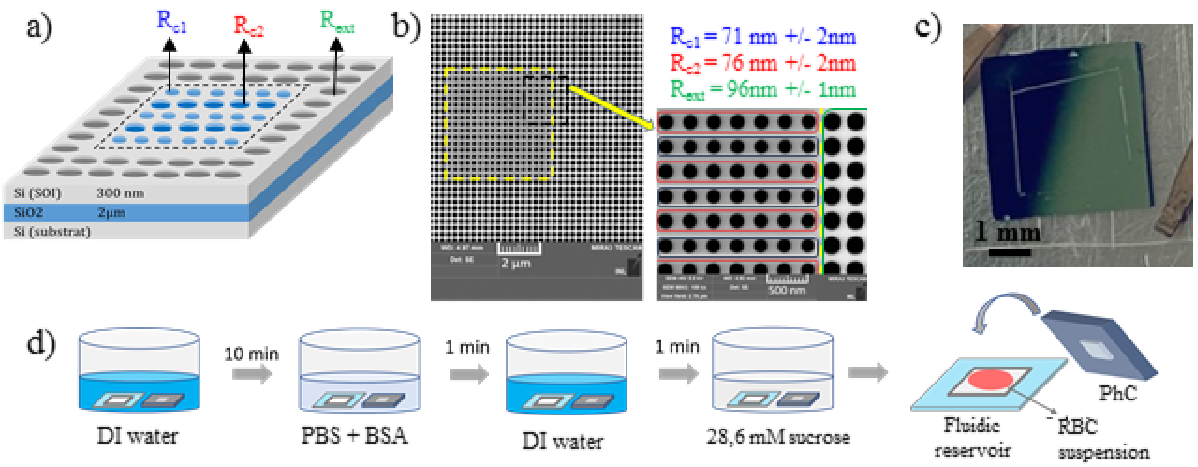

Figure 3.36: Presentation of the double period PhC cavity: a) schematic representation and b) SEM picture of a 5 µm × 5 µm fabricated cavity. The different radii of the holes are defined and reported. c) Picture of an actual optofluidic chip. d) Illustration of the surface treatment protocol, filling and assembly of the optofluidic chamber.

The optofluidic chamber is composed of the substrate implementing the PhC and a PDMS fluidic reservoir. The reservoirs were prepared by spin-coating a$\sim$ 100 µm thick PDMS layer onto glass cover slides, and after curing the PDMS, a window of few mm^2 was carved into the polymer layer. A picture of a typical optofluidic chamber is presented in Figure 3.36c). Prior to assembly, both surfaces were treated in order to prevent RBCs non specific adhesion. Figure 3.36c) illustrates the optimized protocol developed by Ali during his PhD. This protocol includes incubation of both the PhC and the reservoir inside a mixture of PBS and BSA at 0.02% w/w for 10 min. Then the surfaces were washed in DI water in order to favor liquid penetration inside the pores of the PhC cavity. Finally, they were rinced in a 28.6 mM sucrose solution in order to saturate the pores with sucrose to avoid any negative osmotic pressure related effect. In the meantime, 5 µL of whole blood was obtain by finger pricking and mixed with 1 mL of PBS. The cells were washed twice in PBS and resuspended in a mixture of PBS and 28.6 mM isotonic sucrose medium.

Indeed, we have noticed that even in presence of BSA, RBCs suspended in PBS tend to adhere strongly onto the Silicon substrate implementing the PhC. Such phenomena has already been reported in literature [24] and was hypothesized to be caused by the presence of salt ions in the surrounding media. By using a non-ionic buffer such as sucrose, the adhesion of RBCs onto the 5 µm large PhC surface could be inhibited. However, it appeared difficult to perfectly maintain the isotonicity of the blood samples using only sucrose solution. Indeed, we observed shape alteration of the cells suspended in the sucrose buffer, depending on the blood donor and even between different samples from the same donor, that were not observed when the cells were suspended in PBS. Therefore, we decided to mix both buffers, in order to combine their individual advantages. We empirically determined that the best proportion was 100 μL of 28,6 mM sucrose mixed with 30 μL of RBCs suspended in PBS, at an hematocrit of 0.052%. With these proportions, the normal discocyte shape of the cells where maintain and roughly 60% of the cells were not adhered onto the substrate. After filling the reservoir with the blood suspension, the PhC substrate is deposited onto the reservoir, to seal the optofluidic chamber, as illustrated in Figure 3.36d).

The experimental setup used to probe cell deformability is shown in Figure 3.37.

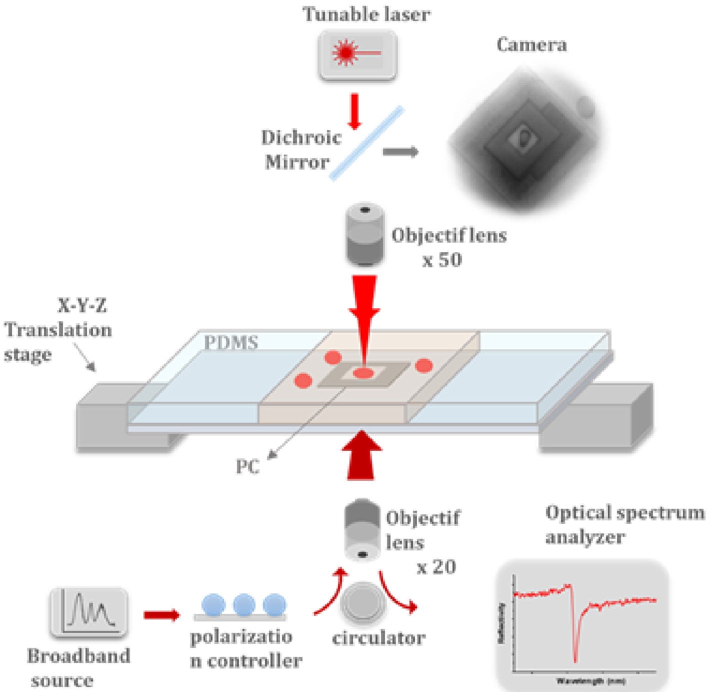

Figure 3.37: Schematic of the optical setup used to mechanically characterize RBCs. The trapping laser - labeled tunable laser on the schematics - will be used to place a cell onto the PhC surface, whereas the broadband source is used from free space to read the PhC cavity resonance. the associated deformation of the object is monitored using a CCD camera.

It can be divided into three parts : (i) a trapping laser used to trap the cell, drag it onto the cavity and deform it, (ii) a chip implementing the PhC and (iii) a broadband infrared laser source to read the resonance of the PhC cavity. The trapping laser, a TSL 510 from Santec which is a tunable laser in the range 1260–1680 nm, is applied on the front-side of the cavity. We worked at a wavelength of 1320 nm. The laser beam is amplified by an optical amplifier and focused by a 50X microscope objective with a Numerical Aperture (NA) of 0.42. The optofluidic chip is composed of the PhC associated with a PDMS reservoir containing the suspension of objects to be characterized. It is placed on a piezoelectric translation stage. The measurement of the cavity resonance from the back-side of the cavity is done using a broadband source from Amonics which ranges from 1250 to 1650 nm. The polarization is controlled thanks to a fiber controller. The light beam is focused onto the sample by a microscope objective having a magnification 20X and a NA = 0.60. The signal reflected from the sample is redirected by the circulator to the spectrum analyzer (Anritsu MS9740A) presenting a maximum resolution of 30 pm. Finally, a visible CCD camera was used to image the cavity and visualize the subsequent deformation of the object.

3.4.5 Application to the discrimination of hRBCs and rRBCs

We propose to apply our approach to the discrimination of healthy and artificially rRBCs. In order to have a drastic variation of deformability, glutaraldehyde was selected to artificially rigidify the cells, as previously reported in literature [9, 74]. Glutaraldehyde is a bifunctional cross-linking agent, which is known to rigidify RBCs by cross-linking proteins in their membrane and their cytoplasm. Briefly, RBCs were resuspended and incubated into a solution of 25% glutaraldehyde, for 30 min at room temperature. After rinsing twice with PBS, rRBCs were suspended in PBS at the appropriate concentration according to the selected mechanical approach. AFM measurements performed with Marie-Charlotte Audry Deschamp, allowed the measurements of young modulus at 70 Pa and 15 kPa for hRBCs and rRBCs respectively. For more details on the AFM measurements, please refer to Appendix C.

The reflectivity spectrum of the cavity alone, *i.e.* without any cell, is recorded as a reference. It is represented in Figure 3.38a as the black crosses, with a resonance at λ = 1338.229 nm obtained through a Fano fit of the experimental data. A RBC is then positioned onto the 5 µm large PhC cavity thanks to the trapping laser. The trapping laser is then set to the minimal power necessary to maintain the cell vertical, considering that the RBC deformation - if any - would be negligible. The picture of the rested hRBC positioned vertically onto the PhC is presented in the left inset. This low power condition will be considered as the condition for which cell is at rest, in the following. The associated reflectivity spectrum is then recorded, as reported in red in Figure 3.38a. The resonance of the cavity corresponding to the presence of the cell at rest (minimum applied optical forces) on top of the cavity is estimated to be λ = 1338.267 nm. The contrast in refractive index associated to the presence of RBCs over the cavity induces a red-shift of the resonance wavelength. The magnitude of this shift depends on the cavity field overlap with the cell; it is estimated to be $\Delta\lambda_1$ = 38 pm.

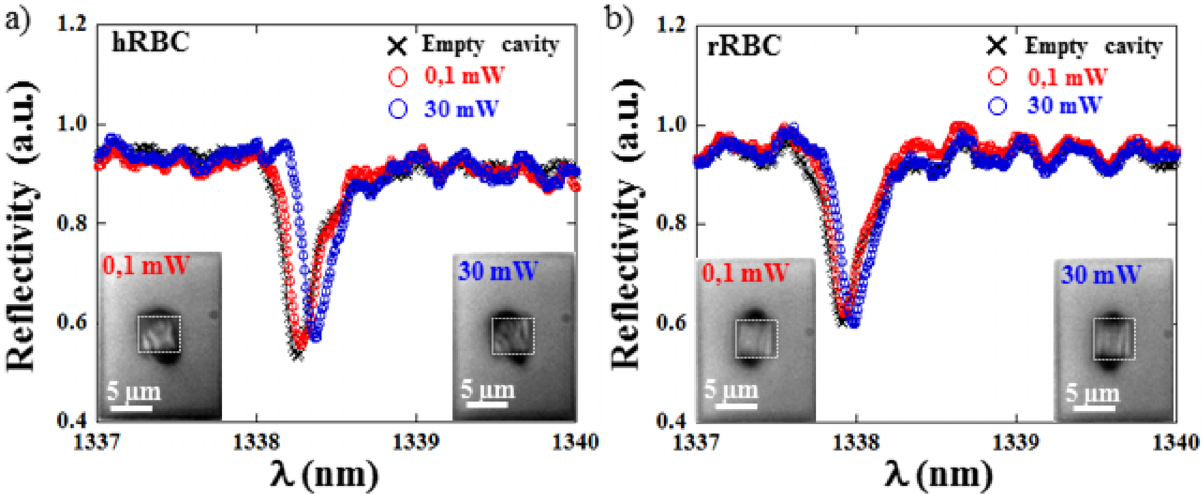

Figure 3.38: Reflectivity measurements of the 5 µm large PhC cavity versus the wavelength λ, in presence of a) a hRBC and b) a rRBC onto the cavity. The black crosses represent the signal for the empty cavity, whereas the red and blue circles illustrate the spectrum for the cell at rest (0.1 mW), and under high laser power (30 mW) respectively. Variation of reflectivity $\delta R/R$, versus the wavelength λ corresponding to c) the hRBC and d) the rRBC.

The trapping power is then set at a higher value (30 mW) in order to induce cell deformation and another measurement is performed (see the blue curve in Figure 3.38a). Once again, the picture of the hRBC under high laser power is reported as inset. A resonance at λ = 1338.363 nm was measured at high laser power. Although is difficult to quantify any cell deformation from the pictures with the current resolution of the imaging system, it seems like the upper "lobe" of the cell is larger at high optical power. A second shift associated with the increase of laser power is estimated to $\Delta\lambda_2$ = 96 pm. We remind the reader that the trapping laser being set at an excitation wavelength of 1320 nm, cannot account for the measured shift . The two main phenomena that can explain $\Delta\lambda_2$ are (i) the cell displacement along z, as well as within the cavity plan, and (ii) its deformation. Indeed, if the object approaches the surface cavity or improve its alignment with the optical mode of the cavity, the effective contact area between the object and the optical mode would rise thus inducing a red-shift. In the same way, the compression of the cell on the surface of the sensor would also increase the effective contact area, also resulting in a red-shift. In fact, it is likely that the red-shift that we observe at high laser power, is actually a combination of the cell approach and deformation.

The experiment is repeated with an artificially rRBC treated with glutaraldehyde according to the protocol discussed earlier. The reflectivity spectra recorded both at rest (0.1 mW) and at high laser power (30 mW) are reported in Figure 3.38b, along with that associated with the empty cavity. The resonance of the empty cavity is measured to be 1337.896, whereas it is estimated to be 1337.932 and 1337.980 nm, at low and high optical power respectively. The two shifts $\Delta\lambda_1$ and $\Delta\lambda_2$ are calculated to be $\sim$ 36 pm and 47.9 pm respectively. We would like to stress that if the rRBC experiences any deformation, it cannot be detected onto the associated pictures (see inset in Figure 3.38b).

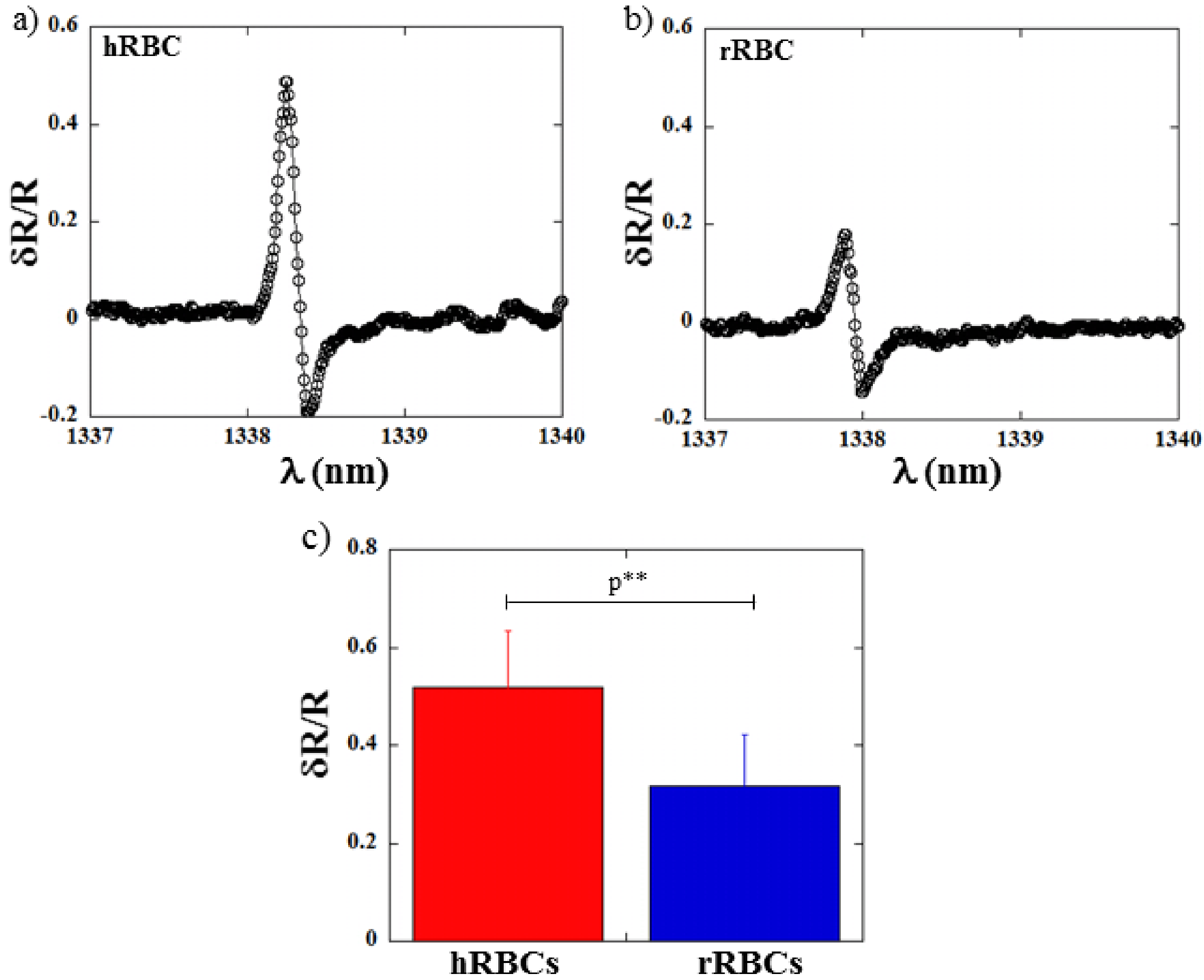

Figure 3.39: Reflectivity variation $\delta R/R$ versus the wavelength λ, in presence of a) a hRBC and b) a rRBC onto the cavity, as optical force is increased (30 mW). c) Maximum value of $\delta R/R$ averaged over 15 hRBCs and 19 rRBCs. The errors bars represent the standard deviation and the statistical analysis has been performed using the student t-test, p**$<$0.0001.

It can be noticed that the first resonance shift $\Delta\lambda_1$ for the hRBC and rRBC are equivalent, which is consistent with the fact that glutaraldehyde treatment is not known to impact neither its volume nor its shape []. In contrast, the second resonance shift $\Delta\lambda_2$ is very different for the two types of cells. Indeed, $\Delta\lambda_2$ associated with hRBC is twice that associated with the glutaraldehyde treated cells. As stated earlier, this second red-shift could be attributed to a combination of cell approach and deformation. However in the case of the rRBC, the cell rigidity is so high (15 kPa) that deformation is unlikely. Therefore, this would suggest that in the measurement of $\Delta\lambda_2$ for the hRBC, a first half of the shift could be attributed to the approach component, whereas the other half could traduce the actual cell deformation. However, more experiments would be needed in order to decipher the contribution of both phenomena in the second red-shift associated with an increase in optical force on the cell. One may also note that both cells get slightly displaced when the trapping power is increased, and this displacement may also impact $\Delta\lambda_2$.

In order to make it easier to visualize the red-shift associated with both cell types when the trapping laser is set at 30 mW, we propose to report the associated variation of reflectivity. The variation of reflectivity is defined as $\delta R/R = (R_{0.1} - R_{30})/R_{0.1}$, where $R_{0.1}$ and R_{30} are the reflectivity spectra in presence of the cell onto the cavity at low optical power (0.1 mW) an high optical power (30 mW) respectively. The corresponding graphs are presented in Figure 3.39a for the hRBC and Figure 3.39b for the rRBC. As presented in the graphs, the variation of reflectivity rises at the resonance wavelength. A maximum variation of $\sim$ 50% is associated with the hRBC, whereas $\delta R/R \sim$ 20% is measured for the rigidified one. The statistical analysis performed on 15 hRBCs and 19 rRBCs reveals that the reflectivity variation $\delta R/R$ at the resonance is a signature typical of the cell type (see Figure 3.39c). Because the only systematic difference between the two types of cell is their deformability, $\delta R/R$ could be used as a relevant readouts to discriminate difference in cellular mechanics.

3.4.6 Conclusion and future developments

We have presented what we believe to be, to the best of our knowledge, the first attempt to exploit the resonance of a PhC cavity to probe the mechanical properties of cells. In a first setup, two different laser sources were used to independently (i) read the PhC cavity and (ii) place a RBC and deform it. The monitoring of the reflectivity of the cavity according to the wavelength showed a first red-shift $\Delta\lambda_1$ associated with the presence of a cell onto the PhC cavity, with a low optical pressure. The preliminary results show that $\Delta\lambda_1$ is nearly independent on the deformability of the cell. On the contrary, as the optical power is increased, the second red-shift $\Delta\lambda_2$ drops by 50% when the deformability of the cells is altered upon glutaraldehyde treatment as already reported [9, 74]. We are currently trying to improve the resolution of the imaging system in order to correlate those measurements with independent quantification of the deformation undergone by the cell due to the trapping laser. Although repeating those preliminary results with different donors would be necessary to assess the RBCs mechanical signature from the resonance of a PhC cavity, our approach seems promising. Those encouraging results have been obtain during Ali Kheir Aldine's PhD and were presented in an international conference and we are currently trying to value it in a publication.

A significant improvement of the current setup would be to use the optical forces, generated by the exited cavity, to deform directly the cells without the use of a trapping laser. In this new version of the setup, the PhC cavity could be couple to a microfluidic channel, in order to deliver the cells sequentially to the sensor. Those developments will be carried out within the framework of the ANR project CELLDANCE (January 2022 - December 2026) which aims to use new PhC, such as metasurfaces, for the discrimination between hRBCs and malaria iRBCs.

Chapter 4

Conclusions and global perspectives

As stated in my former research contributions, I started working on the mechanical properties of RBCs using microfluidics during my PhD. It is within the framework of these activities, started 20 years ago, that I mainly built my research career. During my 2 postdoc experiences, I kept developing microsystems with application in biomedical domains, using biomolecular techniques this time. However, I remained highly convinced that the relationship between the biophysical properties of cells (whether they are dielectric, magnetic, migratory or mechanical properties) and their physiopathological state is one key aspect to provide crucial information to the clinicians.

In this manuscript, I have presented the research carried out during the past 10 years, on the development of microsystems taking advantage of a modification of the cellular mechanics to identify a physiopathological state. The approaches developed for adherent cells such as cancer cells, were based on the relationship between deformability, adhesion and migratory properties of cells. This idea behind this work was to exploit the dynamical behavior of cells migrating either under lateral confinement (between posts), or on nano-topographic features implemented on the substrate to amplify the already existing difference in migratory properties between breast metastatic and cancerous cell lines. The developments regarding the circulating cells have been more substantial. After characterizing comprehensively the oscillating width geometry, we have demonstrated that we were able to identify 3 different diseases of the RBC, namely Hereditary Spherositosis, Sickle Cell Diseases and Malaria. More recently, we have used the pressure drop measurement to discriminate AML cells sensitive to a chemotherapeutic drug (araC) from resistant ones. The preliminary results suggest that cells mechanical phenotype could be used to predict the outcome of the treatment.

During the past 10 years I have worked with colleagues belonging to the same disciplinary field as myself but I have also always sought interaction with other scientific communities. Indeed, I have always favored the interdisciplinary nature of my work, as it is a wonderful way to bring out new ideas and to keep learning new concepts and new techniques.

I had an active role in PhD supervision, as I have co-supervised 1 PhD student on mechanical and magnetic approaches to sort malaria infected cells, 1 PhD student on dielectric approaches to monitor breast cancer cells upon chemotherapy assays and 3 PhD students on mechanical approaches to identify pathological cells. I have also been active (even if not as successful as one would hope) in projects submission to various calls for proposals.
If I had to define the research project that I want to develop in the next few years, I would say that *I want to do the same thing but in a different way*. On one hand, my research project is in a certain continuity of my previous research on the mechanical phenotyping of cells for diagnosis, therapeutic follow up and prognosis applications. A project that is particularly close to my heart is the use of the pressure drop measurement associated to determine if the mechanical properties of AML cells can help predict their response to treatment. A PhD founding to work on that project has been asked to the Doctoral School EEA. We plan to confirm our preliminary results with primary cells from patients for which we know if a

relapse has occurred.
I would also like to pursue addressing new approaches to probe the mechanical properties of cells to perform diagnosis. For example, in the ANR project CELLDANCE (2022-2026), we aim at developing a new nano- optical tweezers method based on an original nanophotonic approach to detect the presence of malaria iRBCs in a blood sample.

On the other hand, my research project opens up to the characterization of more complex biological systems, with more complex architectures and thus totally different mechanics. The project BOTRYPATH (PACK AMBITION RECHERCHE from the Auvergne Rhône-Alpes region), which started in 2022, is part of this dynamic. This project proposes in particular to develop LOC devices intended to carry out the sorting of mono-nuclear fungal spores to accelerate the production of mutant spore lines by biologists. In order to avoid the use of toxic cell markers, we propose to assess the use of Electrical Impedance Spectroscopy (EIS) to probe the spore cytoplasm or to aply mechanical approaches.

In the end, I hope that we will be able to translate our (past or future) developments into something useful for the end-users whether they are biologists or clinicians.

Comme indiqué dans la section décrivant mes précédentes contributions de recherche, j'ai commencé à travailler sur les propriétés mécaniques des globules rouges en utilisant la microfluidique pendant ma thèse. C'est dans le cadre de ces activités, commencées il y a 20 ans, que j'ai principalement construit ma carrière de chercheuse. Au cours de mes deux expériences post-doctorales, j'ai continué à développer des microsystèmes ayant des applications dans le domaine biomédical, en utilisant cette fois-ci des techniques biomoléculaires. Cependant, je suis restée intimement convaincue que la relation entre les propriétés biophysiques des cellules (qu'elles soient diélectriques, magnétiques, migratoires ou mécaniques) et leur état physiopathologique est un aspect clé pour fournir des informations cruciales aux cliniciens.

Dans ce manuscrit, j'ai présenté les recherches menées au cours des 10 dernières années, sur le développement de microsystèmes tirant parti d'une modification de la mécanique cellulaire pour identifier un état physiopathologique. Les approches développées pour les cellules adhérentes telles que les cellules cancéreuses, étaient basées sur la relation entre la déformabilité, l'adhésion et les propriétés migratoires des cellules. L'idée derrière ce travail était d'exploiter le comportement dynamique des cellules migrant soit sous confinement latéral (entre les poteaux), soit sur des substrats nano-structurés pour discriminer ou isoler des lignées métastatiques et cancéreuses.

Les développements concernant les cellules circulantes ont été plus substantiels. Après avoir caractérisé de manière exhaustive la géométrie de section oscillante, nous avons démontré que nous étions en mesure d'identifier 3 maladies différentes du globule rouge, à savoir la sphérositose héréditaire, la drépanocytose et le paludisme. Plus récemment, nous avons utilisé la mesure de la chute de pression pour distinguer les cellules de leucémie myéloïde aigües sensibles à une molécule chimiothérapeutique (en l'occurance araC) des cellules résistantes. Les résultats préliminaires suggèrent que le phénotype mécanique des cellules pourrait être utilisé pour prédire le résultat du traitement.

Au cours des dix dernières années, j'ai travaillé avec des collègues appartenant au même champ disciplinaire que moi, mais j'ai également toujours cherché à interagir avec d'autres communautés scientifiques. En effet, j'ai toujours privilégié la nature interdisciplinaire de mon travail, car c'est un moyen merveilleux de faire émerger de nouvelles idées et de continuer à apprendre de nouveaux concepts et de nouvelles techniques.

J'ai joué un rôle actif dans la supervision d'étudiants en thèse, puisque j'ai co-supervisé 1 thèse sur les approches mécaniques et magnétiques pour trier les cellules infectées par le paludisme, 1 thèse sur les approches diélectriques pour surveiller les cellules cancéreuses du sein lors des essais de chimiothérapie et 3 thèses sur les approches mécaniques pour identifier les cellules pathologiques. J'ai également été active (même si cela n'a pas été autant couronné de succès qu'on pourrait l'espérer) dans la soumission de projets à divers appels à projet.
Si je devais définir le projet de recherche que je souhaite développer dans les prochaines années, je dirais que *je veux continuer à faire la même chose mais de manière différente*.
D'une part, mon projet de recherche s'inscrit dans une certaine continuité de mes recherches précédentes sur le phénotypage mécanique des cellules pour des applications de diagnostic, de suivi thérapeutique et de pronostique. Un projet qui me tient particulièrement à cœur est l'utilisation de la mesure de chute de pression associée pour déterminer si les propriétés mécaniques des cellules de leucémie myéloïde aigüe, peuvent aider à prédire leurs réponses au traitement. Un support de thèse pour travailler sur ce projet a été demandé à l'école doctorale EEA. Nous prévoyons de confirmer nos résultats préliminaires avec des cellules primaires de patients pour lesquels nous savons si une rechute a eu lieu.
J'aimerais également continuer à aborder de nouvelles approches pour sonder les propriétés mécaniques des cellules afin d'effectuer un diagnostic. Par exemple, dans le cadre du projet ANR CELLDANCE (2022-2026), nous souhaitons développer une nouvelle méthode de nano-pinces optiques basée sur une approche nanophotonique originale pour détecter la présence de cellules infectées par le parasite du paludisme dans un échantillon de sang.

D'autre part, mon projet de recherche s'ouvre à la caractérisation de systèmes biologiques inédits pour moi, avec des architectures plus complexes et donc des propriétés mécaniques totalement différentes. Le projet BOTRYPATH (PACK AMBITION RECHERCHE de la région Auvergne Rhône-Alpes), qui a débuté en 2022, s'inscrit dans cette dynamique. Ce projet propose notamment de développer des dispositifs LOC destinés à réaliser le tri de spores fongiques mononucléaires pour accélérer la production de lignées de spores mutantes pour les biologistes. Afin d'éviter l'utilisation de marqueurs cellulaires toxiques, nous proposons d'évaluer l'utilisation de la spectroscopie d'impédance électrique pour sonder le cytoplasme des spores mais également l'utilisation d'approches mécaniques.
Finalement, j'espère que nous serons en mesure de traduire nos développements (passés ou futurs) en quelque chose d'utile pour les utilisateurs finaux, qu'ils soient biologistes ou cliniciens.

Appendix A

Development of a magnetophoretic sorting function [123]

A.1 Introduction

When flowing RBCs in channels which dimensions are smaller than the typical size of the cells, one needs to get rid of stiffer and bigger cells of the sample, such as WBCs, to avoid clogging. To realize the sorting of RBCs and WBCs, several passive microfluidic techniques, where only the action of the flow allows the separation, have been reported in literature. For example, we can cite the microfiltration [64], the Pinched Flow Fractionation (PFF) [133, 82] or the Deterministic Lateral Displacement (DLD) [85, 153]. The main issue with these techniques is the need to highly dilute the sample in order to avoid clogging ; therefore, analysis time can be as long as (1 µL/h) [85]. The active sorting techniques rely on the combined action of the flow and an external force by taking advantage of the specific physical properties of the cells (dielectric [103], optical [140], magnetic [102]. . .) to isolate them.

Our approach is based on their different intrinsic magnetic properties. Indeed, deoxygenated RBCs are paramagnetic whereas WBCs are diamagnetic, that is they are attracted and repealed by strong gradients of magnetic field. In order to implement a sorting based on magnetophoresis, we used an original approach based on the team skills. When others generate gradients of magnetic field by using permanent magnets [34, 78], wires [101] or ferromagnetic microstructures [102, 210], we propose to implement a magnetic composite material derived from PDMS, a non-reactive polymer widely used to fabricate microfluidic systems by soft lithography. The material referred to as iron-PolyDiMethyl Siloxane (i-PDMS), is composed of PDMS doped with microparticles of carbonyl iron in order to acquire ferromagnetic properties - that is able to generate a gradient of magnetic field in presence of external field - while preserving the replication ability of PDMS.

BIOMICROFLUIDICS **8**, 054103 (2014)

Magnetophoretic manipulation in microsystem using carbonyl iron-polydimethylsiloxane microstructures

Magalie Faivre,[1] Renaud Gelszinnis,[1] Jérôme Degouttes,[1] Nicolas Terrier,[1] Charlotte Rivière,[2] Rosaria Ferrigno,[1] and Anne-Laure Deman[1]
[1]*Université de Lyon; Institut des Nanotechnologies de Lyon INL-UMR5270, CNRS, Université Lyon 1, Villeurbanne F-69622, France*
[2]*Université de Lyon; Institut Lumière Matière ILM-UMR 5306, CNRS, Université Lyon 1, Villeurbanne F-69622, France*

(Received 6 July 2014; accepted 22 August 2014; published online 5 September 2014)

This paper reports the use of a recent composite material, noted hereafter i-PDMS, made of carbonyl iron microparticles mixed in a PolyDiMethylSiloxane (PDMS) matrix, for magnetophoretic functions such as capture and separation of magnetic species. We demonstrated that this composite which combine the advantages of both components, can locally generate high gradients of magnetic field when placed between two permanent magnets. After evaluating the magnetic susceptibility of the material as a function of the doping ratio, we investigated the molding resolution offered by i-PDMS to obtain microstructures of various sizes and shapes. Then, we implemented 500 μm i-PDMS microstructures in a microfluidic channel and studied the influence of flow rate on the deviation and trapping of superparamagnetic beads flowing at the neighborhood of the composite material. We characterized the attraction of the magnetic composite by measuring the distance from the i-PDMS microstructure, at which the beads are either deviated or captured. Finally, we demonstrated the interest of i-PDMS to perform magnetophoretic functions in microsystems for biological applications by performing capture of magnetically labeled cells. © *2014 AIP Publishing LLC*. [http://dx.doi.org/10.1063/1.4894497]

I. INTRODUCTION

It is now well established that for numerous analysis and diagnosis performed on biological material — typically blood — trapping and separation functions are very important in microsystems.[1,2] Among other techniques involving various external stresses such as dielectrophoretic,[3,4] acoustic,[5,6] optical,[7,8] and hydrodynamic forces,[9,10] the use of magnetophoresis in microsystems[11–13] has been successfully demonstrated to isolate natively magnetic biological species — for example, deoxygenated red blood cells[14–17] — or magnetically labeled cells,[18–24] or DNA,[25] from non magnetic ones. Indeed, using a hard magnetism approximation, when placed in a magnetic field gradient ($\nabla\cdot\boldsymbol{B}$) a magnetic microparticle which magnetic moment is considered uniform, experiences a magnetic force $\boldsymbol{F}_{mag}$ expressed as follows:

$$\boldsymbol{F}_{mag} = \frac{4\pi r^3}{3\mu_0}\Delta\chi(\boldsymbol{B}\cdot\nabla)\boldsymbol{B}, \qquad (1)$$

where $\Delta\chi = \chi_p - \chi_f$ represents the difference in magnetic susceptibilities, between the particle (χ_p) and the surrounding fluid (χ_f), r is the radius of the particle, and $\mu_0 = 4\pi \times 10^{-7}$ H m^{-1} the vacuum permeability. According to Equation (1), paramagnetic ($\Delta\chi > 0$) and diamagnetic ($\Delta\chi < 0$) species are therefore, respectively, attracted and repelled by high gradients of magnetic field.

In microsystem, the dominant competing force acting on particles is the hydrodynamic drag force $\boldsymbol{F}_{drag}$ defined by Stokes' law (Equation (2)),

$$\boldsymbol{F}_{drag} = 6\pi\eta r(\boldsymbol{v_f} - \boldsymbol{v_p}), \qquad (2)$$

where η is the viscosity, $\boldsymbol{v_p}$ is the velocity of the particle, and $\boldsymbol{v_f}$ is the velocity of the suspending medium.

In order to isolate the magnetic species from the remaining solution, the magnetic force acting on these particles must be greater than the drag force. Controlling the magnetic field distribution on the micrometer scale is a challenge. Actually, magnetophoretic separators implementing permanent magnets or electromagnets[26] — characterized by centimeter to millimeter scale dimensions — at the vicinity of the microfluidic chamber, generate high magnetic field gradients mainly located at the neighbourhood of the magnet edges, and therefore, the magnetic force associated within the channel is small, on the typical scale of biological cells (tens of μm). More recently, it has been shown that magnetophoretic separators using High Gradient Magnetic Separation (HGMS) method can be used to separate biocomponents either based on their intrinsic magnetic properties or using magnetically labeled cells.[15,18,19,27] Moreover, researchers have focused on the generation of high local and controlled magnetic field gradients to overcome the low magnetic forces exerted on biological materials because of their natively small magnetic susceptibilities.

Therefore, several techniques have been reported in the literature to achieve the generation of such controlled and very well located gradients. The injection of some ferromagnetic suspension into a side channel apart from the separation channel have been reported to generate magnetic field gradients sufficient to achieve separation of magnetic beads or cells.[28] However, the flow rate enabling cell capture is relatively low: 6 μl/h. The use of micromagnets located within the channel has been reported to allow the capture of magnetic particles[29] and magnetically labeled bacterial cells[30] thus at a high technological cost. The introduction of ferromagnetic thin wires[14,31,32] or microstructures[15,33,34] mainly made of Nickel, inside the system is the most common method to create controlled local gradient for blood cells sorting and capture. Although these soft ferromagnetic structures allow the control of the magnetic field distribution on the micrometer scale, they are obtained by time-consuming electroplating techniques. Moreover, the heterogeneous integration of metallic materials in PDMS systems can generate leakage issues during operation. However, as previously demonstrated with carbon doped PDMS,[35] PDMS composite materials present many advantages over metallic microstructures for the fabrication of active microfluidic devices. Indeed, we have shown that this material, combining properties of both compounds, allows the easy and fast integration of metallic microstructures using soft-lithography approach while preserving O_2 plasma bonding properties of PDMS substrate and avoiding cumbersome alignment procedure. One recent publication reports the isolation of tumors cells from leukocytes, using a microsystem based on self assembled NdFeB-PDMS composite.[36] The authors report a very high capture efficiency of magnetically labeled leucocytes, leading to an enrichment of the population of tumor cells by a factor of $>10^3$. However, despite these very good results, the use of permanent magnets does not allow the easy and rapid release of the targeted cells, which can be a difficulty for subsequent analysis.

The objective of this paper is therefore to evaluate another PDMS composite — Carbonyl Iron-PDMS, noted hereafter i-PDMS — to generate local gradients of magnetic field and then to carry out magnetophoresis based manipulations (capture or separation) in a microfluidic format. This material is composed of a PDMS matrix doped with carbonyl iron microparticles that give to this composite soft ferromagnetic property as already shown in previous papers.[37–40] In past studies, authors demonstrated that this material can form magnetically actuated membranes[38] to achieve micropumps[39] and mixing functions[37] in MEMS. However, to the best of our knowledge, no study was reported on the use of this material in magnetophoresis based microfluidic functions such as trapping and separation of magnetic species. We aim at demonstrating that i-PDMS composite is suitable to generate high gradients of magnetic field and can be used for magnetophoretic applications such as HGMS. We first report the preparation and characterization of i-PDMS with various doping ratios. Shape of the microstructures as well as the position of the permanent magnets relative to the structures was optimised numerically. Then, 500 μm i-PDMS diamond microstructures integrated along a PDMS microfluidic channel were evaluated for magnetophoresis functions. Trapping capacities of this material are demonstrated with quantitative measurements of the behavior of superparamagnetic microbeads flowing in the microsystem as a function of flow rate. The separation of para- and diamagnetic species is illustrated. Finally, we have highlighted that i-PDMS is suitable to perform magnetophoretic functions for biological applications by showing the capture of magnetically labeled cells.

II. EXPERIMENTAL

A. Preparation of i-PDMS

Carbonyl iron microparticles (dry powder, 7 μm diameter, 97% Fe basis) (Sigma-Aldrich) and PDMS mixture (10/1 w/w of monomer and curing agent, respectively) (Sylgard from Samaro) were thoroughly mixed in a mortar (around 4 min) until obtaining an homogeneous material prior to polymer reticulation. Different carbonyl iron concentrations ranging from 50% to 83% w/w were tested. The homogeneity of the different composites prepared has been verified by SEM (Tescan SEMFEG Mira3) observations of slices of material.

B. Fabrication and preparation of the microsystem

The different microfluidic structures were prepared using soft lithography approaches based on the replication of masters as reported elsewhere.[41] For the integration of i-PDMS microstructures into PDMS channels, this replication was operated in two steps using first the composite and then conventional PDMS, as reported previously.[35] The master was fabricated through standard photolithography method (Figure 1(a)). Briefly, SU8-2035 (Chimie Tech Service) was spin-coated on glass substrate in order to obtain 45 and 36 μm thick masters. Then, i-PDMS was first molded in the dedicated area of the system and after cleaning the eventual i-PDMS smears, the composite was baked in the same conditions as pure PDMS (75 °C for 60 min). Then, conventional PDMS was poured over the whole master and baked (75 °C for 60 min). Due to the good binding of i-PDMS and PDMS, when the PDMS slab was peeled off the master, i-PDMS microstructures remained bound to PDMS. After microscopic observations of the mold, we are confident that no i-PDMS microstructures were left on it. The inlets and outlets were then punched prior to sealing of the PDMS slab to a pre-cut glass substrate by O_2-plasma activation (40 s, $P_{O_2} = 900$ mTorr).

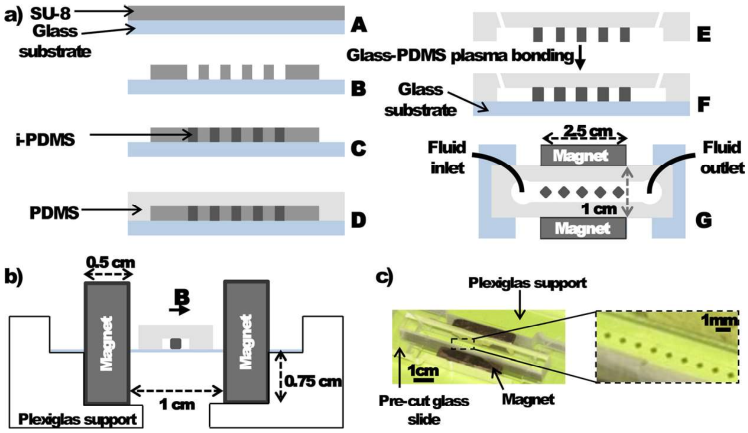

FIG. 1. (a) Fabrication process of microsystems integrating i-PDMS microstructures: (A) SU-8 spin-coating on a glass substrate, (B) SU-8 photolithography and development, (C) i-PDMS deposition and curing, (D) pouring of PDMS and curing, (E) Demolding of the system and punching of the inlets and outlets, (F) side view, and (G) top view of the final microsystem. (b) Schematic side view of the experimental setup presenting the optimized configuration of the permanent magnets regarding to the microsystem. (c) Picture of the microchannel mounted with the magnets. The close-up allows distinguishing the i-PDMS diamond-like microstructures.

C. Preparation of the magnetic microparticle suspension

Different magnetic species were tested in the microsystem. 12 μm in diameter superparamagnetic microparticles — consisting of magnetite in a polystyrene copolymerisate as organic matrix (density 1.2 g/cm^3, $\chi_m = 8.44 \times 10^{-3}$ corresponding to a magnetization of 0.56 emu/g for a magnetic field of 1000 Oe) — and 10 μm in diameter diamagnetic fluorescent microparticles, respectively, purchased from Kisker and Sigma-Aldrich. These particles were suspended at a concentration around 160 beads/μl in filtered Phosphate Buffered Saline (PBS) (Invitrogen) with 3.6% w/w dextran (Mw $= 2 \times 10^6$ *Leuconostoc* spp., from Sigma Life Science). Dextran was used to reduce the sedimentation of the particles during the time of the experiment.

D. Cell magnetic labeling

Human breast cancer cells (GFP MDA-MB-231) were labeled with a stable suspension of maghemite nanoparticles coated with negatively charged citrate molecules (magnetic diameter of 8.3 nm and hydrodynamic diameter of 35 nm) provided by C. Ménager (Laboratoire PESCA, UMR7195, Université Paris 6, France). Confluent cells were incubated for 2 h with a suspension of the negatively charged maghemite nanoparticles ([Fe] = 10 mM) in RPMI culture medium containing 5 mM of sodium citrate (free citrates are used as counterions to stabilize the nanoparticle suspension), followed by a chase period of 1 h in supplemented culture medium. Cells were then detached using trypsin, resuspended in supplemented culture medium to the desired concentration ($\sim 6 \times 10^6$ cells/ml), and injected in the microsystem.

E. Experimental setup

The microsystem was then placed on a custom-made Plexiglas support developed in order to secure the position of the two permanent magnets (Nd/Fe/Br $25 \times 10 \times 5$ mm^3 1,2 T at the pole, polarization in the longest dimension) used to generate the external magnetic field, regarding the microfluidic channel in the optimized configuration. The experimental setup is presented on Figures 1(b) and 1(c). The relative positions of magnets and microchannel were optimized by numerical simulations. Before introducing the magnetic species, the microsystem was passivated with filtered 2% Bovine Serum Albumin (BSA) (Sigma-Aldrich) in PBS to avoid any non-specific adsorption of the particles onto the microchannel walls. The microsystem was then rinsed with filtered PBS. A syringe pump (Harvard Apparatus) was used to inject the beads suspension in the microsystem. Videomicroscopy techniques involving an inverted epifluorescent microscope (Leica DMI4000B) and a camera (Leica DFC340 FX) allowed us to observe the behavior of superpara- and diamagnetic beads in the microsystem. Image J® was used to perform image analysis and to retrieve beads trajectories.

III. RESULTS AND DISCUSSION

A. i-PDMS characterization

We first evaluated the influence of doping ratio (50%, 75%, and 83% w/w) on the structurability and magnetic properties of i-PDMS. We found (INL and Institut Néel, unpublished results) that the magnetization $\boldsymbol{M}$ of i-PDMS composites, as a function of the magnetic field applied $\boldsymbol{H}$, increases with the doping ratio as previously reported by Li *et al.*[37] These curves were exploited in order to calculate the magnetic relative permittivity μ_r as a function of the doping ratio. Indeed, this parameter directly traduces the capacity of the material to generate magnetic field gradient. μ_r, was calculated using Equations (3) and (4),

$$\boldsymbol{M} = \chi_m.\boldsymbol{H}, \tag{3}$$

$$\mu_r = 1 + \chi_m, \tag{4}$$

where $\boldsymbol{M}$ is the resulting magnetization of the composite — converted into A/m, taking into account the density of the material (measured as described in the Appendix) — under the applied magnetic field $\boldsymbol{H}$ (also expressed in A/m) and χ_m is the magnetic susceptibility of the material.

We report the evolution of the relative magnetic permittivity of the composite versus the doping concentration in Figure 2. The results show that μ_r increases with the carbonyl iron concentration. Indeed, μ_r increases from 1.45 to 2.28 when the doping ratio is increased from 50% to 83% w/w. This value is typically of the same order of magnitude than relative permitivity of other magnetic composites.[28] The values of μ_r for i-PDMS are to be compared with a value of μ_r of 6.02, expected for 100% carbonyl iron powder (from the magnetization curve obtained on pure carbonyl iron particles and the associated density value given by the manufacturer). From our previous experience with other PDMS composites,[35] we expect that further increasing the doping ratio would drastically increase the viscosity of i-PDMS and therefore reduce the ability of the material to be processed by replication techniques. Despite its low μ_r value, the i-PDMS is efficient for magnetic separation as demonstrated below. In the future, we plan to increase the μ_r by choosing other doping materials or by adding nanoparticles instead of microparticles.

We studied the effect of doping ratio on structurability of the composite by replication approaches. Several geometric shapes (squares-, disks-, and diamonds-like shapes with various angles) were replicated using soft lithography techniques[41] and resultant i-PDMS structures were characterized by SEM observations (see Figure 3). Satisfactory replication was observed for all doping ratio. In order to maximize the magnetic susceptibility while keeping replication capacity, we selected a doping ratio of 83% w/w, corresponding to a magnetic relative permittivity of 2.28. For this doping, we evaluated the minimal resolution that our replication approach could attain. We managed to obtain microstructures down to 50 μm (typical dimension of the geometric shape: side for squares, diameter for disks and smallest diagonal for diamonds) that exhibit fine shapes and good angle resolutions as illustrated in Figures 3(a)–3(c). Below this limit, the shapes were recognizable but the definition of the angles were not judged satisfactory and the edges were less smooth (Figures 3(d)–3(f)).

B. Application to the generation of magnetic field gradient for HGMS

We aim at highlighting the ability of this composite material to be used to perform separation of magnetic species via trapping. Indeed, in order to trap a superparamagnetic particle flowing in the microfluidic system, the magnetic force has to overcome the drag force exerted by the surrounding fluid on the object, i.e., $\boldsymbol{F}_{mag} > \boldsymbol{F}_{drag}$. As the magnetic susceptibility and the

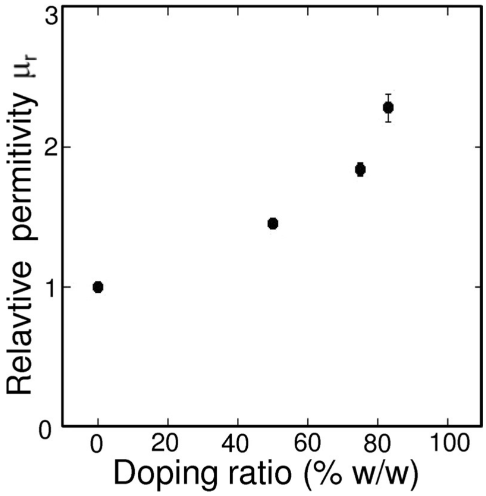

FIG. 2. Relative magnetic permittivity of the composite materials μ_r versus the doping ratio.

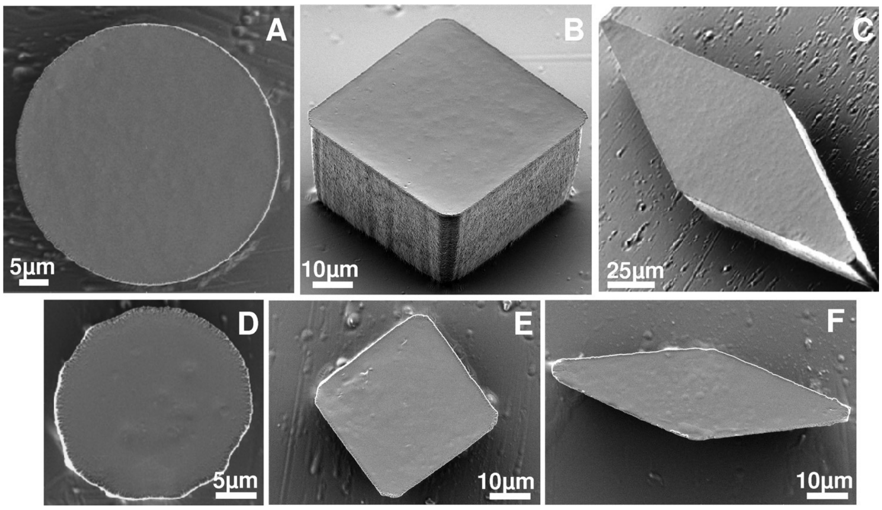

FIG. 3. SEM images of various 83% w/w i-PDMS microstructures. From (a)–(c) characteristic dimension was 50 μm, whereas from (e)–(f) characteristic dimension was 25 μm.

radius of the particle are intrinsic parameters of the species to isolate, the only way to maximize the magnetic force is either to reduce the magnetic susceptibility of the surrounding medium[17] or to maximize $|(\boldsymbol{B}\cdot\nabla)\boldsymbol{B}|$. We chose here to implement microstructures of i-PDMS inside a fluidic microsystem to demonstrate the ability of this composite material to induce sufficiently high magnetic field gradients to perform separation of magnetic species via trapping. For that purpose, we considered a microfluidic channel with a respective width and height of 1 mm and 50 μm, containing 83% w/w i-PDMS microstructures. The magnetic field was produced by applying two permanent magnets facing each other, hence generating a magnetic field as uniform as possible, so that gradients can only be attributed to the presence of i-PDMS microstructures.

1. Configuration of the microsystem

2D computer simulations were performed with ComSol Multiphysics 4.2a® in order to determine the optimum configuration of the microfluidic system to maximize $|(\boldsymbol{B}\cdot\nabla)\boldsymbol{B}|$ generated by i-PDMS microstructures, under uniform magnetic field ($|\boldsymbol{B}|$ computed to be roughly 206.7 mT). We have evaluated the influence of (i) the position of the permanent magnets regarding the microfluidic channel — as defined in Figure 4(a), D, the distance between the two magnets and d, the vertical position of the channel regarding the middle of the magnets are investigated — and (ii) the shape of the i-PDMS microstructures to maximize the gradient generated.

First, the microchannel with a single 500 μm i-PDMS microstructure was centered between the two permanent magnets, as illustrated in Figure 4(a), for d = 0 mm and the effect of the distance D between the two magnets was investigated. The optimum position of the magnets is expected to generate a high $|(\boldsymbol{B}\cdot\nabla)\boldsymbol{B}|$ term in order to maximize the associated magnetic force. We have first simulated a microchannel without i-PDMS structures and checked that the magnetic field generated by the two permanent magnets is nearly uniform and therefore considered constant (data not shown here) for d = 0. Then an i-PDMS microstructure is added to the system. As expected, $|(\boldsymbol{B}\cdot\nabla)\boldsymbol{B}|$ increases as D is decreased (Figure 4(b)). However, for practical reasons, we choose to fix the inter-magnet distance at 10 mm. Indeed, the attraction force between the magnets is so important when they are too close that it becomes difficult to handle and position them on each side of the microfluidic device. Then, we studied the influence of the vertical alignment of the microchannel regarding the magnet height for D = 10 mm. $|(\boldsymbol{B}\cdot\nabla)\boldsymbol{B}|$ is maximized in the channel for d = 0 as presented in Figure 4(c). Therefore, the optimum configuration

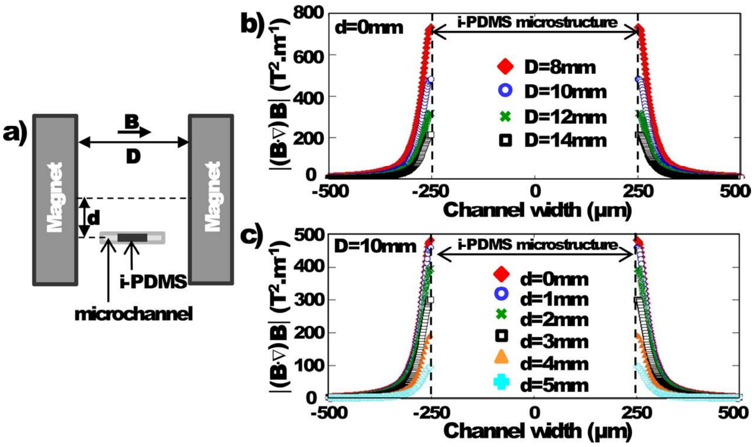

FIG. 4. (a) Schematic representation and definition of the different parameters: D is the distance between the two permanent magnets — the microchannel being in the middle — and d is the vertical shift of the channel position regarding half the magnets height. (b) Evolution of the $|(\boldsymbol{B}\cdot\nabla)\boldsymbol{B}|$ term across the channel width as D is varied, for d = 0 mm. (c) Evolution of the $|(\boldsymbol{B}\cdot\nabla)\boldsymbol{B}|$ term across the channel width as d is varied, for D = 10 mm.

of the setup is chosen to be the microchannel centered horizontally and vertically compared to the two magnets which are spaced 10 mm from each other.

We also studied the effect of the i-PDMS microstructure shape on the gradient of magnetic field generated. Various shapes such as 500 μm disks, squares, and diamonds (typical size is, respectively, diameter, side, and diagonal) were simulated at the center of the microchannel with the optimum configuration determined previously (D = 10 mm and d = 0 mm). The $|(\boldsymbol{B}\cdot\nabla)\boldsymbol{B}|$ term generated by the microstructures was calculated for each shape using the relative permittivity μ_r of the 83% w/w i-PDMS determined previously from the magnetization curves and the measurement of the material density (see the Appendix).

As presented in Figure 5(a), the results show that the diamond-like i-PDMS structure exhibits the highest magnetic field gradients at the tip. When looking at the vicinity of the microstructure, 10 μm away from the composite (see Figure 5(b)), it appears that the diamond-

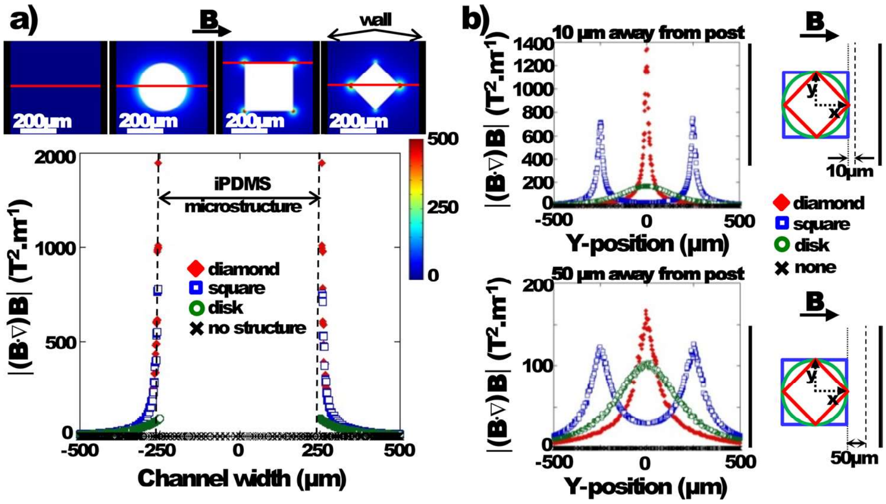

FIG. 5. (a) Evolution of $|(\boldsymbol{B}\cdot\nabla)\boldsymbol{B}|$ along the red line on the surface representation (top images) as a function of the i-PDMS microstructure shape. (b) $|(\boldsymbol{B}\cdot\nabla)\boldsymbol{B}|$ along the y-direction (top) 10 μm and (bottom) 50 μm away from the i-PDMS microstructure — as defined on the sketches on the right — according to the shape.

like shape generates $|(\boldsymbol{B}\cdot\nabla)\boldsymbol{B}|$ values twice as high as the square-like one. $|(\boldsymbol{B}\cdot\nabla)\boldsymbol{B}|$ is still higher for the diamond-like at $50\,\mu$m away from the structure. Therefore, for the rest of the study, the diamond-like microstructure has been selected to demonstrate the capability of i-PDMS to concentrate the magnetic streamlines in a microsystem.

2. Characterization of magnetic trapping

The 1 mm wide microfluidic channel integrating a line of 20 diamond-like microstructures made of 83% w/w i-PDMS was prepared according to the protocol described in Sec. II. A syringe pump is used to apply the flow and inject the magnetic species to separate. The whole setup was placed under an inverted microscope in order to perform videomicroscopic recordings of the particles behavior as they flowed through the system.

We first highlighted the actual distribution of magnetic field lines by injecting a suspension of $12\,\mu$m superparamagnetic microparticles ($\chi_m = 8.44 \times 10^{-3}$) in PBS solution at 160 beads/μl and at a flow rate of $50\,\mu$l/h. As illustrated in Figure 6, the superparamagnetic microbeads were trapped around the composite microstructures highlighting the generation of gradients of magnetic field. Those results demonstrate the concentration of magnetic field lines around the i-PDMS hence generating gradients inducing a magnetic force on the superparamagnetic beads.

It can be noticed that the apparent geometry of the microstructure is modified during the experiment by the aggregation of superparamagnetic particles (Figure 6(a)). This can lead to a decrease of the capture efficiency of the system — due to (i) an increase in the distance between flowing beads and the region of high magnetic gradients and (ii) a slight decrease of the channel section inducing a rise of the drag force — up to the saturation where beads tend to roll on the trapped particles and get released in the circulation. In the rest of the manuscript, the measurements were performed with little coverage of the posts, to ensure to be independent of this change in geometry. One advantage of our composite material is the possibility to reverse the trapping and to release the particles from the structures. As a matter of fact, by removing the permanent magnets and applying a flow, the superparamagnetic particles were

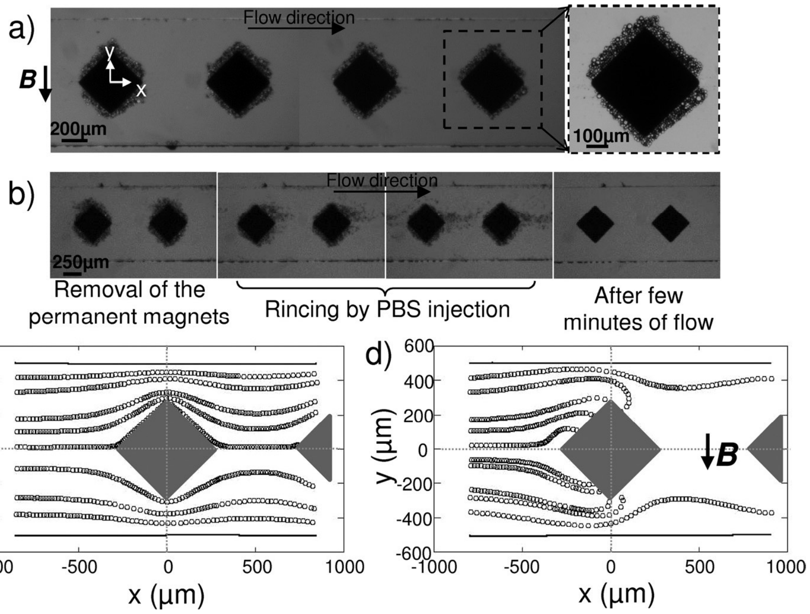

FIG. 6. (a) Capture of superparamagnetic beads suspended in PBS, on several i-PDMS microstructures. The close-up allows distinguishing the amount of beads trapped on a single structure. (b) Emphasize of the reversibility of the capture: the beads can be detached and collected by rinsing after removal of the magnets. Trajectories — extracted from videomicroscopic observations — of superparamagnetic microparticles, suspended in 3.6% w/w dextran in PBS, flowing at $50\,\mu$l/h (c) in absence and (d) in presence of the permanent magnets. The flow is from left to right.

allowed to freely flow off the structure, as illustrated in Figure 6(b). This indicates no residual magnetization of our material after removal of the external magnetic field.

In order to study into details the performances of the trapping of magnetic species by i-PDMS structures, we focused on the behavior of superparamagnetic particles as they flowed at the vicinity of the first diamond structure. However, it was difficult to carry out characterization experiments as microparticles sedimentation occurred within 10 min in the syringe. To attenuate that effect, we suspended superparamagnetic particles in a solution of polymer (dextran at 3.6% w/w in PBS, i.e., $\eta \sim 10$ mPa s) to increase the viscosity of the surrounding fluid, despite the fact that it increases the drag force $\boldsymbol{F}_{drag}$ by a factor 10 (see Equation (2)), and hence impacts the conditions where $\boldsymbol{F}_{mag} > \boldsymbol{F}_{drag}$. This induces a reduction of the capture efficiency. However, we verified experimentally that in a suspension containing 3.6% w/w dextran in PBS, superparamagnetic particles flown through the microsystem at 50 μl/h were still captured on the i-PDMS microstructures in presence of the magnet (Figure 6(c)) whereas the trajectories were symmetrical in absence of the permanent magnets (Figure 6(d)). It was verified that in absence of the two permanent magnets, or when injecting diamagnetic microparticles, no trapping on the i-PDMS occurred. We also checked that in presence of the magnets but with pure PDMS microstructures within the channel, the particles were following the stream lines and showed no attraction towards neither the PDMS microstructures nor towards the channel walls, hence showing that any eventual gradient of magnetic field induced by the two permanent magnets is not strong enough to perturb beads trajectories and can therefore be neglected (see Figure 11 in the Appendix). In the rest of this paper, we will thus consider a situation unfavorable regarding the trapping. One should keep in mind that if working with magnetic species suspended in non-viscous media, the actual capture and deviation efficiencies would be higher than those reported here.

3. Effect of the flow rate on the magnetic trapping

We then investigated the influence of the flow rate on the ability of the i-PDMS microstructures to trap superparamagnetic microbeads. Three different flow rates are studied: 50, 200, and 500 μl/h, which considering a 45 μm high and 1 mm wide microchannel, correspond to typical flow speed of 0.3, 1.2, and 3.1 mm/s, respectively, far from the structure. One may note that for a given flow rate, as particles flow past the i-PDMS microstructure and thus undergo a stronger magnetic force, they accelerate due to the reduction (from 1 mm to 500 μm) of the apparent width of the channel, therefore leading to the doubling of the drag force experienced by the cells. Videomicroscopic recordings of the particles behavior were performed at the vicinity of the first diamond-like shaped microstructure, hence allowing the extraction of several parameters such as bead positions and their velocities. Figure 7(a) reports a time lapse of videomicroscopic images: actual capture and deviation events can be observed on the i-PDMS post already covered with captured superparamagnetic beads. The deviation of the microbeads as they flow close to the i-PDMS structure is measured versus the applied flow, according to the methodology described in Figure 7(a). The positions Y_1 and Y_0 of the beads in the channel are measured, respectively, at $x = -500\,\mu m$ and $x = +500\,\mu m$ — position corresponding to the equidistance between the first and the second microstructure — from the center of the diamond-like shaped structure. Therefore, we performed the study of the deviation of the microbeads $\Delta Y = Y_1 - Y_0$ as a function of their position Y_0 prior to the composite post.

The results are presented in Figure 7(b), in presence and in absence of the two permanent magnets, for a typical flow rate of 200 μl/h. In absence of external magnetic field, the superparamagnetic microbeads follow the stream lines as verified with 1 μm fluorescent nonmagnetic carboxylate microbeads. When a magnetic field is applied, the magnetic particles are affected by the gradient generated by the i-PDMS structures; hence allowing the observation of capture or strong deviation of the beads according to their initial position Y_0 in the channel. However, superparamagnetic particles flowing close to channel walls tend to exhibit the same behavior in absence or in presence of magnetic field, hence traducing the fact that magnetic particles are not affected by the magnetic force when flowing far from the i-PDMS microstructure. This suggests that there is a critical distance above which the objects are not sensitive to

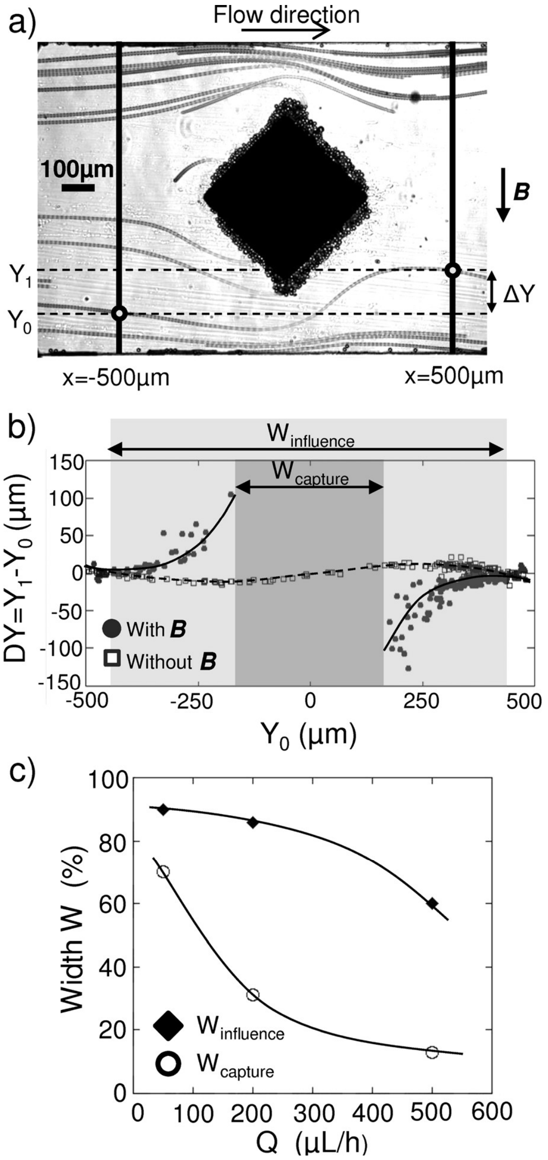

FIG. 7. (a) Z-stack projection of videomicroscopic images representing superparamagnetic particles flowing at the vicinity of an i-PDMS microstructure in presence of an external magnetic field. Y-positions of the beads are measured at two different locations 500 μm, respectively, upstream and downstream of the center of the structure, allowing calculating the deviation of the bead $\Delta Y = Y_1 - Y_0$. (b) Evolution of the deviation ΔY of the beads versus their position upstream of the microstructure, with and without external magnetic field. The beads are flowing at 200 μl/h. The curves are guide for the eyes. We defined $W_{influence}$ (light grey) and $W_{capture}$ (dark grey) as the portion of the channel width where the beads are deviated and captured, respectively. (c) Evolution of $W_{influence}$ and $W_{capture}$ as a function of the flow rate Q. The curves are guides for the eyes.

the ability of the composite posts to concentrate magnetic streamlines. Below this critical distance, the behavior of particles starts to differ when in presence or in absence of the permanent magnets. These results are consistent with the results obtained via numerical simulations (see Figure 5(b)) showing that for a diamond-like i-PDMS microstructure, $|(\boldsymbol{B} \cdot \nabla)\boldsymbol{B}|$ decreases roughly from a factor 7 (1300 to 175 $T^2\ m^{-1}$), respectively, 10 and 50 μm away from the post. Indeed, for Y_0 ranging from -325 to 325 μm, the superparamagnetic beads tend to get deviated towards the microstructure in presence of an external magnetic field. This zone where beads are affected by the gradients of magnetic field generated by the i-PDMS post is defined as the influence window (with a width $W_{influence}$ expressed as a percentage of the total channel width w). When looking at the behavior of particles flowing at the direct proximity of the structure ($-150\,\mu\text{m} < Y_0 < 150\,\mu\text{m}$), we observed that they get trapped on the i-PDMS posts. This second area is defined as the capture window (with a width $W_{capture}$ expressed as a percentage of the total channel width w) associated with the structure.

In order to evaluate the capture efficiency of the system, one approach would be to count the number of particules captured by the i-PDMS post regarding the total number of particules flown in the device. However, despite the increase of the viscosity of the suspending fluid, the beads tend to sediment in the syringe during the experiment, leading to a non uniform distribution of the particles in the channel width. As the magnetic force undergone by the particles depends on their position regarding the i-PDMS structure, this phenomenon could impact any estimation of the capture efficiency; for example, if the beads tend to enter the channel close to the walls, the capture efficiency would be artificially low. The capture window $W_{capture}$ highlights the proportion of the channel width in which particles are captured on the i-PDMS microstructured. Therefore, assuming a uniform distribution of particles in the channel, the capture efficiency of our microsystem is directly traduced by the value of $W_{capture}$.

By repeating these measurements for different flow rates, we studied the influence of the flow rate on the size of the influence and capture windows; the results are summarized on Figure 7(c). Capture and deviation are favored at low flow rate conditions since the capture and deviation windows represents, respectively, 70% and 90% of the channel width at 50 μl/h. When the flow rate is increased, we observed a reduction of both the capture and influence windows. Indeed, the drag force $\boldsymbol{F}_{drag}$ described by Equation (2) varies linearly with the speed contribution $(\boldsymbol{v_f} - \boldsymbol{v_p})$. As $(\boldsymbol{v_f} - \boldsymbol{v_p})$ rises, the drag force increases hence diminishing the contribution of the magnetic force to the resultant total force exerted on the bead. As a consequence, at high flow rate less beads get trapped on the i-PDMS microstructure; however, they tend to be deviated towards the microstructure and thus towards the center of the channel. Typically, at 500 μl/h, the deviation window tends to completely prevail over the capture one. This focusing phenomenon can be exploited in a multistructure configuration, as demonstrated in Sec. III B 4.

We would like to remind the reader that the results presented here are obtained in unfavorable conditions as the viscosity of the suspending medium has been increased (roughly 10 times higher than water viscosity) in order to attenuate the beads sedimentation in the syringe during the time of the experiment. Therefore, it is difficult to compare our results in terms of capture efficiency to those reported in the literature, as most of the published experiments have been performed in aqueous medium, with a viscosity comparable to that of water. However, we try to estimate the equivalent performances of our system in water-like medium. Considering the same magnetic conditions (meaning $\boldsymbol{F}_{mag}$ constant), we can reduce the viscosity of the surrounding medium by a factor of 10 — to reach that of water — while increasing the flow speed of the same amount without changing the drag force and thus the capture efficiency. As we report here 70% capture efficiency at 50 μl/h and for $\eta = 10 \times \eta_{water}$, we can assume that 70% capture efficiency would be achieved with our setup at 500 μl/h for $\eta = 1$ mPa s; such flow rate are comparable to those reported in the literature.[34,42] In order to increase further the performances of our system, work should be done on the optimization of the size of the i-PDMS microstructures, as well as the arrangement of multiple structures.

4. Influence of multiple structures

Indeed, the addition of several diamond-like i-PDMS microstructures along the channel ($h = 36\,\mu$m) can be used to cumulate the effects of capture and deviation of superparamagnetic species (see Figure 8). A bead, flowing at 50 μl/h along the channel, initially outside of the capture window of the first i-PDMS microstructure (for example, the green solid diamond of Figure 8(a)) is deviated until it is captured on the third structure.

At each composite microstructure, the magnetic force deviates the bead until the cumulated effect results in the bead capture. When measured after one, two, and three i-PDMS

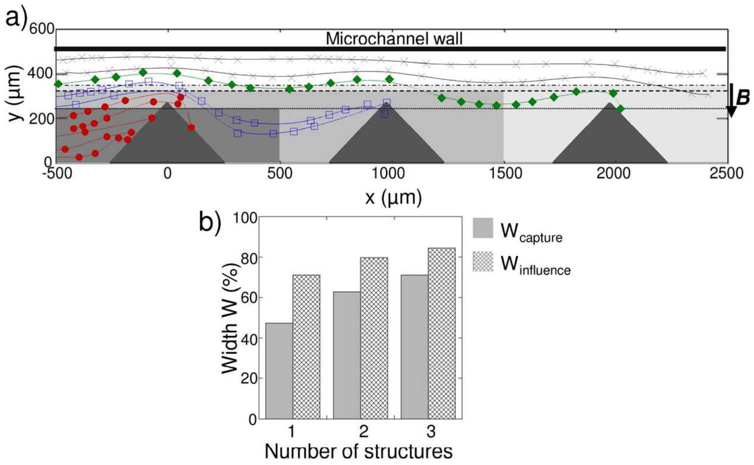

FIG. 8. (a) Trajectories of superparamagnetic microbeads flowing at 50 μl/h along a line of i-PDMS structures implemented in a 36 μm high microfluidic system. (b) Evolution of $W_{capture}$ and $W_{influence}$ as a function of the number of i-PDMS structures considered. Q = 50 μL/h and h = 36 μm.

microstructures, the capture and influence windows are increased. For example, the capture window increases from 47% for the first structure, to 71% after the third structure at 50 μl/h (as reported in Figure 8(b)). The trapping efficiency is thus enhanced with multiple structures at relatively low flow rate. In addition, considering the tendency of the particles to get deviated by one i-PDMS microstructure without being trapped on the post at higher flow rate (i.e., the influence window prevails), using multiple structures at high flow rate would lead to the focalization of beads towards the microsctructures, and therefore towards the center of the channel. Such approach would be suitable for continuous separation of magnetic species in flow.

5. Separation between two populations of beads of different magnetic properties

We also demonstrated the use of this material to perform HGMS of two populations of microparticles differing by their magnetic properties. A mixture of superpara- and fluorescently labeled diamagnetic particles, prepared with respective proportions of (1/4 superpara/dia), is injected in the microsystem at 50 μl/h. As illustrated on Figure 9, we were able to extract the superparamagnetic species using i-PDMS microstructures. As highlighted by the absence of fluorescent signal from the captured objects, the fluorescent diamagnetic particles flow freely past the i-PDMS structure, whereas the superparamagnetic beads are trapped on the composite, hence resulting in their isolation.

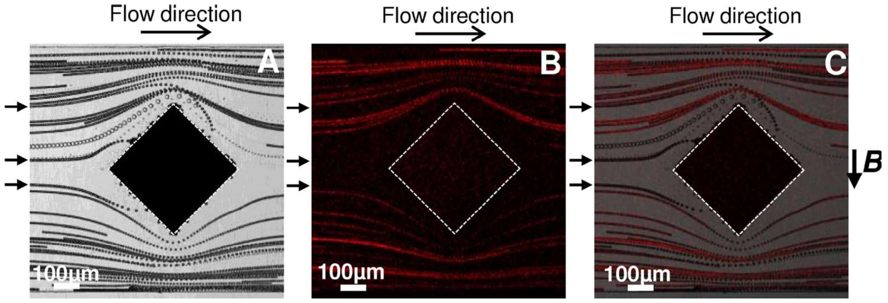

FIG. 9. (a) Bright field and (b) fluorescence z-stack projection of videomicroscopic images representing a mixture of superparamagnetic and fluorescently labeled diamagnetic particles flowing at 50 μl/h in the channel. (c) Overlay of the two previous pictures. Only superparamagnetic beads (black arrows) are captured, as highlighted by the absence of fluorescent signal on the i-PDMS microstructure.

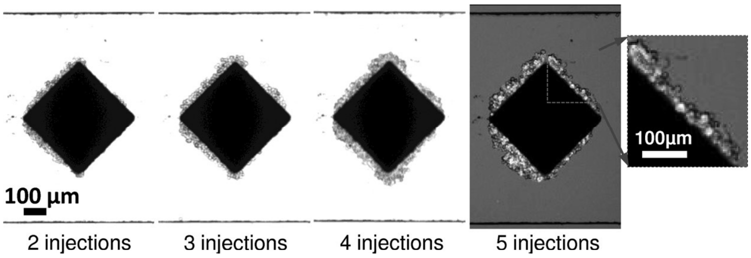

FIG. 10. Bright field images of magnetically labeled cells captured on a i-PDMS microstructure. The last image is an overlay of a bright field and a fluorescent images of the microstructure. The cells accumulate on the composite material, upon cell injections, in presence of the two permanent magnets. Injections induce flow from left to right.

C. Application with biological species

Finally, we demonstrate the potential of i-PDMS to perform magnetophoretic functions in microsystems for biological applications. GFP transfected MDA-MB-231 cells (human breast cancer cells) are magnetically labeled by incubation with maghemite nanoparticles (from PECSA Lab, largely used as magnetic labeling agent[43]) according to the protocol described in Sec. II. Then, the cells suspended in culture medium are injected in the microsystem thanks to a micropipette, in presence of the two permanent magnets, at a concentration of 6.5×10^6 cells/ml. Several injections are performed and pictures of the i-PDMS microstructures are recorded after each injection. As illustrated on Figure 10, cells are captured on the composite material and accumulated according to the different injections.

The typical magnetic susceptibility acquired by the cells upon magnetic labelization has been estimated to $\chi_{cells} = 3.6 \pm 1.6 \times 10^{-3}$, which is equivalent to an average uptake of 2.3 ± 1, 1 pg of iron per cell (protocol detailed in the Appendix). One should notice that the typical magnetic susceptibility of the cells is of the same order of magnitude than the one of the superparamagnetic particles used previously in this study (factor 2.3).

IV. CONCLUSION

In this paper, we have demonstrated that i-PDMS, a carbonyl iron doped PDMS material is suitable for magnetophoretic functions in microsystem such as capture and separation of magnetic species. The composite material combines properties of both compounds and allows easy and fast integration of 3D metalic microstructures using soft lithography approach while preserving O_2 plasma bounding properties of PDMS substrate and avoiding cumbersome alignment procedure. We have reported that an optimum doping ratio of 83% w/w of carbonyl iron in PDMS yields to a composite material with satisfactory relative magnetic susceptibility while keeping its ability to be structured by soft lithography techniques. We have then implemented $500\,\mu$m diamond-like shaped i-PDMS microstructures in a 1 mm wide microfluidic channel according to a configuration which have been optimized by numerical simulations. We have demonstrated the generation of magnetic field gradients, when i-PDMS structures are placed between two permanent magnets. The dynamical study of superparamagnetic particles flowing at the vicinity of such microstructures points out two types of behavior according to their initial position: either beads are captured or they are deviated towards the composite, i.e., the center of the channel. We have shown that by removing the permanent magnets, the magnetic particles can be released in the surrounding medium, hence taking advantage in doping PDMS with soft magnetic microparticles to capture in a reversible way the magnetic species. This can be a critical issue as capture, rinsing, and release steps of species of interest are often required for further analysis or detection. We have also confirmed that flow rate affects the capture efficiency as particles tend to be deviated instead of captured upon increase of the flow rate. Even if at high flow rate or high viscosity, the magnetic trapping is not favored on a single microstructure (the magnetic force cannot overcome the drag force), it is still possible to increase the trapping efficiency by using multiple structures, taking advantage of the magnetic deviation of the particles in the vicinity of each magnetic structures. Moreover, combining multiple structures and high flow rate injection should allow to focus the magnetic species at the center of the microchannel, favouring a continuous separation of the species of interest. Finally, through the separation of particles with different magnetic properties, we have demonstrated that i-PDMS hold promise for new potential applications in HGMS and magnetophoretic functions in microfluidic systems, in particular for biological and medical applications as illustrated here by the capture of magnetically labeled cancer cells. In order to increase further the performances of our system, work should be done on the optimization of the size of the i-PDMS microstructures, as well as the arrangement of multiple structures.

ACKNOWLEDGMENTS

All the experiments presented here have been performed on NanoLyon facilities. This work was supported by CNRS, ANR Oncoscreen, LabEx IMUST, and Région Rhône-Alpes. FST (Faculté des Sciences et des Technologies) and Collegium C2I@Lyon are acknowledged for their contribution to build bio/nano experimental facilities. The authors thank Institut Néel for i-PDMS magnetic characterization and fruitful discussions. They also thank Hichem Mertani (CRCL, UMR INSERM U1052 CNRS UMR5286, France) for providing the GFP breast cancer cells and C. Ménager (Laboratoire PESCA, UMR7195, Université Paris 6, France) for providing the maghemite nanoparticles. R.G. is thankful to DGA and CNRS for a Ph.D. fellowship.

APPENDIX: COMPLEMENTARY INFORMATION

1. Measurement of composite density

The density σ_s of the composite for various doping ratio was measured with a pycnometer, at room temperature and atmospheric pressure, using deionised water ($\sigma = 1$ g/cm^3) as the reference material. For each carbonyl iron concentration, 80 μm thick i-PDMS pieces (3 mm by 3 mm) were prepared and their mass m_s was measured. The composite was then introduced in the pycnometer pre-filled with deionised water, as well as a magnetic stirrer bar which is used to get rid of all the bubbles eventually trapped when introducing the sample in the water. The volume of water is adjusted in order to reach the close-fitting ground glass stopper. The pycnometer is first put on a magnetic stirrer to remove the biggest air bubbles (roughly 1 h), and then put in a sonic bath to remove the finest ones (2 h minimum is required). Finally, the mass m_1 of the gauged pycnometer containing the deionised water, the stirrer bar and the i-PDMS sample, is measured. The same measurement is conducted without the sample and allows estimating m_2, the mass of the pycnometer containing the deionised water and the stirrer bar. The density of the composite is determined by using the following equation:

$$\sigma_s = m_s/(m_1 + m_s - m_2).\sigma. \tag{A1}$$

TABLE I. Table of i-PDMS density according to the carbonyl iron concentration.

Carbonyl iron doping ratio (%)	Density σ_s (g/cm^3)
0	0.965[a]
50	1.64
75	2.43
83	3.65
100	7.86[b]

[a] Value for pure PDMS from the literature (Ref. 44).
[b] Value for pure carbonyl iron microparticles given by manufacturer (see www.sigmaaldrich.com).

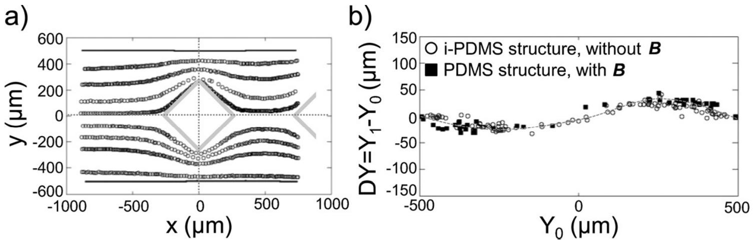

FIG. 11. (a) Trajectories of superparamagnetic microparticles, suspended in 3.6% w/w dextran in PBS, flowing at 50 μl/h, at the vicinity of pure PDMS microstructures, in presence of the permanent magnets. The flow is from left to right. (b) Evolution of the deviation ΔY of the beads versus their position upstream of the microstructure Y_0, for a pure PDMS microstructure with external magnetic field (solid squares) and for a i-PDMS microstructure without the permanent magnets (open circles). The beads are flowing at 50 μl/h. The curve is a guide for the eyes.

One may note that during the preparation of i-PDMS samples, microscopic bubbles may have been trapped in the composite which may lead to a slight underestimation of the materials density. The obtained density values of i-PDMS according to the doping ratio are presented in Table I.

The density measurements are then used to convert the magnetization value $\boldsymbol{M}$ measured on the composites into the appropriate unit (A/m). Then, knowing the applied magnetic field $\boldsymbol{H}$ (in A/m), the magnetic susceptibility χ_m of the material is calculated from Equation (3). Finally, the magnetic relative permittivity μ_r is obtained from Equation (4).

2. Effect of the magnetic field gradient generated by the external magnets

We have verified that the presence of the two permanent magnets, located on each side of the microfluidic chamber implementing pure PDMS microstructures, does not induce any perturbations to the superparamagnetic particles behavior. We have recorded the trajectories of the beads flowing at 50 μl/h in a device where all the microstructures are made of pure PDMS, in presence of the permanent magnets. The trajectories are presented in Figure 11(a). These results analysed in regard with Figure 6(c) show no particular behavior of the superparamagnetic particles, i.e. they undergo no attraction towards neither the PDMS microstructures nor towards the channel walls. To confirm these results, we have measured the deviation of the microbeads as they flow close to the PDMS structure, according to the methodology described in Figure 7(a). Briefly, the positions Y_1 and Y_0 of the beads in the channel are measured, respectively, at $x = -500\,\mu$m and $x = +500\,\mu$m — position corresponding to the equidistance between the first and the second microstructure — from the center of the diamond-like shaped structure. The deviation of the microbeads $\Delta Y = Y_1 - Y_0$ is measured as a function of their position Y_0 prior to the post. The deviation of the beads flowing at 50 μl/h in the neighborhood of a pure PMDS microstructure, in presence of the two permanent magnets are reported in Figure 11(b), as well as deviation of superparamagnetic particles flowing around i-PDMS posts, without the permanent magnets. In both cases, the beads follow the same streamlines, as highlighted by the two sets of data which collapse on the same curve. This highlights that any eventual gradient of magnetic field induced by the two permanent magnets is not strong enough to perturb beads trajectories and can therefore be neglected.

3. Quantification of iron uptake within cells for magnetic labeling

Immediately after labeling, a part of the magnetically labeled cells were used to quantify their iron content, using a magnetophoresis method.[43] Briefly, we measure the velocity of labeled cells attracted towards one single Ne/Fe/Br permanent magnet placed 5 mm from a microchannel (width = 1000 μm and height = 100 μm, Figure 12(a)), knowing the magnetic field gradient (considered uniform over the field of view) generated by the magnet. The iron content of each visualized cell is calculated from the balance of magnetic $\boldsymbol{F}_{mag}$ and viscous $\boldsymbol{F}_{drag}$ forces, respectively, defined in Equations (1) and (2).

The magnetic gradient along the y-direction was calibrated with the 12 μm superparamagnetic beads used previously. Beads were dispersed in a mixture of glycerol and water 71/29 w/w

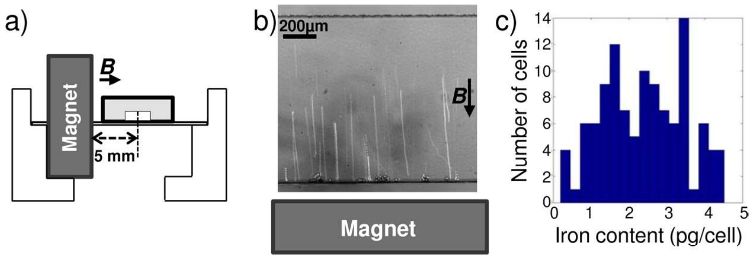

FIG. 12. (a) Schematic representation of the setup. (b) Z-stack projection of videomicroscopic images representing superparamagnetic particles attracted towards the permanant magnet which is located 4.5 mm away from the lower wall. (c) Histogram of the measured iron content per cell.

(viscosity $\eta = 22.5 \times 10^{-3}$ Pa s) and introduced in the microchannel. In absence of flow, their y-velocity was measured as they moved towards the magnet with constant velocity (see Figure 12(b)). The magnetic force $\boldsymbol{F}_{mag}$ was thus precisely counterbalanced by the viscous force: $\boldsymbol{F}_{drag} = \boldsymbol{F}_{mag}$, showing that the magnetic force experienced by each bead was 6.1 ± 2.5 pN. According to Equation (1), this magnetic force was created by the magnetic gradient acting on the superparamagnetic beads. Measuring the drag force and knowing the size and magnetic susceptibility of the superparamagnetic beads, we could thus directly derive the magnetic field gradient along the y-axis in the field of view: $|(\boldsymbol{B}\cdot\nabla)\boldsymbol{B}| = 1 \pm 0.4\,\mathrm{T}^2/\mathrm{m}$, which is of the same order of magnitude as the value computed by numerical simulation in the same configuration ($|(\boldsymbol{B}\cdot\nabla)\boldsymbol{B}| = 0.7\,\mathrm{T}^2/\mathrm{m}$).

Knowing $|(\boldsymbol{B}\cdot\nabla)\boldsymbol{B}|$ in the setup, the mean magnetic susceptibility (or equivalent iron content) for each labeled cell can be computed from y-velocity measurements, again from the balanced of magnetic and viscous forces. This measurement was repeated for 107 cells and they were found to be loaded with an iron content of 2.3 ± 1.1 pg/cells (see Figure 12(c)), corresponding to a magnetic susceptibility $\chi_m = 3.6 \pm 1.6 \times 10^{-3}$.

[1] M. Kersaudy-Kerhoas, R. Dhariwal, M. P. Y. Desmulliez, and L. Jouvet, Microfluid. Nanofluid. **8**, 105 (2010).
[2] M. Toner and D. Irimia, Annu. Rev. Biomed. Eng. **7**, 77 (2005).
[3] K.-H. Han and A. B. Frazier, Lab Chip **8**, 1079 (2008).
[4] P. Gascoyne, C. Mahidol, M. Ruchirawat, J. Satayavivad, P. Watcharasit, and F. F. Becker, Lab Chip **2**, 70 (2002).
[5] A. Nilsson, F. Petersson, H. Jönsson, and T. Laurell, Lab Chip **4**, 131 (2004).
[6] F. Petersson, A. Nilsson, H. Jönsson, and T. Laurell, Anal. Chem. **77**, 1216 (2005).
[7] M. Murata, Y. Okamoto, Y.-S. Park, N. Kaji, M. Tokeshi, and Y. Baba, Anal. Bioanal. Chem. **394**, 277 (2009).
[8] M. MacDonald, G. Spalding, and K. Dholakia, Nature **426**, 421 (2003).
[9] S. J. Tan, L. Yobas, Y. G. Lee, C. N. Ong, and T. C. Lim, Biomed. Microdevices **11**, 883 (2009).
[10] V. Vandelinder and A. Groisman, Anal. Chem. **79**, 2023 (2007).
[11] N. Pamme, Lab Chip **6**, 24 (2006).
[12] N. Pamme, J. C. Eijkel, and A. Manz, J. Magn. Magn. Mater. **307**, 237 (2006).
[13] N. Pamme, Curr. Opin. Chem. Biol. **16**, 436 (2012).
[14] K.-H. Han and A. Bruno Frazier, J. Appl. Phys. **96**, 5797 (2004).
[15] K.-H. Han and A. B. Frazier, Lab Chip **6**, 265 (2006).
[16] Y. Jung, Y. Choi, K.-H. Han, and A. B. Frazier, Biomed. Microdevices **12**, 637 (2010).
[17] F. Shen, H. Hwang, Y. K. Hahn, and J.-K. Park, Anal. Chem. **84**, 3075 (2012).
[18] J. A. Oberteuffer, IEEE Trans. Magn. **9**, 303 (1973).
[19] D. Melville, F. Paul, and S. Roath, IEEE Trans. Magn. **11**, 1701 (1975).
[20] C.-H. Wu, Y.-Y. Huang, P. Chen, K. Hoshino, H. Liu, E. P. Frenkel, J. X. J. Zhang, and K. V. Sokolov, ACS Nano **7**, 8816 (2013).
[21] J. Darabi and C. Guo, Biomicrofluidics **7**, 054106 (2013).
[22] J. Chung, D. Issadore, A. Ullal, K. Lee, R. Weissleder, and H. Lee, Biomicrofluidics **7**, 054107 (2013).
[23] M. T. Glynn, D. J. Kinahan, and J. Ducree, Lab Chip **14**, 2844 (2014).
[24] X. Liu, X. Wang, X. Wu, Z. Zhang, and Y. Zhang, Microsyst. Technol. **20**, 1337 (2014).
[25] J. Wang, K. Morabito, J. X. Tang, and A. Tripathi, Biomicrofluidics **7**, 044107 (2013).
[26] B. D. Plouffe, L. H. Lewis, and S. K. Murthy, Biomicrofluidics **5**, 013413 (2011).
[27] C. S. Owen, Biophys. J. **22**, 171 (1978).
[28] M. Abonnenc, A.-L. Gassner, J. Morandini, J. Josserand, and H. H. Girault, Anal. Bioanal. Chem. **395**, 747 (2009).
[29] L. F. Zanini, N. M. Dempsey, D. Givord, G. Reyne, and F. Dumas-Bouchiat, Appl. Phys. Lett. **99**, 232504 (2011).
[30] J. Pivetal, S. Toru, M. Frenea-Robin, N. Haddour, S. Cecillon, N. M. Dempsey, F. Dumas-Bouchiat, and P. Simonet, Sens. Actuators, B **195**, 581 (2014).
[31] F. Paul, D. Melville, and S. Roath, IEEE Trans. Magn. **18**, 792 (1982).

[32] J. Jung and K.-H. Han, Appl. Phys. Lett. **93**, 223902 (2008).
[33] N. Xia, T. P. Hunt, B. T. Mayers, E. Alsberg, G. M. Whitesides, R. M. Westervelt, and D. E. Ingber, Biomed. Microdevices **8**, 299 (2006).
[34] X. Yu, X. Feng, J. Hu, Z.-L. Zhang, and D.-W. Pang, Langmuir **27**, 5147 (2011).
[35] A.-L. Deman, M. Brun, M. Quatresous, J.-F. Chateaux, M. Frenea-Robin, N. Haddour, V. Semet, and R. Ferrigno, J. Micromech. Microeng. **21**, 095013 (2011).
[36] D. Issadore, H. Shao, J. Chung, A. Newton, M. Pittet, R. Weissleder, and H. Lee, Lab Chip **11**, 147 (2011).
[37] J. Li, M. Zhang, L. Wang, W. Li, P. Sheng, and W. Wen, Microfluid. Nanofluid. **10**, 919 (2011).
[38] F. N. Pirmoradi, J. K. Jackson, H. M. Burt, and M. Chiao, Lab Chip **11**, 3072 (2011).
[39] J. J. Nagel, G. Mikhail, H. Noh, and J. Koo, Proc. SPIE **6172**, 1–9 (2006).
[40] S. Jaffer, B. L. Gray, D. G. Sahota, and M. H. Sjoerdsma, Proc. SPIE **6886**, 68860Q (2008).
[41] D. C. Duffy, J. C. McDonald, O. J. Schueller, and G. M. Whitesides, Anal. Chem. **70**, 4974 (1998).
[42] V. I. Furdui and D. J. Harrison, Lab Chip **4**, 614 (2004).
[43] C. Wilhelm, F. Gazeau, and J.-C. Bacri, Eur. Biophys. J. **31**, 118 (2002).
[44] J. E. Mark, *Polymer Data Handbook* (Oxford University Press, New York, USA, 1999), p. 1274.

A.2 Conclusion on the magnetic sorting

The results demonstrate that i-PDMS is a material able to generate sufficiently important gradients of magnetic field in order to allow sorting between para- and diamagnetic species. Even if we did not actually demonstrate this application in our microsystem, regarding the present results and other works reported in literature, we are confident that, providing an optimization of the material or the geometry, it is able to sort between RBCs and WBCs.

These results, obtained during the PhD of Renaud Gelszinnis (2012-2015) have been published [123] in an peer-reviewed international scientific journal. They have also been presented as both a poster and an oral presentation in international conferences (µTAS 2013 and µFlu 2014, respectively), as well as two proceedings associated to these communications [168, 77]. They also permitted the initiation of a collaboration between our team with the Laboratoire des Multimatériaux et Interfaces (LMI) and the ILM resulting in the obtaining of a Carnot project on the development of a magnetic composite material more efficient [33].

Appendix B

Optimization of the OWC geometry

This is a first attempt to automatize the discrimination of RBCs upon their mechanical properties. Indeed, to facilitate the detection automation, we favored an approach based on the cell residence time in the oscillating width section of the channel. Indeed, the passage of cells at specific location, *i.e.* at the entry and at the exit of the zone of interest can be easily detected using photodiodes or electrodes. We have evaluated if the residence time - more precisely the transit velocity - within the oscillating zone of the channel, was sensitive enough to traduce a modification of cell mechanical properties.

B.1 The OWC geometry

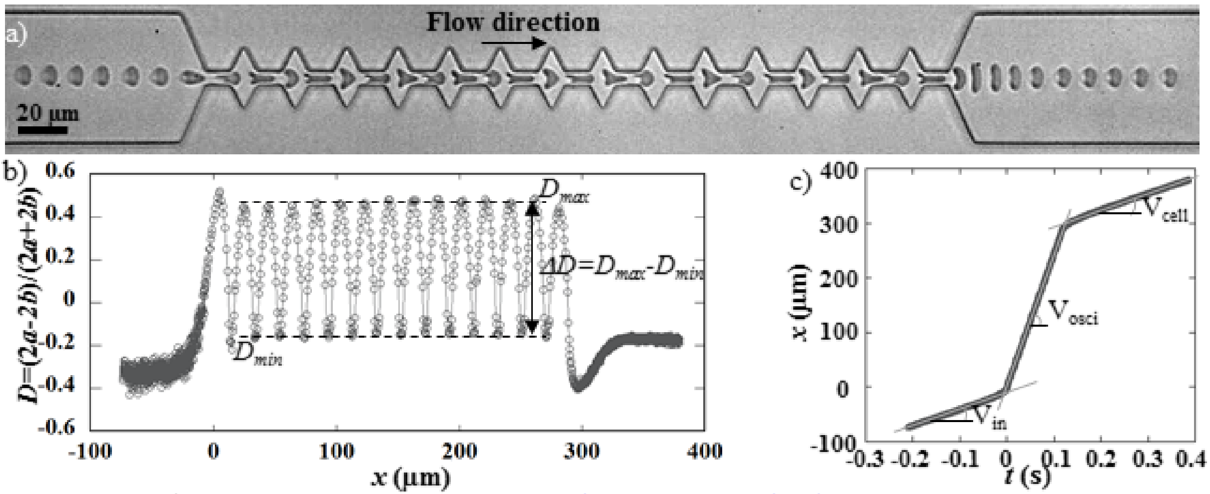

Figure B.1: a) Sequence of deformation of a hRBC flowing in the OWC geometry. b) Deformation index D versus the cell position x in the geometry. The origin of the displacement has been arbitrarily set to be the entry of the first constriction. The mean deformation index of cells being compressed inside a constriction, D_{max}, the mean deformation index of cells being stretched inside a widening, D_{min} and the amplitude of deformation ΔD are defined. c) Position of the cell's center of mass x as a function a time. The origin of the cell's position has been arbitrarily set to be the entry of the entry of the first constriction and the origin of time has been set to correspond with the displacement origin. The slopes of the each part of the curve correspond to the velocity of the cell in the respective zone. The channel height was set to 5 µm and W_o was fixed at 50 µm.

The design and dimensions have already been introduced in Chapter 3 Section 3.2. The sequence of deformation of a hRBC and the associated measurement of D is reminded in Figure B.1. Here, the main channel width W_o was set to 50 µm to minimize cell clogging in the geometry and η_{out} was set to

31.5 mPa.s, so the cells experienced a stretching behavior at the channel exit. Therefore they undergo an elongation at the exit D_{out}, which is extracted as well as the associated shape recovery time τ_r. Mechanically altered RBCs were obtained by incubation of hRBCs at 50 °C for 15 min in a thermal bath, leading to irreversible rigidificaton of RBCs membrane [193, 81]. The flow of both hRBCs and T-rRBCs was studied through the oscillating part of the geometry. Although speed was privileged in order to distinguish mechanically impaired RBCs from healthy ones, some deformation related parameters were also extracted (D_{min}, D_{max} and ΔD, see Figure B.1 for a definition of these parameters) to correlate with dynamical measurements.

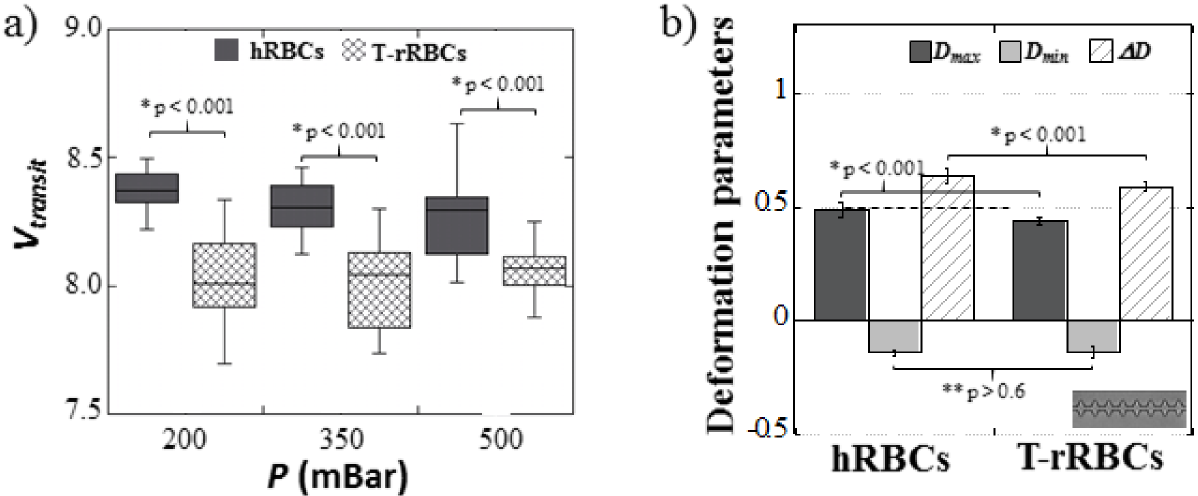

Figure B.2: a) Evolution of $V_{transit} = V_{osci}/V_{cell}$ as a function of the applied pressure P for hRBCs and T-rRBCs flowing in the OWC geometry. Error bars represent standard deviation calculated from 15-20 cells. b) Pooled deformation parameters D_{max}, D_{min} and ΔD for both samples. η_{out} = 31.5 mPa.s and W_o = 50 µm.

As explained previously, in this section we will focus on cell velocities to discriminate cells based on their mechanical properties. The use of such parameter has been considered previously [22, 100, 199] in literature. To overcome any velocity difference due to partial clogging of the channel or other technical issues, we decided to use the normalized transit velocity $V_{transit}$ = V_{osci}/V_{cell}, where V_{osci} and V_{cell} are the cell speed in the oscillating zone of the channel and after exiting the last constriction, respectively. Cell speed at the exit presents less variability than the one at the entry, due to the centering effect of the OWC geometry, it was therefore privileged to normalize the transit velocity. Figure B.2a reports the evolution of $V_{transit}$ as a function of the applied pressure for both samples. We may notice that $V_{transit}$ hardly varies with the applied pressure; it seems to be flow rate independent but rather related to the geometry design and dimensions. hRBCs flow statistically faster than T-rRBCs whatever the applied pressure. $V_{transit}$ can therefore be used to detect alteration of RBC deformability.

Along with the normalized transit velocity, deformation parameters such as D_{max}, D_{min} and ΔD, are measured to try interpret the speed data. Deformation parameters varying hardly upon the applied pressure, the data presented in Figure B.2b are pooled over the different pressure conditions. We can notice from the graph, that the maximal deformation D_{max}, corresponding to the shape of cells being compressed inside a constriction, is statistically larger for hRBCs than for T-rRBCs, as expected. In contrast, both samples experience the same deformation D_{min} in the enlargements, suggesting that W_e and/or L_e are too small to solicit the cell deformability. Consequently, hRBCs have a larger deformation amplitude ΔD than their rigidified counterparts, highlighting the alteration of T-rRBCs deformability. We believe that because T-rRBCs deform less, they resist deformation in the narrowings, hence accumulating delay at each constriction, which would explain their lower transit velocity.

From the previous results, it seems that the geometry permits the distinction between two samples with different mechanical signatures using the transit velocity. However in the optic of improving the difference in transit speed between the two samples, we have investigated the impact of the geometry, the other experimental parameters (η_{out} = 31.5 mPa.s and W_o = 50 µm being maintain identical).

B.2 Impact of geometric parameters

In order to evaluate the effect of each feature of the geometry on the transit velocity of both hRBCs and artificially rRBCs suspensions, we used 5 alternative geometries which are presented in Figure B.3. First, we varied the length of the constrictions by testing an OWC geometry with 30 µm long constrictions, referred to as OWCLC, as well as a unique 290 µm long constriction, referred to as ULC. We also investigated the impact of the enlargement dimensions. To do so, we have flown the RBCs suspensions in an OWC geometry with 30 µm long enlargements, referred to as OWCLE, against 10 µm long enlargements for the classical OWC. Then the width of the constriction was increased to 50 µm to obtain an OWC geometry with wider enlargements, referred to as OWCWE. Finally, an OWC with both wider (50 µm) and longer (30 µm) enlargements, referred to as OWCWLE, was used as a comparison.

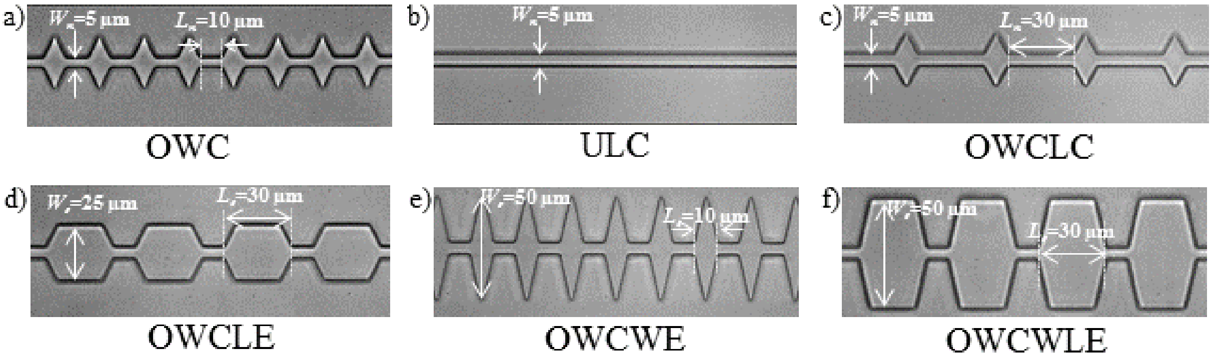

Figure B.3: Microscopic images of the central zone of the different variants of the OWC geometry: a) the reference OWC geometry, b) ULC, c) OWCLC, d) OWCLE, e) OWCWE, and finally f) OWCWLE. The different dimensions of the geometry are reported on the pictures. The channel height was set to 5 µm and W_o was fixed at 50 µm for each channel.

The flow inside the microfluidic channels was simulated using 3D Comsol Multiphysics®, in order to estimate the hydrodynamic resistances R_h for the different geometries investigated. R_h was calculated from the slope representing ΔP as a function Q, where ΔP is the pressure difference between the inlet and outlet and Q is the flow rate obtained from the simulation.

B.2.1 Variation of the constriction dimensions

From the results obtained with the OWC geometry, one explanation to the lower transit speed exhibited by the rigidified sample could be the passage through the constrictions. Therefore, we have first looked at the impact of the length of the narrowing on the flow behavior of both cell types. To illustrate the particularity of this geometry, we report in Figure B.4a the sequence of deformation of a healthy RBCs flowing in OWCLC. The associated deformation as well as that of a T-rRBC is presented as a function of the cell displacement. We can notice from the graph that in the constrictions the deformation reaches a maximum roughly 4 µm after the entry of the restrictions (D = 0.44 and 0.41 for the hRBC and the T-rRBC, respectively), before decreasing slowly until 0.31 or so, 25 µm after the entry. When cells exit the narrowing, the drop in D becomes stiffer to reach a minimum at 2 µm after the entry of the enlargement. This suggests that, as the front of the cells gets accelerated in the constriction, the cells present an important stretching in the flow direction. Once the cells are entirely entered in the narrowings, the back of the cells also accelerates, leading to a slight reduction of the cell deformation now that both ends of the cells have the same speed. Theses observations are in agreement with the dynamics of hRBCs flowing in OWC (B.1b), where the constriction is too small and the cells start to experience the effect of the following enlargement right after reaching the maximum. We then looked at the consequences on the cells transit velocity.

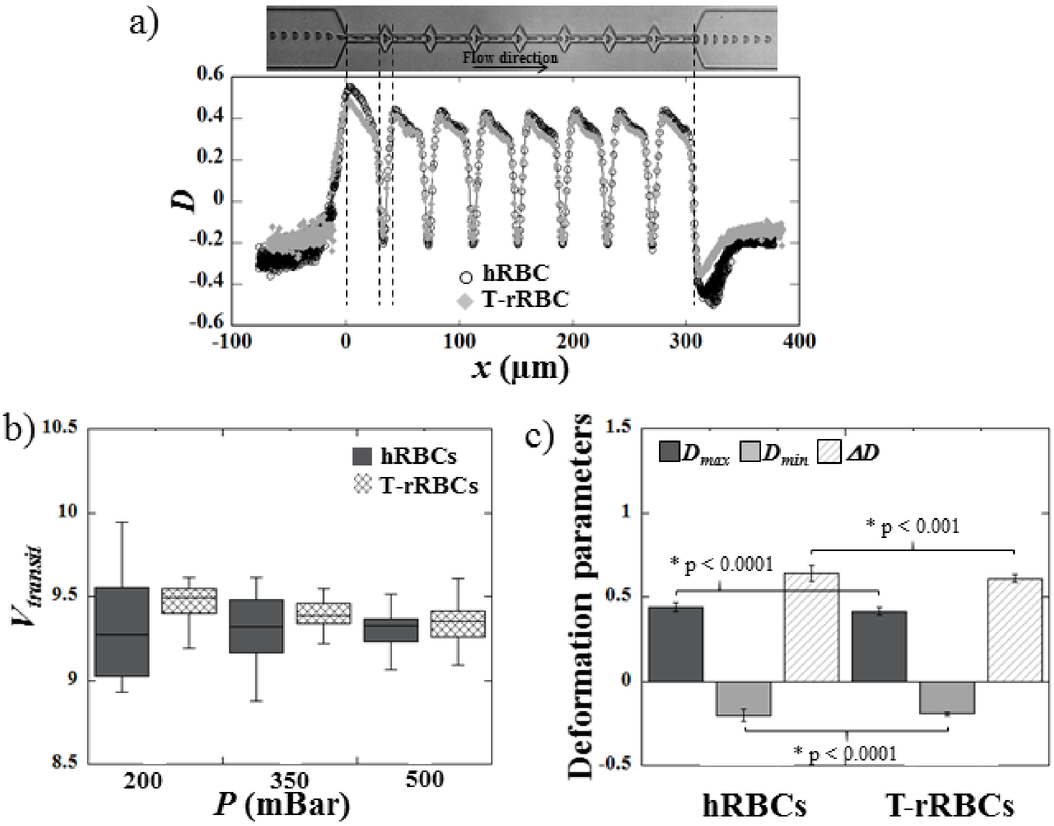

Figure B.4: a) Deformation index versus position of the cell for a hRBC and a T-rRBC flowing in the OWCLC geometry ; the associated sequence of deformation of the healthy cell is presented. The origin of the x-axis was arbitrarily set to be the entry of the first restriction. b) Evolution of the normalized $V_{transit}$ as a function of the applied pressure P for hRBCs and T-rRBCs flowing in the OWCLC geometry. c) Pooled deformation parameters D_{max}, D_{min} and ΔD for both samples.

By increasing the length of the constrictions from 10 µm to 30 µm, we expected to emphasize the difference in transit velocity between the two samples. Surprisingly, Figure B.4b reveals that both samples present the same normalized transit velocity 9.2 - 9.3 (no statistical difference according to the t-test). We can note that hRBCs undergo a normalized $V_{transit}$ higher in OWCLC than in OWC ($V_{transit}$ ~8.5), which can be explained by the difference in hydrodynamic resistances between the two designs, for an equivalent ΔP applied. Regarding the associated deformation parameters reported in Figure B.4c, it appears that in the widenings of the OWCLC geometry, both types of RBCs experience equivalent deformations $D_{min} \sim$ -0.20. In the contrary, in the narrowings, hRBCs are slightly more stretched than T-rRBCs, D_{max} = 0.44 and 0.41, respectively. The difference in D_{max} between both samples is however lower in OWCLC geometry (0.03) than in OWC (0.05). The difference in stretching in the narrowings being light between hRBCs and T-rRBCs, the delay accumulated by the rigid cells would be not enough to induce a statistical difference in transit speed between both cell types.

Results presented in Figure B.4c show that hRBCs and T-rRBCs have the same deformation inside the constrictions D_{max}. Contrarily to the OWC, were both samples showed different values for D_{max}, the length of the constrictions in the OWCLC was sufficient for the cells to adopt the same form in both samples. We can also notice that, cell stretching in the enlargements D_{min} is smaller for the T-rRBC than their healthy counterparts. Although the enlargements were kept at the same dimensions, this difference in D_{min} was not noticed in the OWC. We assume that the increased length of the constrictions causes T-rRBCs to deform less in the widenings. Therefore, it would take less time for T-rRBCs to deform back in the x-direction in order to enter the constriction, leading to a globally faster transit through the OWCLC geometry (Figure B.4b).

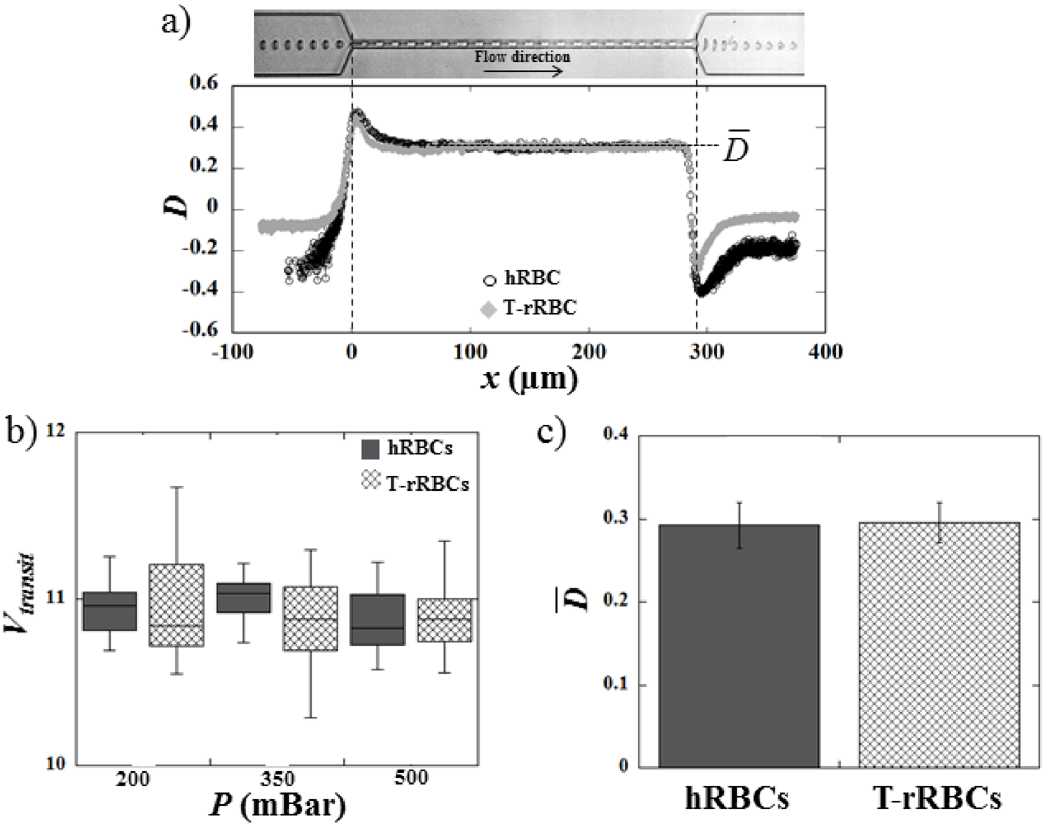

Figure B.5: a) Deformation index versus position of the cell for a hRBC and a T-rRBC flowing in the ULC geometry. The corresponding sequence of deformation of the hRBC is also presented. The origin of the x-axis was arbitrarily set to be the entry of the restriction. b) Evolution of the normalized $V_{transit}$ as a function of the applied pressure P for hRBCs and T-rRBCs flowing in the ULC geometry. c) Pooled stationary deformation inside the restriction $\bar{D}$ for both samples.

To go one step further, we have also studied the behavior of healthy and rigidified RBCs in channels implementing a unique constriction (Figure B.5a). The ULC geometry consists in a 290 µm long constriction - corresponding to the same length as the oscillating zone of the OWC - while the width and depth of the constriction were kept at 5 µm. Figure B.5a shows both the state of deformation of a hRBC and a T-rRBC flowing in the ULC geometry, and the sequence of deformation associated with hRBC in the ULC. The quantification of D confirms the observations made in the OWCLC geometry. Indeed, 4 µm after the entry of the restriction D reaches a maximum around $D \sim 0.48$ for the hRBCs and 0.45 for the T-rRBCs. Then both curves decrease to achieve a plateau value $\bar{D}$ = 0.3, around x = 35-37 µm until they exit the geometric constriction. The constrictions of the OWCLC geometry being only 30 µm long, the cells felt the change in the flow due to the widenings before establishing their stationary shapes.

We present the normalized transit velocity $V_{transit}$ for hRBCs and T-rRBCs and $\bar{D}$ defined as the stationary shape adopted by the cells inside the constriction (see Figure B.5b and c). We can notice in Figure B.5b that $V_{transit}$ does not show any significant difference between the two samples. This can be explained by the fact that both samples experience the same deformation inside the unique constriction

(Figure B.5c). Contrarily to the OWC, the length of the ULC is sufficient to let both samples adopt an identical stationary shape driven by the restriction section, leading to identical transit velocity.

From these results, we can conclude that having longer constrictions is not a suitable solution in order to increase the difference in transit velocity between healthy and thermally rigidified RBCs. Of course reducing the width of the constriction would increase the "friction" of T-rRBCs because of their increased rigidity, and thus improve the discrimination between both samples using the transit velocity. However, it would also increase the probability to clog the channel. Therefore the effect of reduced width of the constriction will not be investigated, as our approach is based on the fact that each cells should be able to flow through the geometry but with a specific signature upon their deformability.

B.2.2 Variation of the enlargement dimensions

Then, we have investigated an OWC geometry with 30 µm long enlargements (OWCLE), with 50 µm wide enlargements (OWCWE) and finally with both wider and longer enlargements (OWCWLE), (50 µm wide and 30 µm long) enlargements.
We have first evaluated the effect of the role of the widening length on the dynamic response of hRBCs in an oscillating width geometry. In Figure B.6a, we show a typical deformation curve for a hRBC and a T-rRBC. We retrieved the oscillations in D which traduce the oscillations in cell shape through the changes in width of the channel. One may notice that D_{min} is smaller in this geometry compared to

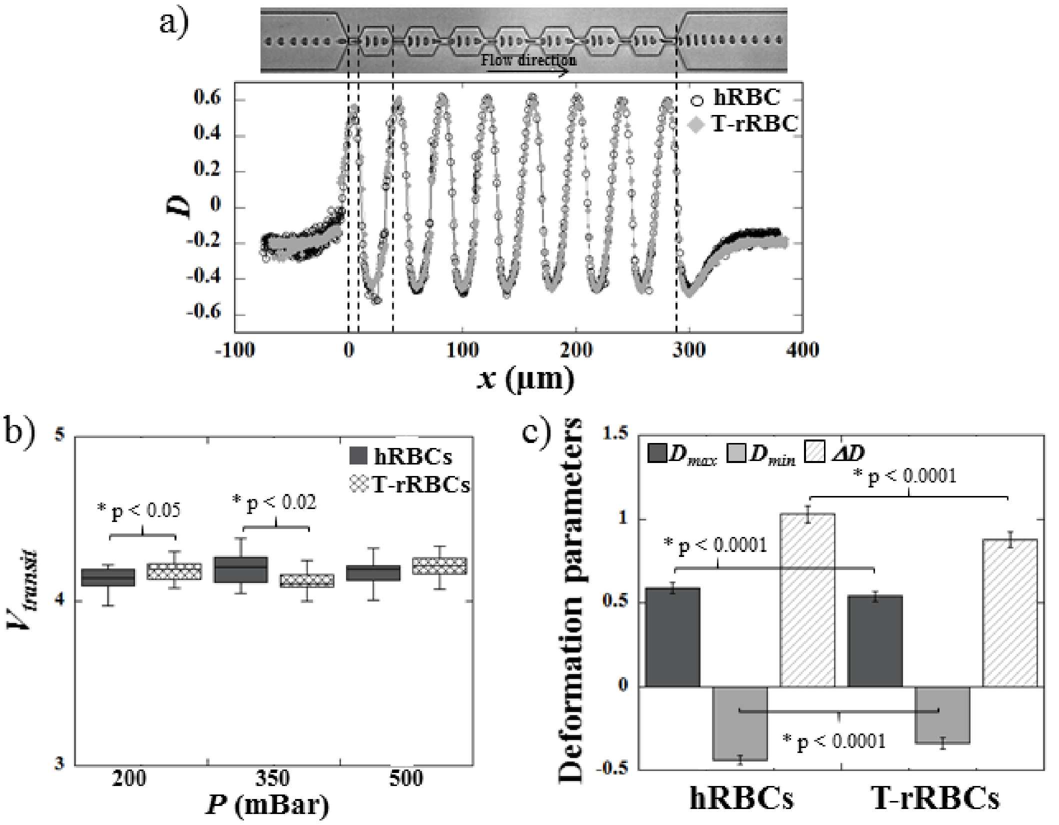

Figure B.6: a) D versus x for a hRBC and a T-rRBC flowing in the OWCLE geometry; with the corresponding hRBC sequence of deformation. b) Evolution of the normalized $V_{transit}$ versus P for hRBCs and T-rRBCs flowing in the OWCLE geometry. c) Pooled deformation parameters D_{max}, D_{min} and ΔD for both samples.

the reference geometry (-0.48 for hRBCs in OWCLE and -0.17 for hRBCs in OWC) hence highlighting a higher deformation in the enlargements in the present chip. We attribute this difference to the fact that in OWC, cells do not have the time to fully stretch in response to the widening, before being sucked again in the next narrowing. In the OWCLE however, they have more time to deform in the y-direction, in response to the extensional flow hence reaching higher D_{min}. In addition the slope of the deformation curve, right after reaching the local minimum, suggests that the cells start the shape recovery process but then are deformed in the other direction, thus accelerating the change in shape. From Figure B.6b we can see that there is almost no statistical difference concerning the normalized velocity $V_{transit}$ of the two samples. We explain this absence in speed difference by the counterbalance of two separated effects. Indeed, T-rRBCs experiencing a smaller stretching in the constriction $(D_{max})_{T-rRBCs} < (D_{max})_{hRBCs}$, they should travel through the geometry at lower speed. On the other hand, they also undergo a smaller stretching than hRBCs in the widenings. Thus, they would take less time to deform back in the x-direction to enter the next constriction, leading to a globally faster transit through the OWCLE geometry. We believe that the two different effects counterbalance each other, leading to an absence of significant difference in cell speed between the two RBCs samples. However, a more thorough study is required in order to prove that hypothesis.

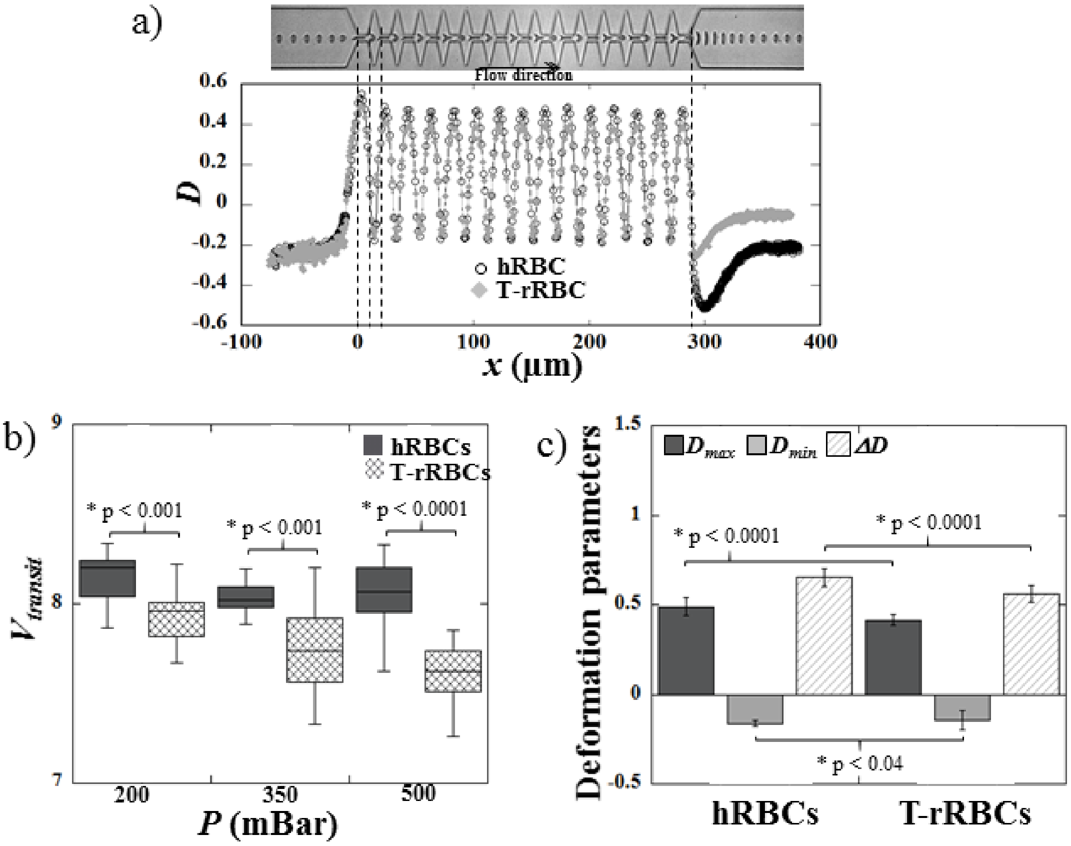

Figure B.7: a) Deformation index versus position of the center of mass of a hRBC and a T-rRBC flowing in the OWCWE geometry and the corresponding sequence of deformation of the hRBC. The origin of the x-axis was arbitrarily set to be the entry of the first restriction. b) Evolution of the normalized $V_{transit}$ as a function of the applied pressure P for hRBCs and T-rRBCs flowing in the OWCWE geometry. c) Pooled deformation parameters D_{max}, D_{min} and ΔD for both samples.

Figure B.7a presents the typical deformation curves for both a hRBCs and a T-rRBCs. The deformation index corresponding to the shape of RBCs inside the constrictions, D_{max} is more or less comparable to that of cells flowing in the OWC geometry, as expected because the neither the width nor the length of the constrictions have been modified. However, we can notice that D_{min} is also comparable between both geometry despite the increase of the widenings width ($D_{min} \sim$ -0.145). Our explanation for this absence of difference is the existence of recirculation at the tip of the enlargements which limit the extensional flow undergone by the RBCs. Therefore, we believe that the "apparent" extensional flow inside the enlargements are not that different inside both geometries. In other words, we believe that in the range of pressure applied during our experiments, the flow lines experienced by cells are similar for both the OWC and OWCLE, because of the recirculations. In the OWCWE geometry, we obtained results quite similar to those in the OWC geometry, *i.e.* D_{min} are equivalent for both RBCs samples, whereas healthy cells are more stretched in the narrowings (D_{max} is higher) than their rigid counterparts (Figure B.7c), leading to a normalized velocity higher for hRBCs than for T-rRBCs (Figure B.7b). Therefore, increasing the width of the enlargements does not seem to have an impact on the relative behavior of both types of RBCs.

Finally, an OWC geometry implementing both wider and longer enlargements has been tested. The deformation curve presented in Figure B.8a is quite similar to that of Figure B.6a. The only difference is that hRBCs are slightly more stretched in the wider and longer widenings in comparison with the ones in the OWCLE geometry ($D_{min} \sim$ -0.48 and -0.4, respectively).

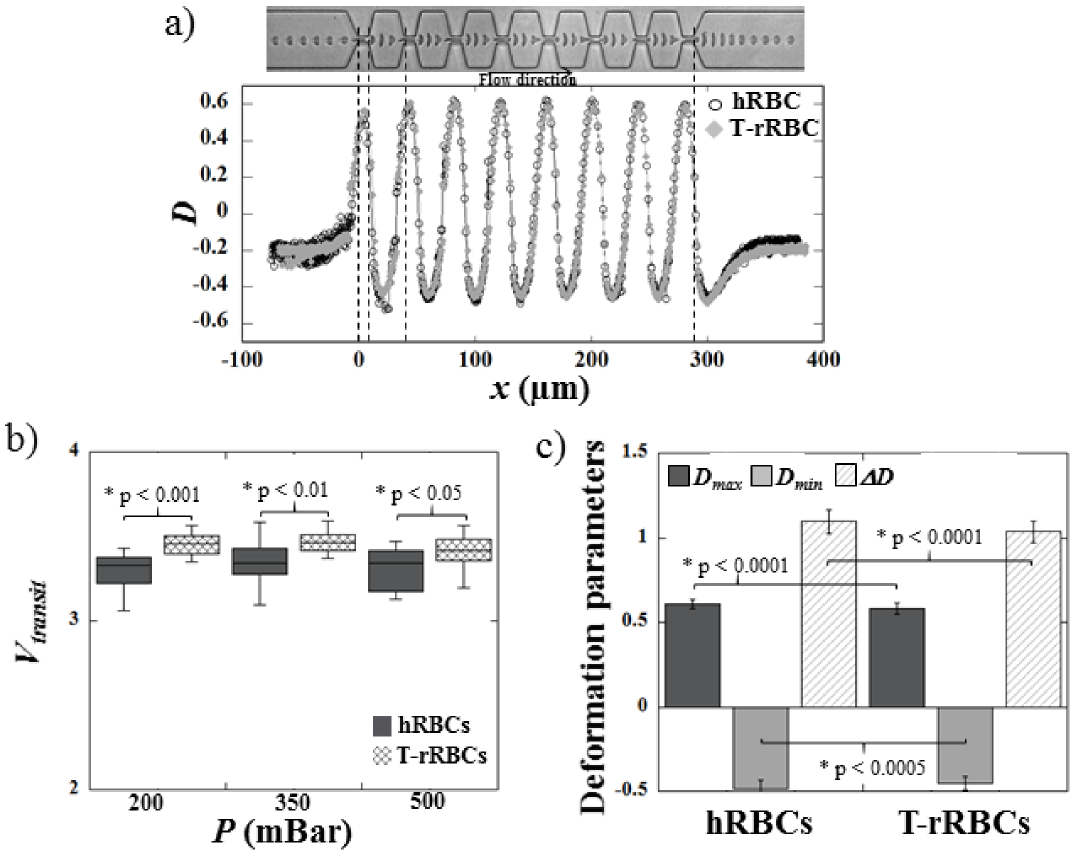

Figure B.8: a) Deformation curves for a hRBC and a T-rRBC flowing in the OWCWLE geometry and the corresponding sequence of deformation of the hRBC. b) $V_{transit}$ versus P for hRBCs and T-rRBCs. c) Pooled deformation parameters D_{max}, D_{min} and ΔD for both samples. η_{out} = 31.5 mPa.s and W_o = 50 µm.

We can observe that T-rRBCs both deform less (Figure B.8b) and flow faster (Figure B.8c) than hRBCs. This difference in velocities is mainly due to the centering effect of this geometry. Indeed, we noticed that, when entering the geometry from a off-centered position, hRBCs tend to follow an oscillatory trajectory in the wider and longer enlargements compared to the T-rRBCs which follow a similar trajectory at first before getting centered earlier as illustrated Figure B.9. Indeed, when "oscillating" hRBCs follow streamlines close to the channel wall, hence increasing the length of the path followed, which is also associated with spending more time in regions of low velocities. This phenomenon seems to be relatively close to that exploited in the PFF introduced by Yamada et al [133]. PFF uses the difference of size between particles pushed against the wall of a microchannel to separate them. Indeed, cells of different sizes will have their centers of mass positioned on different streamlines and thus will have different trajectories. In our case the difference of cell deformation between the hRBCs and the T-rRBCs will produce the same effect. Since T-rRBCs are less deformable, their center of mass will follow a streamline which is further from the wall as illustrated in Figure B.9. In contrast, the more deformable hRBCs will have their center of mass closer to the channel wall and will therefore follow streamlines closer to the wall. Because of the parabolic flow profile, cells flow faster when following streamlines located closer to the center line of the chip. This explains why T-rRBCs are found to flow faster than their healthy counterparts.

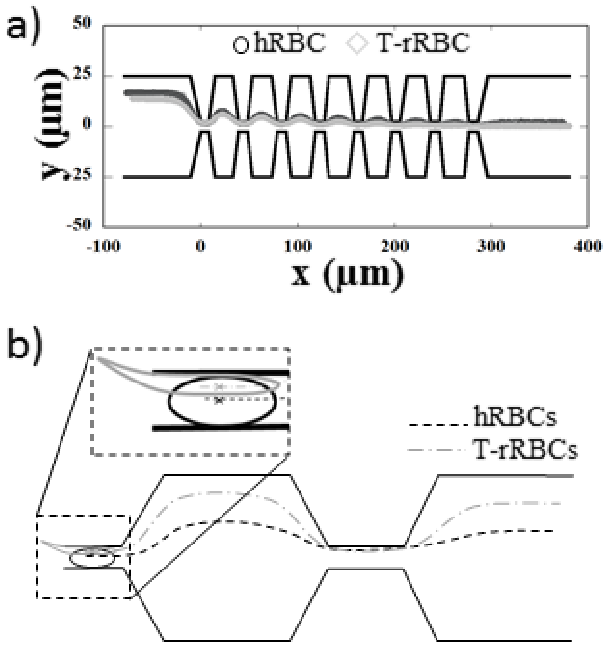

Figure B.9: a) Trajectories of the cell center of mass for a hRBC (open circle) and a T-rRBC (closed diamonds) flowing in the OWCWLE microchannel. The upper and lower walls are also represented. (b) Schematic representation of the streamlines followed by hRBCs and T-rRBCs inside the geometry according to their deformability.

B.3 Balance Sheet and discussion on the best geometry

The different geometries investigated showed different relative transit velocity $V_{transit}$ between the two samples. The results are summed up in Figure B.10a in terms of ratio between the transit velocity of the thermally rigidified sample to that of the healthy one. On the Figure, values lower than 1 are associated with geometries where hRBCs flow faster than T-rRBCs. Indeed, in OWC and OWCWE T-rRBCs deform less in the narrowings, hence possibly accumulating delay at each constriction. Values equal to 1 correspond to geometries where no significant difference was obtained between the two samples; for example OWCLC, ULC and OWCLE. Finally, Figure B.10a reports that T-rRBCs flown faster than hRBCs in OWCWLE, as highlighted by a ratio higher than 1 for this geometry. As explained earlier, hRBCs tend to follow oscillatory trajectories, closer to the wall of the devices, hence spending more time in the geometry than the T-rRBCs.

In order to quantify the efficiency of the geometries and to easily visualize the results, we have calculated $|1-\frac{V_{transit_{T-rRBCs}}}{V_{transit_{hRBCs}}}|$ which corresponds to the difference in % between both samples (see Figure B.10b).

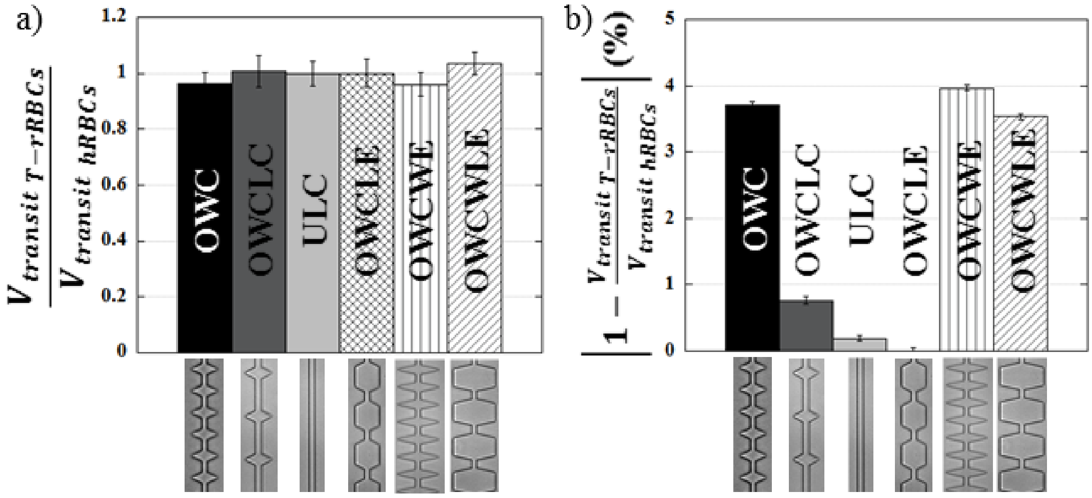

Figure B.10: a) Ratio between the transit velocity of T-rRBCs and hRBCs for the different geometries. b) Normalized difference in transit velocity between the two RBCs samples for the different geometries.

One can notice from the results that the implementation of widenings in a long constriction increases the efficiency of the geometries to discriminate both samples using cells transit speed, as the ULC and OWCLC present differences between both samples lower than 1%. We can also see that OWCLE is the least efficient geometry as it produces the smallest difference in transit speed between healthy and thermally rigidified RBCs (∼ 0%). Finally OWC and OWCWE have almost the same ratio as the wider enlargements did not change dramatically the flow dynamics of RBCs as already stated. Those geometries show a difference in transit velocity of 3.7% and ∼ 4% between the two cell types, respectively for OWC and OWCWE. These two geometries represent the best strategy to discriminate both samples using the cell normalized transit velocity. For the OWCWLE, which presents a difference between T-rRBCs and hRBCs of 3.5%, the ratio length/height of the widenings seem to be the dominant parameter to consider in order to improve even further the OWCWLE. A more thorough study on the enlargements dimensions (width, length, angles . . .) may help optimizing further the OWC efficiency.

One may notice that the measured differences remain lower than 4% for all configurations. However, these differences can still be used to discriminate between the two samples as they are statistically relevant. Moreover, these differences in flowing speed can produce measurable differences in transit time. For instance, the 4% of difference between the normalized transit velocity of both samples in the OWCWE, produce a difference of transit time of the order of ∼ 6.2 ms at 200 mbar. Increasing the geometries length - $i.e.$ the number of repetitions of the constriction associated with a widening - may amplify the measured differences, still, a compromise needs to be found between the channel length and the geometry efficiency. Indeed, an excessively long channel may induce the flow of several cells at the same time in the oscillating part which would impact the hydrodynamic resistance of the geometry and lead to wrong measurements.

Other geometries have been proposed in the literature. For example, Preira et al. used series of interconnected crenelled constrictions with different symmetries to study the deformability of THP-1 cells [159]. In symmetric crenels, after crossing few constrictions, cells reach a stable deformed shape, leading to a faster transit velocity through successive constrictions with a constant orientation. On the other hand, in asymmetric channels cells orientation and the followed streamline are perturbed between two constrictions. Another specific geometry was proposed by Groisman and Quake for the study of a microfluidic rectifier, *i.e.* a channel whose resistance depends on the direction of the flow [8]. Indeed, they used a micro-channel implementing a series of 43 identical diode-like segments and demonstrated that the flow of a non-Newtonian fluid in this geometry is not isotropic even at low Reynolds number. However, to the best of our knowledge, the flow of soft particles in such geometry has not been observed yet. Judging by the results presented here and in Section 3.2, the exploitation of D_{out} and $1/\tau_r$ seems much more promising in terms of discrimination between healthy and mechanically impaired RBCs. Therefore, special efforts have to be focused on the automation of the detection an in particular to the image analysis, in order to reach the throughput compatible with diagnostic applications.

Appendix C

Cells mechanical characterization by AFM

All the experiments have been performed by Marie-Charlotte Audry Deschamp from the DSE team at INL. In this chapter, we will detail briefly the AFM measurements performed on AML cell lines and RBCs.

C.1 Experimental setup

In order to avoid their motion while indenting, cells were adhered on a petri dish treated with poly-L-lysine. Briefly, substrates were submitted to plasma O_2 for 3 min and 100 µL of poly-L-lyisne at 0.001 mg/mL were deposited onto the substrates and left to incubate for 10 min at room temperature. Substrates were then rinsed twice with ultrapure water before being dried. Such poly-L-lysine has been selected in order to find the right compromise between appropriate immobilization of the cells on the substrates and minimal pre-stress exerted onto the cells membrane. Indeed, it has been previously reported that the concentration of poly-L-lysine used to adhere cells onto the substrates impacts the elastic properties of objects under study [170].

200 µL of cell suspension at $3{\times}10^6$ cells/mL were deposited on the coated substrates, left to sediment and adhere for 10 min and 2 hours, in the case of RBCs and AML cells, respectively. Finally, the supernatant was removed and fresh buffer was re-injected onto the sample, to get ride of all the cells which would not be attached to the substrates. Young modulus were measured using a MFP 3d Asylum AFM (Oxford Instruments) in liquid medium. The probe used was a pyrex-nitride probe, implementing a pyramidal tip, with a nominal stiffness of 0.08 N/m. AFM force spectroscopy measurements - force-displacement curves - were performed at room temperature with a probe indentation speed of 200 nm/s.

The associated Young modulus E are extracted by fitting the experimental curves with the Hertz model [87]. For a pyramidal probe, the applied force F is related to the indentation δ by the following equation:

$$F(\delta) = \frac{3tan(\alpha) \times E}{2(1-\nu^2)} \times \delta^2 \tag{C.1}$$

where α is the half-angle at the top of the pyramid (here α = 36°) and ν is the Poisson coefficient, which worth 0.5 for cells.

C.2 AML mechanical characterization by AFM

The two AML cell lines have been mechanically characterized using both the microfluidic pressure drop approach and AFM. The force curves obtained on ML2-S and ML2-R, using AFM, are presented in Figure C.1.

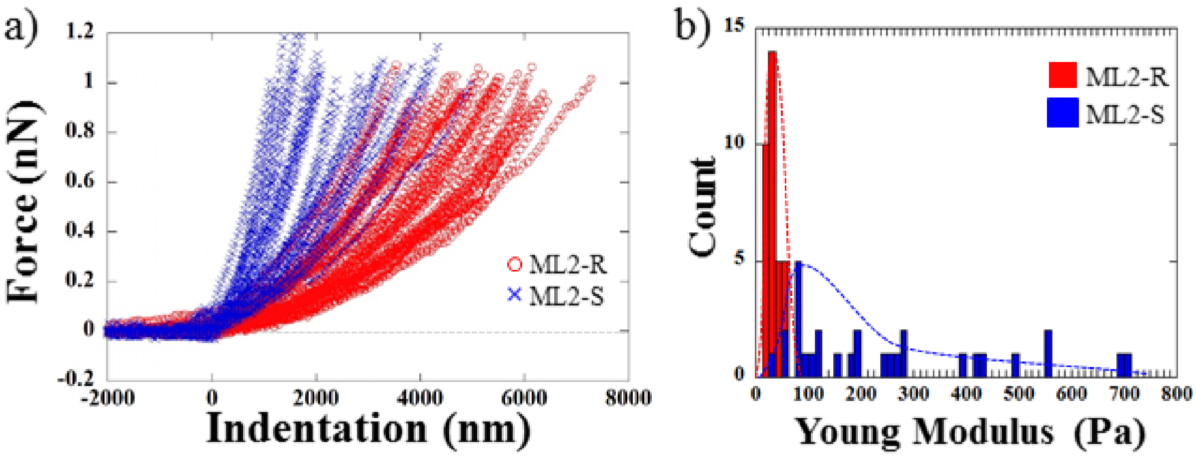

Figure C.1: a) Representation of all the indentation curves measured on the 29 ML2-S (blue crosses) and 38 ML2-R cells (red circles) and b) corresponding histograms. The dashed lines are guide for the eyes.

Figure C.1b presents the distribution of Young's modulus measured by AFM on ML2-S and ML2-R. The Histograms illustrate the normal distribution of ML2-R cells, on the contrary ML2-S present a right skewed distribution. In a symmetrical distribution, such as Gaussian series, the mean, median, and mode are all equal. As a reminder, the mean is the average value of the distribution, the median is its middle value and the mode is the value that occurs most often in the distribution. In a right skewed distribution however, the mode is smaller than the median which is itself smaller than the mean. The different parameters of both distributions can be found in Table C.1.

Table C.1: Parameters of the distributions of ML2-S and ML2-R cells.

Parameter	**ML2-S Young's Modulus**	**ML2-R Young's Modulus**
Mean	251.71 Pa	38.63 Pa
Median	188.78 Pa	30.75 Pa
Mode	∼ 75 Pa	∼ 40 Pa

We can see that in the case of ML2-R, the 3 different parameters - *i.e.* mean, median and mode - are, if not equal, of the same order of magnitude. In the contrary for ML2-S, the three different parameters are very different. One can wonder about the relevance to use the mean of Young modulus as the representative parameter of such distribution. For the sake of simplicity, we will consider that the most appropriate parameter to describe the distribution of Young Modulus of AML cell lines is the mode. Finally, we can notice that the Young modulus of AML cells is of the same order of magnitude than values reported in literature on HL-60, which are model AML cells ($<$ 100 Pa [209] and 200 – 1400 Pa [135]).

C.3 RBCs mechanical characterization by AFM

hRBCs and glutaraldehyde rRBCs have been mechanically characterized using both the optical nanotweezers approach and AFM. The force-displacement curves obtained on hRBCs and rRBCs, using AFM, are presented in Figure C.2. The characterization revealed that the mean young's modulus of healthy and rigidified RBCs have been estimated to 63.4 Pa and 48.4 kPa, respectively. Young modulus of hRBCs have previously been reported in literature to be ranging from ∼ 200 Pa [127] to ∼ 1 kPa [55, 87].
One might want to compare the mechanical signature obtained on both RBCs and AML cells. However, it is difficult to make a direct comparison between results obtained with different geometries, implement-

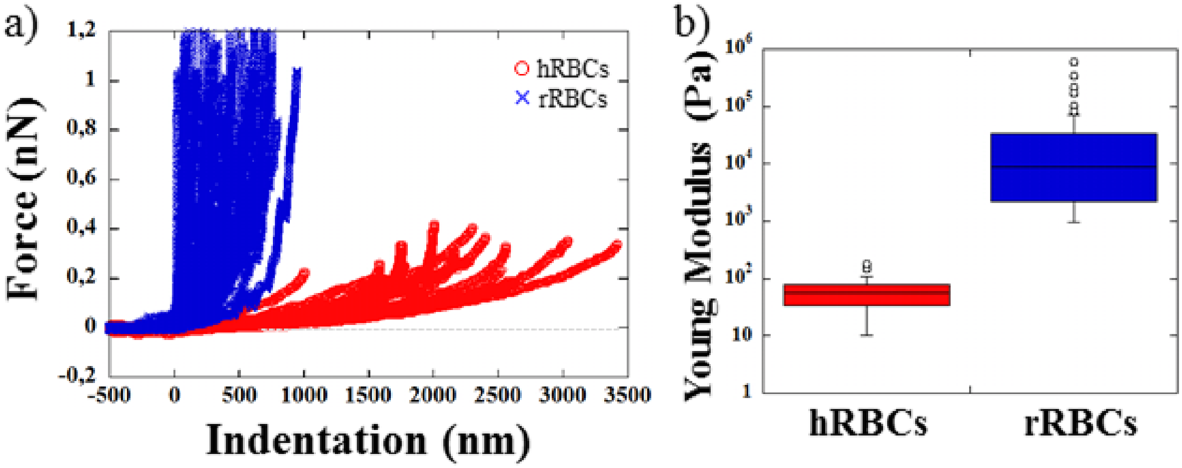

Figure C.2: a) Representation of all the indentation curves measured on the 41 glutaraldehyde rRBCs (blue crosses) and 25 hRBCs (red circles) and b) corresponding Young modulus distributions.

ing different dimensions. Indeed, the pressure drop measurement is not an absolute measurement but highly depends on the device dimensions. Nevertheless, we can try to compare the mean pressure drop associated with the flow of ML2-S and RBCs blocking the constriction in a similar way. In first approximation, we can use the equivalent radius of RBCs - the radius of the sphere with the same volume of a RBC $\sim$ 2.8 µm - to evaluate the occupation rates for RBCs. By using the data from Figure 3.26b and d, as well as Figure 3.32d, we can build the Table C.2. It appears from Table C.2, that for comparable occupation rate, RBCs and ML2-S have pressure drop values of the same order of magnitude, although values associated to ML2-S are slightly lower, which is surprising. Such findings are coherent with our AFM measurements evaluating the Young's modulus of both cell types to be $\sim$ 70 Pa and 63.4 Pa for RBCs and ML2-S, respectively (see Appendix C).

Table C.2: Comparison of pressure drop measurements of RBCs and ML2-S AML cells.

$2a_0/W_c$	$\overline{\Delta P_{max}}$ **for hRBCs**	$\overline{\Delta P_{max}}$ **for ML2-S**
[0.5, 1]	[-0.36, -2.1]	-0.28
[1, 1.5]	[-1.00, -1.84]	-0.76
[1.5, 2]	[-2, -5.5]	-1.96
[2, 2.5]	/	-2.24
[2.5, 3]	/	-4.80

Bibliography

[1] Adamo A., Sharei A., Adamo L., Lee B., Moa S., and Jensen K.F.
Microfluidics-based assessment of cell deformability.
Analytical Chemistry, 84:6438–6443, 2012.
doi: https://doi.org/10.1021/ac300264v.

[2] Amirouche A., Esteves J., Ferrigno R., and Faivre M.
The role of the energy dissipation in the high speed mechanical relaxation of the red blood cells.
In *Proceedings of the 20th International Conference on Miniaturized Systems for Chemistry and Life Sciences*, Dublin, Ireland, 2016.

[3] Amirouche a., Esteves J., Lavoignat A., Picot S., Ferrigno R., and Faivre M.
Dual shape recovery of red blood cells flowing out of a microfluidic constriction.
Biomicrofluidics, 14(2):024116, 2020.
doi: https://doi.org/10.1063/5.0005198.

[4] Ashkin A.
Acceleration and trapping of particles by radiation pressure.
Physical Review Letters, 24(4):156—-159, 1970.
doi: https://doi.org/10.1103/PhysRevLett.24.156.

[5] Ashkin A. and Dziedzic M.
Optical trapping and manipulation of viruses and bacteria.
Science, 235(4795):1517—-1520, 1987.
doi: https://doi.org/10.1126/science.3547653.

[6] Ashkin A., Dziedzic J.M., Bjorkholm J.E., and Chu S.
Observation of a single-beam gradient force optical trap for dielectric particles.
Optics Letters, 11(5):288–290, 1986.
doi: https://doi.org/10.1364/OL.11.000288.

[7] Confavreux A.
Optimization des conditions de migration et de détachement de lignées cancéreuses du cancer du sein en vue de leur tri fonctionnel.
PhD thesis, Université Claude Bernard Lyon 1, 2014.

[8] Groisman A. and Quake S.R.
A microfluidic rectifier: Anisotropic flow resistance at low reynolds numbers.
Physical Review Letters, 92(5):094501, 2004.
doi: https://doi.org/10.1103/PhysRevLett.92.094501.

[9] Lejeune A.
La déformabilité de la cellule cible: un facteur déterminant du mode de phagocytose d'Entamoeba histolytica , souche Laredo.
PhD thesis, Université du Québec à Trois-Rivières, 1991.

[10] Nicolini A., Carpi A., and Tarro G.
Biomolecular markers of breast cancer.
Frontiers in Bioscience, 11(3):1818–1843, 2006.
doi: https://doi.org/10.2741/1926.

[11] Pathak A. and Kumar S.
Independent regulation of tumor cell migration by matrix stiffness and confinement.
Proceedings of the National Academy of Sciences of the United State of America, 109(26):10334–10339, 2012.
doi: https://doi.org/10.1073/pnas.1118073109.

[12] Puliafito A., Ricciardi S., Pirani F., Čermochová V., Boarino L., De Leo N., Primo L., and Descrovi E.
Driving cells with light-controlled topographies.
Advanced Science, 6(14):1801826, 2019.
doi: https://doi.org/10.1002/advs.201801826.

[13] Doyle A.D., Wang F.W., Matsumoto K., and Yamada K.M.
One-dimensional topography underlies three-dimensional fibrillar cell migration.
Journal of Cell Biology, 184(4):481–490, 2009.
doi: https://doi.org/10.1083/jcb.200810041.

[14] Chambers A.F., Groom A.C., and MacDonald I.C.
Dissemination and growth of cancer cells in metastatic sites.
Nature Reviews Cancer, 2(8):563—-572, 2002.
doi: https://doi.org/10.1016/j.tcb.2008.08.007.

[15] Teixeira A.I., Abrams G.A., Bertics P.J., Murphy C.J., and Nealey P.F.
Epithelial contact guidance on well-defined micro- and nanostructured substrates.
Journal of Cell Science, 116(Pt 10):1881–1892, 2003.
doi: https://doi.org/10.1242/jcs.00383.

[16] Yip A.K., Chiam K.H., and Matsudaira P.
Traction stress analysis and modeling reveal that amoeboid migration in confined spaces is accompanied by expansive forces and requires the structural integrity of the membrane-cortex interactions.
Integrative Biology, 7(10):1196–1211, 2015.
doi: https://doi.org/10.1039/C4IB00245H.

[17] Ross A.M., Jiang Z.X., Bastmeyer M., and Lahann J.
Physical aspects of cell culture substrates: Topography, roughness, and elasticity.
Small, 8(3):336—355, 2012.
doi: https://doi.org/10.1002/smll.201100934.

[18] Mello A.P., Volkov Y., Kelleher D., and Prendergast P.J.
Comparative locomotory behavior of t lymphocytes versus t lymphoma cells on flat and grooved surfaces.
Annals of Biomedical Engineering, 31:1106—-1113, 2003.
doi: https://doi.org/10.1114/1.1603261.

[19] Curtis A.S.G., Casey B., Gallagher J.O., Pasqui D., Wood M.A., and Wilkinson C.D.W.
Substratum nanotopography and the adhesion of biological cells. are symmetry or regularity of nanotopography important?
Biophysical Chemistry, 94(3):275—-283, 2001.
doi: https://doi.org/10.1016/S0301-4622(01)00247-2.

[20] Alberts B., Johnson A., Lewis J., Raff M., Roberts K., and Walter P.
Molecular Biology of the Cell, 5rd edn.
Garland Science, New York, 2008.
doi: https://doi.org/10.1002/bmb.20192.

[21] Barazani B., Warnat S., Fine A., and Hubbard T.
Mems squeezer for the measurement of single cell rupture force, stiffness change, and hysteresis.
Journal of Micromechanics and Microengineering, 27:025002, 2017.
doi: https://doi.org/10.1088/1361-6439/27/2/025002.

[22] Hansen B., Pivkin I.V., Diez-Silva M., Goldfless S.J., Dao M., Niles J.C., Suresh S., and Han J.
A microfabricated deformability-based flow cytometer with application to malaria.
Lab on a Chip, 11(6):1065–1073, 2011.
doi: https://doi.org/10.1039/c0lc00472c.

[23] Cooke B.M., Mohandas N., and Coppel R.L.
The malaria-infected red blood cell: structural and functional changes.
Advances in Parasitology, 50:1–86, 2001.
doi: https://doi.org/10.1016/s0065-308x(01)50029-9.

[24] Ahluwalia B.S., McCourt P., Huser T., and HellesøO.G.
Optical trapping and propulsion of red blood cells on waveguide surfaces.
Optics Express, 18(20):129596, 2010.
doi: https://doi.org/10.1364/oe.18.021053.

[25] Donato C., Brunetti G., Dell'Olio F., Armenise M.N., Krauss T.F., and Ciminelli C.
Monitoring of individual bacteria using electro-photonic traps.
Biomedical Optics Express, 10(7):3463–3471, 2019.
doi: https://doi.org/10.1364/BOE.10.003463.

[26] Paul C.D., Mistriotis P., and Konstantopoulos K.
Cancer cell motility: lessons from migration in confined spaces.
Nature reviews Cancer, 17(2):131–140, 2017.
doi: https://doi.org/10.1038/nrc.2016.123.

[27] Rolli C.G., Seufferlein T., Kemkemer R., and Spatz J.P.
Impact of tumor cell cytoskeleton organization on invasiveness and migration: A microchannel-based approach.
PloS One, 5:1—8, 2010.
doi: https://doi.org/10.1371/journal.pone.0008726.

[28] Bettinger C.J., Langer R., and Boreinstein J.T.
Engineering substrate topography at the micro- and nanoscale to control cell function.
Angewandte Chemie, 48(30):5406–5415, 2009.
doi: https://doi.org/10.1002/anie.200805179.

[29] Ranucci C.S. and Moghe P.V.
Substrate microtopography can enhance cell adhesive and migratory responsiveness to matrix ligand density.
Journal of Biomedical Materials Research, 54(2):149—161, 2001.
doi: https://doi.org/10.1002/1097-4636(200102)54:2¡149::AID-JBM1¿3.0.CO;2-O.

[30] Fuard D., Tzvetkova-Chevolleau T., Decossas S., Tracqui P., and Schiavone P.
Optimization of poly-di-methyl-siloxane (pdms) substrates for studying cellular adhesion and motility.
Microelectronic Engineering, 85(5-6):1289–1293, 2008.
doi: https://doi.org/10.1016/j.mee.2008.02.004.

[31] Grier D.
A revolution in optical manipulation.
Nature, 424:810—-816, 2003.
doi: https://doi.org/10.1038/nature01935.

[32] Irimia D. and Toner M.
Spontaneous migration of cancer cells under conditions of mechanical confinement.
Integrative Biology, 1(8-9):506—512, 2009.
doi: https://doi.org/10.1039/b908595e.

[33] Le Roy D., Dhungana D., Ourry L., Faivre M., Ferrigno R., Tamion A., Dupuis V., Salles V., and Deman A.L.
Anisotropic ferromagnetic polymer: a first step for their implementation in microfluidic systems.
AIP Advances, 6(5):056604, 2016.
doi: https://doi.org/10.1063/1.4943927.

[34] Melville D., Paul F., and Roath S.
Direct magnetic separation of red cells from whole blood.
Nature, 255:706, 1975.
doi: https://doi.org/10.1038/255706a0.

[35] Wirtz D., Konstantopoulos K., and Searson P.C.
The physics of cancer: the role of physical interactions and mechanical forces in metastasis.
Nature Reviews Cancer, 11(7):512–522, 2011.
doi: https://doi.org/10.1038/nrc3080.

[36] Hayes D.F.
Prognostic and predictive factors revisited.
The Breast, 14(6):493–499, 2005.
doi: https://doi.org/10.1023/a:1014778713034.

[37] Hayes D.F., Isaacs C., and Stearns V.
Prognostic factors in breast cancer: current and new predictors of metastasis.
Journal of Mammary Gland Biology and Neoplasia, 6(4):375–392, 2001.
doi: https://doi.org/10.1023/a:1014778713034.

[38] Kim D.H., Lipke E.A., Kim P. Cheong R., Thompson S., Delannoy M., Suh K.Y., Tung L., and Levchenko A.
Nanoscale cues regulate the structure and function of macroscopic cardiac tissue constructs.
Proceedings of the National Academy of Sciences of the United State of America, 107:565—-570, 2010.
doi: https://doi.org/10.1073/pnas.0906504107.

[39] Kim D.H., Han K., Gupta K., Kwon K.W., Suh K.Y., and Levchenko A.
Mechanosensitivity of fibroblast cell shape and movement to anisotropic substratum topography gradients.
Biomaterials, 30(29):5433–5444, 2015.
doi: https://doi.org/10.1016/j.biomaterials.2009.06.042.

[40] Gosset D.R., Tse H.T.K., Lee A.S., Ying Y., Lindgreen A.G., Yang O.O., Rao J., Clark A.T., and Di Carlo D.
Hydrodynamic stretching of single cells for large population mechanical phenotyping.
Proceedings of the National Academy of Sciences of the United States of America, 109(20):7630–7635, 2012.
doi: https://doi.org/10.1073/pnas.1200107109.

[41] Sherwood D.R.
Cell invasion through basement membranes: an anchor of understanding.
Trends in cell biology, 16(5):250—-256, 2006.
doi: https://doi.org/10.1016/j.tcb.2006.03.004.

[42] Evans E. and Skalak R.
Mechanics and thermodynamics of biomembranes.
CRC Press, Florida, 1980.
ISBN ISBN 9781315895239.

[43] Lamers E., Walboomers X.F., Domanski M., te Riet J., van Delft F.C.M.J.M., Luttge R., Winnubst L.A.J.A., Gardeniers H.J.G.E., and Jansen J.A.
The influence of nanoscale grooved substrates on osteoblast behavior and extracellular matrix deposition.
Biomaterials, 31(12):3307—3316, 2010.
doi: https://doi.org/10.1016/j.biomaterials.2010.01.034.

[44] Evans E.A.
New membrane concept applied to the analysis of fluid shear- and micropipette-deformed red blood cells.
Biophysical Journal, 26(1):101–114, 1973.
doi: https://doi.org/10.1016/S0006-3495(73)86036-9.

[45] Evans E.A. and Fung Y.C.
Improved measurements of the erythrocyte geometry.
Microvascular research, 4(4):335–347, 1972.
doi: https://doi.org/10.1016/0026-2862(72)90069-6.

[46] Paluch E.K., Aspalter I.M., and Sixt M.
Focal adhesion-independent cell migration.
Annual Review of Cell and Developmental Biology, 32:469–490, 2016.
doi: https://doi.org/10.1146/annurev-cellbio-111315-125341.

[47] Yim E.K., Reano R.M., Pang S.W., Yee A.F., Chen C.S., and Leong K.W.
Nanopattern-induced changes in morphology and motility of smooth muscle cells.
Biomaterials, 26(26):5405—-5413, 2005.
doi: https://doi.org/10.1016/j.biomaterials.2005.01.058.

[48] Balzer E.M., Tong Z., Paul C.D., Hung W.C., Stroka K.M., Boggs A.E., Martin S.S., and Konstantopoulos K.
Spontaneous migration of cancer cells under conditions of mechanical confinement.
The FASEB Journal, 26(8-9):4045—-4056, 2012.
doi: https://doi.org/10.1039/b908595e.

[49] Darling E.M.
Force scanning: a rapid, high-resolution approach for spatial mechanical property mapping.
Nanotechnology, 22:175707, 2011.
doi: https://doi.org/10.1088/0957-4484/22/17/175707.

[50] Nuchsongsin F., Chotivanich K., Charunwatthana P., Fausta O.S., Taramelli D., Day N.P., White N.J., and Dondorp A.M.
Effects of malaria heme products on red blood cell deformability.
American Journal of Tropical Medicine and Hygiene, 77(4):617–622, 2007.
doi: https://doi.org/10.4269/ajtmh.2007.77.617.

[51] Quemeneur F., Quillet C., Faivre M., Viallat A., and Pépin-Donat B.
Gel phase vesicles buckle into specific shapes.

Phys. Rev. Lett., 108(10):108303, 2012.
doi: https://doi.org/10.1103/PhysRevLett.108.108303.

[52] Byfield F.J., Reen R.K., Shentu T.P., Levitan I., and Gooch K.J.
Endothelial actin and cell stiffness is modulated by substrate stiffness in 2d and 3d.
Journal of Biomechanics, 42(8):1114–1119, 2009.
doi: https://doi.org/10.1016/j.jbiomech.2009.02.012.

[53] Fazal F.M. and Block S.M.
Optical tweezers study life under tension, nature photonics.
Nature Photonics, 5:318—-321, 2011.
doi: https://doi.org/10.1038/nphoton.2011.100.

[54] Lim F.Y., Koon Y.L., and Chiam K.H.
A computational model of amoeboid cell migration.
Computer Methods in Biomechanics and Biomedical Engineering., 16(10):1085–1095, 2013.
doi: https://doi.org/10.1080/10255842.2012.757598.

[55] Ciasca G., Papi M., Di Claudio S., Chiarpotto M., Palmieri V., Maulucci G., Nocca G., Rossi C., and De Spirito M.
Mapping viscoelastic properties of healthyand pathological red blood cells at the nanoscale level.
Nanoscale, 7:17030, 2015.
doi: https://doi.org/10.1039/c5nr03145a.

[56] Du G., Ravetto A., Fang Q., and den Toonder J.M.J.
Cell types can be distinguished by measuring their viscoelastic recovery time using a microfluidic device.
Biomedical Microdevices, 13(1):29–40, 2010.
doi: https://doi.org/10.1007/s10544-010-9468-4.

[57] Faure-André G., Vargas P., Yuseff M.I., Heuzé M., Diaz J., Lankar D., Steri V., Manry J., Hugues S., Vascotto F., Boulanger J., Raposo G., Bono M.R., Rosemblatt M., Piel M., and Lennon-Duménil A.M.
Regulation of dendritic cell migration by cd74, the mhc class ii–associated invariant chain.
Science, 322(5908):1705–1710, 2008.
doi: https://doi.org/10.1126/science.1159894.

[58] Prado G., Farutin A., Misbah C., and Bureau L.
Viscoelastic transient of confined red blood cells.
Biophysical Journal, 108(9):2126–2136, 2015.
doi: https://doi.org/10.1016/j.bpj.2015.03.046.

[59] Tomaiuolo G.
Biomechanical properties of red blood cells in health and disease towards microfluidics.
Biomicrofluidics, 8(5):051501, 2014.
doi: https://doi.org/10.1063/1.4895755.

[60] Tomaiuolo G., Barra M., Preziosi V., Cassinese A., Rotoli B., and Guido S.
Microfluidics analysis of red blood cell membrane viscosity.
Lab on a Chip, 11(3):449–454, 2011.
doi: https://doi.org/10.1039/c0lc00348d.

[61] Barabino G.A., Platt M.O., and Kaul D.K.
Sickle cell biomechanics.
Annual Review of Biomedical Engineering, 12:345–367, 2010.
doi: https://doi.org/10.1146/annurev-bioeng-070909-105339.

[62] Bow H., Pivkin I.V., Diez-Silva M., Goldfless S.J., Dao M., Niles J.C., Suresh S., and Han J.
A microfabricated deformability-based flow cytometer with application to malaria.
Lab on a Chip, 11(6):1065–1073, 2011.
doi: https://doi.org/10.1039/c0lc00472c.

[63] Engelhart H. and Sackmann E.
On the measurement of shear elastic moduli and viscosities of erythrocyte plasma membranes by transient deformation in high frequency electric fields.
Biophysical Journal, 54:495–508, 1988.
doi: https://doi.org/10.1016/S0006-3495(88)82982-5.

[64] Ji H., Samper V., Chen Y., Heng C., Lim T., and Yobas L.
Silicon-based microfilters for whole blood cell separation.
Biomedical Microdevices, 16(3):251–257, 2008.
doi: https://doi.org/10.1007/s10544-007-9131-x.

[65] Schmid H., Gosen J.V., Heinich L., Klose H.V., and Volger E.
A counter-rotating “rheoscope chamber” for the study of the microrheology of blood cell aggregation by microscopic observation and microphotometry.
Microvascular Research, 6(3):366—-376, 1973.
doi: https://doi.org/10.1016/0026-2862(73)90086-1.

[66] Stone H.A., Abkarian M., Faivre M., and Smistrup K.
Pressure determination in microfluidic systems, 2007.
https://patents.google.com/patent/US20100064780A1/en.

[67] Prentice-Mott H.V., Chang C.H., Mahadevan L., Mitchison T.J., Irimia D., and Shah J.V.
Biased migration of confined neutrophil-like cells in asymmetric hydraulic environments.
Proceedings of the National Academy of Sciences of the United States of America, 110(52): 21006–21011, 2013.
doi: https://doi.org/10.1073/pnas.1317441110.

[68] Hou H.W., Li Q.S., Lee G.Y.H., Kumar A.P., Ong C.N., and Lim C.T.
Deformability study of breast cancer cells using microfluidics.
Biomedical Microdevices, 11:557–564, 2009.
doi: https://doi.org/10.1007/s10544-008-9262-8.

[69] Doh I, Lee WC, Cho YH, Pisano AP, and Kuypers FA.
Deformation measurement of individual cells in large populations using a single-cell microchamber array chip.
Applied Physics Letters, 100(17):173702, 2012.
doi: https://doi.org/10.1063/1.4704923.

[70] Safeukui I., Buffet P.A., Deplaine G., Perrot S., Brousse V., Ndour A., Nguyen M., Mercereau-Puijalon O., David P.H., Milon G., and Mohandas N.
Quantitative assessment of sensing and sequestration of spherocytic erythrocytes by the human spleen.
Blood, 120(2):424–430, 2012.
doi: https://doi.org/10.1182/blood-2012-01-404103.

[71] Jason I.A. and Putnam A.J.
Extracellular matrix elasticity and topography; material-based cues that affect cell function via conserved mechanisms.
Journal of Biomedical Materials Research Part A, 103(3):1246–1258, 2015.
doi: https://doi.org/10.1002/jbm.a.35254.

[72] Chen J., Zheng Y., Tan Q.Y., Shojaei-Baghini E., Zang Y.L., Li J., Prasad P., You L.D., Wu X.Y., and Sun Y.
Classification of cell types using a microfluidic device for mechanical and electrical measurement on single cells.
Lab on a Chip, 11(18):3174–3181, 2011.
doi: https://doi.org/10.1039/C1LC20473D.

[73] Dai J., Wang Y., Gong J., and Yao Y.
Biointerface anisotropy modulates migration of breast cancer cell.
Colloids and Surfaces B: Biointerfaces, 190:110973, 2020.
doi: https://doi.org/10.1016/j.colsurfb.2020.110973.

[74] Deloach J., Peters S., pinkard O., Glew R., and Ihler G.
Effect of glutaraldehyde treatment on enzyme-loaded erythrocytes.
Biochimica et Biophysica Acta, 496:507–515, 1977.
doi: https://doi.org/10.3109/13813458209103825.

[75] Guck J., Schinkinger S., Lincoln B., Wottawah F., Ebert S., Romeyke M., Lenz D., Erickson H.M., Ananthakrishnan R., Mitchell D., Käs J., Ulvick S., and Bilby C.
Optical deformability as an inherent cell marker for testing malignant transformation and metastatic competence.
Biophysical Journal, 88:3689–3698, 2005.
doi: https://doi.org/10.1529/biophysj.104.045476.

[76] Kim J., Kim H.N., Lim K.T., Kim Y., Pandey S., Garg P., Choung Y.H., Choung P.H., Suh K.Y., and Chung J.H.
Synergistic effects of nanotopography and co-culture with endothelial cells on osteogenesis of mesenchymal stem cells.
Biomaterials, 34(30):7257—-7268, 2013.
doi: https://doi.org/10.1016/j.biomaterials.2013.06.029.

[77] Marchalot J., Gelszinnis R., Deman A.L., Faivre M., Chateaux J.F., Rivière C., Mertani H., and Ferrigno R.
Manipulation of rare cells in microfluidic device using magnetophoresis and dielectrophoresis based on composite-pdms.
In *Proceedings of the 4th European Conference on Microfluidics*, Limerick, Ireland, 2014.

[78] Oberteuffer J.
High gradient magnetic separation.
IEEE Transactions on Magnetics, 9(3):303–306, 1973.
doi: https://doi.org/10.1109/TMAG.1973.1067673.

[79] Park J., Kim D.H., Kim H.N., Wang C.J., Kwak M.K., Hur E., Suh K.Y., An S.S., and Levchenko A.
Directed migration of cancer cells guided by the graded texture of the underlying matrix.
Nature Materials, 15(7):792–801, 2016.
doi: https://doi.org/10.1038/nmat4586.

[80] Park J., Kim D.H., and Levchenko A.
Topotaxis: A new mechanism of directed cell migration in topographic ecm gradients.
Biophysical Journal, 114(6):1257–1263, 2018.
doi: https://doi.org/10.1016/j.bpj.2017.11.3813.

[81] Picot J., Ndour P.A., Lefevre S.D., El Nemer W., Tawfik H., Galimand J., Da Costa L., Ribeil J.A., de Montalembert M., Brousse V., Le Pioufle B., Buffet P., Le Van Kim C., and Français O.
A biomimetic microfluidic chip to study the circulation and mechanical retention of red blood cells in the spleen.
American Journal of Hematology, 90(4):339–345, 2015.
doi: https://doi.org/10.1002/ajh.23941.

[82] Takagi J., Yamada M., Yasuda M., and Seki M.
Continuous particle separation in a microchannel having asymmetrically arranged multiple branches.
Lab on a Chip, 5(7):778–784, 2005.
doi: https://doi.org/10.1039/b501885d.

[83] Tan J. and Saltzman W.M.
Topographical control of human neutrophil motility on micropatterned materials with various surface chemistry.
Biomaterials, 23(15):3215—3225, 2002.
doi: https://doi.org/10.1016/S0142-9612(02)00074-1.

[84] Wang J., Petefish J.W., Hillier A.C., and Schneider J.C.
Epitaxially grown collagen fibrils reveal diversity in contact guidance behavior among cancer cells.
Langmuir, 31(1):307–314, 2015.
doi: https://doi.org/10.1021/la503254x.

[85] Davis J.A., Inglis D.W., Morton K.J., Lawrence D.A., Huang L.R., Chou S.Y., Sturm J.C., and Austin R.H.
Deterministic hydrodynamics: taking blood apart.
Proceedings of the National Academy of Sciences of the United States of America, 103(40): 14779–14784, 2006.
doi: https://doi.org/10.1073/pnas.0605967103.

[86] Martinez Santa Maria J.A., Montalibet A., McAdams E., Faivre M., and Ferrigno R.
Effect of electrode material on the sensitivity of interdigitated electrodes used for electrical cell-substrate impedance sensing technology.
In *IEEE Eng. Med. Biol. Soc.*, Jeju, Korea, 2017.
doi: https://doi.org/10.1109/EMBC.2017.8036948.

[87] Maciaszek J.L. and Lykotrafitis G.
Sickle cell trait human erythrocytes are significantly stiffer than normal.
Journal of Biomechanics, 44:657–661, 2011.
doi: https://doi.org/10.1016/j.jbiomech.2010.11.008.

[88] Garcia-Arcos J.M., Chabrier R., Deygas M., Nader G., Barbier L. ans Sáez P.J., Mathur A., Vargas P., and Piel M.
Reconstitution of cell migration at a glance.
Journal of Cell Science, 132:jcs225565, 2019.
doi: https://doi.org/10.1242/jcs.225565.

[89] Mauritz J.M.A., Tiffert T., Seear R., Lautenschläger F., Esposito A., Lew V.L., Guck J., and Kaminskia C.F.
Detection of plasmodium falciparum-infected red blood cells by optical stretching.
Journal of Biomedical Optics, 15(3):030517, 2010.
doi: https://doi.org/10.1117/1.3458919.

[90] Shelby J.P., White J., Ganesan K., Rathod P.K., and Chiu D.T.
A microfluidic model for single-cell capillary obstruction by plasmodium falciparum infected erythrocytes.
Proceedings of the National Academy of Sciences of the United States of America, 100(25): 14618–14622, 2003.
doi: https://doi.org/10.1073/pnas.2433968100.

[91] Thiery J.P., Acloque H., Huang R.Y.J., and Nieto M.A.
Epithelial-mesenchymal transitions in development and disease.
Cell, 139(5):871–890, 2009.
doi: https://doi.org/10.1016/j.cell.2009.11.007.

[92] Horobin J.T., Sabapathy S., and Simmonds M.J.
Repetitive supra-physiological shear stress impairs red blood cell deformability and induces hemolysis.
Artificial Organs, 41(11):1017–1025, 2017.
doi: https://doi.org/10.1111/aor.12890.

[93] Dohlakia K. and Reece P.
Optical micromanipulation takes hold.
Nano Today, 1:18—-27, 2006.
doi: https://doi.org/10.1016/S1748-0132(06)70019-6.

[94] Okamoto K. and Kawata S.
Radiation force exerted on subwavelength particles near a nanoaperture.
Physical Review Letters, 83(22):4534, 1999.
doi: https://doi.org/10.1103/PhysRevLett.83.4534.

[95] Wilson K., Lewalle A., Fritzsche M., Torogate R., Duke T., and Charras G.
Mechanisms of the leading edge protrusion in interstitial migration.
Nature Communication, 4:2896, 2013.
doi: https://doi.org/10.1038/ncomms3896.

[96] Wolf K., Mazo I., Leung H., Engelke K., Von Andrian U.H., Deryugina E.I., Strongin A.Y., Bröcker E.B., and Friedl P.
Compensation mechanism in tumor cell migration: mesenchymal-amoeboid transition after blocking of pericellular proteolysis.
The Journal of cell biology, 160(7):267—-277, 2003.
doi: https://doi.org/10.1083/jcb.200209006.

[97] Wolf K., te Lindert M., Krause M., Alexander S., te Riet J., Willis A.L., Hoffman R.M., Figdor C.G., Weiss S.J., and Friedl P.
Physical limits of cell migration: control by ecm space and nuclear deformation and tuning by proteolysis and traction force.
Journal of Cell Biology, 201(7):1069–1084, 2013.
doi: https://doi.org/10.1083/jcb.201210152.

[98] Diehl K.A., Foley J.D., Nealey P.F., and Murphy C.J.
Nanoscale topography modulates corneal epithelial cell migration.
Journal of Biomedical Materials Research Part A, 75(A):603—611, 2005.
doi: https://doi.org/10.1002/jbm.a.30467.

[99] Chaw K.C., Manimaran M., Tay F.E.H., and Swaminathan S.
A quantitative observation and imaging of single tumor cell migration and deformation using a multi-gap microfluidic device representing the blood vessel.
Microvascular research, 72(3):153—160, 2006.
doi: https://doi.org/10.1016/j.mvr.2006.06.003.

[100] Nyberg K.D., Scott M.B., Bruce S.L., Gopinath A.B., Bikos D., Mason T.G., Kim J.W., Choig H.S., and Rowat A.C.
The physical origins of transit time measurements for rapid, single cell mechanotyping.
Lab on a Chip, 16(17):3330–3339, 2016.
doi: https://doi.org/10.1039/c6lc00169f.

[101] Han K.H. and Frazier A.B.
Continuous magnetophoretic separation of blood cells in microdevice format.
Journal of Applied Physics, 96(10):5797–5802, 2004.
doi: https://doi.org/10.1063/1.1803628.

[102] Han K.H. and Frazier A.B.
Paramagnetic capture mode magnetophoretic microseparator for high efficiency blood cell separations.
Lab on a Chip, 6:265–273, 2006.
doi: https://doi.org/10.1039/B514539B.

[103] Han K.H. and Frazier A.B.
Lateral driven continuous dielectrophoretic microseparators for blood cells suspended in a highly conductive medium.
Lab on a Chip, 8(7):1079–1086, 2008.
doi: https://doi.org/10.1039/B802321B.

[104] Riching K.M., Cox B.L., Salick M.R., Pehlke C., Riching A.S., Ponik S.M., Bass B.R., Crone W.C., Jiang Y. Weaver A.M., Eliceiri K.W., and Keely P.J.
3d collagen alignment limits protrusions to enhance breast cancer cell persistence.
Biophysical Journal, 107(11):2546–2558, 2014.
doi: https://doi.org/10.1016/j.bpj.2014.10.035.

[105] Stroka K.M., Jiang H., Chen S.H., Tong Z., Wirtz D., Sun S.X., and Konstantopoulos K.
Water permeation drives tumor cell migration in confined microenvironments.
Cell, 157(3):611–23, 2014.
doi: https://doi.org/10.1016/j.cell.2014.02.052.

[106] Stroka K.M., Gu Z., Sun S.X., and Konstantopoulos K.
Bioengineering paradigms for cell migration in confined microenvironments.
Current Opinion in Cell Biology, 30:41–50, 2014.
doi: https://doi.org/10.1016/j.ceb.2014.06.001.

[107] Suh K.Y., Park M.C., and Kim P.
Capillary force lithography: A versatile tool for structured biomaterials interface towards cell and tissue engineering.
Advanced Functional Materials, 19(17):2699—-2712, 2009.
doi: https://doi.org/10.1002/adfm.200900771.

[108] Da Costa L., Galimand J., Fenneteau O., and Mohandas N.
Hereditary spherocytosis, elliptocytosis, and other red cell membrane disorders.
Blood Rev, 27(4):167–178, 2013.
doi: https://doi.org/10.1016/j.blre.2013.04.003.

[109] Dintenfass L.
Internal viscosity of the red cell and a blood viscosity equation.
Nature, 219:956—958, 1968.
doi: https://doi.org/10.1038/219956a0.

[110] Milord L.
Dispositifs innovants pour le piégeage optique : cavité étendue à double période et structure hybride cristal photonique-nanoantennes.
PhD thesis, INSA, 2016.

[111] Novotny L., Brian R.X., and Xie X.S.
Theory of nanometric optical tweezers.
Physical Review Letters, 79(4):645–648, 1997.
doi: https://doi.org/10.1103/PhysRevLett.79.645.

[112] Blanco L.A. and Nieto-Vesperinas M.
Optical forces near subwavelength apertures in metal discs.
Journal of Optics A: Pure and Applied Optics, 9(8):235–238, 2007.
doi: https://doi.org/10.1088/1464-4258/9/8/S17.

[113] Villanueva L.G., de Pastilla A., and Faivre M.
Chapter 4: Mechanics for fluidics and bio-devices.
In Barbillon G., Bosseboeuf A., Chun K., Ferrigno R., and Français O., editors, *Engineering of Micro/Nano Biosystems*, chapter 4, pages 201–213. Springer Nature, Singapore, 2019.
doi: https://doi.org/10.1007/978-981-13-6549-2.

[114] Abkarian M., Faivre M., and Stone H.A.
High-speed microfluidic differential manometer for cellular-scale hydrodynamics.
Proceedings of the National Academy of Sciences of the United States of America, 103(3):538––542, 2006.
doi: https://doi.org/10.1073/pnas.0507171102.

[115] Abkarian M., Faivre M., and Viallat A.
Swinging of red blood cells under shear flow.
Phys. Rev. Lett., 98(18):188302, 2007.
doi: https://doi.org/10.1103/PhysRevLett.98.188302.

[116] Abkarian M., Faivre M., Horton R., Smistrup K., Best-Popescu C.A., and Stone H.A.
Cellular-scale hydrodynamics.
Biomedical Material, 3(3):034011, 2008.
doi: https://doi.org/10.1088/1748-6041/3/3/034011.

[117] Bergert M., Erzberger A., Desai R.A., Aspalter I.M., Oates A.C., Charras G., Salbreux G., and Paluch E.K.
Force transmission during adhesion-independent migration.
Nature Cell Biology, 17(4):524–529, 2015.
doi: https://doi.org/10.1038/ncb3134.

[118] Cubizolles M., Cosnier M.L., Faivre M., and Pouteau P.
Method for assaying plasma enzymes in whole blood, 2011.
https://patents.google.com/patent/US8426156B2/en.

[119] Faivre M.
Drops, vesicles and red blood cells : Deformability and behavior under flow.
PhD thesis, Université Joseph Fourier - Grenoble I, 2006.

[120] Faivre M., Abkarian M., Bickraj K., and Stone H.A.
Geometrical focusing of cells in a microfluidic device: an approach to separate blood plasma.
Federation Proceedings, 43(2):147–159, 2006.

[121] Faivre M., Caillat P., Cubizolles M., Peponnet C., and Vauchier C.
Method and apparatus for counting thrombocytes, 2010.
https://patents.google.com/patent/US8699777B2/en.

[122] Faivre M., Peltié P., Planat-Chrétien A., Cosnier M.L., Cubizolles M., Nogier C., Négrier C., and Pouteau P.
Coagulation dynamics of a blood sample by multiple scattering analysis.
J. Biomed. Opt., 16(5):057001, 2011.
doi: https://doi.org/10.1117/1.3573813.

[123] Faivre M., Gelszinnis R., Degouttes J., Terrier N., Rivière C., Ferrigno R., and Deman A.L.
Magnetophoretic manipulation in microsystem using i-pdms microstructures.
Biomicrofluidics, 8(5):054103, 2014.
doi: https://doi.org/10.1063/1.4894497.

[124] Faivre M., Renoux C., Bessaa A., Da Costa L., Joly P., Gauthier A., and Connes P.
Mechanical signature of red blood cells flowing out of a microfluidic constriction is impacted by membrane elasticity, cell surface-to-volume ratio and diseases.

Frontiers in Physiology, 11:576, 2020.
doi: https://doi.org/10.3389/fphys.2020.00576.

[125] Gnerlich M., Perry S.F., and Tatic-Lucic S.
A submersible piezoresistive mems lateral force sensor for a diagnostic biomechanics platform.
Sensors and Actuators A: Physical, 188:111–119, 2012.
doi: https://doi.org/10.1016/j.sna.2012.05.033.

[126] Lester M. and Nieto-Vesperinas M.
Optical forces on microparticles in an evanescent laser field.
Optics Letters, 24(14):936—-938, 1999.
doi: https://doi.org/10.1364/ol.24.000936.

[127] Li M., LIU L., XI N., WANG Y., DONG Z., XIAO X., and ZHANG W.
Atomic force microscopy imaging and mechanical properties measurement of red blood cells and aggressive cancer cells.
Science China, Life Sciences, 55(11):968–973, 2012.
doi: https://doi.org/10.1007/s11427-012-4399-3.

[128] Mak M. and Erickson D.
A serial micropipette microfluidic device with applications to cancer cell repeated deformation studies.
Integrative Biology, 5:1374–1384, 2013.
doi: https://doi.org/10.1039/c3ib40128f.

[129] Nishino M., Tanaka H., Oqura H., Inoue Y., Koh T., Fujita K., and Sugimoto H.
Serial changes in leukocyte deformability and whole blood rheology in patients with sepsis or trauma.
The Journal of trauma, 59(6):1425–1431, 2010.
doi: https://doi.org/10.1097/01.ta.0000197356.83144.72.

[130] Righini M., Girard C., and Quidant R.
Light-induced manipulation with surface plasmons.
Journal of Optics : A Pure and Applied Optics, 10:093001, 2008.
doi: https://doi.org/10.1088/1464-4258/10/9/093001.

[131] Wang M., Cheng B., Liu H., Huang G., Han L., Li F., and Xu F.
Microchannel stiffness and confinement jointly induce the mesenchymal-amoeboid transition of cancer cell migration.
Nano Letters, 19(9):5949–5958, 2019.
doi: https://doi.org/10.1021/acs.nanolett.9b01597.

[132] Xavier M., Rosendahl P., Herbig M., Kräter M., Spencer D., Bornhäuser M., Oreffo R.O.C., Morgan H., Guck J., and Otto O.
Mechanical phenotyping of primary human skeletal stem cells in heterogeneous populations by real-time deformability cytometry.
Integrative Biology, 8:616–623, 2016.
doi: https://doi.org/10.1039/c5ib00304k.

[133] Yamada M., Nakashima M., and Seki M.
Pinched flow fractionation: continuous size separation of particles utilizing a laminar flow profile in a pinched microchannel.
Analytical Chemistry, 76(18):5465—-5471, 2004.
doi: https://doi.org/10.1021/ac049863r.

[134] Johnson M.D., Torri J.A., Lippman M.E., and Dickson R.B.

Regulation of motility and protease expression in pkc-mediated induction of mcf-7 breast cancer cell invasiveness.
Experimental Cell Research, 247(1):105–113, 1999.
doi: https://doi.org/10.1006/excr.1998.4336.

[135] Rosenbluth M.J., Lam W.A., and Fletcher D.A.
Force microscopy of nonadherent cells: A comparison of leukemia cell deformability.
Biophysical Journal, 90(8):2994–3003, 2006.
doi: https://doi.org/10.1529/biophysj.105.067496.

[136] Simmonds M.J. and Meiselman H.J.
Prediction of the level and duration of shear stress exposure that induces subhemolytic damage to erythrocytes.
Biorheology, 53:237–249, 2016.
doi: https://doi.org/10.3233/BIR-16120.

[137] Driscoll M.K., Sun X., Guven C., Fourkas J.T., and Losert W.
Cellular contcat guidance through dynamic sensing of topography.
ACS Nano, 8(4):3546–3555, 2014.
doi: https://doi.org/10.1021/nn406637c.

[138] Cosnier M.L., Caillat P., Cubizolles M., Faivre M., Peltié P., Peponnet C., Pouteau P., Vauchier C., and Talini L.
Apparatus and disposable device for performing blood tests, 2010.
https://patents.google.com/patent/WO2010128221A1/en.

[139] Gardel M.L., Sabass B., Ji L., Danuser G., Schwartz U.S., and Waterman C.M.
Traction stress in focal adhesions correlates biphasically with actin retrograde flow speed.
Journal of Cell Biology, 183(6):999–1005, 2008.
doi: https://doi.org/10.1083/jcb.200810060.

[140] MacDonald M.P., Spalding G.C., and Dholakia K.
Microfluidic sorting in an optical lattice.
Nature, 426:421–424, 2003.
doi: https://doi.org/10.1038/nature02144.

[141] Clark M.R., Mohandas N., and Shohet S.B.
Osmotic gradient ektacytometry: comprehensive characterization of red cell volume and surface maintenance.
Blood, 61(5):899–910, 1983.
doi: https://doi.org/10.1182/blood.V61.5.899.899.

[142] Doolin M.T. and Stroka K.M.
Integration of mesenchymal stem cells into a novel micropillar confinement assay.
Tissue Engineering Part C: Methods, 25(11):662–676, 2019.
doi: https://doi.org/10.1089/ten.TEC.2019.0083.

[143] Nelson M.T., Short A., Cole S.L., Gross A.C., Winter J., Eubank T.D., and Lannutti J.J.
Preferential, enhanced breast cancer cell migration on electrospun nanofiber 'cell highways'.
BMC Cancer, 14:825, 2014.
doi: https://doi.org/10.1186/1471-2407-14-825.

[144] Conklin M.W., Eickhoff J.C., Riching K.M., Pehlke C.A., Eliceiri K.W., Provenzano P.P., Friedl A., and Keely P.J.
Aligned collagen is a prognostic signature for survival in human breast carcinoma.
American Journal of Pathology, 178(3):1221–1232, 2011.
doi: https://doi.org/10.1016/j.ajpath.2010.11.076.

[145] Balaban N., Schwarz U., Riveline D., Goichberg P., Tzur G., Sabanay I., Mahalu D., Safran S., Bershadsky A., Addadi L., and Geiger B.
Force and focal adhesion assembly: a close relationship studied using elastic micropatterned substrates.
Nature Cell Biology, 3:466–472, 2001.
doi: https://doi.org/10.1038/35074532.

[146] Kramer N., Walzl A., Unger C., Rosner M., Krupitza G., Hengstschläger M., and Dolznig H.
In vitro cell migration and invasion assays.
Mutation research, 752(1):10–24, 2012.
doi: https://doi.org/10.1016/j.mrrev.2012.08.001.

[147] Mohandas N. and Evans E.
Mechanical properties of the red cell membrane in relation to molecular structure and genetic defects.
Annual Review of Biophysics, 23:787—-818, 1994.
doi: https://doi.org/10.1146/annurev.bb.23.060194.004035.

[148] Mohandas N., Clark M.R., Jacobs M.S., and Shohet S.B.
Analysis of factors regulating erythrocyte deformability.
The Journal of clinical investigation, 66(3):563—-573, 1980.
doi: https://doi.org/10.1172/JCI109888.

[149] Nakashima N. and Beutler E.
Erythrocyte cellular and membrane deformability in hereditary spherocytosis.
Blood, 53(4):481–485, 1979.
doi: https://doi.org/10.1182/blood.V53.3.481.481.

[150] Couture O., Faivre M., Pannacci N., Babataheri A., Servois V., Tabeling P., and Tanter M.
Ultrasound internal tattooing.
Med. Phys., 38(2):1116–1123, 2011.
doi: https://doi.org/10.1118/1.3548068.

[151] Otto O., Rosendahl P., Mietke A., Golfier S., Herold C., Klaue D., Girardo S., Pagliara S., Ekpenyong A., Jacobi A., Wobus M., Töpfner N., Keyser U.F., Mansfeld J., Fischer-Friedrich E., and Guck J.
Real-time deformability cytometry: on-the-fly cell mechanical phenotyping.
Nature Methods, 12:2560–2567, 2015.
doi: https://doi.org/10.1038/nmeth.3281.

[152] Baskurt O.K. and Meiselman H.J.
Determination of red blood cell shape recovery time constant in a couette system by the analysis of light reflectance and ektacytometry.
Biorheology, 33:489–503, 1996.
doi: https://doi.org/10.1016/S0006-355X(97)00037-1.

[153] Beech P., Holm S.H., Adolfsson K., and Tegenfeldt J.O.
Sorting cells by size, shape and deformability.
Lab on a Chip, 12:1048–1051, 2012.
doi: https://doi.org/10.1039/C2LC21083E.

[154] Chaumet P., Rahmani A., and Nieto-Vesperinas M.
Optical trapping and manipulating of nano-objects with an apertureless probe.
Physical Review Letters, 88(12):123601, 2002.
doi: https://doi.org/10.1103/PhysRevLett.88.123601.

[155] Friedl P.
Prespecification and plasticity: shifting mechanisms of cell migration.
Current opinion in cell biology, 16(1):14—-23, 2004.
doi: https://doi.org/10.1016/j.ceb.2003.11.001.

[156] Friedl P., Zanker K.S., and Bröcker E.B.
Cell migration strategies in 3-d extracellular matrix: differences in morphology, cell matrix interactions, and integrin function.
Microscopy Research and Technique, 43(5):369–378, 1998.
doi: https://doi.org/10.1002/(SICI)1097-0029(19981201)43:5¡369::AID-JEMT3¿3.0.CO;2-6.

[157] Kang P., Schein P., Serey X., O'Dell D., and Erickson D.
Nanophotonic detection of freely interacting molecules on a single influenza virus.
Scientific Reports, 5:12087, 2015.
doi: https://doi.org/10.1038/srep12087.

[158] Pouteau P., Faivre M., Peltié P., and Planat-Chrétien A.
Method and a device for characterizing the coagulation or sedimentation dynamics of a fluid such as blood or blood plasma, 2010.
https://patents.google.com/patent/US9442125B2/en.

[159] Preira P., Leoni T., Valignat M.P., Lellouch A.M., Robert P., Forel J.M., Papazian L., Dumenil G., Bongrand P., and Théodoly O.
Microfluidic tools to investigate pathologies in the blood microcirculation.
International Journal of Nanotechnology, 9(3-7):529–547, 2012.
doi: https://doi.org/10.1504/ijnt.2012.045340.

[160] Preira P., Grandne V., Forel J.M., Gabriele S., Camara M., and Theodoly O.
Passive circulating cell sorting by deformability using microfluidic gradual filter.
Lab on a Chip, 13(1):161–170, 2013.
doi: https://doi.org/10.1039/c2lc40847c.

[161] Saraogi V.and Padmapriya P., Paul A., Tatu U.S., and Natarajan V.
Change in spectrum of brownian fluctuations of optically trapped red blood cells due to malarial infection.
Journal of Biomedical Optics, 15(3):037003, 2010.
doi: https://doi.org/ 10.1117/1.3427142.

[162] Sharma P., Sheets K., Elankumaran S., and Singh Nain A.
The mechanistic influence of aligned nanofibers on cell shape, migration and blebbing dynamics of glioma cells.
Integrative Biology, 5(8):1007–1088, 2013.
doi: https://doi.org/10.1039/c3ib40073e.

[163] Wallin P., Zandén C., Carlberg B., Hellström Erkenstram N., Liu J., and Gold J.
A method to integrate patterned electrospunfibers with microfluidic systems to generate complex microenvironments for cell culture applications.
Biomicrofluidics, 6(024131), 2012.
doi: https://doi.org/10.1063/1.4729747.

[164] Provenzano P.P., Eliceiri K.W., Campbell J.M., Inman D.R., White J.G., and Keely P.J.
Collagen reorganization at the tumor-stromal interface facilitates local invasion.
BMC Medicine, 4:38, 2006.
doi: https://doi.org/10.1186/1741-7015-4-38.

[165] Guo Q., Reiling S.J., Rohrbach P., and Ma H.S.
Microfluidic biomechanical assay for red blood cells parasited by plasmodium falciparum.

Lab on a Chip, 12(6):1143–1150, 2012.
doi: https://doi.org/10.1039/C2LC20857A.

[166] Shen Q., Hill T., Cai X., Bui L., Barakat R., Hills E., Almugaiteeb T., Babu A., Mckernan P.H., and M. Zalles.
Physical confinement during cancer cell migration triggers therapeutic resistance and cancer stem cell-like behavior.
Cancer Letters, 506:142–151, 2021.
doi: https://doi.org/10.1016/j.canlet.2021.01.020.

[167] Agrawal R., Smart T., Nobre-Cardoso J., Richards C., Bhatnagar R., Tufail A., Shima D., Jones P.H., and Pavesio C.
Assessment of red blood cell deformability in type 2 diabetes mellitus and diabetic retinopathy by dual optical tweezers stretching technique.
Scientifc Reports, 6:15873, 2016.
doi: https://doi.org/10.1038/srep15873.

[168] Gelszinnis R., Faivre M., Degouttes J., Terrier N., Ferrigno R., and Deman A.L.
Magnetophoretic manipulation in microsystem using i-pdms microstructures.
In *Proceedings of the 17th International Conference on Miniaturized Systems for Chemistry and Life Sciences*, pages 146–148, Freiburg, Germany, 2009.

[169] Liu R., Wang X., Chen G.Y., Dalerba P., Gurney A., Hoey T., Sherlock G., Lewicki J., Shedden K., and Clarke M.F.
The prognostic role of a gene signature from tumorigenic breast-cancer cells.
The New England Journal of Medicine, 356(3):217–226, 2007.
doi: https://doi.org/10.1056/NEJMoa063994.

[170] Sorkin R., Bergamaschi G., Kamsma D., Brand G., Dekel E., Ofir-Birin Y., Rudik A., Gironella M., Ritort F., Regev-Rudzki N., Roosb W.H., and Wuite G.J.L.
Probing cellular mechanics with acoustic force spectroscopy.
Molecular Biology of the Cell, 29:2005–2011, 2018.
doi: https://doi.org/10.1091/mbc.E18-03-0154.

[171] Therisod R., Tardif M., Marcoux P.R., Picard E., Jager J.B., Hadji E., Peyrade D., and Houdré R.
Gram-type differentiation of bacteria with 2d hollow photonic crystal cavities.
Applied Physics Letters, 113(11):111101, 2018.
doi: https://doi.org/10.1063/1.5037849.

[172] Gonzàlez-Cruz R.D., Fonseca V.C., and Darling E.M.
Cellular mechanical properties reflect the differentiation potential of adipose-derived mesenchymal stem cells.
Proceedings of the National Academy of Sciences of the United States of America, 109(24): E1523, 2012.
doi: https://doi.org/10.1073/pnas.1120349109.

[173] Waught R.E. and Agre P.
Reductions of erythrocyte membrane viscoelastic coeffients reflect sprectrin deficiencies in hereditary spherocytosis.
Journal of Clinical Investigation, 81:133—-141, 1988.
doi: https://doi.org/10.1146/annurev.bb.23.060194.004035.

[174] Rowe R.G. and Weiss S.J.
Breaching the basement membrane: who, when and how ?
Trends in cell biology, 18(11):560—-574, 2008.
doi: https://doi.org/10.1016/j.tcb.2008.08.007.

[175] Hawkins R.J., Piel M., Faure-André G., Lennon-Dumenil A., Joanny J., Prost J., and Voituriez R.
Pushing off the walls: A mechanism of cell motility in confinement.
Physical Review Letters, 102:058103, 2009.
doi: https://doi.org/10.1103/PhysRevLett.102.058103.

[176] Hawkins R.J., Poincloux R., Benichou O., Piel M., Chavrier P., and Voituriez R.
Spontaneous contractility-mediated cortical flow generates cell migration in three-dimensional environments.
Biophysical Journal, 101(5):1041–1045, 2011.
doi: https://doi.org/10.1016/j.bpj.2011.07.038.

[177] Hochmuth R.M., Worthy P.R., and Evans E.A.
Red cell extensional recovery and the determination of membrane viscosity.
Biophysical Journal, 26(1):101–114, 1979.
doi: https://doi.org/10.1016/S0006-3495(79)85238-8.

[178] Huruta R.R., Barjas-Castro M.J., Saad S.T.O., Costa F.F., Fontes A., Barbosa L.C., and Cesar C.L.
Mechanical properties of stored red blood cells using optical tweezers.
Blood, 92(8):2975—-2977, 1998.
doi: https://doi.org/10.1182/blood.V92.8.2975.

[179] Boyden S.
The chemotactic effect of mixtures of antibody and antigen on polymorphonuclear leucocytes.
The Journal of Experimental Medicine, 115(3):453–466, 1962.
doi: https://doi.org/10.1084/jem.115.3.453.

[180] Chen S., Hourwitz M.J., Campanello L., Fourkas J.T., Losert W., and Parent C.A.
Actin cytoskeleton and focal adhesions regulate the biased migration of breast cancer cells on nanoscale asymmetric sawteeth.
ACS Nano, 13(2):1454—1468, 2019.
doi: https://doi.org/10.1021/acsnano.8b07140.

[181] Hénon S., Lenormand G., Richert A., and Gallet F.
A new determination of the shear modulus of the human erythrocyte membrane using optical tweezers.
Biophysical Journal, 76:1145–1151, 1999.
doi: https://doi.org/10.1016/S0006-3495(99)77279-6.

[182] Huang S., Undisz A., Diez-Silva M., Dao M. Bow H., and Han J.
Dynamic deformability of plasmodium falciparum-infected erythrocytes exposed to artesunate in vitro.
Integrative Biology: Quantitative Biosciences From Nano to Macro, 5(2):414–422, 2013.
doi: https://doi.org/10.1039/c2ib20161e.

[183] Kutner S., Breuer W.V., Ginsburg H., Aley S.B., and Cabantchik Z.I.
Characterization of permeation pathways in the plasma membrane of human erythocytes infected with early stages of plasmodium falciparum: Association with parasite development.
Journal of Cellular Physiology, 125(3):521–527, 1985.
doi: https://doi.org/10.1002/jcp.1041250323.

[184] Lee S., Ahn K.H., Lee S.J., Sun K., Goedhart P.T., and Hardeman M.R.
Shear induced damage of red blood cells monitored by the decrease of their deformability.
Korean-Australian Rheology Journal, 16(3):141–146, 2004.

[185] Lefort S.
Unpublished preliminary results from crcl.
Unpublished results, 2021.

[186] Massaoudi S.
Etude théorique et expérimentale des matériaux à bandes interdites photoniques bidimensionnels en micro-onde : application à l'ultraréfraction.
PhD thesis, Université Paris Sud, 2005.

[187] Suresh S.
Biomechanics and biophysics of cancer cells.
Acta Biomaterialia, 3:413–438, 2007.
doi: https://doi.org/10.1073/pnas.1120349109.

[188] Suresh S., Spatz J., Mills J.P., Micoulet A., Dao M., Lim C.T., Beil M., and Seufferlein T.
Connections between single-cell biomechanics and human disease states: gastrointestinal cancer and malaria.
Acta Biomaterialia, 59(6):1425–1431, 2005.
doi: https://doi.org/10.1016/j.actbio.2004.09.001.

[189] Watari S., Hayashi K., Wood J.A., Russell P., Nealey P.F., Murphy C.J., and Genetos D.C.
Modulation of osteogenic differentiation in hmscs cells by submicron topographically-patterned ridges and grooves.
Biomaterials, 33:128—136, 2012.
doi: https://doi.org/10.1016/j.biomaterials.2011.09.058.

[190] Hur S.C., Henderson-MacLennan N.K., McCabe E.R., and Di Carlo D.
Deformability-based cell classification and enrichment using inertial microfluidics.
Lab on a Chip, 11:912–920, 2011.
doi: https://doi.org/10.1039/C0LC00595A.

[191] Choi S.J., Yoo P.J., Baek S.J., Kim T.W., and Lee H.H.
An ultraviolet-curable mold for sub-100-nm lithography.
Journal of the American Chemical Society, 126(25):7744—-7745, 2004.
doi: https://doi.org/10.1021/ja048972k.

[192] Haghparast S.M.A., Kihara T., and Miyake J.
Distinct mechanical behavior of hek293 cells in adherent and suspended states.
PeerJ, 3:E1131, 2015.
doi: https://doi.org/10.7717/peerj.1131.

[193] Lee S.S., Yim Y., Ahn K.H., and Lee S.J.
Extensional flow-based assessment of red blood cell deformability using hyperbolic converging microchannel.
Biomedical Microdevices, 11:1021–1027, 2009.
doi: https://doi.org/10.1007/s10544-009-9319-3.

[194] Das T., Maiti T.K., and Chakraborty S.
Augmented stress-responsive characteristics of cell lines in narrow confinements.
Integrative Biology, 3(6):684–695, 2011.
doi: https://doi.org/10.1039/c1ib00001b.

[195] Hänscheid T.
Diagnosis of malaria: a review of alternatives to conventional microscopy.
Clinical and Laboratory Haematology, 21(4):235–245, 1999.
doi: https://doi.org/10.1046/j.1365-2257.1999.00220.x.

[196] Herricks T, Antia M, and Rathod PK.
Deformability limits of plasmodium falciparum-infected red blood cells.
Cellular Microbiology, 11(9):1340–1353, 2009.
doi: https://doi.org/10.1111/j.1462-5822.2009.01334.x.

[197] Lämmermann T. and Sixt M.
Mechanical modes of 'amoeboid' cell migration.
Current Opinion in Cell Biology, 21(6):636–644, 2009.
doi: https://doi.org/10.1016/j.ceb.2009.05.003.

[198] Lämmermann T., Bader B.L., Monkley S.J., Worbs T., Wedlich-Söldner R., Hirsch K., Keller M., Förster R., Critchley D.R., Fässler R., and Sixt M.
Rapid leukocyte migration by integrin-independent flowing and squeezing.
Nature, 453(7191):51—-55, 2008.
doi: https://doi.org/10.1038/nature06887.

[199] Fisher T.C., Van der Waart F.J., and Meiselman H.J.
The influence of suspending phase viscosity on the passage of red blood cells through capillary-size micropores.
Biorheology, 33(2):153—-168, 1996.
doi: https://doi.org/10.1016/0006-355X(96)00013-3.

[200] Smart T.J., Richards C.J., Bhatnagar R., Pavesio C., Agrawal R., and Jones P.H.
A study of red blood cell deformability in diabetic retinopathy using optical tweezers.
In *Proc. SPIE 9548, Optical Trapping and Optical Micromanipulation XII*, page 954825, San Diego, California, United States, 2015.
https://doi.org/10.1117/12.2191281.

[201] Fischer T.M., Haest C.W.M., Stöhr M., Kamp D., and Deuticke B.
Selective alteration of erythrocyte deformability by sh-reagents. evidence for an involvement of spectrin in membrane shear elasticity.
Biochimica et Biophysica Acta, 510(2):270–282, 1978.
doi: https://doi.org/10.1016/0005-2736(78)90027-5.

[202] Ruprecht V., Wieser S., Callan-Jones A., Smutny M., Morita H., Sako K., Barone V., Ritsch-Marte M., Sixt M., Voituriez R., and Heisenberg C.P.
Cortical contractility triggers a stochastic switch to fast amoeboid cell motility.
Cell, 160(4):673–685, 2015.
doi: https://doi.org/10.1016/j.cell.2015.01.008.

[203] van der Meer A.D., Poot A.A., Feijen J., and Vermes I.
Analyzing shear stress-induced alignment of actin filaments in endothelial cells with a microfluidic assay.
Biomicrofluidics, 4(1):011103, 2010.
doi: https://doi.org/10.1063/1.3366720.

[204] van Leest T. and Caro J.
Cavity enhanced optical trapping of bacteria using a silicon photonic crystal.
Lab on a chip, 13(22):4358–4365, 2013.
doi: https://doi.org/10.1039/C3LC50879J.

[205] van Zijl F., Krupitza G., and Mikulits W.
Initial steps of metastasis: cell invasion and endothelial transmigration.
Mutation research, 728(1-2):23—34, 2011.
doi: https://doi.org/10.1016/j.mrrev.2011.05.002.

[206] Čižmár T., Garcés-Chávez V., Dholakia K., and Zemánek P.
Optical conveyor belt for delivery of submicron objects.
Applied Physics Letters, 86(17):174101, 2005.
doi: https://doi.org/10.1063/1.1915543.

[207] Čižmár T., Šiler M., Šerý M., Zemánek P., Garcés-Chávez V., and Dholakia K.
Optical sorting of submicrometer objects in a motional standing wave.
Physical Review B, 74(3):035105, 2006.
doi: https://doi.org/10.1103/PhysRevB.74.035105.

[208] Beattie W., Qin X., Wang L., and Ma H.
Clog-free cell filtration using resettable cell traps.
Lab on a Chip, 14(15):2657—-2665, 2014.
doi: https://doi.org/10.1039/C4LC00306C.

[209] Lam W.A., Rosenbluth M.J., and Fletchher D.A.
Chemotherapy exposure increases leukemia cell stiffness.
Neoplasia, 109(8):3505–3508, 2007.
doi: https://doi.org/10.1182/blood-2006-08-043570.

[210] Yu X., Feng X., Hu J., Zhang Z.L., and Pang D.W.
Controlling the magnetic field distribution on the micrometer scale and generation of magnetic bead patterns for microfluidic applications.
Langmuir, 27:5147–5156, 2011.
doi: https://doi.org/10.1021/la104400m.

[211] Huang X.D., Bao L.R., Cheng X., Guo L.J., Pang S.W., and Yee A.F.
Reversal imprinting by transferring polymer from mold to substrate.
Journal of Vacuum Science & Technology B, 20:2872—-2876, 2002.
doi: https://doi.org/10.1116/1.1523404.

[212] Deng Y., Davis S.P., Yang F., Paulsen K.S., Kumar M., DeVaux R.S., Wang X., Conklin D.S., Oberai A., Herschkowitz J.I., and Chung A.J.
Inertial microfluidic cell stretcher (imcs): Fully automated, high-throughput, and near real-time cell mechanotyping.
Small, 13(28):148–149, 2017.
doi: https://doi.org/10.1002/smll.201700705.

[213] Fu Y., Chin L.K., Bourouina T., Liu A.Q., and VanDongen A.M.J.
Nuclear deformation during breast cancer cell transmigration.
Lab on a Chip, 12(19):3774–3778, 2012.
doi: https://doi.org/10.1039/C2LC40477J.

[214] Kim Y., Kim K., and Park Y.
Chapter 10: Measurement techniques for red blood cell deformability: Recent advances.
In Moschandreou TE, editor, *Blood Cell. An overview of studies in hematology*, chapter 10. IntechOpen, 2012.
doi: http://dx.doi.org/10.5772/50698.

[215] Qiang Y., Liu J., Dao M., Suresh S., and Du E.
Mechanical fatigue of human red blood cells.
Proceedings of the National Academy of Sciences of the United States of America, 116(40): 19828–19834, 2019.
doi: https://doi.org/10.1073/pnas.1910336116.

[216] Wang Y., Gong J., and Yao Y.
Extracellular nanofiber-orchestrated cytoskeletal reorganization and mediated directional migration of cancer cells.
Nanoscale, 12(5):2183–3193, 2020.
doi: https://doi.org/10.1039/c9nr10143h.

[217] Zheng Y., Shojaei-Baghini E., Azad A., Wang C., and Sun Y.
High-throughput biophysical measurement of human red blood cells.
Lab on a Chip, 12(14):2560–2567, 2012.
doi: https://doi.org/10.1039/C2LC21210B.

[218] Liu Z., Lee S.J., Park S., Konstantopoulos K., Glunde K., Chen Y., and Barman I.
Cancer cells display increased migration and deformability in pace with metastatic progression.
The FASEB Journal, 34(7):9307–9315, 2020.
doi: https://doi.org/10.1096/fj.202000101RR.

[219] Khan Z.S. and Vanapalli S.A.
Probing the mechanical properties of brain cancer cells using a microfluidic cell squeezer device.
Biomicrofluidics, 7:011806, 2013.
doi: https://doi.org/10.1063/1.4774310.

Mechanical phenotyping of cell in microsystems to detect pathologies

Key Words : Microfluidics ; Mechanical phenotyping ; Red Blood Cells ; Cancerous cells ; Pathologies ; Diagnostic.

Abstract:
One of the primary applications of the mechanical phenotyping is the identification of pathological cells. Indeed various pathologies and modifications of cell states are reported to influence cell mechanical properties. For example, variation of Red Blood Cells deformability is associated with malaria, white blood cells deformability varies in sepsis and acute respiratory distress syndrome, increase deformability of metastatic cancer cells have been observed, finally drop of stiffness during stem cell differentiation have been highlighted. A better understanding of cell deformability and its interactions with physical environment may imply enormous developments in disease diagnostics, therapeutics and drug screening assays.

For the past 10 years, my work has been structured around the development of microfluidic tools dedicated to 2 different cell types:

- The characterization of **adherent cells** migrating on a substrate was addressed using innovative approaches, combining mechanical and migratory properties of cancer cells.
- **Circulating cells**, passively carried by the flow, have been studied through the detection and therapeutic followup of malaria and the relationship between chemotherapy resistance and mechanical response of acute myeloid leukemia cells.

Phénotypage mécanique de cellules en microsystème pour la détection de pathologies

Mots clefs: Microfluidique ; Phénotypage mécanique ; Globules rouges ; Cellules cancéreuses ; Pathologies ; Diagnostique.

Abstract:
L'une des principales applications du phénotypage mécanique est l'identification des cellules pathologiques. En effet, diverses pathologies et modifications des états cellulaires sont rapportées comme pouvant influencer les propriétés mécaniques des cellules. Par exemple, une variation de déformabilité des globules rouges est associée au paludisme, la déformabilité des globules blancs varie dans la sepstisémie et le syndrome de détresse respiratoire aiguë, une augmentation de la déformabilité des cellules cancéreuses métastatiques a été observée, enfin une baisse de la rigidité au cours de la différenciation des cellules souches a été mise en évidence. Une meilleure compréhension de la déformabilité des cellules et de ses interactions avec l'environnement physique pourrait entraîner d'énormes développements dans le diagnostic des maladies, le suivi thérapeutique et le criblage de médicaments.

Depuis une dizaine d'années, mon travail s'articule autour du développement d'outils microfluidiques dédiés à 2 types cellulaires différents :

- La caractérisation de **cellules adhérentes** migrant sur un substrat, a été abordée en utilisant des approches innovantes, combinant les propriétés mécaniques et migratoires des cellules cancéreuses.

- Les **cellules circulantes**, portées passivement par le flux, ont été étudiées à travers la détection et le suivi thérapeutique du paludisme et le lien entre résistance à la chimiothérapie et réponse mécanique des cellules de leucémie myéloïde aigüe.